THE EFFECTS OF LNG-SLOSHING

ON THE GLOBAL RESPONSES OF LNG-CARRIERS

A Dissertation

by

SEUNG JAE LEE

Submitted to the Office of Graduate Studies of
Texas A&M University
in partial fulfillment of the requirements for the degree of

DOCTOR OF PHILOSOPHY

May 2008

Major Subject: Ocean Engineering

THE EFFECTS OF LNG-SLOSHING

ON THE GLOBAL RESPONSES OF LNG-CARRIERS

A Dissertation

by

SEUNG JAE LEE

Submitted to the Office of Graduate Studies of
Texas A&M University
in partial fulfillment of the requirements for the degree of

DOCTOR OF PHILOSOPHY

Approved by:

Chair of Committee,	Moo-Hyun Kim
Committee Members,	Cheung H. Kim
	Robert E. Randall
	Robert H. Stewart
Head of Department,	David V. Rosowsky

May 2008

Major Subject: Ocean Engineering

ABSTRACT

The Effects of LNG-Sloshing on the Global Responses of LNG-carriers.

(May 2008)

Seung Jae Lee, B.S., Pusan National University; M.S., Pusan National University

Chair of Advisory Committee: Dr. Moo-Hyun Kim

The coupling and interactions between ship motion and inner-tank sloshing are investigated by a potential-viscous hybrid method in time domain. For the time domain simulation of vessel motion, the hydrodynamic coefficients and wave forces are obtained by a potential-theory-based 3D diffraction/radiation panel program in frequency domain. Then, the corresponding simulations of motions in time domain are carried out using the convolution-integral method. The liquid sloshing in a tank is simulated in time domain by a Navier-Stokes solver. A finite difference method with SURF scheme, assuming a single-valued free surface profile, is applied for the direct simulation of liquid sloshing. The computed sloshing forces and moments are then applied as external excitations to the ship motion. The calculated ship motion is in turn inputted as the excitation for liquid sloshing, which is repeated for the ensuing time steps. For comparison, linear inner-fluid motion was calculated using a 3D panel program and it is coupled with the vessel motion program in the frequency domain. The developed computer programs are applied to a barge-type FPSO hull equipped with two partially filled tanks. The time domain simulation results show reasonably good agreement when compared with MARIN's experimental results. The frequency domain results qualitatively reproduce the trend of coupling effects but the peaks are usually over-predicted. It is seen that the coupling effects on roll motions

appreciably change with filling level. The most pronounced coupling effects on roll motions are the shift or split of peak frequencies. The pitch motions are much less influenced by the inner-fluid motion compared to roll motions.

A developed program is also applied to a more realistic offloading configuration where a LNG-carrier is moored with a floating terminal in a side-by-side configuration. First, a hydrodynamic interaction problem between two bodies is solved successfully in frequency and time domain. A realistic mooring system, including fender, hawser, and simplified mooring system, is also developed to calculate the nonlinear behavior of two bodies in time domain simulation. Then, the LNG-carrier and sloshing problem are coupled in frequency and time domain, similar to the method in the MARIN-FPSO case. Sloshing effect on LNG-carrier motion is investigated with respect to different tank filling levels including various conditions such as gap distance between two bodies, selection of dolphin mooring system, and different cases of environmental conditions using wave, wind, and current.

DEDICATION

This dissertation is dedicated,

with love and respect,

to my parents.

ACKNOWLEDGEMENTS

This dissertation would not have been possible without the help and guidance of my advisor, Professor Moo-Hyun Kim. His insight and comments were always helping me complete this dissertation. I also deeply appreciate his continuous encouragement from the start.

I would like to thank Dr. Cheung Hun Kim, Dr. Robert E. Randall, and Dr. Robert H. Stewart for their excellent service as my academic committee advisors. They showed me how to approach a research problem through invaluable academic experiences and challenging questions.

Special thanks to American Bereau of Shipping (ABS) in Houston for supporting valuable projects during my Ph.D study.

Dr. Hae Jin Choi and Dr. Kwang Hyo Jung have never stopped leading me in the right direction with kind and heart filled guidance. I particularly wish their families happy lives all the time. I also owe many thanks to all the members of the Pusan National University alumni in Texas A&M University (PNUaggies) for sharing every moment with me.

Finally, I would like to express my special love and gratitude to my parents. They have been a constant source of my energy. My little sister and brother, Tae-hee and Jun-seok, should also be thanked for their love that will last during my whole life.

TABLE OF CONTENTS

LIST OF FIGURES

LIST OF TABLES

Page

CHAPTER I

INTRODUCTION

In the conventional ship-motion analysis, the effects of inner free surface and its sloshing inside the liquid container are usually ignored. Recent experimental and numerical studies have shown that the coupling effect between liquid cargo sloshing and LNG (Liquefied Natural Gas) ship motion can be significant at certain partial filling levels. This effect is of great concern to the LNG FPSO/FSRU operation in the production site and offloading operation of LNG-carriers close to LNG terminal. The coupling effects are expected to become more important as the size of LNG-carriers significantly increases with greater market demand as shown in Fig. 1.1.
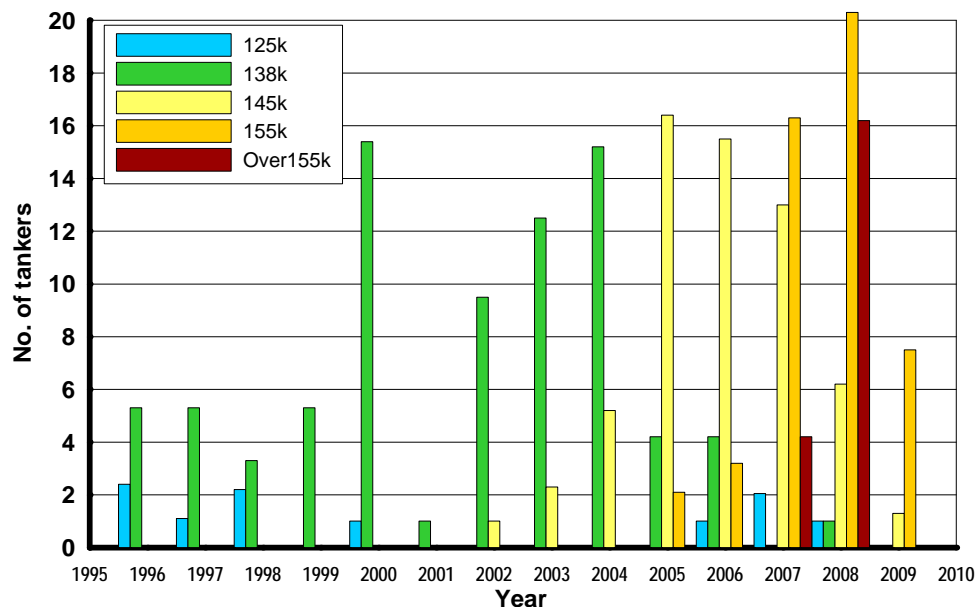
Fig. 1.1 Changing trend of LNG tanker capacity.

This dissertation follows the style and format of the Journal of Ocean Engineering.

The increase of LNG-carrier carrying capacity has caused practical and academic attention to focus on sloshing phenomenon. From a practical point of view, the more complicated nature of sloshing (such as ullage pressure effect, viscous effect, and compressibility effect, ullage vapor condensation, and hydro-elasticity effect) makes the experimental study inevitable. The extension of this experimental data to prototype scale can be categorized as another big topic on it due to limitation of mechanical model size, similitude problem between model and prototype, even different applicable scaling laws of physical properties. From an academic perspective, however, evaluation of local pressure for structural analysis or global force for ship motion analysis by simulation of sloshing fluid is a major concern. In this study, sloshing analysis methods for coupling with ship motion will be investigated in frequency and time domain.

The response of a LNG-carrier during offloading operation is one of the crucial factors to the safety and operability of offshore LNG terminals. Nevertheless, the influence of the time-varying liquid cargo and its sloshing on global tanker motions for various loading conditions has rarely been investigated; as a result, the present study investigates the coupling effects between the vessel and inner-fluid motions in partially filled conditions are investigated in both frequency and time domains.

Faltinsen et al (2000) developed nonlinear sloshing analysis method and Faltinsen and Timokha (2001) have extended this method to multimodal method based on an asymptotic expansion of the fluid response. The method has been developed in detail for 2-D and 3-D flow (Faltinsen et al., 2003) in rectangular tanks.

The coupling between ship motion and sloshing has been studied by Molin et al. (2002), Malenica (2003), and Newman (2005) based on linear potential theory in the

frequency domain. In time domain, Rognebakke and Faltinsen (2003) studied coupling effect in 1-D box-shaped tank and compared it with experiments. Park et al. (2005) calculated sloshing behavior with irregular ship motion without the coupling of ship motion and sloshing phenomenon. Kim et al. (2005) studied the effect of sloshing on ship motion with 2-D sloshing calculation and Lee et al. (2007) studied sloshing effect on ship's roll motion with 3-D calculation of a single tank.

In the present study, a 3D time domain potential-viscous hybrid method for a vessel with multiple tanks has been developed. All the hydrodynamic coefficients of ship motion are calculated by three-dimensional panel method and they are incorporated in the time domain equation through convolution integral and Kramers-Kronig relation. Since the nonlinear viscous sloshing calculation is used in the present paper, the free-surface motion inside the liquid tank is not necessarily small. However, for simplicity, the single-valued surface profile is assumed, and very violent free-surface motions such as overturning and splash are not considered. For comparison, a linear potential program in frequency domain assuming small motions of liquid sloshing has also been independently developed. When the inner-fluid motion is mild, both approaches should produce similar coupling effects unless viscous effects are important. It is reported in Bass et al. (1985) and Lee et al. (2005) that the viscous effect on liquid sloshing motion is not necessarily significant.

When solving the motion of LNG-carrier, linear potential theory and 3D panel method (Lee, 1995) are used under the assumption of small-amplitude ship and wave motions. It is well known that the linear diffraction-radiation potential theory reproduces the vessel motions fairly well, with the exception of the roll. The vessel motions are simulated in time domain using the inverse Fourier transform of the frequency domain

equation (Kim et al., 1999). In the time domain vessel-motion simulation, the nonlinear hull viscous damping is also included.

A FDM-based sloshing analysis program has been used for the numerical simulation of liquid motion inside the tank including impact pressure (Kim, 2001). When the fluid motion is violent, the tank boundaries are exposed to impact loads, in which some local physical phenomena are extremely difficult to reproduce. For example, splash and wave breaking are typical phenomena in violent flows, but too much effort is needed for such a reproduction (Kim, 2001). The primary concern of the sloshing program in this paper is the global fluid motion which causes non-breaking or non-splash loads on the tank wall; therefore, local phenomena with such strong nonlinearity are not considered.

The ship and liquid-cargo motions are coupled by the kinematic and dynamic relations, meaning the vessel motions excite the tank sloshing while the sloshing-induced loads in turn influence vessel motions. The calculated ship motions, both with or without considering liquid sloshing, are then compared with the model test results. The model test was conducted by MARIN as a part of SALT JIP (Gaillarde et al., 2004). The numerical results generally compare well with the measured data.

CHAPTER II

DYNAMICS OF FLOATING STRUCTURES

2.1 Introduction

We will review the wave loads and dynamic response of floating structures based on Boundary Value Problem (BVP). Wave theory of first- and second-order are reviewed and then diffraction theory for floating structures are discussed with first- and second-order potential forces in both frequency and time domain. Morison formula for including inertia and drag force in time domain will be also presented. Finally equation of motion of floating structures is established followed by integration scheme in time domain.

2.2 Wave Theory Formulation

Boundary value problem with kinematic and dynamic boundary conditions need be established and solved for deriving wave theory. Assuming irrotational flow fluid velocity vector can be expressed using velocity potential which is a scalar function. Ignoring viscous effect of fluid, velocity vectors and pressures using velocity potentials are

$$u = \frac{\partial \Phi}{\partial x}, \quad v = \frac{\partial \Phi}{\partial y}, \quad w = \frac{\partial \Phi}{\partial z} \tag{2.1}$$

$$p = -\rho g z - \rho \frac{\partial \Phi}{\partial t} - \frac{1}{2}\left(\Phi_x^2 + \Phi_y^2 + \Phi_z^2\right) \tag{2.2}$$

where u, v and w denote velocity vectors of fluid particle with respect to x, y and z, respectively. The coordinate system is located on mean water level, z is positive upward and x and y axes are on the mean water level following the right hand rule. Equation (2.2)

is expressing pressure p in fluid field using Bernoulli equation where ρ is fluid density and g is gravitational acceleration.

The governing equation with assumption of irrotational, incompressible and continuous flow is provided by Laplace's equation:

$$\nabla^2\Phi = \frac{\partial^2\Phi}{\partial x^2} + \frac{\partial^2\Phi}{\partial y^2} + \frac{\partial^2\Phi}{\partial z^2} = 0 \tag{2.3}$$

A few of boundary conditions are needed to be defined to solve equation (2.3). General boundary conditions for ocean wave problem are introduced. For bottom of the ocean, vertical component of water particle's velocity is zero which means the sea bed is impermeable:

$$\frac{\partial\Phi}{\partial z} = 0 \quad \text{at} \quad z = -d \tag{2.4}$$

where d is water depth. On the free surface, wave is satisfying two boundary conditions: kinematic and dynamic boundary conditions. Kinematic boundary condition states that water particle on the free surface is assumed to remain on free surface:

$$\frac{\partial\eta}{\partial t} + u\frac{\partial\eta}{\partial x} + v\frac{\partial\eta}{\partial y} - \frac{\partial\Phi}{\partial t} = 0 \quad \text{at} \quad z = \eta(x,y,t) \tag{2.5}$$

where $\eta(x,y,t)$ is the free surface elevation in spatial coordinate and time. The dynamic free surface boundary condition is expressed with assumption that the pressure on the free surface must be atmospheric pressure:

$$\rho\frac{\partial\Phi}{\partial t} + \frac{1}{2}\left(\Phi_x^2 + \Phi_y^2 + \Phi_z^2\right) + \rho gz = 0 \quad \text{at} \quad z = \eta(x,y,t) \tag{2.6}$$

The exact solution of Laplace equation with boundary conditions stated above is usually difficult to obtain due to nonlinear terms of free surface boundary conditions. Therefore assuming small wave amplitude compared to wave length and water depth, the perturbation method can be used to obtain approximated solution of acceptable accuracy.

The solution Φ assumed to be expressed as a power series in terms of a non-dimensional perturbation parameter ε:

$$\Phi = \sum_{n=1}^{\infty} \varepsilon^n \Phi^{(n)} \tag{2.7}$$

where $\Phi^{(n)}$ denotes nth order solution of Φ, and ε is wave slope as:

$$\varepsilon = \frac{2A}{L} = \frac{kA}{\pi} \tag{2.8}$$

where A, L, and k is wave amplitude, wave length, and wave number defined as $k=2\pi/L$, respectively. Similarly, wave elevation η can be also expressed as:

$$\eta = \sum_{n=1}^{\infty} \varepsilon^n \eta^{(n)} \tag{2.9}$$

These power series in equation (2.7) and (2.9) are valid asymptotically for small value of ε which means that higher order terms are smaller than the lower order terms.

Substituting equations (2.7) and (2.8) into governing equation (2.3) and expanding kinematic and dynamic boundary conditions into Taylor series about mean water level, then governing equations and boundary conditions can be solved at each order of ε. The summary of linear and second-order wave theory resulting from equations order of ε and ε^2 are as follows.

First-order velocity potential and free surface elevation:

$$\Phi^{(1)} = \mathrm{Re}\left[-\frac{igA}{\omega} \frac{\cosh k(z+d)}{\cosh kd} e^{i(kx\cos\theta + ky\sin\theta - \omega t)} \right] \tag{2.10}$$

$$\eta^{(1)} = A\cos(kx\cos\theta + ky\sin\theta - \omega t) \tag{2.11}$$

Second-order velocity potential and free surface elevation:

$$\Phi^{(2)} = \mathrm{Re}\left[-\frac{3}{8}\omega A^2 \frac{\cosh 2k(z+d)}{\sinh^4 kd} e^{i(2kx\cos\theta + 2ky\sin\theta - 2\omega t)} \right] \tag{2.12}$$

$$\eta^{(2)} = A^2 \frac{\cosh kd}{\sinh^3 kd} \cos(2kx\cos\theta + 2ky\sin\theta - 2\omega t) \tag{2.13}$$

where A is the wave amplitude, ω is the wave frequency, k is the wave number, and θ is the incident wave angle.

The foregoing wave theory for regular ocean waves is applicable to ocean waves simulation in laboratory and to limited types of full scale ocean waves where a swell sea state can be approximated by long-crested regular waves. In the real case of sea state, however, sea state is fully developed by wind and must be irregular. To describe this irregular sea state, various wave spectra such as JONSWAP (Joint North Sea Wave Observation Project) and Pierson-Moskowitz are proposed and used by most of ocean engineers.

The simulated irregular waves using given wave spectrum $S(\omega)$ can be expressed by superposition of large number of linear waves:

$$\eta(x,t) = \sum_{i=1}^{N} A_i \cos(k_i x + \omega_i t + \varepsilon_i) = \text{Re}\left[\sum_{i=1} A_i e^{i(k_i x - \omega_i t + \varepsilon_i)} \right] \tag{2.14}$$

$$A_i = \sqrt{2 \cdot S(\omega) \cdot \Delta\omega} \tag{2.15}$$

where N is number of linear waves, $\Delta\omega$ is frequency interval, and ε_i is phase angle selected by random function. There are various ways of selecting $\Delta\omega$ as presented in Fig. 2.1. In this study, fixed frequency with small random element is being used with small $\Delta\omega$ to avoid repeatability of simulation in time domain.
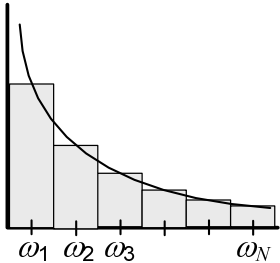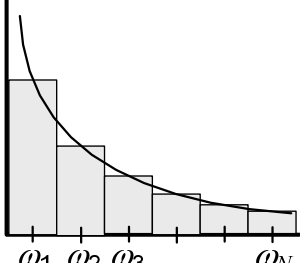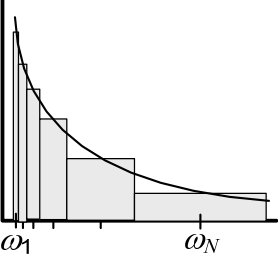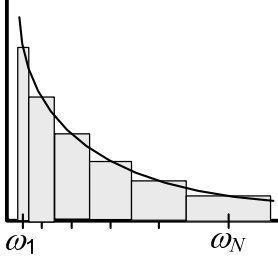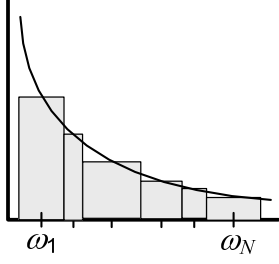
TEqual frequency spacing		
Fixed frequency	Fixed freq. with small random element	

Limit of simulation time: $T_{\max} = \dfrac{2\pi}{\Delta\omega}$

$\omega_i = \omega_k + \delta_i \quad \left(-\dfrac{\Delta\omega_k}{2} \leq \delta_i \leq +\dfrac{\Delta\omega_k}{2} \right)$

Unequal frequency spacing		
Equal Period	Equal Area	Random Frequency (Monte Carlo Method)

$\omega_i = \dfrac{2\pi}{(N-i)\cdot\Delta T}$ $\omega_i = f\left(N, S(\omega)\right)$ $\omega_i = Random$

Large $\Delta\omega$ in high freq.   Analytically integrable $S(\omega)$ Long computation time

Fig. 2.1 Various ways of simulating waves using spectrum.

2.3   Wave Loads on Structures

When water depth is in deep water condition, diffraction of wave around the structure is significant for large-displacement structure such as tanker based FPSO and TLP. Therefore diffraction theory is proposed as most appropriate method to predict wave loads on the structure. On the other hand in case of slender member, Morison's formula is

being used to including inertia and drag forces. In this section, discussion on both diffraction theory and Morison's formula will be presented.

2.3.1 Diffraction and Radiation Theory

Now we review on the boundary value problem for the interaction of incident waves with a large three-dimensional body. In section 2.2, total velocity potential Φ was introduced satisfying Laplace equation in equation (2.3), bottom boundary condition (equation (2.4)), and free surface boundary conditions (equation (2.5) and (2.6)) . When structure is located in fluid domain, the body boundary condition using directional normal vector **n** can be express as

$$\frac{\partial \Phi}{\partial \mathbf{n}} = V_n \quad \text{on body surface} \tag{2.16}$$

where V_n is normal velocity on body surface

Also diffraction potential Φ_D and radiation potential Φ_R should satisfy following Sommerfeld radiation condition at far field boundary which means that diffraction and radiation potential vanish at a great distance from the structure:

$$\lim_{r \to \infty} \sqrt{r} \left(\frac{\partial \Phi_{D,R}}{\partial r} \pm ik\Phi_{D,R} \right) = 0 \tag{2.17}$$

where r is the radial distance from the center of the structure.

Total velocity potential Φ can be decomposed into the incident potential Φ_I, diffraction potential Φ_D, and radiation potential Φ_R. All these decomposed velocity potential can also be written as a perturbation series under assumption of small wave amplitude with respect to the wave slope parameter ε in similar way in Section 2.2.

$$\Phi = \sum_{n=1}^{\infty} \varepsilon^n \Phi^{(n)} = \sum_{n=1}^{\infty} \varepsilon^n \left(\Phi_I^{(n)} + \Phi_D^{(n)} + \Phi_R^{(n)} \right) \tag{2.18}$$

where $\Phi^{(n)}$ denotes nth order solution of Φ, and solutions up to second-order will be discussed in this section.

2.3.2 First-Order Hydrodynamic Forces

The first-order interaction between a monochromatic incident wave and freely floating three dimensional body will be investigated. The total first-order potential can be re-written as:

$$\begin{aligned}\Phi^{(1)} &= \left(\Phi_I^{(1)} + \Phi_D^{(1)} + \Phi_R^{(1)} \right) \\ &= \mathrm{Re}\left\{ \left[\phi_I^{(1)}(x,y,z) + \phi_D^{(1)}(x,y,z) + \phi_R^{(1)}(x,y,z) \right] e^{-i\omega t} \right\}\end{aligned} \tag{2.19}$$

The first-order incident potential $\phi_I^{(1)}$ in equation(2.10) is re-written as:

$$\phi_I^{(1)} = \mathrm{Re}\left[-\frac{igA}{\omega} \frac{\cosh k(z+d)}{\cosh kd} e^{i(kx\cos\theta + ky\sin\theta - \omega t)} \right] \tag{2.20}$$

We can write the boundary value problems for the first-order diffraction $\phi_D^{(1)}$ and radiation potential $\phi_R^{(1)}$:

$$\nabla^2 \phi_{D,R}^{(1)} = 0 \qquad\qquad \text{in the fluid } (z < 0) \tag{2.21}$$

$$\left(-\omega^2 + g \frac{\partial}{\partial z} \right) \phi_{D,R}^{(1)} = 0 \qquad\qquad \text{on the free surface } (z = 0) \tag{2.22}$$

$$\frac{\partial \phi_{D,R}^{(1)}}{\partial z} = 0 \qquad\qquad \text{on the bottom } (z = -d) \tag{2.23}$$

$$\frac{\partial \phi_D^{(1)}}{\partial n} = \frac{\partial \phi_I^{(1)}}{\partial n} \qquad\qquad \text{on the body surface} \tag{2.24}$$

$$\frac{\partial \phi_R^{(1)}}{\partial n} = -i\omega \mathbf{n} \cdot \left(\mathbf{\xi}^{(1)} + \mathbf{\alpha}^{(1)} \times \mathbf{r} \right) \qquad \text{on the body surface} \tag{2.25}$$

$$\lim_{r \to \infty} \sqrt{r} \left(\frac{\partial}{\partial r} \pm ik \right) \phi_{D,R} = 0 \qquad \text{at far field} \tag{2.26}$$

where **r** represents the position vector on body surface, r denotes radian distance from the origin, **n** denotes outward unit normal vector at the body surface. The first-order translational motion $\boldsymbol{\Xi}^{(1)}$ and rotational motion $\boldsymbol{\Theta}^{(1)}$ can be expressed as:

$$\boldsymbol{\Xi}^{(1)} = \mathrm{Re}\left\{\boldsymbol{\xi}^{(1)} e^{-i\omega t}\right\}, \quad \boldsymbol{\xi}^{(1)} = \left\{\xi_1^{(1)}, \xi_2^{(1)}, \xi_3^{(1)}\right\} \tag{2.27}$$

$$\boldsymbol{\Theta}^{(1)} = \mathrm{Re}\left\{\boldsymbol{\alpha}^{(1)} e^{-i\omega t}\right\}, \quad \boldsymbol{\alpha}^{(1)} = \left\{\alpha_1^{(1)}, \alpha_2^{(1)}, \alpha_3^{(1)}\right\} \tag{2.28}$$

where the subscripts 1,2 and 3 in equation (2.27) denote translational mode (surge, sway, and yaw) and in equation (2.28) denote rotational mode (roll, pitch, and yaw) with respect to x-, y-, and z-axis, respectively. Simply we re-write six-degree-of-freedom first-order motion as:

$$\zeta_i = \xi_i^{(1)} \qquad\qquad \text{for } i = 1,2,3 \tag{2.29}$$

$$\zeta_i = \alpha_{i-3}^{(1)} \qquad\qquad \text{for } i = 4,5,6 \tag{2.30}$$

Radiation potential can be decomposed into six-degree-of-freedom mode as:

$$\phi_R^{(1)} = \sum_{i=1}^{6} \zeta_i \phi_i^{(1)} \tag{2.31}$$

where $\phi_i^{(1)}$ represents the first-order velocity potential of the rigid body motion with unit amplitude in the ith mode in the absence of incident waves. These potential $\phi_i^{(1)}$ also should be satisfying all boundary conditions, i.e. bottom boundary condition, free surface boundary condition, far field radiation conditions, and body boundary conditions. The body boundary condition equation (2.25) can be re-written by replacing $\phi_i^{(1)}$,

$$\frac{\partial \phi_i^{(1)}}{\partial n} = n_i \qquad\qquad i=1,2,3 \tag{2.32}$$

$$\frac{\partial \phi_i^{(1)}}{\partial n} = (\mathbf{r} \times \mathbf{n})_{i-3} \qquad\qquad i=4,5,6 \tag{2.33}$$

on the body surface.

We can obtain first-order forces, moments, and free-surface elevation by solving first-order diffraction ($\phi_D^{(1)}$) and radiation ($\phi_R^{(1)}$) potentials. Using perturbation method, first-order hydrodynamic pressure $P(t)$ and free-surface elevation $\eta(t)$ are:

$$P^{(1)} = -\rho \frac{\partial \Phi^{(1)}}{\partial t} \tag{2.34}$$

$$\eta^{(1)} = -\frac{1}{g} \frac{\partial \Phi^{(1)}}{\partial t} \qquad \text{at } z = 0 \tag{2.35}$$

By direct integration over the instantaneous wetted body surface $S(t)$ we can obtain total forces and moments on the body:

$$\mathbf{F}(t)_j = \begin{cases} \iint\limits_{S_B} P n_j \, dS & j=1,2,3 \\ \iint\limits_{S_B} P(\mathbf{r} \times \mathbf{n})_j \, dS & j=4,5,6 \end{cases} \tag{2.36}$$

where, S_B is the wetted body surface when the body is remaining in calm water satisfying first-order boundary value problem. The first-order hydrodynamic forces can be expressed as following different terms.

$$\mathbf{F}^{(1)} = \mathbf{F}_{HS}^{(1)} + \mathbf{F}_R^{(1)} + \mathbf{F}_{EX}^{(1)} \tag{2.37}$$

where $\mathbf{F}_{HS}^{(1)}$ is hydrostatic restoring force and moment, $\mathbf{F}_R^{(1)}$ is force and moment from radiation potential, and $\mathbf{F}_{EX}^{(1)}$ is wave exciting force and moment caused by incident and diffraction potentials.

The hydrostatic restoring forces $\mathbf{F}_{HS}^{(1)}$ represent force and moment induced by hydrostatic pressure change due to the motion of the body. We can write:

$$\mathbf{F}_{HS}^{(1)} = -\mathbf{K}\boldsymbol{\zeta}^{(1)} \tag{2.38}$$

where $\zeta^{(1)}$ is the first-order motion of the body as in equations (2.29) and (2.30), and

K is the hydrostatic restoring stiffness matrix whose components are:

$$K_{33} = \rho g A_w$$

$$K_{34} = K_{43} = \rho g A_w y_f$$

$$K_{35} = K_{53} = -\rho g A_w x_f$$

$$K_{44} = \rho g \left(S_{22} + \forall z_b \right) - mg z_b \qquad (2.39)$$

$$K_{45} = K_{54} - \rho g S_{12}$$

$$K_{46} = -\rho g \forall x_b + mg x_g$$

$$K_{55} = \rho g \left(S_{11} + \forall z_b \right) - mg z_b$$

$$K_{56} = -\rho g \forall y_b + mg y_g$$

where $\forall$ is buoyancy force from the mean body wetted volume, A_w is the water plane

area, (x_f, y_f) is the location of the center of the flotation in the horizontal plane, $(x_g, y_g,$

$z_g)$ is the location of the canter of the gravity, and (x_b, y_b, z_b) is the location of the

canter of the gravity, and

$$S_{11} = \iint_{S_B} x^2 dS$$

$$S_{22} = \iint_{S_B} y^2 dS \qquad (2.40)$$

$$S_{33} = \iint_{S_B} z^2 dS$$

The forces and moment from radiation potential, $\mathbf{F}_R^{(1)}$, comes from added mass and

radiation damping due to first-order motions of the rigid body. We can write:

$$\mathbf{F}_R^{(1)} = \mathrm{Re}\left([\mathbf{f}]\{\boldsymbol{\zeta}^{(1)}\}\right) \tag{2.41}$$

where

$$\mathbf{f} = f_{ij} = -\rho \iint_{S_B} \frac{\partial \phi_i}{\partial n} \phi_j dS \qquad i,j = 1,2,\cdots,6 \tag{2.42}$$

The coefficients f_{ij} are complex as a result of the free surface condition, and the real and imaginary parts depend on the frequency ω. These coefficients can be written as:

$$f_{ij} = -\omega^2 M_{ij}^a - i\omega C_{ij} \tag{2.43}$$

Therefore equation(2.41) can be re-written as:

$$\mathbf{F}_R^{(1)} = \mathrm{Re}\left(\mathbf{M}^a \cdot \ddot{\boldsymbol{\zeta}}^{(1)} + \mathbf{C} \cdot \dot{\boldsymbol{\zeta}}^{(1)}\right) \tag{2.44}$$

where, $\mathbf{M}^a$ is add mass coefficients matrix and $\mathbf{C}$ is radiation damping coefficients matrix.

The last term in equation (2.37), $\mathbf{F}_{EX}^{(1)}$, represents first-order exciting force and moment on the body as follow:

$$\mathbf{F}_{EX}^{(1)} = \mathrm{Re}\left\{-\rho A e^{-i\omega t} \iint_{S_0} (\phi_I + \phi_D)\frac{\partial \phi_j}{\partial n} dS\right\} \qquad j = 1,2,\cdots,6 \tag{2.45}$$

We can see that first-order exciting force and moment are proportional to the incident wave amplitude A and frequency dependent. The exciting forces from a unit amplitude incident wave is called Linear Transfer Function (LTF) which represents relation between incident wave elevation and the first-order diffraction forces on the body.

2.3.3 Second-Order Hydrodynamic Forces

The second-order diffraction and radiation potential provide second-order forces and moments acting on the floating body. The second-order total pressure is:

$$P^{(2)} = -\rho \frac{\partial \Phi^{(2)}}{\partial t} - \frac{1}{2}\rho\left(\nabla\Phi^{(1)}\right)^2 \tag{2.46}$$

Above equation (2.46) can be re-written in the presence of bichromatic waves:

$$P^{(2)} = \mathrm{Re}\left[A_j A_l p_{jl}^+ e^{-i\omega^+ t} + A_j A_l^* p_{jl}^- e^{-i\omega^- t} \right] \tag{2.47}$$

where $p_{jl}^\pm$ represents the sum and difference frequency quadratic transfer functions for the pressure. The complete second-order pressure generally includes two separate contributions: (1) the quadratic products of the first-order potentials p_q, and (2) the second-order potential itself p_p. These two components are given by:

$$p_{jl}^\pm = p_{qjl}^\pm + p_{pjl}^\pm \tag{2.48}$$

$$p_{qjl}^+ = \left[-\frac{1}{4}\rho_0 \nabla\phi_j^{(1)} \cdot \nabla\phi_l^{(1)} \right] \Big/ A_j A_l \tag{2.49}$$

$$p_{qjl}^- = \left[-\frac{1}{4}\rho_0 \nabla\phi_j^{(1)} \cdot \nabla\phi_l^{(1)*} \right] \Big/ A_j A_l^* \tag{2.50}$$

$$p_{pjl}^\pm = \frac{1}{2}\rho_0 i\omega^\pm \phi^\pm \Big/ \left(A_j A_l, A_j A_l^* \right) \tag{2.51}$$

Using given hydrodynamic pressure, the second-order wave force and moment on the body can be obtained by direct integration of the hydrodynamic pressure over the instantaneous wetted body surface, S_B. The second-order force and moment can be written as sum of four different components:

$$\mathbf{F}^{(2)} = \mathbf{F}_R^{(2)} + \mathbf{F}_P^{(2)} + \mathbf{F}_q^{(2)} + \mathbf{F}_{HS}^{(2)} \tag{2.52}$$

where $\mathbf{F}_R^{(2)}$ is contribution from the second-order radiation potential, $\mathbf{F}_P^{(2)}$ is from second-order potential, $\mathbf{F}_q^{(2)}$ is from quadratic product of first-order potential, $\mathbf{F}_{HS}^{(2)}$ is from second-order hydrostatic coefficient. For example, the force components of $\mathbf{F}_P^{(2)}$ and $\mathbf{F}_q^{(2)}$ are:

$$\mathbf{F}_p^{(2)} = -\rho \iint_{S_B} \frac{\partial \Phi}{\partial t} \mathbf{n} dS \tag{2.53}$$

$$\mathbf{F}_p^{(2)} = -\rho \iint_{S_B} \left[\frac{1}{2} \left(\nabla \Phi^{(1)} \right)^2 + \left(\mathbf{\Xi}^{(1)} + \mathbf{\alpha}^{(1)} \times \mathbf{r} \right) \frac{\partial}{\partial t} \left(\nabla \Phi^{(1)} \right) \right] \mathbf{n} dS$$
$$+ \frac{1}{2} \rho g \int_{WL} \left[\eta_r^{(1)} - \left(\xi_3^{(1)} + y\alpha_1^{(1)} - x\alpha_2^{(1)} \right) \right] \mathbf{N} dl + \mathbf{\alpha}^{(1)} \times \mathbf{F}^{(1)} \tag{2.54}$$
$$- \rho g A_w \left[\alpha_2^{(1)} \left(x_f \alpha_1^{(1)} - y_f \alpha_2^{(1)} \right) \right] \mathbf{k}$$

where $\mathbf{N} = \mathbf{n} \big/ (1 - n_3^2)^{\frac{1}{2}}$, $\mathbf{k}$ represents the unit vector in the z-direction, and $\eta_r^{(1)}$ is the relative wave height. The second-order force from radiation and hydrostatics are similar to that of the first-order problem. The wave damping and added mass at the sum- and difference-frequency can be obtained from first-order solutions, and the hydrostatic restoring coefficients are identical to that of the first-order problem. The second-order wave exciting forces in the presence of bichromatic waves can be defined as

$$\mathbf{F}_{EX}^{(2)} = \mathrm{Re} \sum_{j=1}^{2} \sum_{l=1}^{2} \left[A_j A_l f_{jl}^+ e^{-i\omega^+ t} + A_j A_l^* f_{jl}^- e^{-i\omega^- t} \right] \tag{2.55}$$

$$f_{jl}^{\pm} = f_{qjl}^{\pm} + f_{pjl}^{\pm} \tag{2.56}$$

where $f_{jl}^{\pm}$ are the complete sum- and difference-frequency exciting force Quadratic Transfer Functions (QTF). For example, QTF for fixed body can be written as:

$$f_{qjl}^{+} = \left[-\frac{\rho}{4} \iint_{S_B} \left(\nabla \phi_j^{(1)} \cdot \nabla \phi_l^{(1)} \right) n dS - \frac{\rho \omega_j \omega_l}{4} \int_{WL} \phi_j^{(1)} \cdot \phi_l^{(1)} N dl \right] \Big/ A_j A_l \tag{2.57}$$

$$f_{qjl}^{-} = \left[-\frac{\rho}{4} \iint_{S_B} \left(\nabla \phi_j^{(1)} \cdot \nabla \phi_l^{(1)*} \right) n dS - \frac{\rho \omega_j \omega_l}{4} \int_{WL} \phi_j^{(1)} \cdot \phi_l^{(1)*} N dl \right] \Big/ A_j A_l^* \tag{2.58}$$

$$f_{pjl}^{\pm} = \left[\rho i \omega^{\pm} \iint_{S_B} \left(\phi_I^{\pm} + \phi_D^{\pm} \right) n dS \right] \Big/ \left(A_j A_l, A_j A_l^* \right) \tag{2.59}$$

2.3.4   Wave Loads in Time Domain

In this section, I will figure out extending monochromatic and bichromatic solutions which were described in previous section to the random waves. Generally, linear and second-wave hydrodynamic forces on a body under stationary Gaussian random waves can be written as a two term Volterra series in time domain as follow.

$$\mathbf{F}^{(1)}(t) + \mathbf{F}^{(2)}(t) = \int_{-\infty}^{\infty} h_1(\tau)\eta(t-\tau)d\tau + \int_{-\infty}^{\infty} \int_{-\infty}^{\infty} h_2(\tau_1 \tau_2)\eta(t-\tau_1)\eta(t-\tau_2)d\tau_1 d\tau_2 \tag{2.60}$$

where $\eta(t)$ is the wave elevation at the reference point, $h_1(\tau)$ and $h_2(\tau_1\tau_2)$ are linear and quadratic impulse response functions, respectively. We recall that the wave elevation can be written as a sum of frequency components as in equation (2.14). Therefore equation (2.60) can be re-written as a equivalent form in linear and bi-frequency domain. In the presence of unidirectional waves of N components, the wave exciting force due to incident wave and diffraction potentials can be expressed as:

$$\mathbf{F}_I^{(1)}(t) = \mathrm{Re}\left[\sum_{j=1}^{N} A_j \mathbf{L}(\omega_j) e^{i\omega_j t} \right] \tag{2.61}$$

$$\mathbf{F}_I^{(2)}(t) = \mathrm{Re}\left[\sum_{j=1}^{N}\sum_{k=1}^{N} A_j A_k^* \mathbf{D}(\omega_j,\omega_k) e^{i(\omega_j-\omega_k)t} + \sum_{j=1}^{N}\sum_{k=1}^{N} A_j A_k^* \mathbf{S}(\omega_j,\omega_k) e^{i(\omega_j+\omega_k)t}\right] \qquad (2.62)$$

where asterisk(*) denotes complex conjugate, $\mathbf{L}(\omega_j)$ is Linear Transfer Function (LTF),

$\mathbf{D}(\omega_j,\omega_k)$ and $\mathbf{S}(\omega_j,\omega_k)$ are the difference- and sum-frequency Quadratic Transfer

Function (QTF).

When a body is forced to oscillate in fluid, the wave will be generated and

propagating outward the body as time increases. These waves will continuously affect fluid

pressure on the body and this pressure field also affecting force acting on the body for all

subsequent instant. The *time memory effect* concept are introduced to describe force from

radiation potential. The pressure forces acting on the body from radiation potential in time

domain can be expressed as:

$$\mathbf{F}_R = -\mathbf{M}^a(\infty)\ddot{\zeta} - \int_{-\infty}^{t} \mathbf{R}(t-\tau)\dot{\zeta}(\tau)d\tau \qquad (2.63)$$

where $\mathbf{M}^a(\infty)$ is added mass coefficients at infinite frequency, and second term,

convolution integral, represents wave force on the body from the waves generated by body

motion prior to time t. $\mathbf{R}(t)$ is *retardation function* or *time memory function* that is

related to frequency domain solution of the radiation problem. It can be expressed as

follow:

$$\mathbf{R}(t) = \frac{2}{\pi}\int_{0}^{\infty} \mathbf{C}(\omega)\cos(\omega t)d\omega \qquad (2.64)$$

where $\mathbf{C}(\omega)$ is the radiation damping coefficient at frequency ω. Equation (2.64)

represents retardation function $\mathbf{R}(t)$ is Inverse Fourier Transform of radiation damping

coefficient $\mathbf{C}(\omega)$ and, radiation damping coefficient $\mathbf{C}(\omega)$ is, inversely, Fourier

Transform of retardation function $\mathbf{R}(t)$. The added mass coefficient at infinite frequency

can be expressed as:

$$\mathbf{M}^a(\infty) = \mathbf{M}^a(\omega) + \int_0^\infty \mathbf{R}(t)\frac{\sin(\omega t)}{\omega}dt \tag{2.65}$$

where $\mathbf{M}^a(\omega)$ is added mass coefficient at frequency ω.

We can obtain energy spectrum of linear, sum- and difference-frequency diffraction forces using Fourier transform on the equations (2.61) and (2.62) as follows:

$$S_F^{(1)}(\omega) = S_\eta(\omega)|L(\omega)|^2 \tag{2.66}$$

$$S_F^{(2)+}(\omega) = 8\int_0^{\omega/2}\left|S\left(\frac{\omega}{2}+\mu,\frac{\omega}{2}-\mu\right)\right|^2 S_\eta\left(\frac{\omega}{2}+\mu\right)S_\eta\left(\frac{\omega}{2}-\mu\right)d\mu \tag{2.67}$$

$$S_F^{(2)-}(\omega) = 8\int_0^\infty\left|D\left(\mu,\omega-\mu\right)\right|^2 S_\eta(\mu)S_\eta(\omega-\mu)d\mu \tag{2.68}$$

where $S_\eta(\omega)$ is wave amplitude spectrum, $S_F^{(1)}(\omega)$ is linear wave force spectrum, $S_F^{(2)+}(\omega)$ and $S_F^{(2)-}(\omega)$ are the second-order sum- and difference-frequency wave force spectra, respectively.

2.3.5 *Morison's Formula*

In case of slender cylindrical members on the floating platform where the diameter of the member is small compared to the wave length, we usually can neglect diffraction effect and have to consider viscous effect dominantly. In order to solve this problem, the Morison's formula is widely used for calculating wave force in practical sense. In the Morison's formula the wave load, per unit length of the structure, normal to the section of slender structure with diameter D, which is small compared to with the wave length, is expressed by sum of an inertial and drag force:

$$F_n = C_m \rho \frac{\pi D^2}{4} \dot{u}_n - C_a \rho \frac{\pi D^2}{4} \ddot{x}_n + \frac{1}{2} \rho C_d (u_n - \dot{x}_n)|u_n - \dot{x}_n| \tag{2.69}$$

where ρ is density of fluid, C_a is the added mass coefficient, $C_m (=1+C_a)$ is the inertial coefficient and C_d is drag coefficient. $\dot{u}_n$ and u_n are the acceleration and velocity of fluid normal to the structure, respectively, and $\ddot{x}_n$ and $\dot{x}_n$ are acceleration and velocity of structure, respectively. This empirical formula assumes that fluid kinematics are calculated at reference point of structure and fluid is undisturbed by the existence of the structure. First two terms in equation (2.69) are inertia force composed of Froude-Krylov force and added mass effect. The last term in equation (2.69) is drag force with respect to relative velocity between fluid and body motion. This relative velocity term represents drag force contribution to both wave exciting force and damping to the motion of the body. In this study of floating terminal and vessel, viscous effect due to drag force of slow drifting motion is included by using this Morison's formula by arranging plates whose mass is zero along projected area at the direction where viscous effect is needed.

2.4   Motion of Floating Structures

We have discussed, in previous sections, the theory and formulation of prediction of hydrodynamic force on floating structures. In this section, formulation of equation of body motion induced by hydrodynamic forces is introduced and solution in frequency and time domain including numerical integration scheme is established.

2.4.1   Equation of Motion in Regular Waves

From Newton's second law, conservation of momentum, the equilibrium between inertia of the structure and external forces can be expressed as:

$$m\frac{d^2\mathbf{x}_G}{dt^2} = \mathbf{f} \tag{2.70}$$

$$\mathbf{I}\frac{d\varphi}{dt} + \boldsymbol{\omega}\times(\mathbf{I}\boldsymbol{\omega}) = \mathbf{m} \tag{2.71}$$

where m is constant mass of structure, $\mathbf{x}_G = \{x_G, y_G, z_G\}$ is coordinate of body center of gravity, $\mathbf{f}$ and $\mathbf{m}$ is external force and moment, $\mathbf{I}$ is moment of inertia, $\boldsymbol{\omega}$ is angular velocity. If we assume small angular displacement of body motion, nonlinear term $\boldsymbol{\omega}\times(\mathbf{I}\boldsymbol{\omega})$ in equation (2.71) can be negligible. Therefore above two equations can be combined in one linear equation of motion as follows:

$$\mathbf{M}\ddot{\boldsymbol{\zeta}} = \mathbf{F}(t) \tag{2.72}$$

where $\mathbf{F}(t)$ is external forces, such as hydrostatic, hydrodynamic forces, mooring lines forces, sloshing forces. $\ddot{\boldsymbol{\zeta}}$ is acceleration vector of body motion vector $\boldsymbol{\zeta} = \{\zeta_1, \cdots, \zeta_6\}$ in six degree of freedom. Notation $\{\zeta_1, \zeta_2, \zeta_3\}$ represent linear motion of structure at origin in x, y, z direction (surge, sway and heave), and $\{\zeta_4, \zeta_5, \zeta_6\}$ are rotations along x, y, z direction (roll, pitch, and yaw). $\mathbf{M}$ is 6×6 mass matrix of body which is defined as:

$$M_{ij} = \begin{bmatrix} m & 0 & 0 & 0 & mz_G & -my_G \\ 0 & m & 0 & -mz_G & 0 & mx_G \\ 0 & 0 & m & my_G & -mx_G & 0 \\ 0 & -mz_G & my_G & I_{11} & I_{12} & I_{13} \\ mz_G & 0 & -mx_G & I_{21} & I_{22} & I_{23} \\ -my_G & mx_G & 0 & I_{31} & I_{32} & I_{33} \end{bmatrix} \tag{2.73}$$

where $\{x_G, y_G, z_G\}$ is location of center of gravity with respect to origin of body fixed coordinate system. m and I_{ij} are mass and moment of structure, respectively, which is defined as:

$$m = \iiint_{V_B} \rho_B dV \tag{2.74}$$

$$I_{ij} = \iiint_{V_B} \rho_B \left[x \cdot x \delta_{ij} - x_i \cdot x_j \right] dV \tag{2.75}$$

where ρ_B is density of body mass, V_B is the body volume and δ_{ij} is the Kronecker delta function.

2.4.2 Frequency Domain Solution

Equation (2.72) about body motion in six degree of freedom can be rearranged using equations (2.38) and (2.44) as follows:

$$\left[\mathbf{M} + \mathbf{M}^a(\omega) \right] \ddot{\zeta} + \mathbf{C}(\omega)\dot{\zeta} + \mathbf{K}\zeta = \mathbf{F}(\omega) \tag{2.76}$$

where $\mathbf{M}^a(\omega)$ is the added mass matrix, $\mathbf{C}(\omega)$ is wave damping matrix, and $\mathbf{K}$ is the hydrostatic restoring stiffness matrix, and $\mathbf{F}(\omega)$ is external force vector due to wave, mooring, sloshing, etc. In frequency domain where linear superposition rule can be applied, nonlinearity in the system needs to be linearized. For example, viscous roll damping which is the quantity playing important role in ship motion can be included using critical damping. And sloshing effect, even though this is strongly nonlinear phenomenon, can also be linearized and implemented by adding inertia and hydrostatic force into each terms in equation (2.76). The body motions corresponding to the first-order and second-order wave exciting forces can be expressed as:

$$\zeta^{(1)}(\omega) = RAO(\omega) \cdot \mathbf{F}^{(1)}(\omega) \tag{2.77}$$

$$\zeta^{(2)\pm}(\omega^{\pm}) = RAO(\omega^{\pm}) \cdot \mathbf{F}^{(2)\pm}(\omega^{\pm}) \tag{2.78}$$

where $RAO(\omega)$ is the Response Amplitude Operator which is defined as:

$$RAO(\omega) = \left[-\omega^2 \left\{\mathbf{M} + \mathbf{M}^a(\omega)\right\} - i\omega\mathbf{C}(\omega) + \mathbf{K}\right]^{-1} \tag{2.79}$$

Once the $RAO(\omega)$ is obtained, response of the structure in random waves can be also obtained using linear spectrum analysis:

$$S_\zeta(\omega) = |RAO(\omega)|^2 \left[S_F^{(1)}(\omega) + S_F^{(2)\pm}(\omega)\right] \tag{2.80}$$

where $S_\zeta(\omega)$ is structure motion spectrum, $S_F^{(1)}(\omega)$ and $S_F^{(2)\pm}(\omega)$ are the first- and second- order wave force spectra, respectively, which are introduced in equation (2.66) to (2.68).

2.4.3 Time Domain Solution

As we discussed in previous section, solving the equation of motion in frequency domain is straightforward and simple. Even with the linearization of the nonlinear drag forces, where an iterative calculation is needed, frequency domain analysis provides more efficient way than the time domain analysis. In practice, therefore, frequency domain analysis is widely used in initial design stage of structures where optimization of structure is the primary goal. In the detail stage, however, error due to nonlinear quantity in frequency domain analysis may not be acceptable where critical nonlinear effect is significant such as mooring or riser systems. Therefore, time domain analysis is commonly taking advantages in conformal design stage. In this section, derivation of numerical scheme of time domain equation of motion will be presented.

Using equation (2.63), radiation potential force, total external force on structure can be expressed as follows:

$$\left[\mathbf{M} + \mathbf{M}^a(\infty)\right]\ddot{\boldsymbol{\zeta}} + \mathbf{K}\boldsymbol{\zeta} = \mathbf{F_I}(t) + \mathbf{F_C}(t,\dot{\boldsymbol{\zeta}}) + \mathbf{F}_N(t,\dot{\boldsymbol{\zeta}}) \tag{2.81}$$

where $\mathbf{M^a}(\infty)$ is added mass coefficient matrix in equation (2.65), $\mathbf{F_I}(t)$ is first- and second-order wave exciting force on the structure, $\mathbf{F}_N(t,\dot{\zeta})$ is the nonlinear drag forces from Morison's formula, and $\mathbf{F_C}(t,\dot{\zeta})$ is radiation damping force as follows:

$$\mathbf{F_C}(t,\dot{\zeta}) = \int_{-\infty}^{t} R(t-\tau)\dot{\zeta}\,d\tau \tag{2.82}$$

where $R(t)$ is retardation function in equation (2.64). The forces due to mooring lines are not included in this equation and will be discussed in Chapter III.

There are many numerical integration schemes to solve above second-order differential equations. In this study, I will use Adams-Moulton method which provides second-order accuracy to solve the equation. The reason why I use this method is that the finite element analysis of mooring lines is developed using the same method and final coupled equation of structure-mooring lines will be solved together at each time step. In order to apply Adams-Moulton scheme to second-order differential equation (2.81), we can firstly separate this equation into two first-order differential equations as follows.

$$\overline{\mathbf{M}}\dot{\boldsymbol{\xi}} = \mathbf{F_I}(t) + \mathbf{F_C}(t,\dot{\zeta}) + \mathbf{F}_N(t,\dot{\zeta}) - \mathbf{K}\zeta \tag{2.83}$$

$$\dot{\zeta} = \boldsymbol{\xi} \tag{2.84}$$

where $\overline{\mathbf{M}} = \mathbf{M} + \mathbf{M}^{\infty}(\infty)$.

Next, integration of each above equations for time step from $t^{(n)}$ to $t^{(n+1)}$ yields following equations.

$$\overline{\mathbf{M}}\boldsymbol{\xi}^{(n+1)} = \overline{\mathbf{M}}\boldsymbol{\xi}^{(n)} + \int_{t^{(n)}}^{t^{(n+1)}} \left(\mathbf{F_I} + \mathbf{F_C} + \mathbf{F}_N\right)dt + \int_{t^{(n)}}^{t^{(n+1)}} -\mathbf{K}\zeta\,dt \tag{2.85}$$

$$\zeta^{(n+1)} = \zeta^{(n)} + \int_{t^{(n)}}^{t^{(n+1)}} \boldsymbol{\xi}\,dt \tag{2.86}$$

Adams-Moulton scheme I am about to apply is:

$$\int_{t^{(n)}}^{t^{(n+1)}} x\,dt = \frac{\Delta t}{2}\left[x^{(n)} + x^{(n+1)}\right] \tag{2.87}$$

After applying Adams-Moulton scheme to equation (2.85) and (2.86), we have:

$$\overline{\mathbf{M}}\boldsymbol{\xi}^{(n+1)} = \overline{\mathbf{M}}\boldsymbol{\xi}^{(n)} + \frac{\Delta t}{2}\left(\mathbf{F}_I^{(n+1)} + \mathbf{F}_I^{(n)} + \mathbf{F}_C^{(n+1)} + \mathbf{F}_C^{(n)} + \mathbf{F}_N^{(n+1)} + \mathbf{F}_N^{(n)}\right)$$
$$-\frac{\Delta t}{2}\mathbf{K}\left(\boldsymbol{\zeta}^{(n+1)} + \boldsymbol{\zeta}^{(n)}\right) \tag{2.88}$$

$$\boldsymbol{\xi}^{(n+1)} = \frac{2}{\Delta t}\left(\boldsymbol{\zeta}^{(n+1)} - \boldsymbol{\zeta}^{(n)}\right) - \boldsymbol{\xi}^{(n)} \tag{2.89}$$

Now we have two linear algebraic equation with unknown quantities $\boldsymbol{\xi}^{(n+1)}$ and

$\boldsymbol{\zeta}^{(n+1)}$. Here we have to notice that convolution term $\mathbf{F}_C^{(n+1)}$ from retardation function and

drag forces $\mathbf{F}_N^{(n+1)}$ from Morison's formula are unknown variables at time step $t^{(n+1)}$. To

avoid iterative procedure to compute these terms, I introduce Adams-Bashfort scheme for

following nonlinear force terms:

$$\int_{t^{(n)}}^{t^{(n+1)}} \mathbf{F}_C\,dt = \begin{cases} \Delta t\,\mathbf{F}_C^{(0)} & \text{for } n=0 \\ \dfrac{\Delta t}{2}\left(3\mathbf{F}_C^{(n)} - \mathbf{F}_C^{(n-1)}\right) & \text{othewise} \end{cases} \tag{2.90}$$

$$\int_{t^{(n)}}^{t^{(n+1)}} \mathbf{F}_N\,dt = \begin{cases} \Delta t\,\mathbf{F}_N^{(0)} & \text{for } n=0 \\ \dfrac{\Delta t}{2}\left(3\mathbf{F}_N^{(n)} - \mathbf{F}_N^{(n-1)}\right) & \text{othewise} \end{cases} \tag{2.91}$$

Then by combining equation (2.88) to (2.91), we can obtain final integration

equation as follows.

$$\left[\frac{4}{\Delta t^2}\overline{\mathbf{M}} + \mathbf{K}\right]\Delta\boldsymbol{\zeta} = \frac{4}{\Delta t^2}\overline{\mathbf{M}}\boldsymbol{\xi}^{(n)} + \left(\mathbf{F}_I^{(n+1)} + \mathbf{F}_I^{(n)}\right) + \left(3\mathbf{F}_C^{(n)} + \mathbf{F}_C^{(n-1)}\right) + \left(3\mathbf{F}_N^{(n)} + \mathbf{F}_N^{(n-1)}\right)$$
$$- 2\mathbf{K}\boldsymbol{\zeta}^{(n)} + 2\mathbf{F}_0 \tag{2.92}$$

where

$$\Delta\boldsymbol{\zeta} = \boldsymbol{\zeta}^{(n+1)} - \boldsymbol{\zeta}^{(n)} \tag{2.93}$$

and $\mathbf{F}_0$ is constant force such as a net buoyancy force on the structure for balancing the

mooring lines system. Once $\Delta\zeta$ is calculated from equation (2.92), $\xi^{(n+1)}$ and $\zeta^{(n+1)}$ can

be obtained from equation (2.89) and (2.93), respectively. These values are used in

computing the right hand side of equation (2.92) for next time step. While using the

Adams-Bashforth scheme was for the purpose of avoiding iterative procedure, this scheme

may cause numerical instability. To overcome this problem, smaller time step is required

to ensure both numerical stability and accuracy. However, time step to be used in mooring

line analysis is much smaller enough to solve nonlinearity of mooring line and, in this

study, I am using same time step of motion analysis and mooring line analysis. Therefore

time step in solving total equation of motion is generally controlled by mooring analysis

and naturally meets this requirement.

CHAPTER III

MOORING LINE DYNAMICS

3.1   Introduction

In the previous Chapter II, the analysis of the hydrodynamic loads and corresponding motions of a floating structure are presented. Now we will study on analysis of mooring system of floating structures. Various types of mooring lines and systems are used to maintain floating structure's position and avoid drift away from a target position. In this chapter, the theoretical background and numerical formulations of the static and dynamic analysis of mooring lines and risers will be discussed. To import and export oil and gas products, risers are used in connecting between seabed and the platform. These risers also contribute to position keeping of the floating platform, not intended in design purpose. The usage of Steel Catenary Risers (SCR) is recently increasing in deep water platforms due to its effective costs. Therefore risers can be added to mooring system and analyzed in hydrodynamic sense in the same way as mooring lines are using.

The slender rod theory is commonly used for the analysis of mooring line and riser. The advantage of slender rod theory is that single global coordinate system is used to develop governing equation. In this study, we apply the elastic rod theory derived by Nordgen (1974) and Garret (1982), and the formulation and numerical schemes are following RAN (2000) that equations are numerically solved by the finite element method (FEM) in time domain.

3.2 Slender Rod Theory

The slender rod theory uses the position of the center line of rod in space to express deformation of the rod. As illustrated in Fig. 3.1, we can define location vector $\mathbf{r}(s,t)$, where s is the arc length along the rod and t is time.
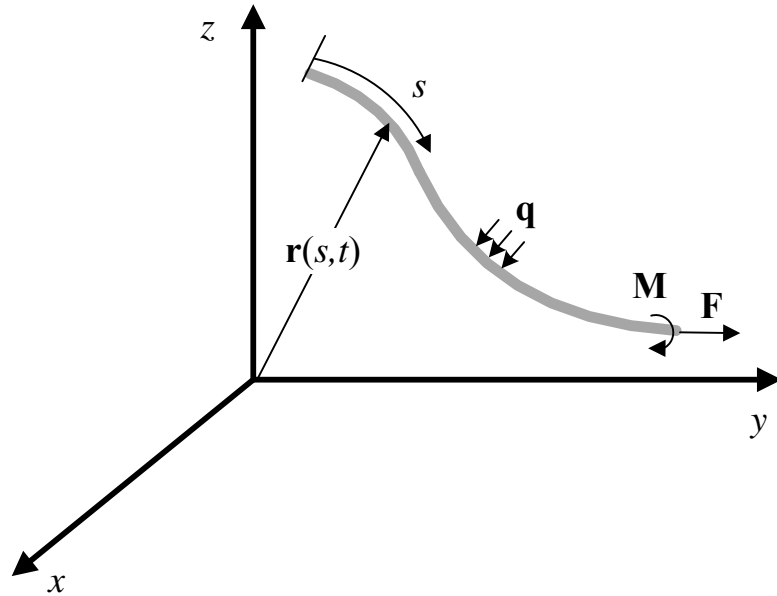
Fig. 3.1 Coordinate system for slender rod.

Firstly we assume rod is inextensible that arc length s is not changing if rod is deformed or not. The equation of motion can be derived using the equilibrium of the linear force and moment for a segment of rod with unit arc length as follows.

$$\mathbf{F}' + \mathbf{q} = \rho \ddot{\mathbf{r}} \tag{3.1}$$

$$\mathbf{M}' + \mathbf{r}' \times \mathbf{F}' + \mathbf{m} = \mathbf{0} \tag{3.2}$$

where prime(') and dot(˙) denotes differential with respect to arc length and time, respectively, $\mathbf{F}$ and $\mathbf{M}$ are force and moment along the center line, respectively, $\mathbf{q}$ is applied force per unit length, ρ is mass of the rod per unit length. For an elastic rod with

equal principle stiffness, the bending moment is proportional to curvature and is directed along the bi-normal. Thus the resultant moment $\mathbf{M}$ can be written as:

$$\mathbf{M}' = \mathbf{r}' \times EI\mathbf{r}'' + H\mathbf{r}' \tag{3.3}$$

where EI is the bending stiffness and H is the torque. By substituting the equation (3.3) into equation (3.2):

$$\mathbf{r}' \times \left[\left(EI\mathbf{r}'' \right)' + \mathbf{F} \right] + H'\mathbf{r}' + H\mathbf{r}'' + \mathbf{m} = \mathbf{0} \tag{3.4}$$

and the scalar product of the above equation with $\mathbf{r}'$ yields:

$$H' + \mathbf{m} \cdot \mathbf{r}' = \mathbf{0} \tag{3.5}$$

By assuming no distributed torsional motion in line element and torque is small enough, H and $\mathbf{m}$ are assumed to be zero. Thus equation (3.4) can be rewritten as:

$$\mathbf{r}' \times \left[\left(EI\mathbf{r}'' \right)' + \mathbf{F} \right] = \mathbf{0} \tag{3.6}$$

Using a scalar function $\lambda(s,t)$, the resulting force in equation (3.6) can be written as:

$$\mathbf{F} = -\left(EI\mathbf{r}'' \right)' + \lambda \mathbf{r}' \tag{3.7}$$

The scalar product of equation (3.7) with $\mathbf{r}'$ is:

$$\lambda = \mathbf{F} \cdot \mathbf{r}' - \left(EI\mathbf{r}'' \right)' \cdot \mathbf{r}' = T - EI\kappa^2 \tag{3.8}$$

where $T = \mathbf{F} \cdot \mathbf{r}'$ is the local tension and $\kappa (\kappa^2 = -\mathbf{r}' \cdot \mathbf{r}''')$ is the local curvature of the rod. Combining equation (3.7) and (3.1):

$$-\left(EI\mathbf{r}'' \right)'' + \left(\lambda \mathbf{r}' \right)' + \mathbf{q} = \rho \ddot{\mathbf{r}} \tag{3.9}$$

Assuming rod in inextensible, the $\mathbf{r}$ must satisfy the inextensibility condition:

$$\mathbf{r}' \cdot \mathbf{r}' = 1 \tag{3.10}$$

If the rod is linear and small extensible, the above inextensibility condition equation (3.10) can be extended:

$$\frac{1}{2}\left(\mathbf{r}'\cdot\mathbf{r}'-1\right)=\frac{T}{AE}\approx\frac{\lambda}{AE} \tag{3.11}$$

The scalar function $\lambda(s,t)$ is called a Lagrangian multiplier and position vector $\mathbf{r}(s,t)$ can be obtained from equation (3.9) through (3.11) with appropriate initial conditions, boundary conditions, and applied force $\mathbf{q}$. The applied force on the rod can be decomposed into the gravity force, hydrostatic force, and hydrodynamic force as follows.

$$\mathbf{q}=\mathbf{w}+\mathbf{F^s}+\mathbf{F^d} \tag{3.12}$$

where $\mathbf{w}$ is the weight of the rod per unit length, $\mathbf{F^s}$ is the hydrostatic force on the rod per unit length, and $\mathbf{F^d}$ is the hydrodynamic force per unit length. The hydrostatic force can be expressed as follows.

$$\mathbf{F^s}=\mathbf{B}-\left(P\mathbf{r}'\right)' \tag{3.13}$$

where $\mathbf{B}$ represents the buoyancy force of the rod per unit length, and the P is the hydrostatic pressure in scalar function at the point $\mathbf{r}$ on the rod.

The hydrodynamic force on the rod can be computed using Morison's formula:

$$\begin{aligned}\mathbf{F^d}&=-C_A\ddot{\mathbf{r}}^n+C_M\dot{\mathbf{V}}^n+C_D\left|\mathbf{V}^n-\dot{\mathbf{r}}^n\right|\left(\mathbf{V}^n-\dot{\mathbf{r}}^n\right)\\&=-C_A\ddot{\mathbf{r}}^n+\overline{\mathbf{F}}^{\mathbf{d}}\end{aligned} \tag{3.14}$$

where C_A is the added mass coefficient of the rod per unit length, C_M is the inertia coefficient of the rod per unit length per unit normal acceleration, C_D is the drag coefficient per unit length per unit normal velocity. $\mathbf{V}^n$ and $\dot{\mathbf{V}}^n$ are fluid particle's velocity and acceleration normal to the rod centerline, which can be expressed as:

$$\mathbf{V}^n = (\mathbf{V} - \dot{\mathbf{r}}) - \left[(\mathbf{V} - \dot{\mathbf{r}}) \cdot \mathbf{r}'\right]\mathbf{r}' \tag{3.15}$$

$$\dot{\mathbf{V}}^n = \dot{\mathbf{V}} - (\mathbf{V} \cdot \dot{\mathbf{r}}) \cdot \mathbf{r}' \tag{3.16}$$

where $\dot{\mathbf{V}}$ and $\mathbf{V}$ are the total fluid particle's acceleration and velocity at the center line of the rod under assumption of undisturbed fluid field by the existence of the rod. The rod's acceleration and velocity normal to its centerline $\ddot{\mathbf{r}}^n$ and $\dot{\mathbf{r}}^n$, in equation (3.14), can be calculated from the following equations:

$$\dot{\mathbf{r}}^n = \dot{\mathbf{r}} - (\dot{\mathbf{r}} \cdot \mathbf{r}')\mathbf{r}' \tag{3.17}$$

$$\ddot{\mathbf{r}}^n = \ddot{\mathbf{r}} - (\ddot{\mathbf{r}} \cdot \mathbf{r}')\mathbf{r}' \tag{3.18}$$

We can combine equations (3.12) through (3.14) with (3.10) to obtain the equation of the rod with its weight, hydrostatic and hydrodynamic forces in fluid.

$$\rho\ddot{\mathbf{r}} + C_a\rho_w\ddot{\mathbf{r}}^n + \left(EI\mathbf{r}''\right)'' - \left(\tilde{\lambda}\mathbf{r}'\right)' = \tilde{\mathbf{w}} + \overline{\mathbf{F}}^d \tag{3.19}$$

where

$$\tilde{\lambda} = T + P - EI\kappa^2 = \tilde{T} - EI\kappa^2 \tag{3.20}$$

$$\tilde{\mathbf{w}} = \mathbf{w} + \mathbf{B} \tag{3.21}$$

$$\tilde{T} = T + P \tag{3.22}$$

and $\tilde{\mathbf{w}}$ denotes effective weight and $\tilde{T}$ denotes effective tension.

3.3   Finite Element Model

The governing equations (3.11) and (3.19) are nonlinear that is difficult to be solved analytically. Therefore, we employ finite element method to solve these equations and can write weak form of (3.19) as follow.

$$\int_0^L \left[A_l \left(\rho \ddot{r}_i + C_a \ddot{r}_i^n \right) + EIA_i'' r_i'' + \tilde{\lambda} A_i' r_i' - A_i \left(\tilde{w}_i + \bar{F}_i^d \right) \right] ds$$
$$= EIr_i'' A_l' \Big|_0^L + \left[\tilde{\lambda} r_i' - \left(Br_i'' \right)' \right] A_l \Big|_0^L \tag{3.23}$$

where A_l is interpolation function, and $U_{il}(t)$ is the unknown coefficient to be solved that are defined as:

$$r_i(s,t) = A_l(s)U_{il}(t) \tag{3.24}$$

and

$$\delta r_i(s,t) = A_l(s)\delta U_{il}(t) \tag{3.25}$$

The linear and small extensibility condition, i.e., equation (3.11) can also be re-written as:

$$\int_0^L P_m \left[\frac{1}{2}(r_r' \cdot r_r' - 1) - \frac{\lambda}{AE} \right] ds = 0 \tag{3.26}$$

where P_m is also interpolation function as follow

$$\lambda(s,t) = P_m(s)\lambda_m(t) \tag{3.27}$$

The cubic shape functions for $A_l(s)$ and quadratic shape function for $P_m(s)$ are defined as follow.

$$\begin{aligned}
A_1 &= 1 - 3\xi^2 + 2\xi^3 \\
A_2 &= L\left(\xi - 2\xi^2 + \xi^3 \right) \\
A_3 &= 3\xi^2 - 2\xi^3 \\
A_4 &= L\left(-\xi^2 + \xi^3 \right)
\end{aligned} \tag{3.28}$$

$$\begin{aligned}
P_1 &= 1 - 3\xi^2 + 2\xi^3 \\
P_2 &= 4\xi(1 - \xi) \\
P_3 &= \xi(2\xi - 1)
\end{aligned} \tag{3.29}$$

where $\xi = \dfrac{s}{L}$.

The position r_i, the tangent r_i', and the Lagrangian multiplier λ are selected to be continuous at the node point between adjacent elements. Therefore the parameters U_{ij} and λ_m are defined as:

$$
\begin{aligned}
&U_{i1} = r_i(0,t), \quad U_{i2} = r_i'(0,t), \\
&U_{i3} = r_i(L,t), \quad U_{i4} = r_i'(L,t), \\
&\lambda_1 = \lambda(0,t), \quad \lambda_2 = \lambda(\frac{L}{2},t), \quad \lambda_3 = \lambda(L,t)
\end{aligned}
\tag{3.30}
$$

Therefore the unknown quantities are to be solved at the position vector and tangent vectors at the two end nodes of the elements, and the scalar function λ. The λ represents the line tension at the end nodes and the midpoint. The equation of motion for the element can be written by substituting equations (3.18), (3.24), and (3.27) into equation (3.23) as follow.

$$
\left(M_{ijlk} + M_{ijlk}^a \right)\ddot{U}_{jk} + \left(K_{ijlk}^1 + \lambda_n K_{nijlk}^2 \right)U_{jk} - \mathbf{F}_{il} = 0
\tag{3.31}
$$

where

$$
M_{ijlk} = \int_0^L \rho A_l A_k \delta_{ij}\,ds
\tag{3.32}
$$

$$
M_{ijlk}^a = C_A \left[\int_0^L A_l A_k \delta_{ij}\,ds - \int_0^L \left(A_l A_k A_s' A_t'\,ds \right)U_{it}U_{js} \right]
\tag{3.33}
$$

$$
K_{ijlk}^1 = \int_0^L EIA_l'' A_k'' \delta_{ij}\,ds
\tag{3.34}
$$

$$
K_{nijlk}^2 = \int_0^L P_n A_l' A_k' \delta_{ij}\,ds
\tag{3.35}
$$

$$
F_{il} = \int_0^L \left(\tilde{w}_i + \bar{F}_i^d \right) A_l\,ds
\tag{3.36}
$$

and δ_{ij} denotes the Kronecker Delta function, M_{ijlk} is mass, M_{ijlk}^{a} is added mass, K_{ijlk}^{1} is the material stiffness that comes from the bending stiffness EI, and K_{nijlk}^{2} is the stiffness from tension and the curvature of the rod. Equation (3.26) can be written as:

$$G_m = A_{mil}U_{kl}U_{ki} - B_m - C_{mn}\lambda_n = 0 \tag{3.37}$$

where

$$A_{mil} = \frac{1}{2}\int_0^L P_m A_l' A_k' ds \tag{3.38}$$

$$B_m = \frac{1}{2}\int_0^L P_m ds \tag{3.39}$$

$$C_{mn} = \frac{1}{AE}\int_0^L P_m P_n ds \tag{3.40}$$

The equations (3.31) and (3.37) are resultant equations of motion which have 12 second-order ordinary differential equations and 3 algebraic equation in 3 dimensional problem. Following sections will discuss the numerical scheme for solving these nonlinear equations.

3.4 Formulation of Static Problem

Before solving governing equations in dynamic problem, static equilibrium problem must be solved, thus fist term in equation (3.31) which is related to time dependency can be ignored and the governing equations of rod become following nonlinear algebraic equations:

$$R_{il} = 0 \tag{3.41}$$

$$G_m = 0 \tag{3.42}$$

where,

$$R_{il} = \left(K^1_{ijlk} + \lambda_n K^2_{nijlk} \right) U_{jk} - \mathbf{F}_{il} \tag{3.43}$$

where $\mathbf{F}_{il}$ is a static forcing term from the gravity force, drag force from the steady current and other applied static forces on the rod. The Newton-Raphson's iterative method is used to solve the nonlinear equations. The equations (3.41) and (3.42) can be expressed as follow using the Taylor series expansion.

$$R_{il}^{(n+1)} = R_{il}^{(n)} + \frac{\partial R_{il}}{\partial U_{jk}} \left(\Delta U_{jk} \right) + \frac{\partial R_{il}}{\partial \lambda_n} \left(\Delta \lambda_n \right) = 0 \tag{3.44}$$

$$G_m^{(n+1)} = G_m^{(n)} + \frac{\partial G_m}{\partial U_{jk}} \left(\Delta U_{jk} \right) + \frac{\partial G_m}{\partial \lambda_n} \left(\Delta \lambda_n \right) = 0 \tag{3.45}$$

Writing above equations in matrix form:

$$\begin{bmatrix} K'^{0(n)}_{ijlk} & K'^{1(n)}_{iln} \\ D'^{0(n)}_{mjk} & D'^{1(n)}_{mn} \end{bmatrix} \left\{ \begin{array}{c} \Delta U_{jk} \\ \Delta \lambda_n \end{array} \right\} = \left\{ \begin{array}{c} -R_{il}^{(n)} \\ -G_m^{(n)} \end{array} \right\} \tag{3.46}$$

where,

$$K'^{0(n)}_{ijlk} = K^1_{ijlk} + \lambda_n^{(n)} K^2_{nijlk} \tag{3.47}$$

$$K'^{1(n)}_{iln} = K^2_{nijlk} U_{jk}^{(n)} = \left(\int_0^L P_n A'_l A'_k ds \right) U_{jk}^{(n)} \tag{3.48}$$

$$D'^{0(n)}_{mjk} = A_{mkp} U_{jp}^{(n)} = \left(\int_0^L P_m A'_k A'_p ds \right) U_{jp}^{(n)} \tag{3.49}$$

$$D'^{1(n)}_{mn} = -C_{mn} = -\frac{1}{AE} \int_0^L P_m P_n ds \tag{3.50}$$

$$R_{il}^{(n)} = \left(K^1_{ijlk} + \lambda_n K^2_{nijlk} \right) U_{jk}^{(n)} - \mathbf{F}_{il} \tag{3.51}$$

$$G_m^{(n)} = \int_0^L P_m \left[\frac{1}{2} \left\{ \left(A'_p U_{rp}^{(n)} \right) \left(A'_q U_{rq}^{(n)} \right) - 1 \right\} - \frac{1}{AE} P_t \lambda_t^{(n)} \right] ds \tag{3.52}$$

Equation (3.46) can be re-written as following form after renumbering by Ran (2000).

$$\mathbf{K}^{(n)}\left(\Delta\mathbf{y}\right) = \mathbf{F}^{(n)} \tag{3.53}$$

where $\mathbf{K}$ represents stiffness matrix and the column vector $\mathbf{y}$ consists of U_{jk} and λ_n as follow.

$$\mathbf{y} = \begin{bmatrix} U_{11} & U_{12} & U_{21} & U_{22} & U_{31} & U_{32} & \lambda_1 & \lambda_2 & U_{13} & U_{14} & U_{23} & U_{24} & U_{33} & U_{34} & \lambda_3 \end{bmatrix}^T \tag{3.54}$$

The force vector $\mathbf{F}$ is expressed as follow.

$$\mathbf{F} = \begin{bmatrix} R_{11} & R_{12} & R_{21} & R_{22} & R_{31} & R_{32} & -G_1 & -G_2 & R_{13} & R_{14} & R_{23} & R_{24} & R_{33} & R_{34} & -G_3 \end{bmatrix}^T \tag{3.55}$$

and

$$\Delta\mathbf{y} = \mathbf{y}^{(n+1)} - \mathbf{y}^{(n)} \tag{3.56}$$

An iterative procedure is applied with initial guess of U and λ to solve equations. The stiffness $\mathbf{K}$ and force vector $\mathbf{F}$ in equation (3.53) are calculated to solve $\Delta\mathbf{y}$ again. This iterative procedure continues until $\Delta\mathbf{y}$ is smaller than tolerance defined in advance.

The force vector $\mathbf{F}$ can be written as follow from right hand side of the equation (3.23):

$$
\mathbf{F}^r = \begin{bmatrix}
-\lambda r_1' + \left(B r_1'' \right)' \big|_{s=0} \\
-EI r_1'' \big|_{s=0} \\
-\lambda r_2' + \left(B r_2'' \right)' \big|_{s=0} \\
-EI r_2'' \big|_{s=0} \\
-\lambda r_3' + \left(B r_3'' \right)' \big|_{s=0} \\
-EI r_3'' \big|_{s=0} \\
0 \\
0 \\
\lambda r_1' - \left(B r_1'' \right)' \big|_{s=L} \\
EI r_1'' \big|_{s=L} \\
\lambda r_2' - \left(B r_2'' \right)' \big|_{s=L} \\
EI r_2'' \big|_{s=L} \\
\lambda r_3' - \left(B r_3'' \right)' \big|_{s=L} \\
EI r_3'' \big|_{s=L} \\
0
\end{bmatrix}
=
\begin{bmatrix}
-N_1^{[1]} \\
-L_1^{[1]} \\
-N_2^{[1]} \\
-L_2^{[1]} \\
-N_3^{[1]} \\
-L_3^{[1]} \\
0 \\
0 \\
-N_1^{[2]} \\
-L_1^{[2]} \\
-N_2^{[2]} \\
-L_2^{[2]} \\
-N_3^{[2]} \\
-L_3^{[2]} \\
0
\end{bmatrix}
\tag{3.57}
$$

where the superscripts [1] and [2] denote the first end of the element ($s = 0$) and the second end ($s = L$) of an element, respectively. $\mathbf{N} = \{N_1, N_2, N_3\}^T$ is the nodal resultant force and $\mathbf{L} = \{L_1, L_2, L_3\}^T$ is the nodal resultant moment $\mathbf{M}(\mathbf{L} \times \mathbf{r}')$. After solving the variables U and λ at $n+1$ step iteratively, the resultant force at the end nodes of an element can be obtained from force vector $\mathbf{F}^r$ and force vector at $n+1$ step, $\mathbf{F}^{(n+1)}$, can be determined as follow.

$$
\mathbf{F}^r = -\mathbf{F}^{(n+1)} \tag{3.58}
$$

3.5 Formulation of Time Domain Dynamic Problem

In order to formulate the dynamic problem, time dependent term that was removed in static problem analysis is recovered, thus we recall equation (3.31) and stretch condition equation (3.37):

$$\widehat{M}_{ijlk}\ddot{U}_{jk} = -\left(K_{ijlk}^1 + \lambda_n K_{nijlk}^2\right)U_{jk} + \mathbf{F}_{il} = \widehat{\mathbf{F}}_{il} \tag{3.59}$$

$$G_m = A_{mil}U_{kl}U_{ki} - B_m - C_{mn}\lambda_n = 0 \tag{3.60}$$

where,

$$\widehat{M}_{ijlk} = M_{ijlk} + M_{ijlk}^a \tag{3.61}$$

$$\widehat{\mathbf{F}}_{il} = -\mathbf{F}_{il}^1 - \mathbf{F}_{il}^2 + \mathbf{F}_{il} \tag{3.62}$$

$$\mathbf{F}_{il}^1 = K_{ijlk}^1 U_{jk} \tag{3.63}$$

$$\mathbf{F}_{il}^2 = \lambda_n K_{nijlk}^2 U_{jk} \tag{3.64}$$

Note that the equation (3.59) is a second-order differential equation and (3.60) is algebraic equation. To solve second-order equation (3.59) numerically, we can establish two first-order ordinary equations as follows:

$$\widehat{M}_{ijlk}\dot{V}_{jk} = \widehat{\mathbf{F}}_{il} \tag{3.65}$$

$$\dot{U}_{jk} = V_{jk} \tag{3.66}$$

Integrating the above two equations from time $t^{(n)}$ to $t^{(n+1)}$ yields:

$$\int_{t^{(n)}}^{t^{(n+1)}} \widehat{M}_{ijlk}\dot{V}_{jk}\,dt = \int_{t^{(n)}}^{t^{(n+1)}} \widehat{F}_{il}\,dt \tag{3.67}$$

$$\int_{t^{(n)}}^{t^{(n+1)}} \dot{U}_{jk}\,dt = \int_{t^{(n)}}^{t^{(n+1)}} V_{jk}\,dt \tag{3.68}$$

Knowing $\widehat{M}_{ijlk}$ contains the added mass which is not the constant with respect to time dependent, however, we approximate the time varying $\widehat{M}_{ijlk}$ in time interval $\Delta t(t^{(n+1)} - t^{(n)})$ to a constant $\widehat{M}_{ijlk}^{(n+\frac{1}{2})}$, that means the mass at $t^{(n)} + \dfrac{\Delta t}{2}$. Then the integrations in equation (3.67) can be simply written within second-order accuracy as

follow:

$$\widehat{M}_{ijlk}^{(n+\frac{1}{2})}\dot{V}_{jk}^{(n+1)} + \widehat{M}_{ijlk}^{(n+\frac{1}{2})}\dot{V}_{jk}^{(n)} = \int_{t(n)}^{t(n+1)} \widehat{\mathbf{F}}_{il}dt \tag{3.69}$$

And the right hand side of the equation (3.68) can be expressed as follows using first-order Adams-Moulton's scheme, or a trapezoidal rule:

$$U_{jk}^{(n+1)} = U_{jk}^{(n)} + \frac{\Delta t}{2}\left(V_{jk}^{(n+1)} + V_{jk}^{(n)}\right) \tag{3.70}$$

Re-arranging equation (3.69) and (3.70)(3.86), we can obtain:

$$\frac{4}{\Delta t^2}\widehat{M}_{ijlk}^{(n+\frac{1}{2})}\Delta U_{jk} = \frac{4}{\Delta t^2}\widehat{M}_{ijlk}^{(n+\frac{1}{2})}V_{jk}^{(n)} + \frac{2}{\Delta t}\int_{t^{(n)}}^{t^{(n+1)}} \widehat{\mathbf{F}}_{il}dt \tag{3.71}$$

$$V_{jk}^{(n+1)} = \frac{2}{\Delta t}\left(\Delta U_{jk}\right) - V_{jk}^{(n)} \tag{3.72}$$

where

$$\Delta U_{jk}^{(n+1)} = U_{jk}^{(n+1)} - U_{jk}^{(n)} = \frac{\Delta t}{2}\left(V_{jk}^{(n+1)} + V_{jk}^{(n)}\right) \tag{3.73}$$

and the integral term in right hand side of equation (3.71) can be expressed as follow:

$$\int_{t^{(n)}}^{t^{(n+1)}} \widehat{\mathbf{F}}_{il}dt = -\int_{t^{(n)}}^{t^{(n+1)}} \mathbf{F}_{il}^1 dt - \int_{t^{(n)}}^{t^{(n+1)}} \mathbf{F}_{il}^2 dt + \int_{t^{(n)}}^{t^{(n+1)}} \mathbf{F}_{il}dt \tag{3.74}$$

Applying trapezoidal rules to first two terms in above equation, we have:

$$\begin{aligned}
\int_{t^{(n)}}^{t^{(n+1)}} \mathbf{F}_{il}^1 dt &= \frac{\Delta t}{2}\left(\mathbf{F}_{il}^{1(n+1)} + \mathbf{F}_{il}^{1(n)}\right) \\
&= \frac{\Delta t}{2}\left[K_{ijlk}^1 \Delta U_{jk} + 2K_{ijlk}^1 U_{jk}^{(n)}\right]
\end{aligned} \tag{3.75}$$

$$\int_{t^{(n)}}^{t^{(n+1)}} \mathbf{F}_{il}^2 dt = \frac{\Delta t}{2}\left(\mathbf{F}_{il}^{2(n+1)} + \mathbf{F}_{il}^{2(n)}\right)$$

$$= \frac{\Delta t}{2}\left[\lambda_n^{(n+1)} K_{nijlk}^2 U_{jk}^{(n+1)} + \lambda_n^{(n)} K_{nijlk}^2 U_{jk}^{(n)}\right]$$

$$\approx \frac{\Delta t}{2}\left[\lambda_n^{(n+\frac{1}{2})} K_{nijlk}^2 U_{jk}^{(n+1)} + \lambda_n^{(n+\frac{1}{2})} K_{nijlk}^2 U_{jk}^{(n)}\right] \tag{3.76}$$

$$= \frac{\Delta t}{2}\left[2\lambda_n^{(n+\frac{1}{2})} K_{nijlk}^2 U_{jk}^{(n)} + 2K_{nijlk}^2 U_{jk}^{(n)}\Delta\lambda_n + \lambda_n^{(n-\frac{1}{2})} K_{nijlk}^2 \Delta U_{jk}\right]$$

where $\Delta\lambda_n = \lambda_n^{(n+\frac{1}{2})} - \lambda_n^{(n-\frac{1}{2})}$. The third term in right hand side of equation (3.74) is including the applied force $\mathbf{F}_{il}$ which is from gravity and hydrodynamic forces. The gravity force is independent of time, but the hydrodynamic force obtained from Morison's formula is unknown at time step $(n+1)$ since this hydrodynamic force is function of the unknown rod position and velocity. Therefore, the Adams-Bashforth explicit scheme can be used as previously introduced:

$$\int_{t^{(n)}}^{t^{(n+1)}} \mathbf{F}_{il} dt = \begin{cases} \Delta t \mathbf{F}_{il}^{(0)} & \text{for } n=0 \\ \dfrac{\Delta t}{2}\left(3\mathbf{F}_{il}^{(n)} - \mathbf{F}_{il}^{(n-1)}\right) & \text{otherwise} \end{cases} \tag{3.77}$$

Combining equations (3.69), (3.70), (3.75), (3.76), (3.77), we have time integral equation of equation (3.59) as follows:

$$\left[\frac{4}{\Delta t^2}\widehat{M}_{ijlk}^{(n+\frac{1}{2})} + K_{ijlk}^1 + \lambda_n^{(n-\frac{1}{2})} K_{nijlk}^2\right]\Delta U_{jk} + 2K_{nijlk}^2 U_{jk}^{(n)}\left(\Delta\lambda_n\right)$$

$$= \frac{4}{\Delta t^2}\widehat{M}_{ijlk}^{(n+\frac{1}{2})} V_{jk}^{(n)} + \left(3\mathbf{F}_{il}^{(n)} - \mathbf{F}_{il}^{(n-1)}\right) - 2\left(K_{ijlk}^1 + \lambda_n^{(n-\frac{1}{2})} K_{nijlk}^2\right)U_{jk}^{(n)} \tag{3.78}$$

The time varying mass term $\widehat{M}_{ijlk}^{(n+\frac{1}{2})}$ can be approximated using Adams-Bashforth scheme:

$$\widehat{M}_{ijlk}^{(n+\frac{1}{2})} = \frac{1}{2}\left(3\widehat{M}_{ijlk}^{(n)} - \widehat{M}_{ijlk}^{(n-1)}\right) \tag{3.79}$$

For the stretch condition equation (3.60), G_m^{n+1} at time step $(n+1)$ can be

approximated from G_m^n at time step (n) using Taylor expansion as follow:

$$
\begin{aligned}
0 &= 2G_m^{(n+1)} \approx 2G_m^{(n)} + 2\frac{\partial G_m}{\partial U_{jk}}\Delta U_{jk} + 2\frac{\partial G_m}{\partial \lambda_n}\Delta \lambda_n \\
&= 2G_m^{(n)} + 2K_{mijlk}^2 U_{il}\Delta U_{jk} - 2C_{mn}\Delta \lambda_n \\
&= 2G_m^{(n)} + \widehat{D}_{mjk}^{t0(n)}\Delta U_{jk} - 2\widehat{D}_{mn}^{t1(n)}\Delta \lambda_n
\end{aligned}
\tag{3.80}
$$

Note that equation is multiplied by 2, for the numerical convenience, to make element stiffness matrix symmetric. The equation of motion (3.78) and stretch condition equation (3.80) can be re-written in a similar matrix form to the static problem analysis.

$$
\begin{bmatrix} \widehat{K}_{ijlk}^{t0(n)} & \widehat{K}_{lin}^{t1(n)} \\ \widehat{D}_{mjk}^{t0(n)} & \widehat{D}_{mn}^{t1(n)} \end{bmatrix}
\begin{Bmatrix} \Delta U_{jk} \\ \Delta \lambda_n \end{Bmatrix} =
\begin{bmatrix} \widehat{R}_{il} \\ -\widehat{G}_m \end{bmatrix}
\tag{3.81}
$$

where

$$
\widehat{K}_{ijlk}^{t0(n)} = \frac{2}{\Delta t^2}\left(3\widehat{M}_{ijlk}^{(n)} - \widehat{M}_{ijlk}^{(n-1)}\right) + K_{ijlk}^1 + \lambda_n^{(n-\frac{1}{2})}K_{nijlk}^2
\tag{3.82}
$$

$$
\widehat{K}_{lin}^{t1(n)} = 2K_{nijlk}^2 U_{jk}^{(n)}
\tag{3.83}
$$

$$
\widehat{D}_{mjk}^{t0(n)} = 2K_{nijlk}^2 U_{jk}^{(n)}
\tag{3.84}
$$

$$
\widehat{D}_{mn}^{t1(n)} = 2D_{mn}^{t1(n)}
\tag{3.85}
$$

$$
\begin{aligned}
\widehat{R}_{il} &= \frac{2}{\Delta t^2}\left(3\widehat{M}_{ijlk}^{(n)} - \widehat{M}_{ijlk}^{(n-1)}\right) + \left(3\mathbf{F}_{il}^{(n)} - \mathbf{F}_{il}^{(n-1)}\right) \\
&\quad -2\left(K_{ijlk}^1 + \lambda_n^{(n-\frac{1}{2})}K_{nijlk}^2\right)U_{jk}^{(n)}
\end{aligned}
\tag{3.86}
$$

$$
\widehat{G}_m^{(n)} = 2G_m^{(n)}
\tag{3.87}
$$

The formulation of coefficients in above equations, such as K_{ijlk}^1, K_{nijlk}^2 and $G_m^{(n)}$, are same as those in static formulation, while superscript n in dynamic analysis indicates nth time step instead of nth iteration in static analysis. The final equation of motion for a

rod element can be written in a matrix form as follows:

$$\widehat{\mathbf{K}}^{(n)}\left(\Delta \mathbf{y}\right) = \widehat{\mathbf{F}}^{(n)} \qquad \text{at time step } n \tag{3.88}$$

where $\mathbf{y}$ is written in equation (3.54), $\widehat{\mathbf{K}}$ and $\widehat{\mathbf{F}}$ are similar to those in static problem.

And also nodal resultant force can be obtained as follow.

$$\mathbf{F}^r = -\widehat{\mathbf{F}}^{(n+1)} \tag{3.89}$$

3.6   Modeling of the Seabed

In general catenary mooring system, mooring lines or risers near the anchor may lie on the seabead. Interaction between seabed and steel catenary riser (SCR) is very important in riser design purpose. In this section, modeling of interaction between mooring lines/riser and seabed playing an important part in numerical analysis will be discussed.

The horizontal friction effect between line and seabed is neglected in numerical modeling. In the vertical direction, however, the seabed can be modeled as a quadratic elastic spring in vertical direction. Locating mean water level on the x-y plane, interaction force vector $\mathbf{f} (= f_x \mathbf{i} + f_y \mathbf{j} + f_z \mathbf{k})$ can be expressed as:

$$f_x = 0 , f_y = 0 , f_z = \begin{cases} c(r_z - D)^2 & \text{for } r_z - D < 0 \\ 0 & \text{for } r_z - D \geq 0 \end{cases} \tag{3.90}$$

where D represents the water depth or vertical distance between the seabed and the origin of coordinate system, and r_z is the z-component of the position vector $\mathbf{r} (= r_x \mathbf{i} + r_y \mathbf{j} + r_z \mathbf{k})$ of the line. Including seabed interaction force vector $\mathbf{F}_{il}^{sb}$, the equation of motion (3.31) is re-written as follows:

$$\left(M_{ijlk} + M^{a}_{ijlk} \right) \ddot{U}_{jk} + \left(K^{1}_{ijlk} + \lambda_{n} K^{2}_{nijlk} \right) U_{jk} = F_{il} + \mathbf{F}^{sb}_{il} \tag{3.91}$$

where

$$
\begin{aligned}
\mathbf{F}^{sb}_{il} &= \begin{cases} \int_{0}^{L} A_{l} \delta_{i3} c (r_{3} - D)^{2} & \text{for } r_{3} - D < 0 \\ 0 & \text{for } r_{3} - D \geq 0 \end{cases} \\
&= \begin{cases} \int_{0}^{L} A_{l} \delta_{i3} c (\delta_{i3} A_{k} U_{jk} - D)^{2} & \text{for } r_{3} - D < 0 \\ 0 & \text{for } r_{3} - D \geq 0 \end{cases}
\end{aligned} \tag{3.92}
$$

and, δ_{i3} is Kronecker Delta function as follow:

$$\delta_{i3} = \begin{cases} 1 & \text{for } i=3 \\ 0 & \text{otherwise} \end{cases} \tag{3.93}$$

For the static analysis, the stiffness matrix is modified as follows using Newton's method:

$$
\begin{aligned}
K^{3}_{ijlk} &= \frac{\partial \mathbf{F}^{sb}_{il}}{\partial U_{jk}} \\
&= \begin{cases} \int_{0}^{L} 2 A_{l} \delta_{i3} c \delta_{j3} A_{k} (\delta_{m3} A_{n} U^{(n)}_{mn} - D)^{2} & \text{for } r_{3} - D < 0 \\ 0 & \text{for } r_{3} - D \geq 0 \end{cases}
\end{aligned} \tag{3.94}
$$

Above additional stiffness K^{3}_{ijlk} due to seabed interaction is added to K^{t0}_{ijlk} defined in equation (3.46). In the time domain analysis, time integral of seabed interaction force vector $\mathbf{F}^{sb}_{il}$ can be carried out using the trapezoidal rule and the stiffness matrix modified as follows:

$$\int_{t^{(n)}}^{t^{(n+1)}} \mathbf{F}^{sb}_{il} dt = \frac{\Delta t}{2} \left(\mathbf{F}^{f(n+1)}_{il} + \mathbf{F}^{f(n)}_{il} \right) = \frac{\Delta t}{2} \left[K^{3}_{ijlk} \Delta U_{jk} + 2 \mathbf{F}^{sb(n)}_{il} \right] \tag{3.95}$$

Therefore, equation of motion in time domain, equation (3.78), can include seabed effect as follow:

$$\left[\frac{4}{\Delta t^2} \widehat{M}_{ijlk}^{\left(n+\frac{1}{2}\right)} + K_{ijlk}^1 + \lambda_n^{\left(n-\frac{1}{2}\right)} K_{nijlk}^2 \right] \Delta U_{jk} + 2 K_{nijlk}^2 U_{jk}^{(n)} \left(\Delta \lambda_n \right)$$

$$= \frac{4}{\Delta t^2} \widehat{M}_{ijlk}^{\left(n+\frac{1}{2}\right)} V_{jk}^{(n)} + \left(3\mathbf{F}_{il}^{(n)} - \mathbf{F}_{il}^{(n-1)} + 2\mathbf{F}_{il}^{sb(n)} \right) - 2\left(K_{ijlk}^1 + \lambda_n^{\left(n-\frac{1}{2}\right)} K_{nijlk}^2 \right) U_{jk}^{(n)}$$

(3.96)

CHAPTER IV

COUPLING SHIP MOTION AND SLOSHING PROBLEMS

4.1 Introduction

In this chapter, coupling ship motion and sloshing problem is done in two domains: frequency domain and time domain. Fig. 4.1 illustrates how two problems are coupled in both frequency and time domain by stating each program module that is being used.
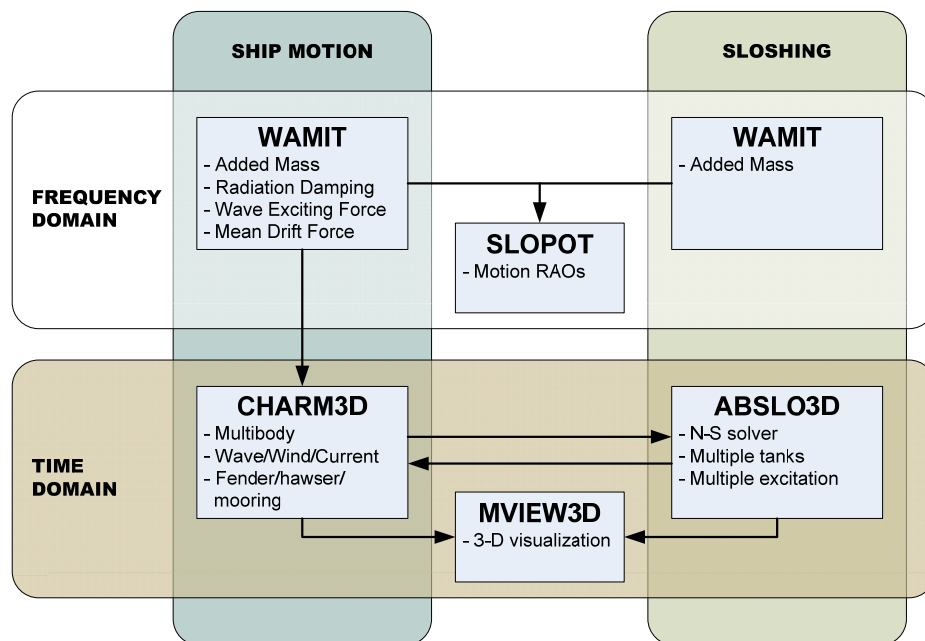
Fig. 4.1 Big picture of ship motion and sloshing coupling.

4.2 Frequency Domain Calculation

Now, in Chapter IV and V, we will discuss the coupling ship motion problem and sloshing problem in both frequency domain and time domain, respectively. In this chapter, two problems are combined in frequency domain where the linear potential theory is valid.

To calculate hydrodynamic coefficients in frequency domain, the 3-D potential panel method program WAMIT is used. Sloshing phenomenon is implemented into frequency domain by calculating added mass and hydrostatic correction due to the existence of inner free surface of floating structure. Finally, these two problems are combined into an equation of motion and solved to get ship motion RAO. The verification of coupling two problems in frequency domains will be done by comparing them with the results of the MARIN-FPSO experiment. The model FPSO was equipped with two sloshing tank and experiments are carried out for various filling levels and wave environmental conditions. Since this experiment is a part of SALT-JIP, some of the experimental data are presented only for comparison with calculation without scale on data.

4.2.1   Ship Motion

4.2.1.1   Hydrodynamic Coefficients

In the frequency domain ship motion calculation, a panel-based 3D diffraction and radiation program, called WAMIT, is used to obtain hydrodynamic coefficients and linear/drift wave forces. The detailed mathematical background has been discussed in Chapter II.

4.2.1.2   Effect of Irregular Frequency

In the linear potential solution by integral equation method, we may have erroneous results at discrete frequencies called irregular frequencies, whose behavior is similar to that of resonance. This phenomenon is due to non-uniqueness of integral equation at irregular frequencies corresponding to the Dirichlet eigen frequencies for the closed domain defined by the interior free surface inside the body boundary. F. John

(1950) demonstrated that irregular frequencies occurred when the following adjoint interior-potential problem had eigen frequencies as shown in Fig. 4.2.

$$\psi(x,T) = \frac{\psi_y(x,T)}{k_n^{irr}}$$

$$\psi(o,y) = 0 \qquad \nabla^2\psi(x,y) = 0 \qquad \psi(B,y) = 0$$

$$\psi(x,0) = 0$$

Fig. 4.2 Adjoint interior boundary value problem

Interior potential $\psi(x,y)$ satisfies the fo llowing conditions:

Inside the cylinder in the region bounded by the immersed surface of the body and the extension of the free surface inside the cylinder;

$$\nabla^2\psi = \frac{\partial^2\psi}{\partial x^2} + \frac{\partial^2\psi}{\partial y^2} = 0 \tag{4.1}$$

On the extension of the free surface inside the cylinder, k_n^{irr} being the wave number corresponding to the irregular frequency ω_n^{irr}, $n=1,2,3\ldots$;

$$\psi_y - k_n^{irr}\psi = 0 \tag{4.2}$$

On the surface of the cylinder below the free surface.

$$\psi = 0 \tag{4.3}$$

In summary, boundary conditions for a rectangular section with bean B and draft T are:

$$\psi(o, y) = 0 \qquad\qquad \text{on Left} \qquad\qquad (4.4)$$

$$\psi(B, y) = 0 \qquad\qquad \text{on Right} \qquad\qquad (4.5)$$

$$\psi(x,T) = \frac{\psi_y(x,T)}{k_n^{irr}} \qquad\qquad \text{on Free surface} \qquad\qquad (4.6)$$

$$\psi(x,0) = 0 \qquad\qquad \text{on Bottom} \qquad\qquad (4.7)$$

The irregular wave frequency can be obtained by separation of variables in the Laplace equation. Eigen function can be written using separating variables such as:

$$\psi(x, y) = \sum_{n=1}^{\infty} b_n(y) \cdot \sin\left(\frac{n\pi x}{B}\right) \qquad\qquad (4.8)$$

$$\begin{cases} \dfrac{\partial^2 \psi}{\partial x^2} = -\sum_{n=1}^{\infty} \dfrac{n^2 \pi^2}{B^2} b_n(y) \cdot \sin\left(\dfrac{n\pi x}{B}\right) \\[4mm] \dfrac{\partial^2 \psi}{\partial y^2} = \sum_{n=1}^{\infty} b_n''(y) \cdot \sin\left(\dfrac{n\pi x}{B}\right) \end{cases} \qquad\qquad (4.9)$$

Governing equation (4.1) can be expressed as follow by using equation (4.9):

$$\sum_{n=1}^{\infty} b_n''(y) \cdot \sin\left(\frac{n\pi x}{B}\right) - \sum_{n=1}^{\infty} \frac{n^2 \pi^2}{B^2} b_n(y) \cdot \sin\left(\frac{n\pi x}{B}\right) = 0 \qquad\qquad (4.10)$$

$$b_n''(y) - \frac{n^2 \pi^2}{B^2} b_n(y) = 0 \qquad\qquad (4.11)$$

$$b_n(y) = A_n e^{\frac{n\pi}{B} y} + C_n e^{-\frac{n\pi}{B} y} \qquad\qquad (4.12)$$

Therefore solution equation (4.8) is:

$$\psi(x, y) = \sum_{n=1}^{\infty} \left\{ \left(A_n e^{\frac{n\pi}{B} y} + C_n e^{-\frac{n\pi}{B} y} \right) \cdot \sin\left(\frac{n\pi x}{B}\right) \right\} \qquad\qquad (4.13)$$

Eigenfunction is:

$$\psi_n(x, y) = \left(A_n e^{\frac{n\pi}{B} y} + C_n e^{-\frac{n\pi}{B} y} \right) \cdot \sin\left(\frac{n\pi x}{B}\right) \qquad\qquad (4.14)$$

Applying bottom boundary condition $\psi(x,0) = 0$ to equation (4.14):

$$\left(A_n + C_n\right) \cdot \sin\left(\frac{n\pi x}{B}\right) = 0 \tag{4.15}$$

$$C_n = -A_n \tag{4.16}$$

Therefore equation (4.14) is,

$$\begin{aligned}
\psi_n(x, y) &= \left(A_n e^{\frac{n\pi}{B}y} + C_n e^{-\frac{n\pi}{B}y}\right) \cdot \sin\left(\frac{n\pi x}{B}\right) \\
&= A_n \left(e^{\frac{n\pi}{B}y} - e^{-\frac{n\pi}{B}y}\right) \cdot \sin\left(\frac{n\pi x}{B}\right) \\
&= A_n \cdot 2 \cdot \sinh\left(\frac{n\pi}{B}y\right) \cdot \sin\left(\frac{n\pi x}{B}\right)
\end{aligned} \tag{4.17}$$

Again, applying free surface boundary condition to equation (4.17)

$$\psi(x, T) = \frac{\psi_y(x, T)}{k_n^{irr}} \quad \text{at} \quad y = T \tag{4.18}$$

$$\begin{cases}
\psi_y(x, T) = \dfrac{\partial \psi(x, T)}{\partial y} = \dfrac{n\pi}{B} \cdot A_n \cdot 2 \cdot \cosh\left(\dfrac{n\pi}{B}T\right) \cdot \sin\left(\dfrac{n\pi x}{B}\right) \\[3mm]
\psi(x, T) = A_n \cdot 2 \cdot \sinh\left(\dfrac{n\pi}{B}T\right) \cdot \sin\left(\dfrac{n\pi x}{B}\right)
\end{cases} \tag{4.19}$$

$$k_n^{irr} = \frac{\psi_y(x, T)}{\psi(x, T)} = \frac{n\pi}{B} \frac{\cosh\left(\dfrac{n\pi}{B}T\right)}{\sinh\left(\dfrac{n\pi}{B}T\right)} = \frac{n\pi}{B} \coth\left(\frac{n\pi}{B}T\right) \tag{4.20}$$

Finally, irregular wave number k_n^{irr} and frequency ω_n^{irr} from disperse relation

are:

$$k_n^{irr} = \frac{n\pi}{B} \coth\left(\frac{n\pi}{B}T\right) \tag{4.21}$$

$$\omega_n^{irr} = \sqrt{k_n^{irr} g \tanh(k_n^{irr} T)} \tag{4.22}$$

Calculated irregular frequencies of LNGC-145K are shown in Table 4.1.

Table 4.1 Irregular frequencies of LNGC-145K.

mode (n)	Transverse mode			Longitudinal mode				
	1	2	3	1	2	3	4	5
wave number (k_n^{irr})	0.104	0.154	0.220	0.084	0.086	0.089	0.092	0.097
Irregular frequency (ω_n^{irr}) [rad/s]	0.93	1.20	1.46	0.80	0.81	0.83	0.85	0.88

In the present simulation, I used the BEM program where the irregular frequencies are numerically removed. For example, the effect of irregular frequency on radiation damping coefficients and Linear Transfer Function (LTF) of LNG-carrier (LNG-145K) is presented in Fig. 4.3 and Fig. 4.4. Using irregular frequency option, we can observe that irregular frequency around 0.95rad/s and 1.2 rad/s is removed safely and all hydrodynamic coefficients are used with irregular frequency removal in this study.
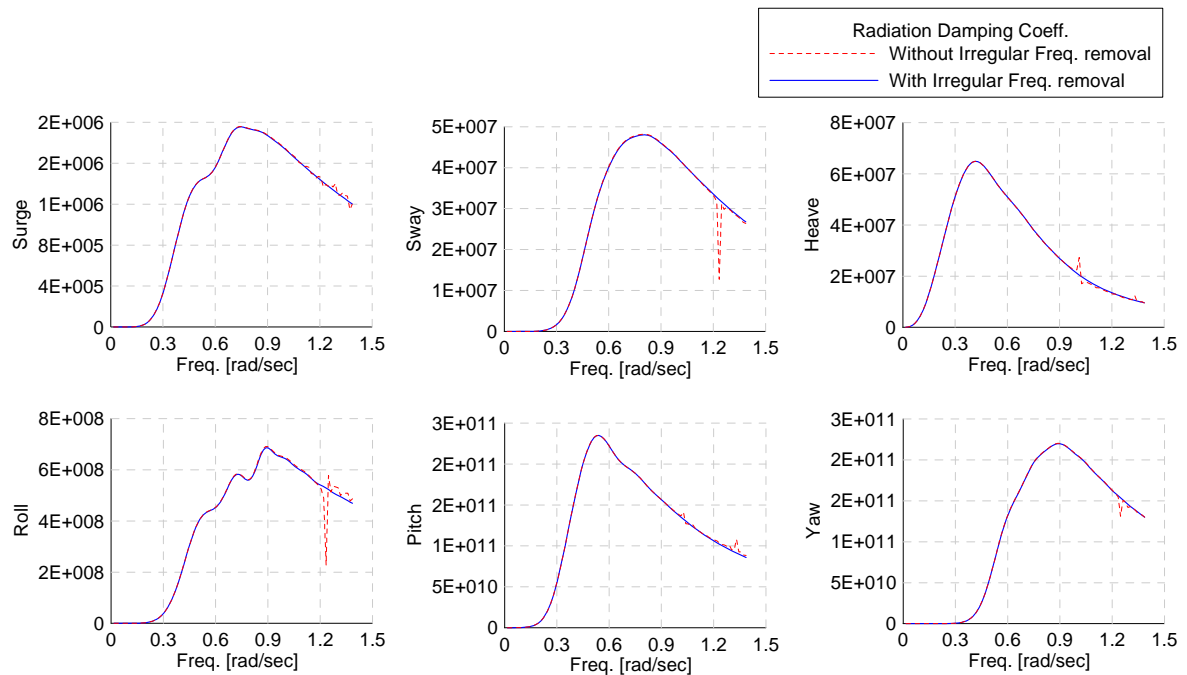
Fig. 4.3 Radiation damping coefficient of LNGC-145K.
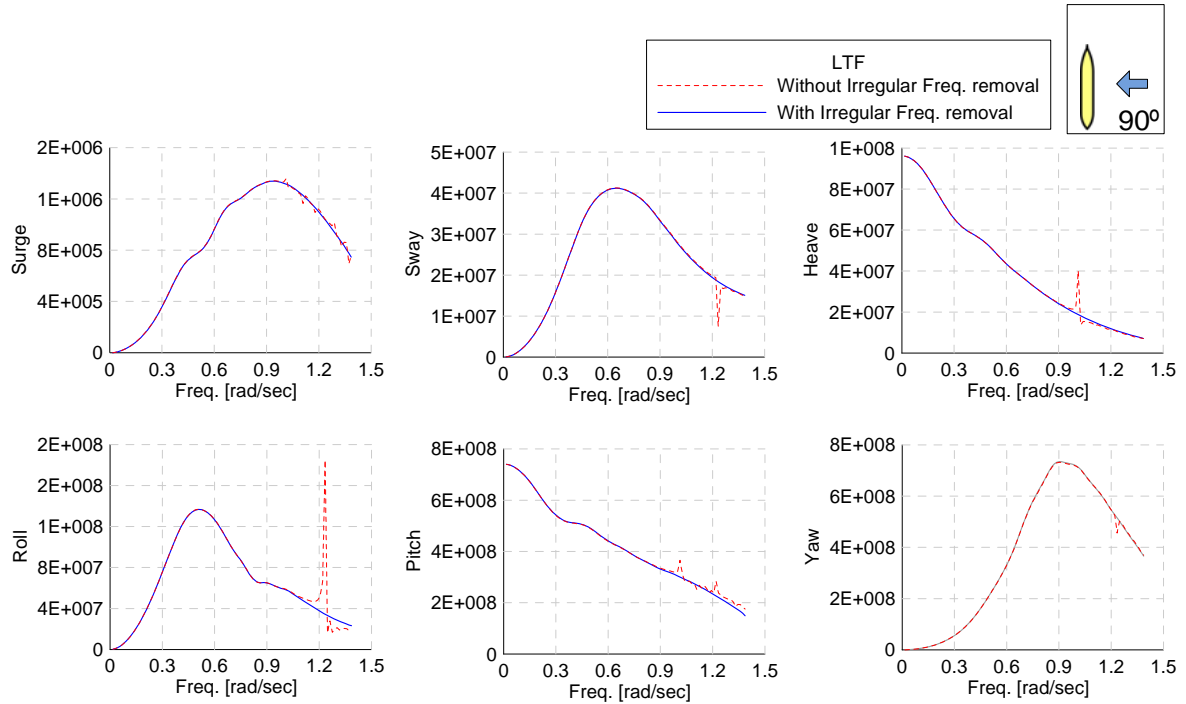
Fig. 4.4 Linear transfer function of LNGC-145K.

4.2.2   *Sloshing Analysis in Frequency Domain*

In most of the cases of sloshing phenomenon, inertia effect is dominant except very low filling level in which viscous damping of sloshing fluid is playing significant role. When sloshing is taken into frequency domain problem, two things are needed: inertia of sloshing fluid and restoring stiffness correction due to the presence of inner free surface inside the tank. Since potential theory is used to calculate added mass, viscous damping of sloshing fluid is not considered in this study.

4.2.2.1   **Analytic Sloshing Natural Frequency**

Natural frequency of sloshing tank at each mode, as shown in Fig. 4.5, can be obtained from disperse relation of the wave.
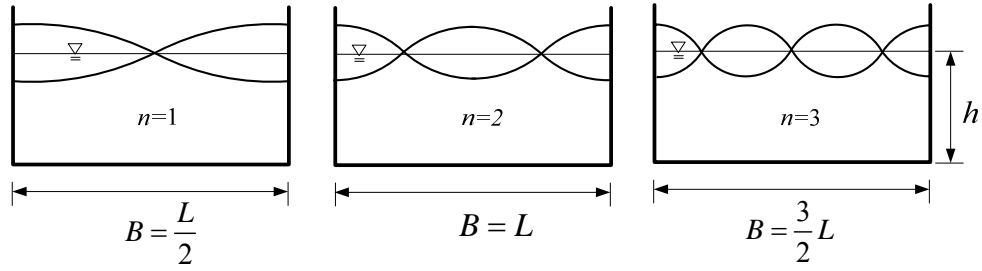
Fig. 4.5 Transverse natural frequency of sloshing tank.

From disperse relation for general water depth,

$$\omega^2 = kg \tanh(kh) \tag{4.23}$$

where ω is wave frequency, k is wave number, g is gravitational acceleration, and h is water depth. Replacing wave frequency and wave number with period and wave length:

$$\left(\frac{2\pi}{T}\right)^2 = \left(\frac{2\pi}{L}\right) g \tanh\left(\frac{2\pi}{L} h\right) \tag{4.24}$$

Then wave period is,

$$T = \frac{2\pi}{\sqrt{\left(\frac{2\pi}{L}\right) g \tanh\left(\frac{2\pi}{L} h\right)}} = \frac{\sqrt{2\pi L}}{\sqrt{g \tanh\left(\frac{2\pi}{L} h\right)}} \tag{4.25}$$

Relation between wave length and breadth of tank is,

$$B = \frac{n}{2} L \quad , \quad L = \frac{2}{n} B \tag{4.26}$$

Finally, natural period for each mode is,

$$T_n = \frac{\sqrt{2\pi \left(\frac{2}{n} B\right)}}{\sqrt{g \tanh\left(\frac{2\pi}{\left(\frac{2}{n} B\right)} h\right)}} = \frac{\sqrt{\frac{4\pi B}{n}}}{\sqrt{g \tanh\left(\frac{n\pi h}{B}\right)}} = \frac{2\sqrt{\pi B}}{n\sqrt{g \tanh\left(\frac{n\pi h}{B}\right)}} \tag{4.27}$$

4.2.2.2 Added Mass of Sloshing Fluid

When considering the dynamic effects of sloshing phenomenon, the inertia force is more important than damping or restoring forces. In this regard, the added mass of sloshing fluid is shown in Fig. 4.7. The 3D panel method was also used in the calculation of the added mass of sloshing fluid. Fig. 4.6 shows an example of the grid generation for sloshing tanks at the filling level of 37%. When plural tanks are equipped on a single hull, we can calculate the total added mass of each tank's sloshing fluid at a time by generating each tank's grid together as shown in Fig. 4.6. Grid generation needs to be done from the bottom of tank up to the free surface of sloshing fluid, meaning each different filling level needs each grid generation to represent the added mass of sloshing fluid.
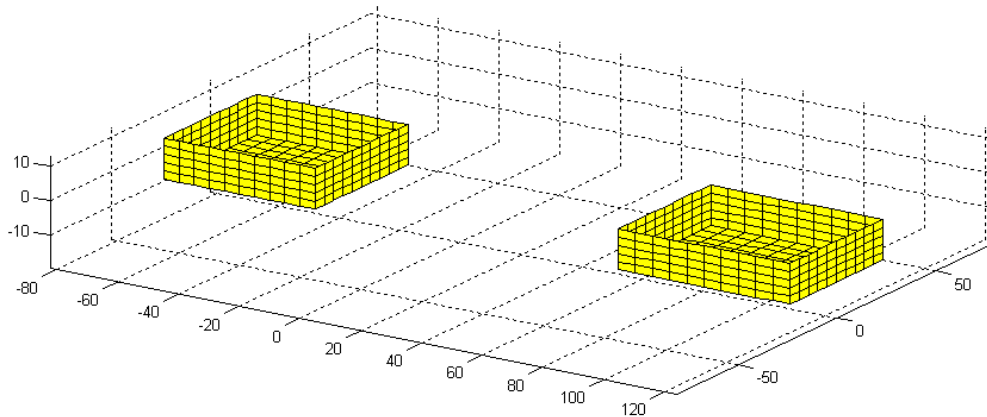
Fig. 4.6 Grid generation for sloshing tanks (Filling level:37%).

Fig. 4.7 shows an example of the roll added mass calculated by 3D panel method for three different filling levels. At each filling level, a resonance peak frequency is observed. Near the resonance frequencies, we observe the sharp rise and fall of a roll added moment of inertia. The simulated resonance frequency is well matched against analytic values of sloshing resonance frequency.
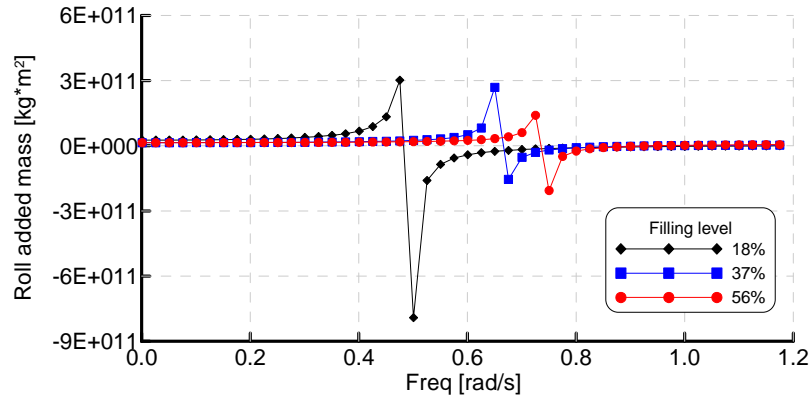
Fig. 4.7 Example of sway added mass of sloshing fluid.

4.2.2.3 Hydrostatic Force Correction

The presence of inner free surface causes a change of bare hull's restoring stiffness.
Fig. 4.8 illustrates change of restoring force due to the inclination of the ship.
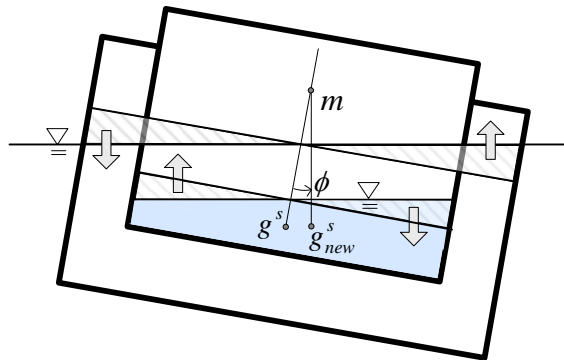
Fig. 4.8 Restoring force correction due to inner fluid.

When the center of gravity of inner fluid g^s is moved to a new position g^s_{new}
due to ship inclination of ϕ, the whole ship's restoring force will be decreased as much as
the inner free surface's contribution:

$$\text{Restoring force} = W \cdot \overline{GM} \cdot \sin\phi - w^s \cdot \overline{g^s m} \cdot \sin\phi$$

$$= \left(W \cdot \overline{GM} - w^s \cdot \overline{g^s m} \right) \sin\phi$$

$$= \left(W \cdot \overline{GM} - w^s \cdot \overline{g^s m} \right) \phi \tag{4.28}$$

$$= \left(W \cdot \overline{GM} - \rho^s V^s g \cdot \frac{I^s}{V^s} \right) \phi$$

$$= \left(W \cdot \overline{GM} - I^s \rho^s g \right) \phi$$

where, w^s is weight of inner fluid, $\overline{g^s m} = \dfrac{I^s}{V^s}$, I^s is second moment of inertia of inner

free surface with respect to x-axis, V^s is volume of inner fluid. ρ^s is density of inner

fluid, g is gravitational acceleration. The last term in the equation (4.28) represents

change of restoring stiffness:

$$\mathbf{K}^s = I^s \rho^s g \tag{4.29}$$

From the equation (4.29), it can be observed that change of the restoring force due

to inner fluid is affected by only second moment of inertia of inner free surface with

respect to rotational axis and density of inner fluid, and it is not affected by filling level

(volume of inner fluid) or location of tanks.

4.2.3 CouplingTtwo Problems in Frequency Domain

Under the assumption of small-amplitude ship and liquid motions, ship motion and

sloshing problems can be coupled in the frequency domain based on linearized potential

flow theory. We recall the equation of motion:

$$\left[\mathbf{M} + \mathbf{M}^a(\omega) \right] \ddot{\boldsymbol{\zeta}} + \mathbf{C}(\omega) \dot{\boldsymbol{\zeta}} + \mathbf{K} \boldsymbol{\zeta} = \mathbf{F}(t) \tag{4.30}$$

where $\mathbf{M}$ and $\mathbf{M}^a(\omega)$ are a ship's real mass and added mass matrices, $\mathbf{C}(\omega)$ is

radiation damping matrix, and $\mathbf{K}$ is restoring matrix. In roll, viscous effect may be

important. In such a case, viscous effects can be included by adding the linear equivalent

damping coefficient $C_{44}^*(\omega)$ to $C_{44}(\omega)$

$$C_{44}^*(\omega) = 2\gamma\sqrt{\left\{M_{44} + M_{44}^a(\omega)\right\}K_{44}} \tag{4.31}$$

where γ is the damping ratio of the system damping divided by critical damping. The

body-motion and force vectors can be written as

$$\begin{aligned}
\boldsymbol{\zeta} &= \mathrm{Re}\left\{\zeta_{j,0}e^{i\omega t}\right\} \\
\mathbf{F}(t) &= \mathrm{Re}\left\{F_{j,0}e^{i\omega t}\right\}
\end{aligned} \tag{4.32}$$

The coupling of ship motion and liquid sloshing can be investigated by adding the

hydrodynamic force vectors of inner fluid motion to the right hand side of equation(4.30):

$$\left[\mathbf{M} + \mathbf{M}^a(\omega)\right]\ddot{\boldsymbol{\zeta}} + \left[\mathbf{C}(\omega) + \mathbf{C}_{44}^*(\omega)\right]\dot{\boldsymbol{\zeta}} + \mathbf{K}\boldsymbol{\zeta} = \mathbf{F}(t) + \mathbf{F}^s(t) \tag{4.33}$$

$\mathbf{F}^s(t)$ in equation (4.33) represents the force vector due to liquid motion. I only

considered the inertia force of the sloshing since there is no radiation damping for the

internal problem.

$$\mathbf{F}^s(t) = \mathbf{M}^{as}(\omega)\ddot{\boldsymbol{\zeta}} + \mathbf{K}^s\boldsymbol{\zeta} \tag{4.34}$$

where $\mathbf{M}^{as}(\omega)$ is sloshing fluid's added mass.

The hydrostatic effect of internal fluid can be included as the reduction of restoring

force due to inner free-surface effect, as shown in equation (4.35):

$$\mathbf{K}^s = I^s \rho^s g \tag{4.35}$$

where I^s is the second moment of inner free surface with respect to the axis of rotational

motion, ρ^s is density of inner fluid, and g is gravitational acceleration.

The resulting coupled equation of motion can be written as

$$\left[-\left\{\mathbf{M}+\mathbf{M}^{a}(\omega)-\mathbf{M}^{as}(\omega)\right\}\omega^{2}+i\omega\left[\mathbf{C}(\omega)+\mathbf{C}_{44}^{*}(\omega)\right]+\left\{\mathbf{K}-\mathbf{K}^{s}\right\}\right]\boldsymbol{\varsigma}_{j,0}=\mathbf{F}_{j,0} \qquad (4.36)$$

4.3   Time Domain Calculation

In time domain analysis, the potential-based linear ship motion program is coupled with the viscous-flow-based nonlinear tank sloshing program. In ship motion calculation, taking advantages of time domain analysis, non-linear effect such as viscous roll damping and surge-sway damping using Morison's formula are included using adequate modeling. Also a mooring system with mooring lines, hawser, and fender is implemented in this time domain analysis.

4.3.1   Motion Calculation

All of the hydrodynamic coefficients were first calculated in the frequency domain and then, the corresponding forces were converted to those for time domain including convolution integral (Kim & Yue, 1991), initially introduced in Chapter II and shown in equation (4.37).

$$\mathbf{F}_{R}=-\mathbf{M}(\infty)\ddot{\zeta}-\int_{-\infty}^{t}\mathbf{R}(t-\tau)\dot{\zeta}(\tau)d\tau \qquad (4.37)$$

where the convolution integral represents the memory effects of the wave force on the platform from the waves generated by platform motion prior to time t. $\mathbf{R}(t)$ is called retardation function and is related to the frequency domain radiation damping. The formula for $\mathbf{R}(t)$ is given by

$$\mathbf{R}(t)=\frac{2}{\pi}\int_{0}^{\infty}\mathbf{C}(\omega)\cos(\omega t)d\omega \qquad (4.38)$$

where $\mathbf{C}(\omega)$ is the radiation/wave damping coefficients at respective frequencies. The length of the retardation function should be large enough to allow for full decay at the end

of the steps as shown in Fig. 4.9 and Fig. 4.10 as examples. In general, multi-body case

needs a longer length of retardation function than that of single-body case as presented in

Fig. 4.10 in order to reflect hydrodynamic effect due to the gap between bodies.
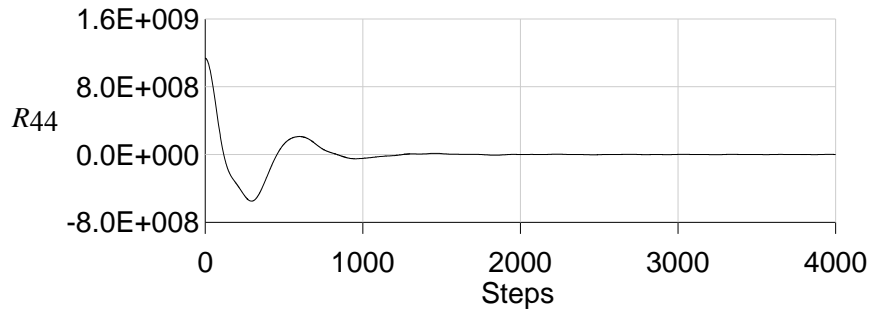
Fig. 4.9 Example of roll retardation function for single-body case.
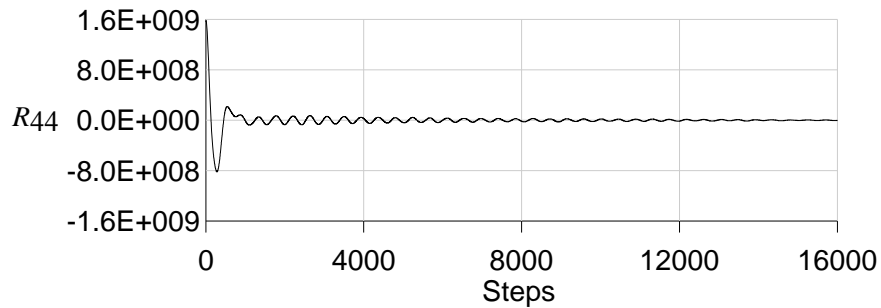
Fig. 4.10 Example of roll retardation function for two body case.

The term $\mathbf{M}^a(\infty)$ in the equation (4.37) is the added mass of the body at infinite

frequency. The infinite added mass coefficients can be obtained from

$$\mathbf{M}^a(\infty) = \mathbf{M}^a(\omega) + \int_0^\infty \mathbf{R}(\omega)\frac{\sin(\omega t)}{\omega}dt \tag{4.39}$$

where $\mathbf{M}^a(\omega)$ is the added mass at frequency ω. Then the total potential hydrodynamic

force can be obtained by the summation of incident wave force, added mass, and radiation

damping forces.

4.3.1.1 Roll Viscous Damping

Time domain program is taking more advantages than frequency domain program in non-linear effect modeling. The viscous effect (one of non-linear effect) of roll, surge and sway viscous damping in time domain is modeled with appropriate ways. In roll mode, viscous damping is so important as radiation damping that it cannot be ignored. In this study, quadratic roll damping model is used as equations (4.40) and (4.41).

$$b_x^{(1)} \cdot \dot{x} + b_x^{(2)} \cdot \dot{x} \cdot |\dot{x}| \tag{4.40}$$

$$b_x^{(1)} = 2 \cdot p \cdot \frac{a_x}{T_x} \quad b_x^{(2)} = \frac{3}{8} \cdot q \cdot a_x \tag{4.41}$$

where a_x is total mass in roll mode, p, q are damping coefficients as shown in Table 5.5. Coefficients p, q are obtained from free decay experiment of the model and adjusted for matching roll amplitude with experimental result.

4.3.1.2 Surge and Sway Viscous Damping

Viscous damping also affects surge and sway mode motion in time domain unlike potential force from boundary value problem. Viscous damping in surge and sway direction is included using Morison's formula by arranging flat plates on each surge and sway direction as shown in Fig. 4.11 as an example.

Wichers (1998) proposed hull drag coefficients with consideration and without consideration of current effect for the tanker. These values will be adjusted for matching surge and sway motion amplitude and all projected areas, as viewed from each direction, will be divided for giving contribution to yaw motion.
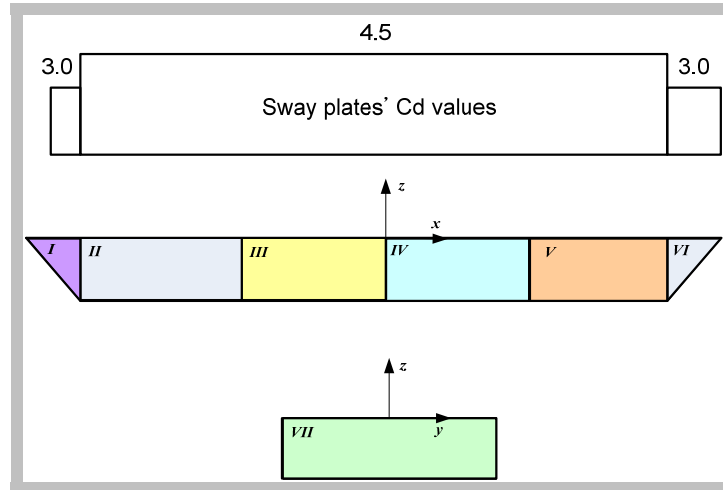
Fig. 4.11 Arrangement of surge and sway plate for Morison's formula.

4.3.2 Irregular Wave Spectrum

To simulate irregular wave in time domain, I use the JONSWAP spectrum in the following way:

$$S(\omega) = \frac{5H_s^2\omega_p^4}{16\omega^5}(1-0.287\ln\gamma)\exp\left[-\frac{5}{4}\left(\frac{\omega_p}{\omega}\right)^4\right]\gamma^r \tag{4.42}$$

where H_s is the significant wave height, ω is frequency, ω_p is the peak frequency, and γ is the over shooting parameter. The symbol r is defined by

$$r = \exp\left[\frac{-(\omega-\omega_p)^2}{2\sigma^2\omega_p^2}\right] \tag{4.43}$$

where $\sigma = 0.07$ when $\omega < \omega_p$ and $\sigma = 0.09$ when $\omega > \omega_p$. As we discussed and introduced in equations (2.14) and (2.15), the generation of wave elevation from a spectrum must be careful to a simulate more realistic sea state. In this study, I use equal frequency spacing with fixed representing frequency method obeying following limitation to avoid the repeating of wave time series.

$$T_{\max} = \frac{2\pi}{\Delta\varpi} \tag{4.44}$$

Fig. 4.12 is an example of JONSWAP wave spectrum.
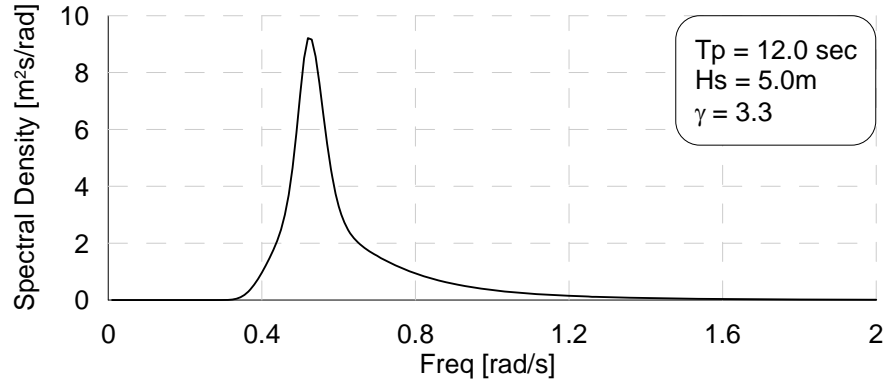
Fig. 4.12 Example of JONSWAP wave spectrum.

4.3.3 Mean Drift Force (Newman's approximation)

The slow drift wave loads can be large when the mean wave loads are also large, suggesting that slow drift motions are important when the volume of a structure is large. However, the computation of second-order diffraction/radiation potential is very intensive. In calculating slowly-varying vessel motions without this complexity in time domain, the so-called Newman's approximation was used. In other words, the second-order difference-frequency wave-force quadratic transfer functions (QTFs) are approximated by their diagonal values (mean drift forces and moments). We recall second-order wave loads from Chapter II,

$$\mathbf{F}_I^{(2)}(t) = \mathrm{Re}\left[\sum_{j=1}^{N}\sum_{k=1}^{N} A_j A_k^* \mathbf{D}(\omega_j,\omega_k)e^{i(\omega_j-\omega_k)t} + \sum_{j=1}^{N}\sum_{k=1}^{N} A_j A_k^* \mathbf{S}(\omega_j,\omega_k)e^{i(\omega_j+\omega_k)t} \right] \tag{4.45}$$

Since natural frequency of floating terminal or LNG-carrier's surge-sway-yaw motion is very low, only second-order difference-frequency quadratic transfer function

$\mathbf{D}(\omega_j,\omega_k)$ is important and sum-frequency quadratic transfer function, $\mathbf{S}(\omega_j,\omega_k)$, which is related to springing in high frequency, can be neglected. Newman's approximation implies that difference-frequency quadratic transfer function, $\mathbf{D}(\omega_j,\omega_k)$, can be approximated as :

$$\mathbf{D}(\omega_j,\omega_k)=\mathbf{D}(\omega_k,\omega_j)=\frac{1}{2}\left(\mathbf{D}(\omega_j,\omega_j)+\mathbf{D}(\omega_k,\omega_k)\right) \tag{4.46}$$

This approximation is valid when the system's natural frequencies are very small, like the horizontal motions of the present problem. It is shown in Kim et al. (2005) that this simpler approach produces reasonable results in the case of a turret-moored FPSO when compared with the more accurate, time-consuming full-QTF method. The Newman's approximation, however, may not be very reliable when water depth is in shallow water condition. The wave drift damping is expected to be small compared to other drag components, and thus is not included in this study (Arcandra, 2001).

4.3.4 *Sloshing Analysis in Time Domain (ABSLO3D)*

The tank sloshing in time domain is solved by the Navier-Stokes equation. The developed computer program (Kim, 2001) can handle the liquid sloshing in 3D multiple tanks simultaneously.

To analyze the liquid sloshing inside a partially-filled tank under forced excitation, two coordinate systems are employed, as shown in Fig. 4.13. This improved program is now capable of multiple excitations of each multiple tank as in Fig. 4.13. This study, however, is only calculating cases of multiple tanks excited by one excitation coordinate system; in other words, multiple tanks are located in one floating body, and only one excitation force will be applied to multiple tanks at the same time. A tank-fixed coordinate

is defined at the center of the tank bottom, rotating with respect to point *G*. Another Cartesian coordinate system *(X, Y, Z)* is defined at the origin *G*, and it has the translational motion with velocity $\mathbf{U}$. Assuming incompressible fluid, the equations governing the flow inside the tank are the continuity and Navier-Stokes equations,

$$\nabla \cdot \mathbf{u} = 0 \tag{4.47}$$

$$\frac{D\mathbf{u}}{Dt} = -\frac{1}{\rho}\nabla p + \nu \nabla^2 \mathbf{u} + \mathbf{F} \tag{4.48}$$

where $\mathbf{u} = (u_x, u_y, u_z)$ is the velocity vector, defined in the tank-fixed coordinates. The symbols $\rho, \nu, p, \mathbf{F}$ are the liquid density, kinematic viscosity, pressure, and external force vectors, respectively. while D/Dt indicates the material derivative.
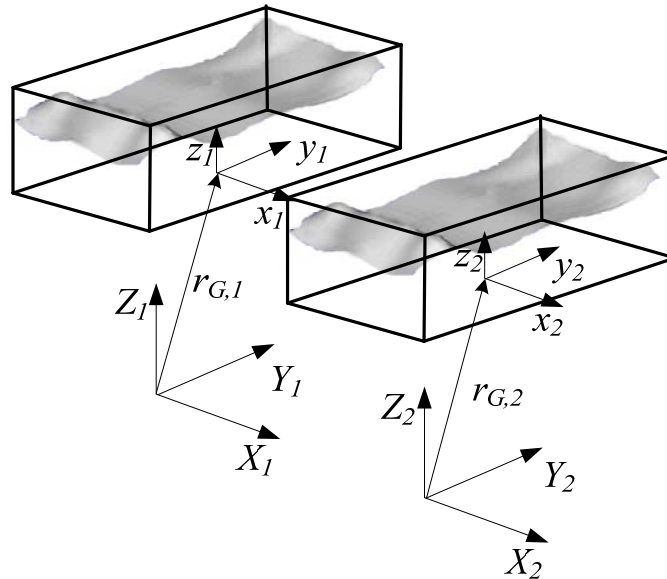

Fig. 4.13 Coordinate system of sloshing analysis program.

The external force consists of the gravitational force, translational and rotational inertia forces. In these cases, $\mathbf{F}$ takes the following form:

$$\mathbf{F} = \mathbf{g} - \frac{d\mathbf{U}}{dt} - \frac{d\boldsymbol{\Omega}}{dt} \times (\mathbf{r} - \mathbf{R}) - 2\boldsymbol{\Omega} \times \frac{d(\mathbf{r} - \mathbf{R})}{dt} - \boldsymbol{\Omega} \times \{\boldsymbol{\Omega} \times (\mathbf{r} - \mathbf{R})\} \qquad (4.49)$$

where $\mathbf{g}$ and $\boldsymbol{\Omega}$ are the gravitational vector and rotational velocity vector. In addition, $\mathbf{r}$ and $\mathbf{R}$ are the position vectors of the considered point and the origin G. The second term of the right-hand side is the translational inertia, while the third, fourth, and fifth terms are due to the rotational motions, which are the angular acceleration, Coriolis, and centrifugal forces. It should be noticed that these forces are defined with respect to the tank-fixed coordinate system.

On the free surface boundary, both the kinematic and dynamic conditions should be satisfied.

$$\frac{D\mathbf{r}_f}{Dt} = \mathbf{u}_f \qquad (4.50)$$

$$p_f = p_{atm} \qquad (4.51)$$

where the subscript f means the values on free surface and p_{atm} is the atmospheric or ullage pressure inside of tank. Besides, a proper condition is necessary on the tank walls and internal members.

The present study focuses on a simplified sloshing problem without highly violent liquid motions including splash and breaking. As is well known, the sloshing flow can become strongly nonlinear, particularly near the resonance frequencies. Such strong nonlinearity includes wave breaking, particle splash, jet flow, and impact occurrence. It is extremely difficult to take all of these complicated local phenomena into account, and such violent local flows, while very critical to the structural damage of tank walls, may not be of importance in global ship motion analysis. In this regard, the free surface boundary is assumed to be a single-valued function. Then the kinematic free-surface boundary

condition can be written as follows:

$$\frac{\partial \eta}{\partial t} + \mathbf{u} \cdot \nabla \eta = 0 \qquad (4.52)$$

where η indicates the free-surface elevation.

As an example of test running of ABSLO3D, Fig. 4.14 shows free decay of free surface when a single impulse-like sway motion is removed after 3.14 seconds. Free surface elevation is measured at the center of the first tank. Two identical tanks are forced to move at the same time. The length of each tank is 5 m, breadth of tank is 10 m, height of tank is 10m and the tank is filled to 20% of tank height. Free surface was increased due to impulse-like tank motion and it slowly decayed during 30 seconds.
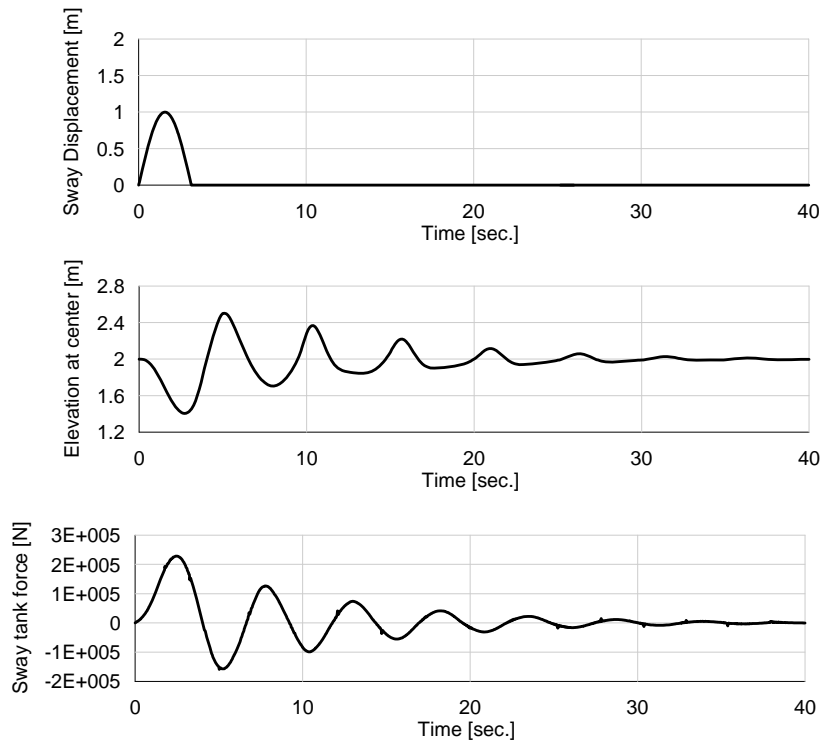

Fig. 4.14 Free decay test of ABSLO3D.

4.3.5 Coupling Two Problems in Time Domain

The coupling between tank sloshing and ship motion can be done by adding

sloshing force vector into the right-hand side of equation (4.30) as follows:

$$\mathbf{F}(t) = \mathbf{F}^{ext}(t) + \mathbf{F}_S(t) \tag{4.53}$$

where $\mathbf{F}^{ext}(t)$ is the external excitation force vector on hull surface by waves and hydrodynamic reactions, while $\mathbf{F}_S(t)$ is the sloshing-induced force acting internally on the tank. The mass matrix $\mathbf{M}$ in equation (4.30) represents the total ship mass including fluid mass inside the tank. The mass and hydrostatic matrices are modified for different volumes of liquid. Since the inertia force as a rigid fluid mass is included in the sloshing program, I need to cancel out its effect by adding the fluid mass inertia in the right-hand side of equation (4.30).

$$\mathbf{F}_S(t) = \mathbf{F}^{int}(t) + \mathbf{M}_S \ddot{\zeta} \tag{4.54}$$

where $\mathbf{M}_S$ is fluid's mass diagonal matrix and $\mathbf{F}^{int}(t)$ is the force vector from the sloshing program including hydrostatic and dynamic forces by fluid motions.

In the MARIN-FPSO experiment, drafts of each filling level is kept as the same value by adjusting ballast for each different filling level. Therefore, computational simulation of each filling level in which vertical mass distribution of fluid is different requires modification of the restoring coefficient as shown in Fig. 4.15.
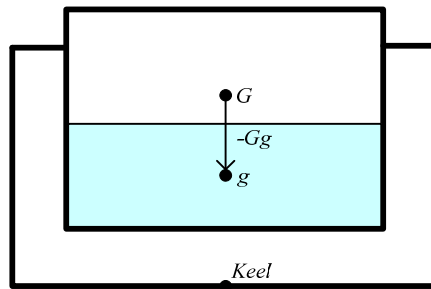

Fig. 4.15 Modification of roll restoring coefficient.

In this figure, G is the original center of gravity of body and ballast, and g is the center of gravity of fluid. Due to the existence of inner fluid in computation instead of ballast weight in the experiment, roll restoring coefficient K_{44} is modified as equation (4.55).

$$K_{44}^* = K_{44} + K_{44}' \\ = K_{44} + \rho g V_{liquid}(Gg) \tag{4.55}$$

where,

$$Gg = \overline{Keel \cdot g} - \overline{Keel \cdot G} \tag{4.56}$$

When the center of gravity of fluid is lower than the original center of gravity of body, as in Fig. 4.15, restoring force will be reduced, and the reverse is also true. Now we have final ship motion and sloshing coupled equation in time domain.

$$\left[\mathbf{M} + \mathbf{M}^a(\infty) - \mathbf{M}_S\right]\ddot{\zeta} + \left[\mathbf{K} + K_{44}'\right]\zeta = \mathbf{F_I}(t) + \mathbf{F_C}(t,\dot{\zeta}) + \mathbf{F}_N(t,\dot{\zeta}) + \mathbf{F}_S(t) \tag{4.57}$$

In this equation, the ship and sloshing motions are coupled by kinematic and dynamic relations in that vessel motions are exciting the tank sloshing, while the sloshing-induced loads in turn influence vessel motions.

CHAPTER V

CASE STUDY I: DYNAMIC ANALYSIS OF MARIN-FPSO*

5.1   Principal Particulars

In this chapter, coupling program of ship motion and sloshing will be investigated by a comparison with the experiment result of the LNG-FPSO experiment carried out by MARIN (Maritime Research Institute of Netherlands) as a part of SALT-JIP. The main goal of this experiment is to investigate the coupling effect between the FPSO motion and sloshing liquid motion in two tanks as shown in Fig. 5.1. Two tanks are filled with fresh water and tested for three different filling levels (18%, 37%, and 56% of tank height) at the same filling level of each tank. The LNG-FPSO is moored by soft springs to avoid drift away against wave force. The wave is the only external environmental force and wave headings are tested for three different angles (head, quartering, and beam sea conditions).

On this MARIN-FPSO, two sloshing tanks are equipped as shown in Table 5.1. The length of aft tank (No.4) is 6.936 m longer than the forward tank (No.2). Breadth and height of the two tanks are similarly designed. The principal particulars of both the MARIN-FPSO and mooring system are presented in Table 5.2. Shape of the hull is similar to barge type, and external mooring stiffness is modeled by linear spring for surge, sway, and yaw modes.
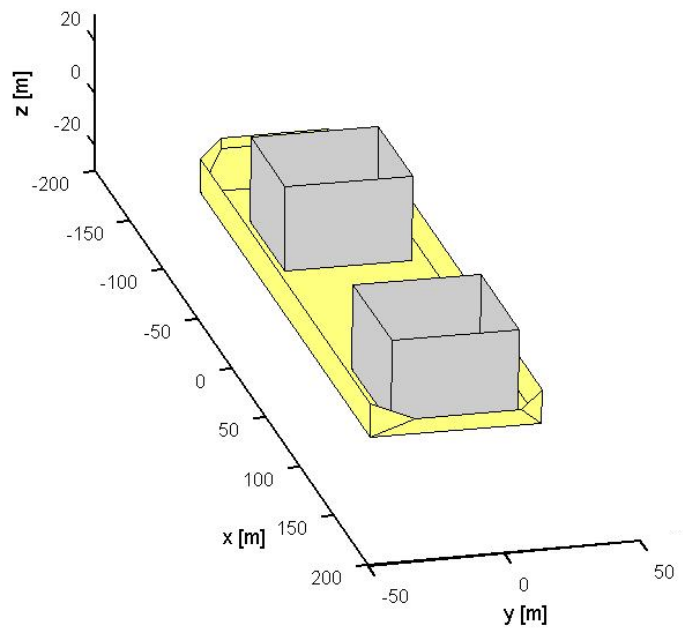
Fig. 5.1 General sketch of MARIN-FPSO and LNG tanks arrangement.

Table 5.1 Characteristics of sloshing tanks.

Designation	Magnitude
AFT TANK no.4 (inner dimensions given)	
Tank aft from aft perpendicular	61.08 m
Tank bottom from keel line	3.3 m
Tank length	49.68 m
Tank breadth	46.92 m
Tank height	32.23 m
FORWARD TANK no.2 (inner dimensions given)	
Tank aft from aft perpendicular	209.54 m
Tank bottom from keel line	3.3 m
Tank length	56.616 m
Tank breadth	46.92 m
Tank height	32.23 m

Table 5.2 Principal particulars of FPSO (bare hull) and mooring system.

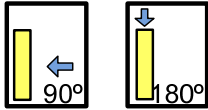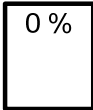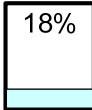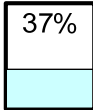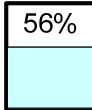| Description		Magnitude
Length between perpendicular		285.0 m
Breadth		63.0 m
Draught		13.0 m
Displacement volume		220,017.6 m^3
Displacement mass in seawater		225,518.0 ton
Longitudinal COG		142.26 m
Transverse metacentric height		15.30 m
Vertical center of gravity		16.71 m
Vertical center of buoyancy		6.596 m
Transverse metacenter above base line		32.01 m
Mass radius of gyration around X-axis		19.49 m
Mass radius of gyration around Y-axis		78.42 m
Mass radius of gyration around Z-axis		71.25 m
Mooring stiffness	Surge	6.50×10^5 N/m
	Sway	2.43×10^6 N/m
	Yaw	1.76×10^8 N·m/rad

5.2 Simulation Conditions

In this case, wind and current are not considered in order to investigate the dynamic coupling effect between ship motion due to wave and sloshing motion at different filling levels. As shown in Table 5.3, wave heading is selected as three different directions: head sea, quartering sea, and beam sea conditions. Significant wave height, peak period, and γ factor are selected to be consistent with MARIN experimental conditions. Sloshing

tanks are filled at four filling levels, 0%, 18%, 37%, and 56% of tank height, levels are also tested by MARIN.

Table 5.3 Simulation environment.

Wind	N/A	
Current	N/A	
Wave	Heading	
	Significant height	5.0 m
	Peak period	12 sec
	γ of JONSWAP spectrum	3.3
Filling levels		

5.3   Hydrodynamic Coefficients of Ship

In order to calculate hydrodynamic coefficients in frequency domain, we need to generate panels on the hull surface as shown in Fig. 5.2. Total number of panels for this barge-type hull is 2300.
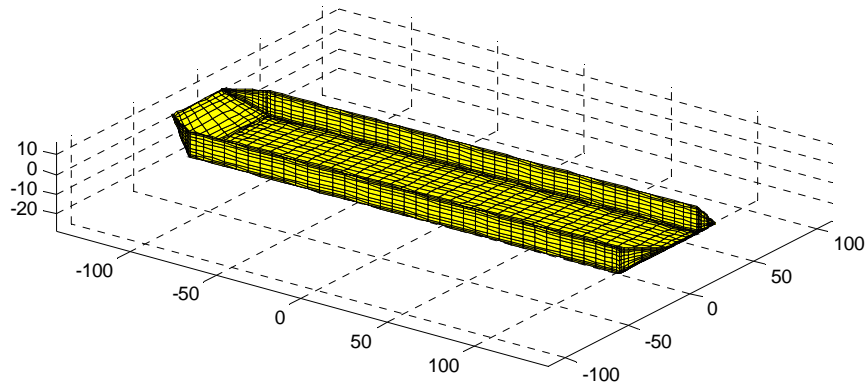
Fig. 5.2 Grid generation of hull for 3D panel method (Number of panels=2300).

By solving diffraction/radiation problem using a constant panel method program, called WAMIT, I can obtain added mass, radiation-damping coefficients, LTFs (linear transfer function), mean drift forces, and motion RAOs (response amplitude operator) as shown in examples from Fig. 5.3 through Fig. 5.9.

Fig. 5.3 Added mass of MARIN-FPSO.
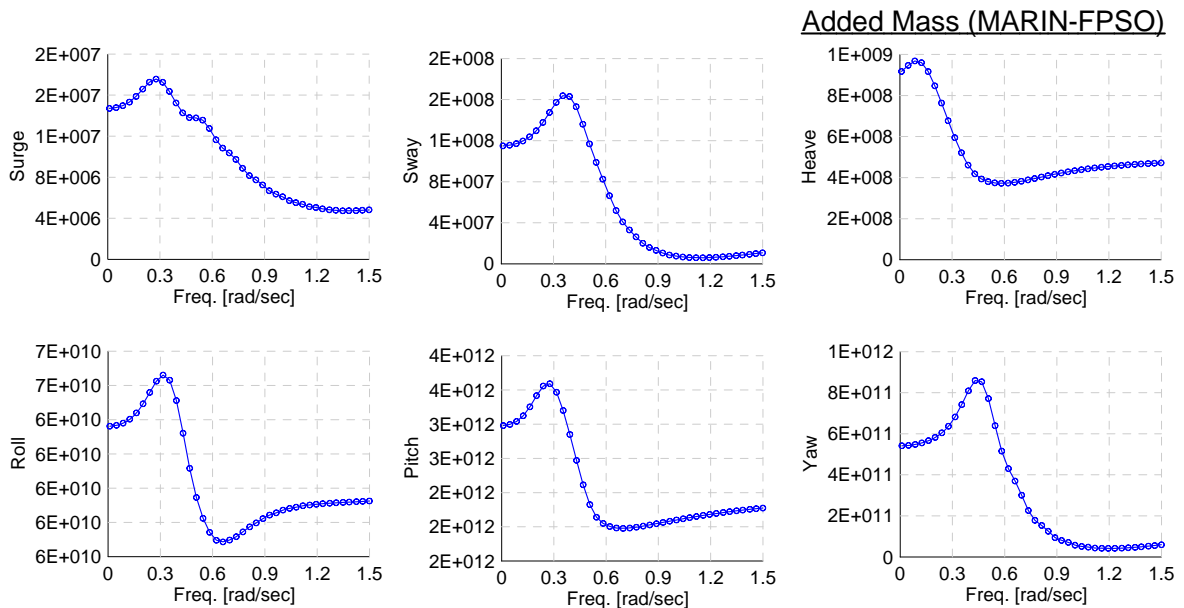
Radiation Damping Coeffcients (MARIN-FPSO)
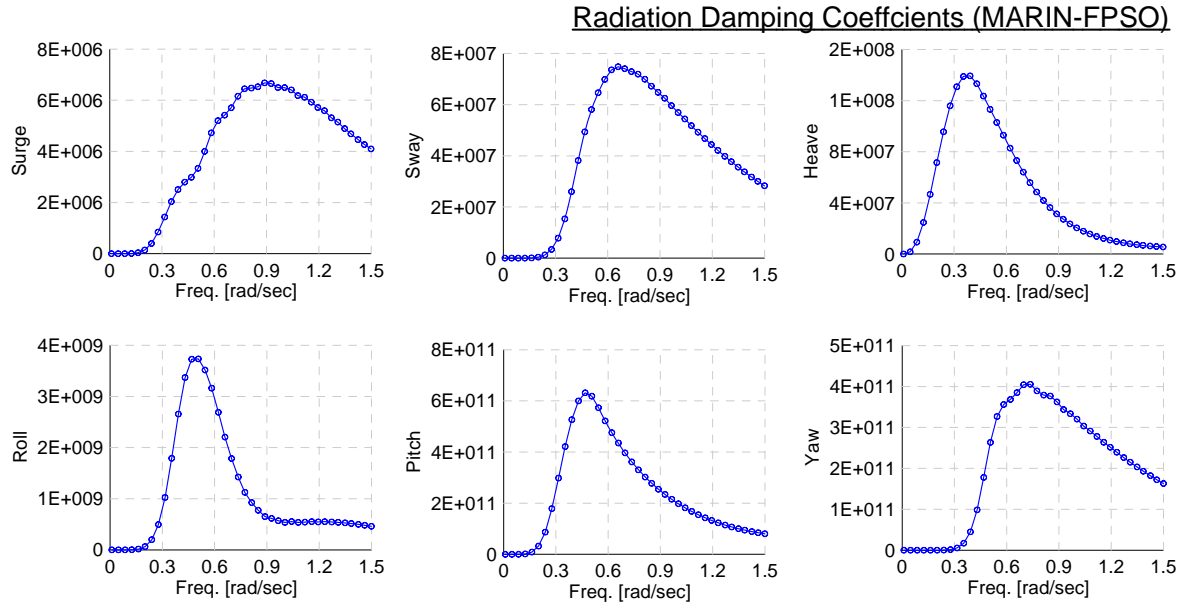
Fig. 5.4 Radiation damping coefficients of MARIN-FPSO.

Linear Transfer Function (MARIN-FPSO)

90⁰
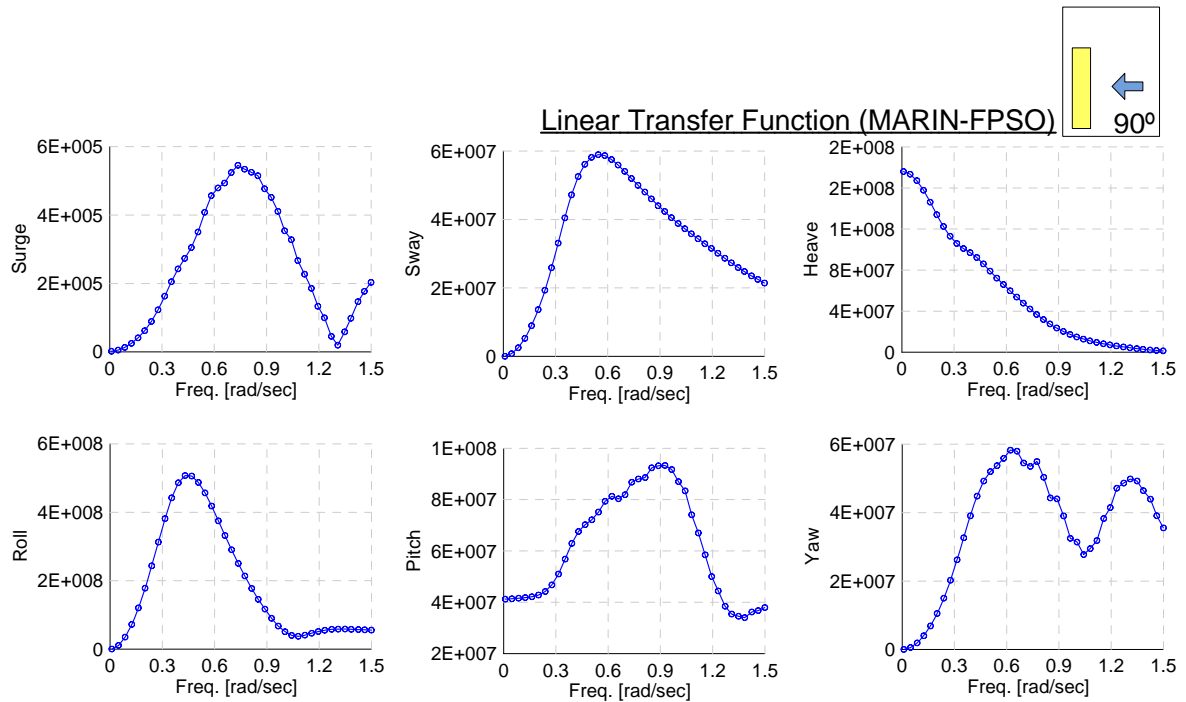
Fig. 5.5 Linear transfer function of MARIN-FPSO (wave heading=90deg)

Mean Drift Force (MARIN-FPSO)
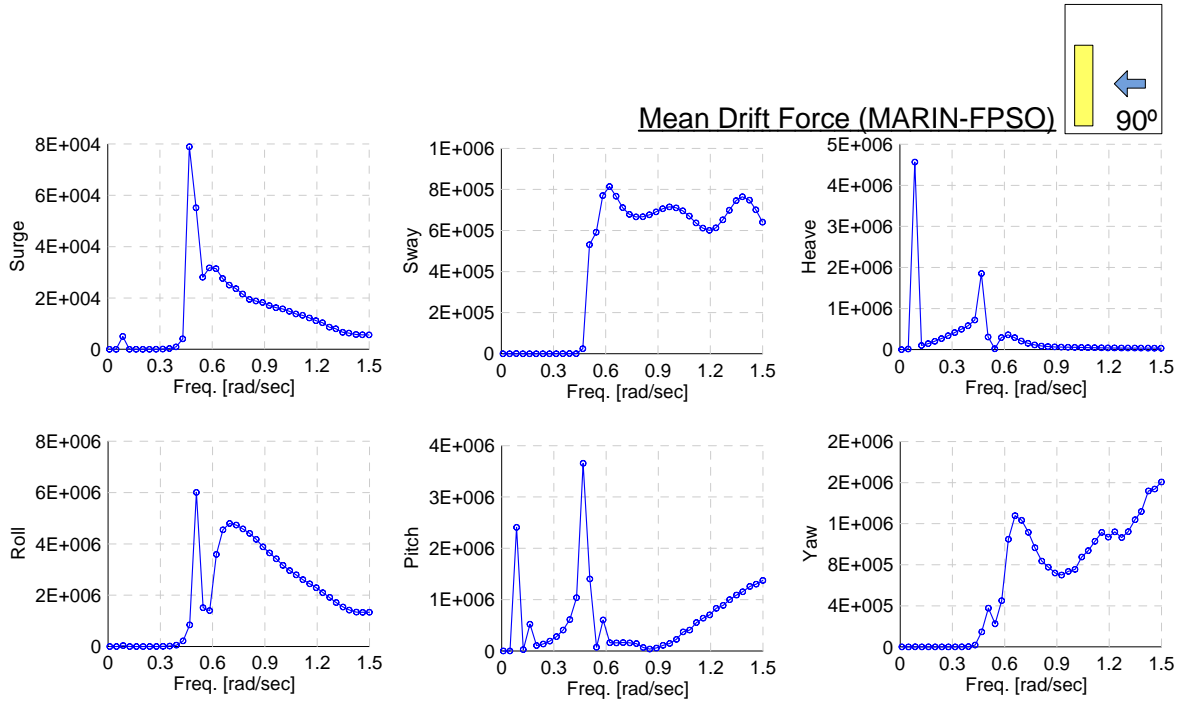
Fig. 5.6 Mean drift force of MARIN-FPSO (wave heading=90deg)
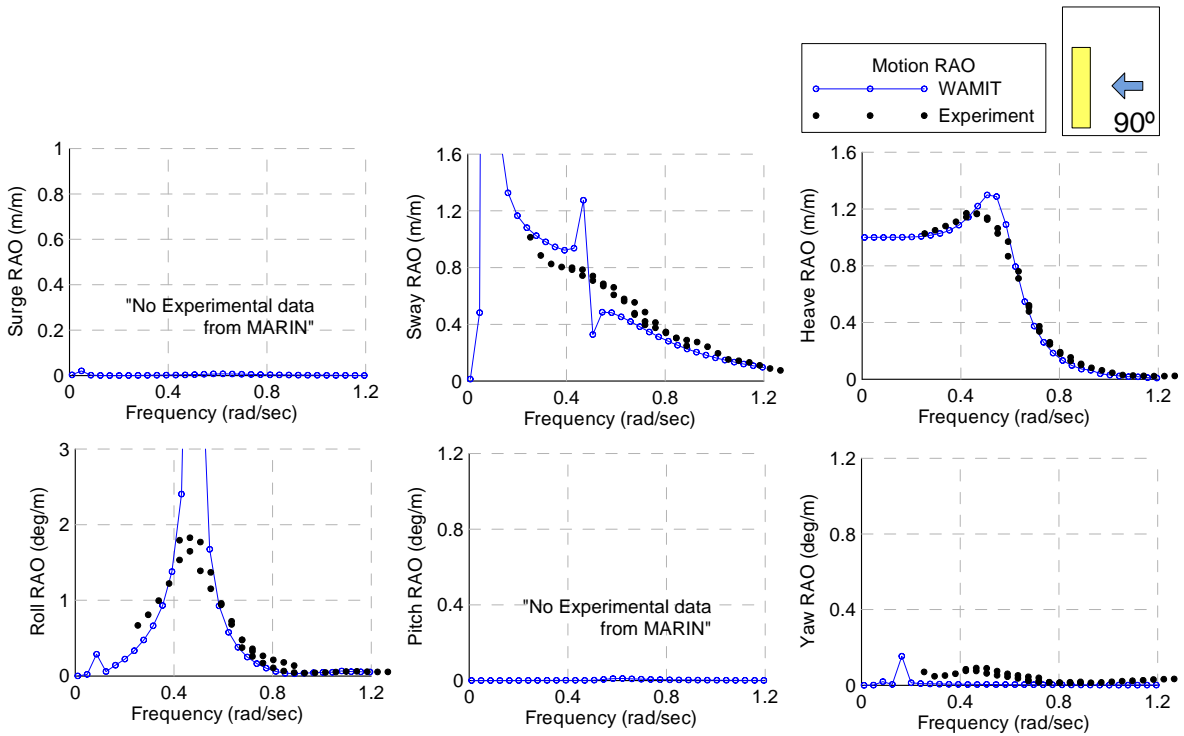
Fig. 5.7 Measured and predicted motion RAOs (wave heading=90deg)
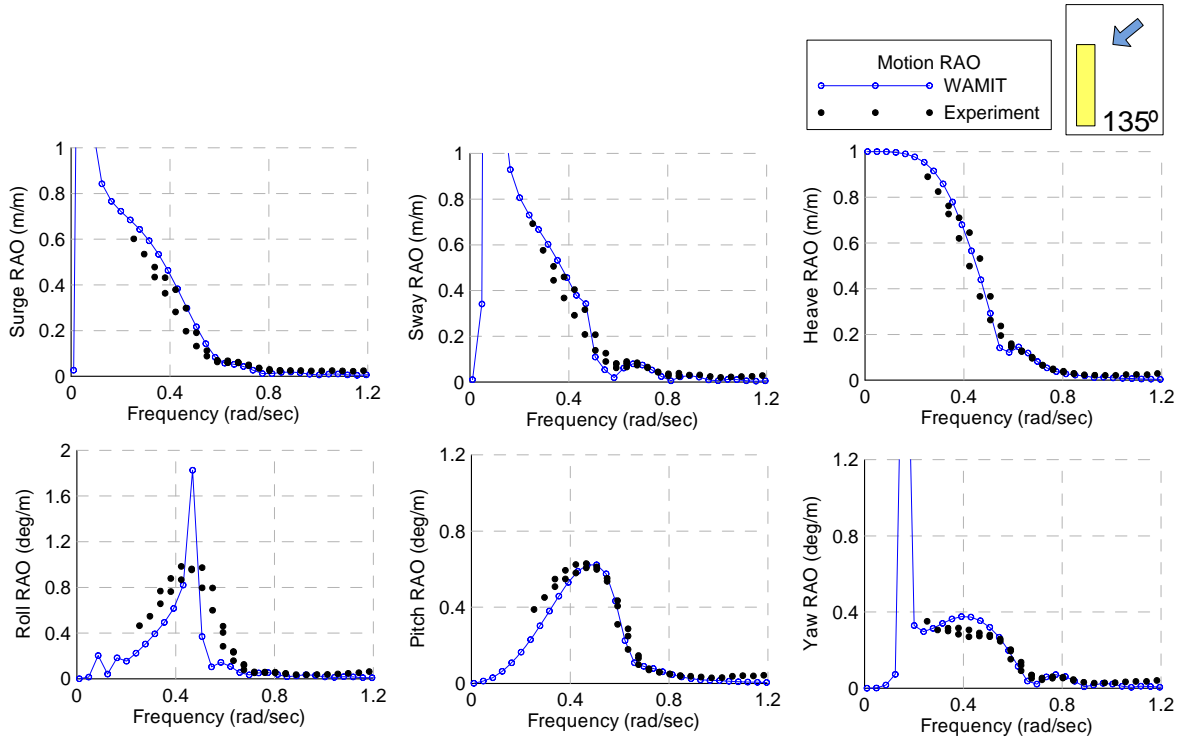
Fig. 5.8 Measured and predicted motion RAOs (wave heading=135deg)
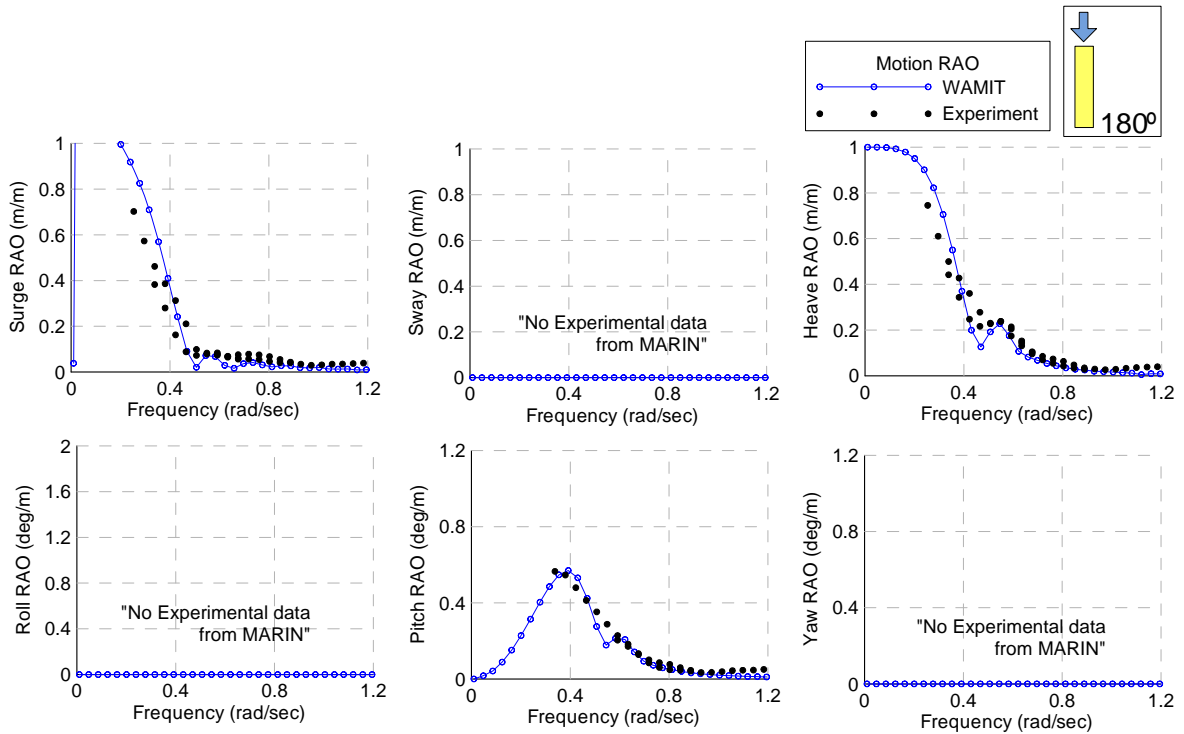
Fig. 5.9 Measured and predicted motion RAOs (wave heading=180deg)

Calculated motion RAOs for each wave heading angles are compared with the experiment results from MARIN. In beam sea condition, Fig. 5.7, experimental data of surge and pitch are not provided from MARIN. Motion resonance of sway at 0.1 rad/s is due to an external simple spring mooring system to avoid drift away, and this motion also slightly affects to roll and yaw motion. Sway resonance around 0.45 rad/s is due to roll resonance motion. The motion RAOs under 135 degree wave heading condition are shown in Fig. 5.8. Since potential theory is used, as also shown in beam sea condition, the roll amplitude is over-predicted near resonance, without including viscous effects. Other than that, the agreement between the prediction and measurement is acceptable. Fig. 5.9 shows comparison of surge heave and pitch motion RAOs at head sea condition, and it too shows a good agreement with the general fact that the experimental result does not show rapid change due to the viscous effect.

5.4   Coupling Two Problems in Frequency Domain

5.4.1   Sloshing Added Mass

MARIN-FPSO has two tanks at fore and apt part, as shown in Table 5.1. The added mass of two tanks will be calculated at a time and total sloshing added mass will be added to equation of single-body. Fig. 5.10 shows grid generation of each three filling levels. The total number of panels used in the case is 600 for both 18% and 37% filling levels and 1000 for 56% filling level. Sloshing natural frequency is calculated in Table 5.4 for transverse and longitudinal modes. Since the two tanks have the same breadth, transverse natural frequency is the same value at each tank and longitudinal natural frequency is different as much as different length of each tank.
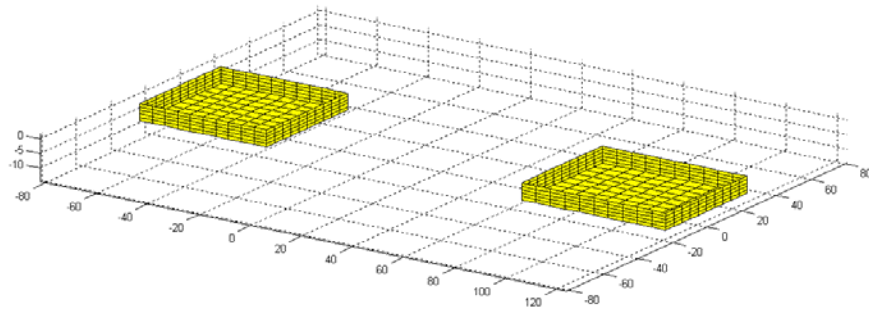
(a)
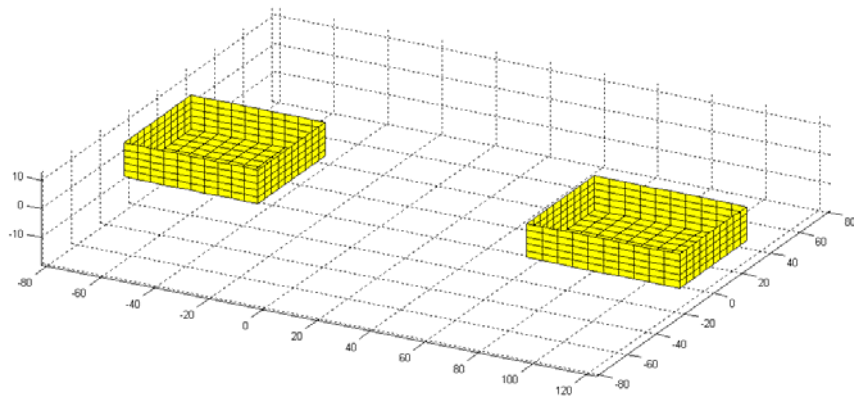
(b)
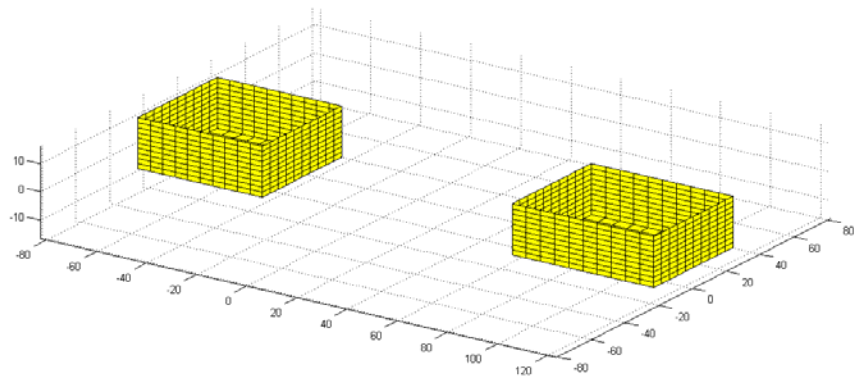
(c)

Fig. 5.10 Grid generation of sloshing tanks for each filling level of
(a) 18% (b) 37%, and (c) 56%.

Table 5.4 Natural frequencies of FPSO and sloshing tanks.

		Natural frequencies (rad/sec)					
		Transverse mode		Longitudinal mode			
Bare hull		Roll : 0.50		Pitch : 0.47			
		1st	2nd	Apt tank		Fore tank	
				1st	2nd	1st	2nd
Sloshing Tanks	FL:18%	0.49	1.31	0.47	1.25	0.41	1.11
	FL:37%	0.66	1.55	0.63	1.50	0.56	1.37
	FL:56%	0.74	1.61	0.71	1.56	0.64	1.44
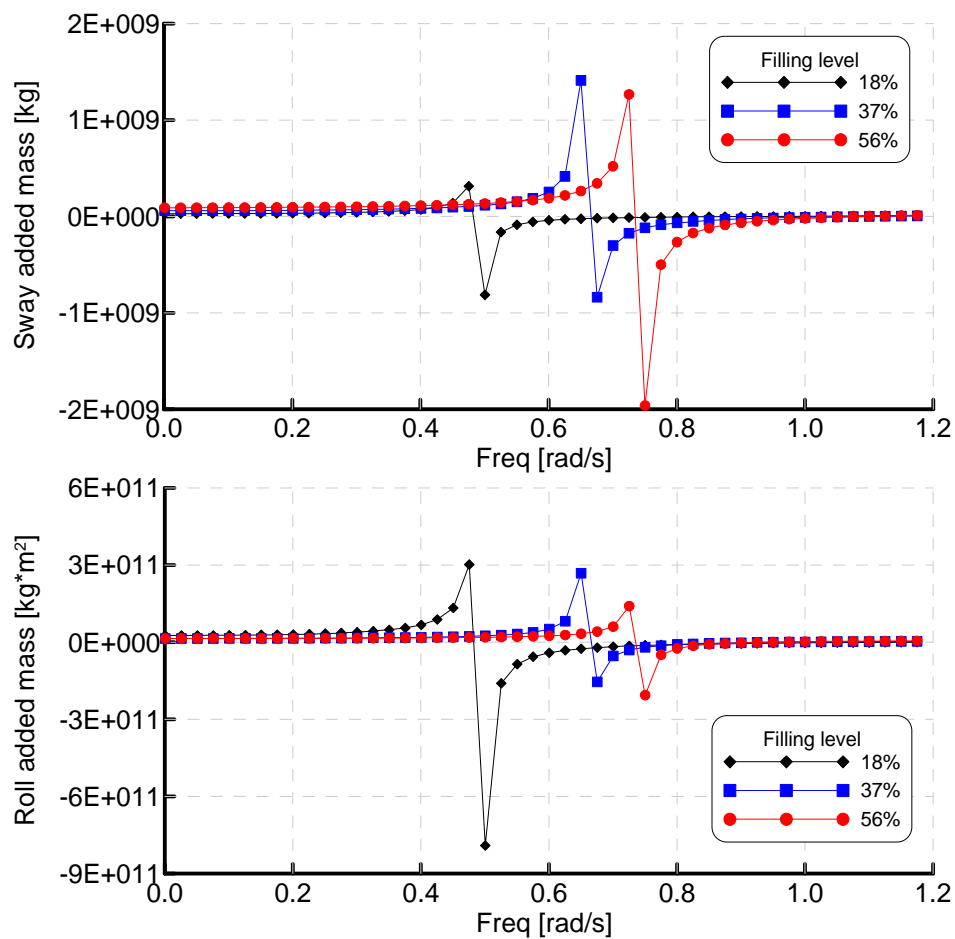
Fig. 5.11 Sway and roll added mass of MARIN-FPSO's sloshing fluid.

For example, calculated sway and roll sway added mass is plotted in Fig. 5.11. Since sway and roll must have the same transverse natural frequency, each mode has a sharp peak at corresponding analytic natural frequency in Table 5.4.

5.4.2 Motion RAO Results

Now, ship motion and sloshing coupling effect in frequency domain will be discussed by checking roll motion RAO, which is most dangerous mode due to the least restoring force of all the modes. Fig. 5.12 represents RAOs of roll motion at different filling levels with beam sea condition. Each figure includes the experimental results obtained from irregular wave model test and frequency domain results.
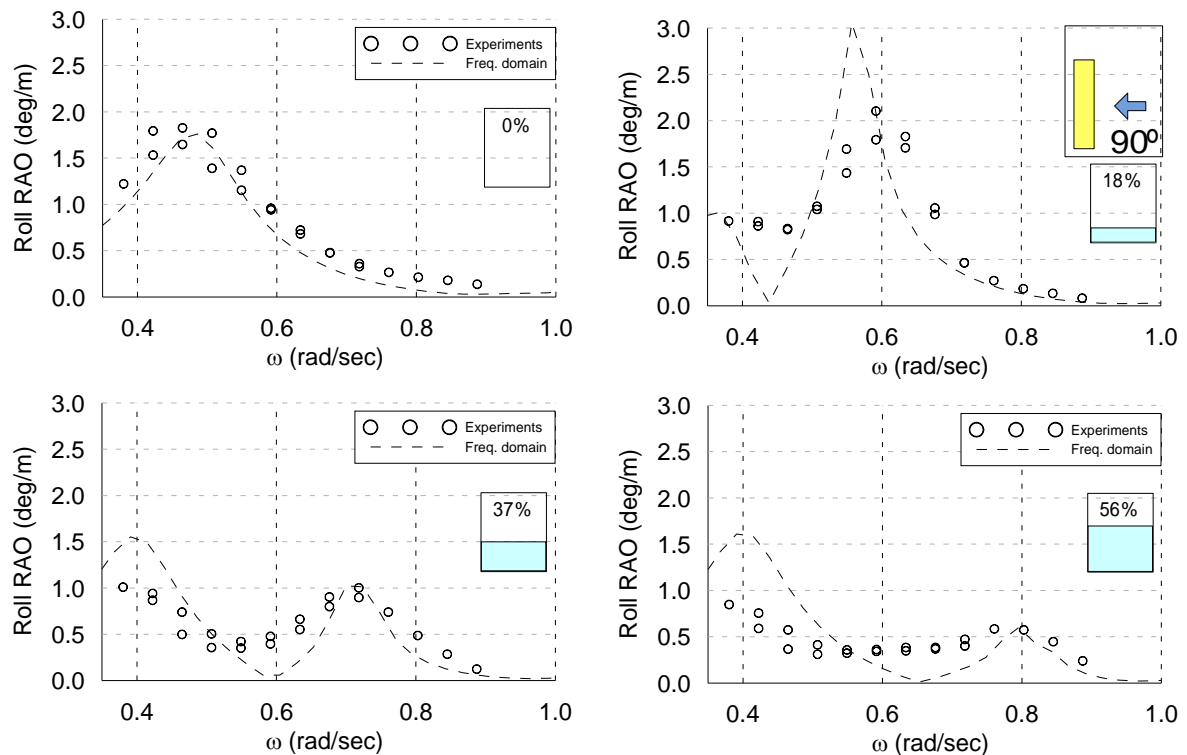
Fig. 5.12 Comparison of coupling effect of roll motion

(Frequency domain, wave heading = 90deg)

When there is no sloshing, roll natural frequency is located naturally at 0.45 rad/s in both experiments and frequency domain. For the 18% filling level case, calculation result shows that the natural frequency of roll is moved around 0.6 rad/s and roll motion is almost zero around 0.45 rad/s. The experiment result is not showing this phenomenon clearly, due to viscous effect. In sloshing phenomenon at lower filling levels, viscous effect is more dominant than inertia effect; therefore, coupling result in frequency domain with linear potential theory, which does not include viscous effect, is not demonstrating this viscous effect. In 37% and 56% filling levels, we can clearly see the split of peaks in the roll RAOs.

Since the sloshing resonance frequency of 56% is farther from the hull resonance frequency, we observe greater separation distance between the two peaks. When I consider roll RAOs near the bare-hull's natural frequency 0.5(rad/s), the roll motions continue to decrease with the fill ratio. On the other hand, the roll amplitudes near 0.8(rad/s) continue to increase with the fill ratio. Therefore, the inner liquid motions can increase or decrease the roll motions depending on incident wave frequencies. The peak frequency of the present input spectrum is around 0.5(rad/s), which explains why roll motions continue to decrease with increasing filling level. This frequency domain linear potential results show a similar trend but the resonance peaks are significantly over-predicted because viscous and nonlinear free-surface effects are not included.

Coupling effect in head sea condition is presented with pitch motion RAO at different filling levels. An example is shown in Fig. 5.13.
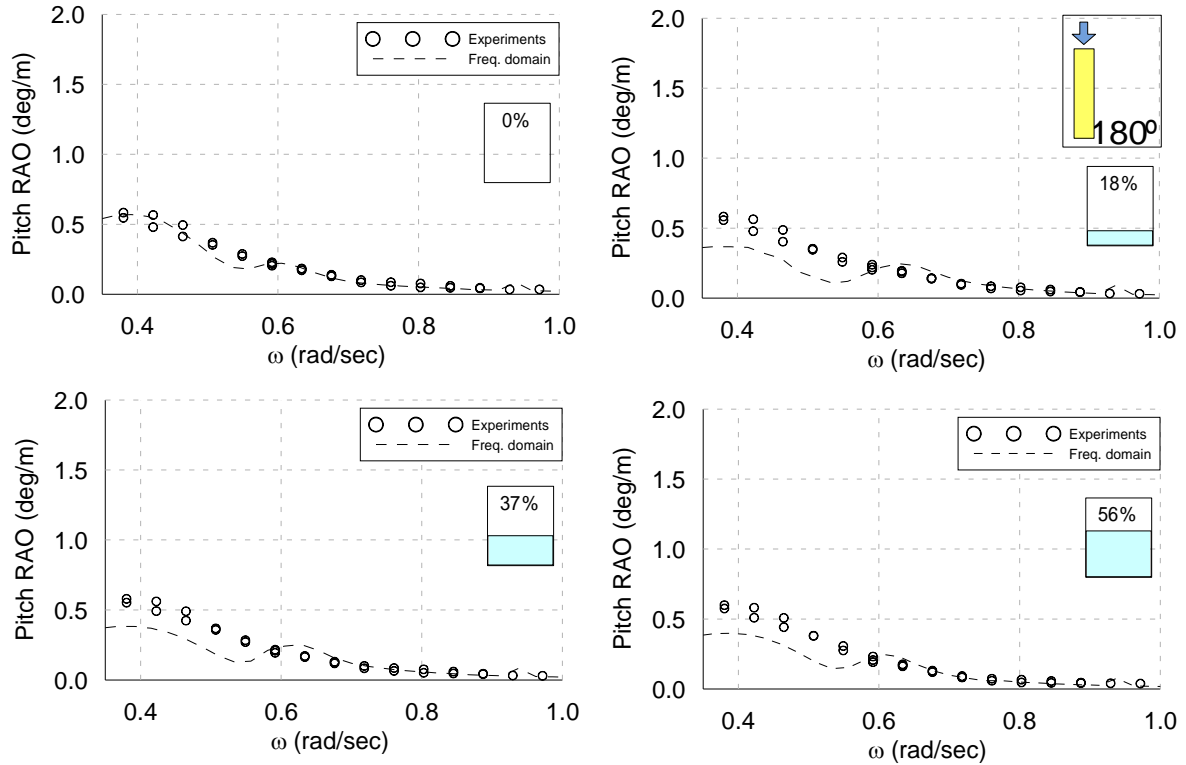
Fig. 5.13 Comparison of coupling effect of roll motion

(Frequency domain, wave heading = 180deg)

For head sea condition with pitch motions, it can be expected that the coupling effects of liquid cargo and hull motion are less significant. It is primarily due to the fact that the inertia of longitudinal hull is much larger than the dynamic effect of liquid motion. In all cases in Fig. 5.13, the effects of liquid cargo sloshing in pitch motions are very minor.

5.5 Coupling Two Problems in Time Domain

5.5.1 Regular Wave Test without Sloshing

First, we discussed in previous chapters that time domain ship motion program is using hydrodynamic potential forces from frequency domain by converting to time domain forces using retardation function. Calculated diagonal terms of retardation of MARIN-

FPSO are shown in Fig. 5.14.
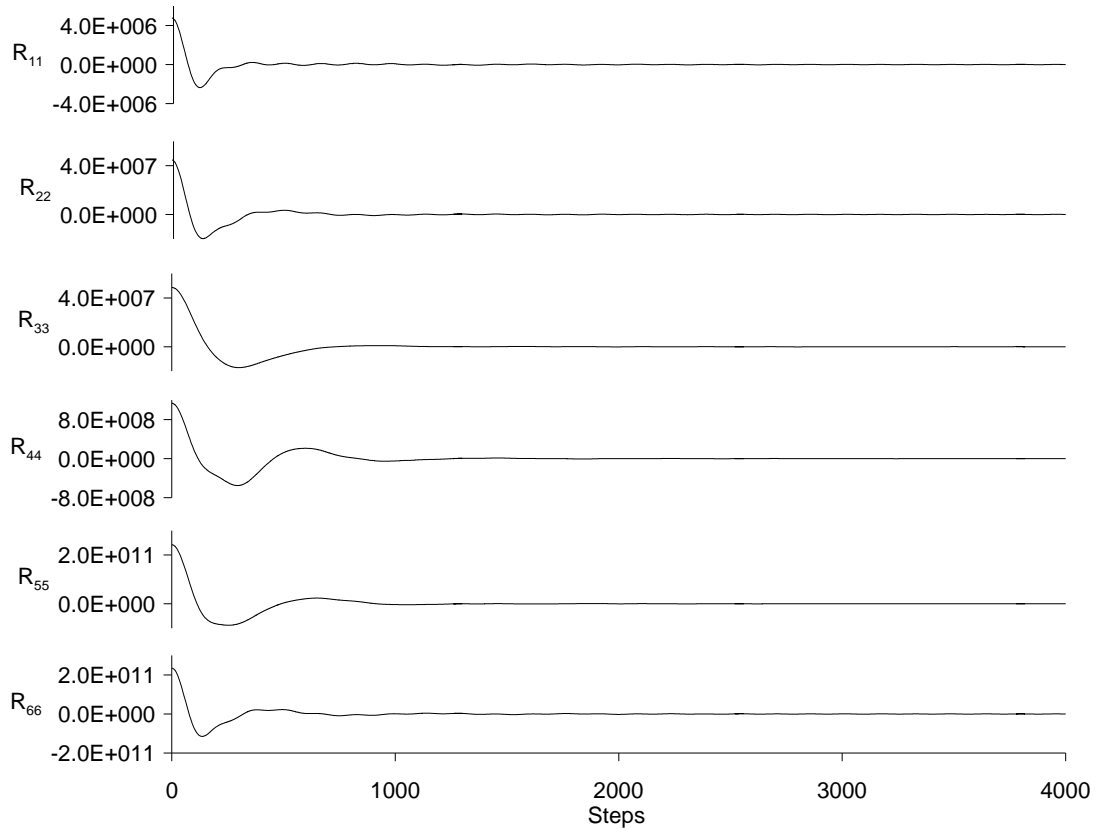
Fig. 5.14 Retardation functions of MARIN-FPSO.

Using these potential forces, time domain must provide exactly the same results with frequency domain results. The validity of the time domain program can be tested by checking motion amplitude for a single frequency regular wave. As examples, heave and pitch motion RAO of regular wave test for 135deg wave heading angle are presented in Fig. 5.15. Since heave and pitch are mostly affected by potential force, results of these two modes must also be exactly the same as those of frequency domain results. As we can see, regular wave test of time domain program provides these results of frequency by WAMIT.
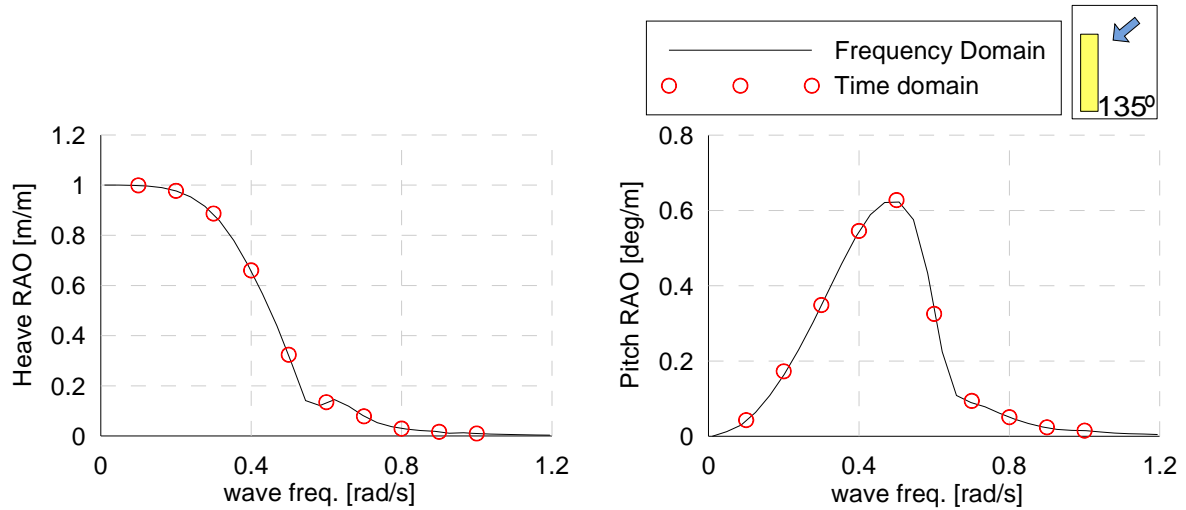
Fig. 5.15 Regular wave test of MARIN-FPSO.

5.5.2   *Viscous Damping Modeling*

The inclusion of viscous damping is particularly important for roll motions. Linear and quadratic damping model are used in roll and the respective coefficients were obtained from the free-decay tests in calm water. The damping values are further tuned to represent their increase in waves as in Table 5.5. Roll motion amplitude is adjusted using linear and quadratic damping model, and an example of time series and comparison of spectral density function between simulation and experiments are presented in Fig. 5.16.

The mass-less plates is used for including drag effect in surge and sway direction with Morison's formula. Arrangement of surge and sway plates is presented in Fig. 5.17, and drag coefficients and areas of each plate are listed in Table 5.6.

Table 5.5 Coefficients for quadratic roll damping model.

Damping coefficients in use		
Wave Heading	p	q
90deg	0.9001	0.0281
135deg	0.1001	0.0281
180deg	0.1001	0.0281
Damping coefficients from MARIN experiments		
	p	q
POS.	0.2371	-0.0109
NEG.	0.1562	0.0792
DOUBLE	0.2001	0.0281
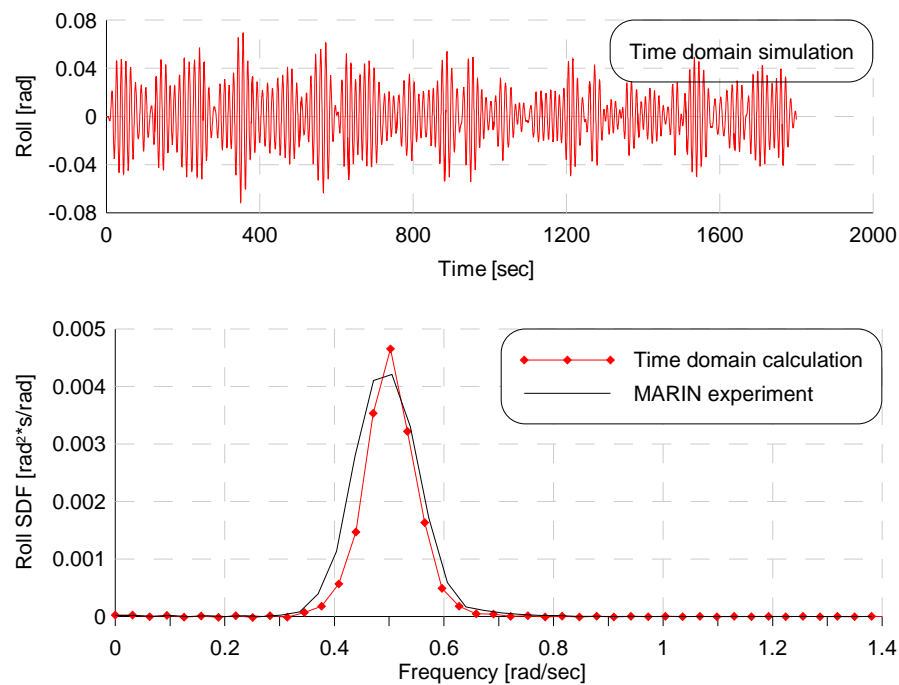
Fig. 5.16 Time series and Spectral Density Function of roll (Wave heading = 90 deg)
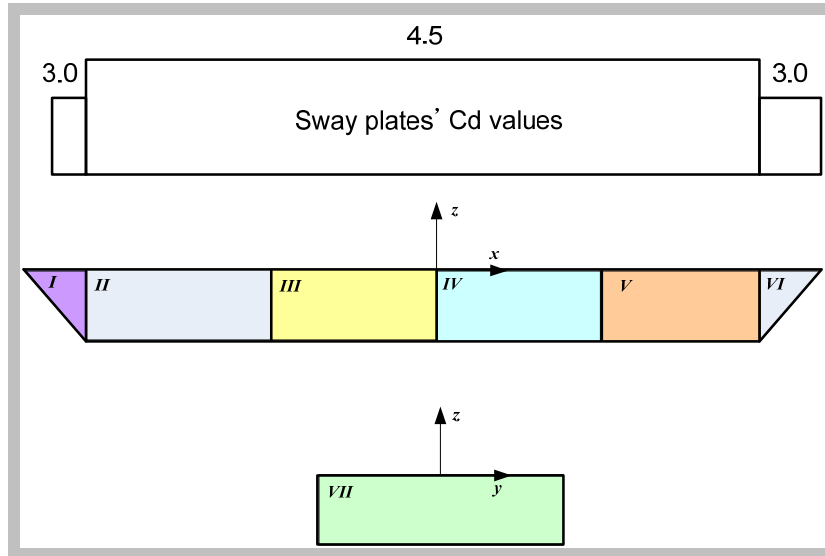
Fig. 5.17 Surge and sway plates of MARIN-FPSO.

Table 5.6 Surge and sway plates of MARIN-FPSO.

	No.	C_d	Area (m^2)	$0.5\rho A C_d$
	I	3.0	130.000	199875.00
	II	4.5	807.690	1655764.50
	III	4.5	807.690	1655764.50
Sway plates	IV	4.5	807.690	1655764.50
	V	4.5	807.690	1655764.50
	VI	3.0	117.000	179887.50
Surge plate	VII	300.0	819.000	125921250.00

For the surge plate, an extraordinary large value is used for beam sea condition since normal velocity at surge is very small under beam sea condition. At head sea condition, surge plate is not used since calculated surge amplitude is already well matching with experiment as shown in Fig. 5.18. The time series and spectral density function of surge and sway in beam sea case are presented in Fig. 5.19 and Fig. 5.20, respectively.
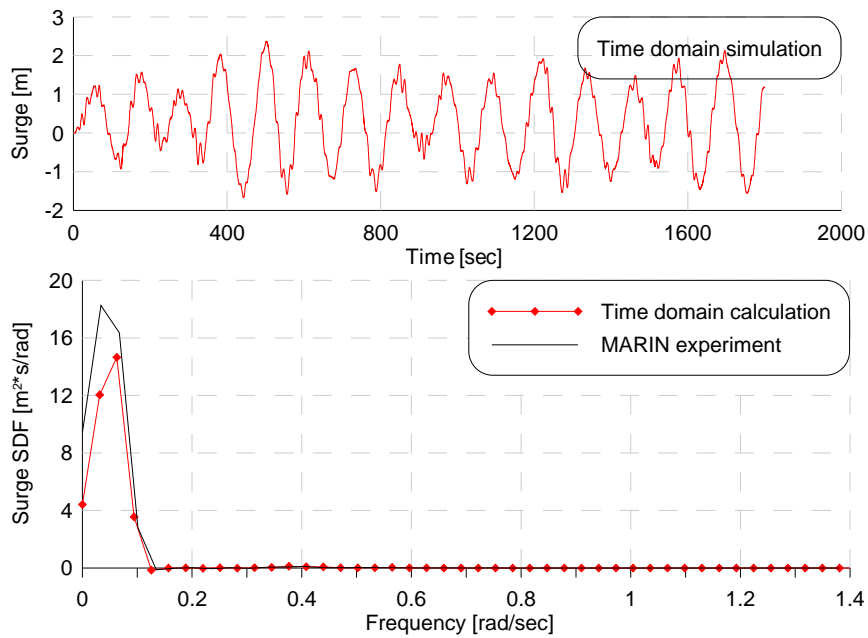
Fig. 5.18 Time series and Spectral Density Function of surge (Wave heading = 180 deg)
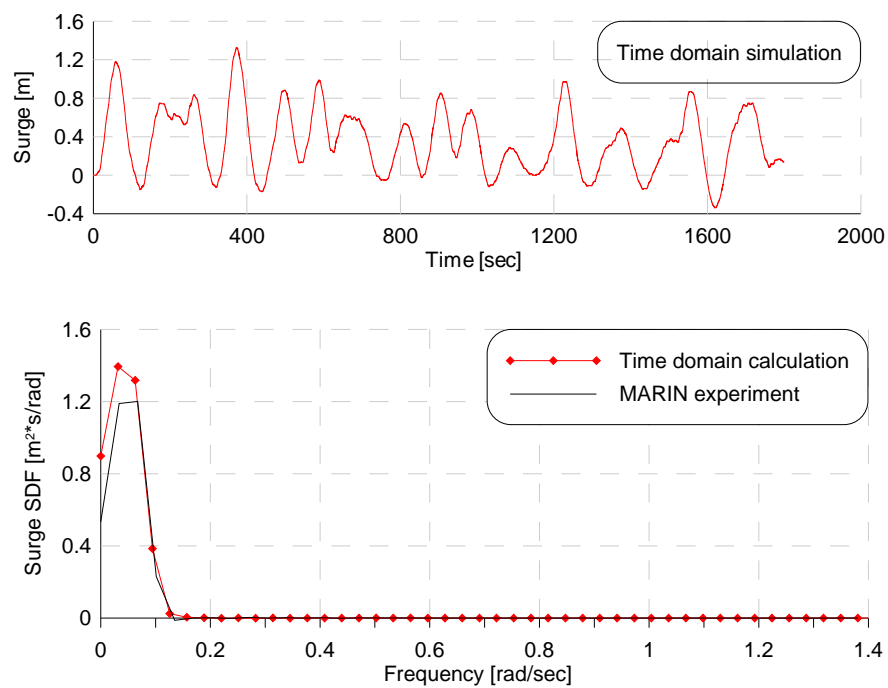
Fig. 5.19 Time series and Spectral Density Function of surge (Wave heading = 90 deg)
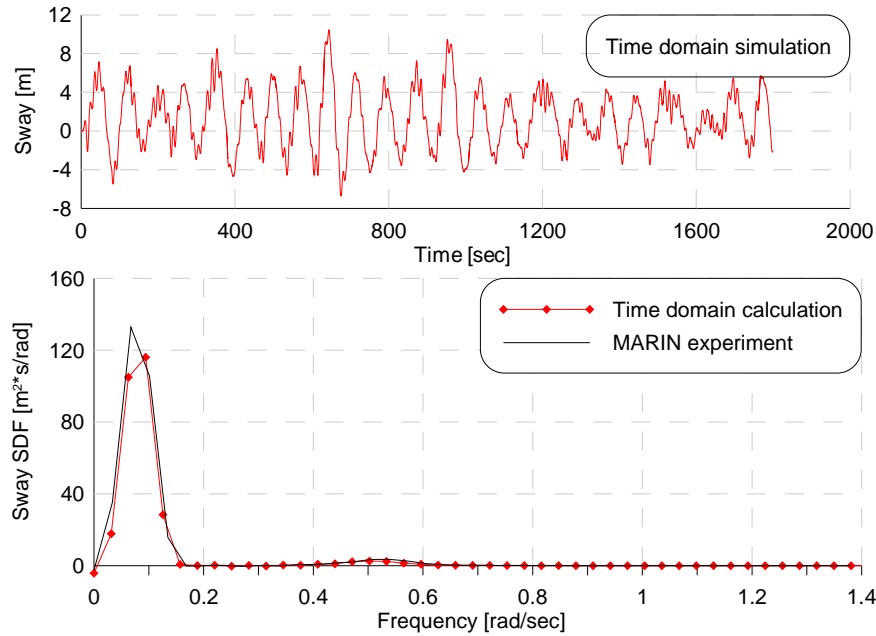
Fig. 5.20 Time series and Spectral Density Function of sway (Wave heading = 90 deg)

5.5.3 Free Decay Test with Sloshing

To better understand the inherent physics in ship and inner-fluid-motion interactions, free decay tests of roll and pitch are conducted for different filling levels as shown in Fig. 5.21 and Fig. 5.22. In Fig. 5.21, the bare-hull's roll natural frequency is 0.50 rad/s and the initial roll displacement is 5deg. Since MARIN-FPSO is barge-type, we can observe that the overall roll viscous damping is large. With 18% filling ratio, the natural frequency of sloshing is 0.49 rad/s, which is very close to that of bare-hull. As a result, the initial free-decay motion may strongly agitate the inner fluid motion, and therefore, phase shift occurs starting from the second roll period. The resulting roll amplitude is not decaying, but instead slightly increases temporarily at 3rd roll period due to the resonant inner-fluid motion. In this case, the roll damping cannot be calculated based on the traditional way using logarithmic decrement. It can also be noticed that the peak amplitudes are appreciably smaller than those of bare-hull. As for the 56% fill-ratio case,

the transverse natural sloshing frequency is 0.74 rad/s, which is higher than that of bare hull. As a result, resonant sloshing motion does not occur by the initial free-decay motions. With the inner liquid, the roll natural period is slightly increased and the overall damping becomes appreciably bigger, especially for larger amplitude. The increased damping is mainly due to the phase shift of inner-fluid motion and the inner-fluid viscosity/nonlinearity, which cannot be explained by the linear potential theory alone. The presented free-decay results with different levels of inner fluid are very similar to those experimental results by the 24th ITTC benchmark tests for damaged-ship stability.

The corresponding pitch free-decay simulation is also shown in Fig. 5.22. The figure shows that the free pitch motion of the coupled system is almost not affected by the inner-fluid motion due to the ship's longitudinal inertia. The hull damping is much larger than those caused by inner fluid motion. This phenomenon will also be confirmed in the ensuing simulations of roll and pitch motions with inner liquid in irregular waves. Next, the same free-decay test is also conducted, as shown in Fig. 5.23, in the presence of a regular wave of amplitude=1.67m whose frequency=0.74 is close to the sloshing natural frequency of 56% case. As can be seen in the bare-hull case, the floater oscillates at its natural frequency in the beginning. After the transient responses are sufficiently attenuated, the floater reaches a steady-state response oscillating at the wave exciting frequency. The transient part is very similar to that of Fig. 5.21, in the case of 18% filling, while the non-decaying steady-state part is analogous to the bare-hull case since the sloshing motion is expected to be small (being far away from the first and second sloshing natural frequencies) at the given wave exciting frequency. In the case of 56% filling, on the other hand, the steady-state ship motion becomes appreciably larger than that of bare-hull since

the natural frequency of the first mode sloshing is the same as wave excitation frequency.
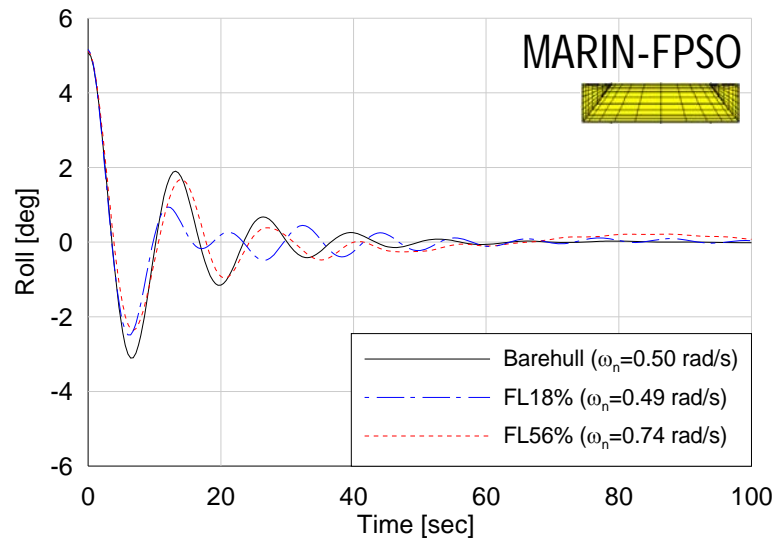
Fig. 5.21 Roll free decay test of MARIN-FPSO.
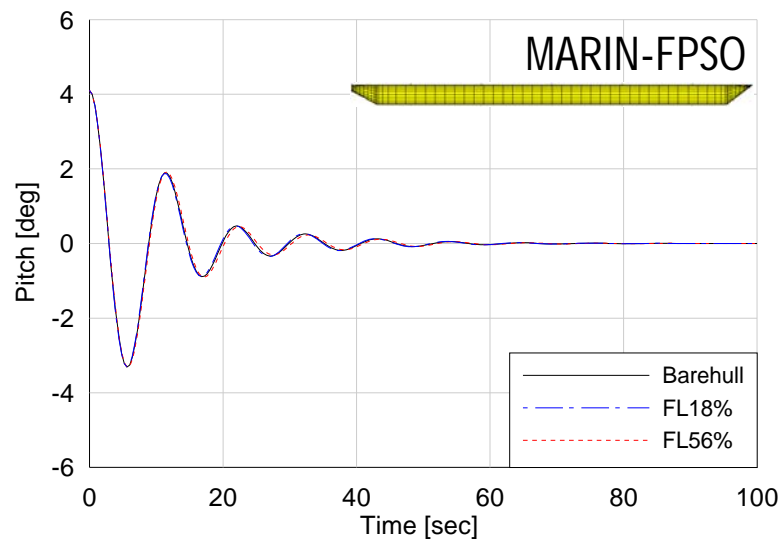
Fig. 5.22 Pitch free decay test of MARIN-FPSO.
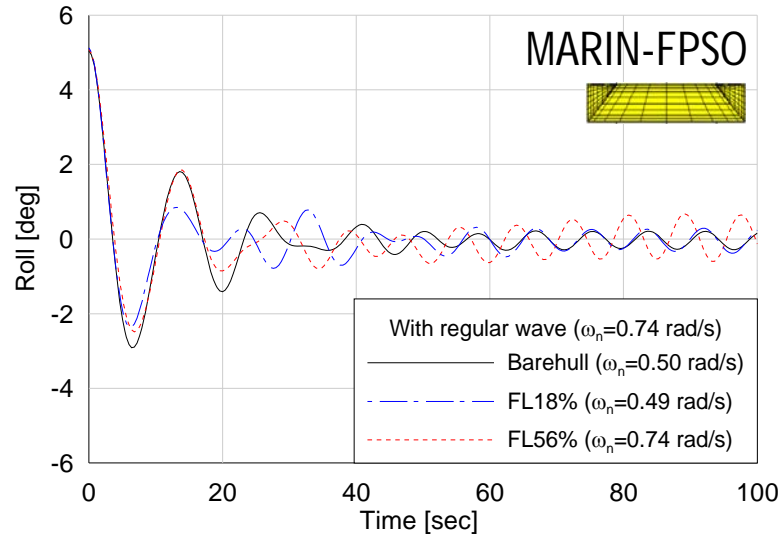
Fig. 5.23 Roll free decay test of MARIN-FPSO with regular wave amplitude 1.67m.

5.5.4 *Irregular Wave Test with Sloshing*

To simulate a more realistic sea state, an irregular wave test of motion-sloshing coupling effect is investigated. In the sloshing calculation, three different filling levels (18%, 37% and 56%) are considered and the two tanks are filled at the same level for each filling level. For the present simulation, no wind or current is involved, and the roll and pitch-motion changes with sloshing are considered in beam and head waves, respectively.

Fig. 5.24 shows the input spectrum of incident wave field. Fig. 5.25 through Fig. 5.27 show a comparison between experiment and calculation of roll motion for beam sea condition at different filling levels Fig. 5.25 shows roll spectra for 0% filling level. The simulated spectra show good agreement with the experimental results. Fig. 5.26 and Fig. 5.27 show the roll spectra for 18% and 37% filling levels, which include tank sloshing effects on ship motions. The most important coupling effect is the shift of resonance peaks in roll. Particularly for 37% filling level, the single peak is split into two separated, smaller peaks both in experiment and simulation. The secondary peak is related to the natural

frequency of the lowest tank sloshing mode (see Table 5.4).

To see this phenomenon more clearly, the time series and spectrum of the tank induced roll moment caused by inner liquid motions are plotted in Fig. 5.28 and Fig. 5.29. As can be expected, the excitation spectrum has two separate peaks: one close to the peak wave frequency and the other at the sloshing natural frequency. The increased response near 0.74 rad/s in Fig. 5.27 is due to the large sloshing-induced loading in Fig. 5.29. In the case of 18% filling level, the roll natural frequency coincides with the lowest sloshing natural frequency, and thus the split of resonance peaks does not happen. It is also expected in Fig. 5.26 that the liquid sloshing is violent with the excitation near the resonance frequency, which may cause the slight increase of experimental roll-motion amplitude; however, in the numerical simulation, such highly violent liquid motions are not modeled, so numerical values are lower than the measured data. The discrepancy in spectra (representing amplitude squared) in Fig. 5.26 results in much smaller differences in time series.
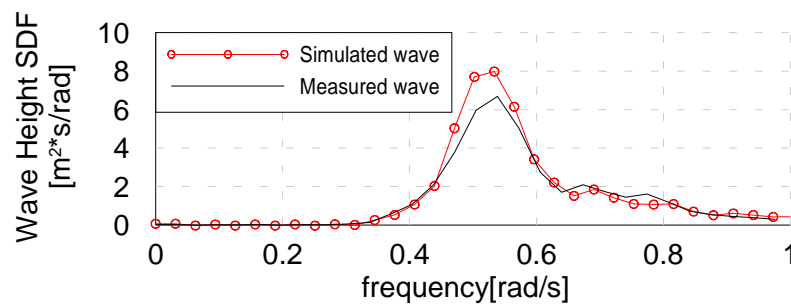
Fig. 5.24 Wave spectral density (Hs=5.0m, γ=3.3).
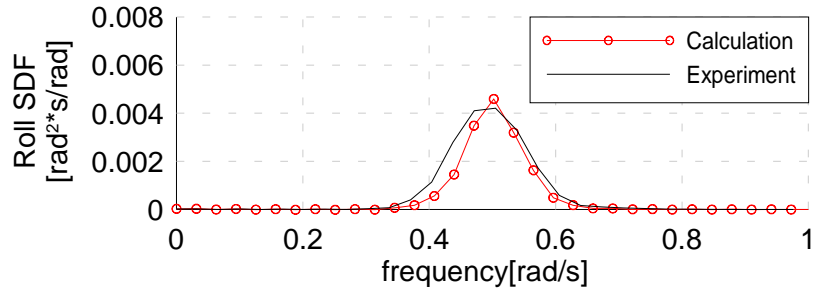
Fig. 5.25 Simulated and experimental results of 0% filling level.
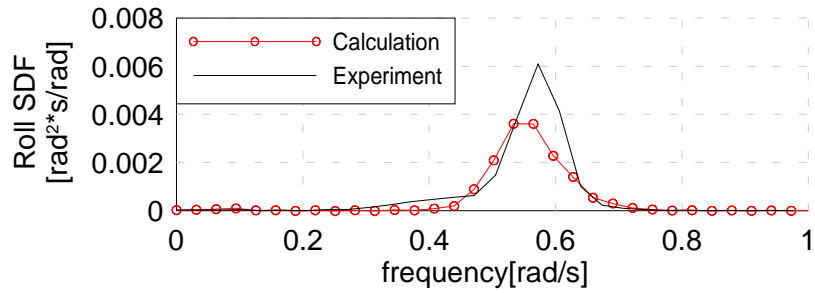
Fig. 5.26 Simulated and experimental results of 18% filling level.
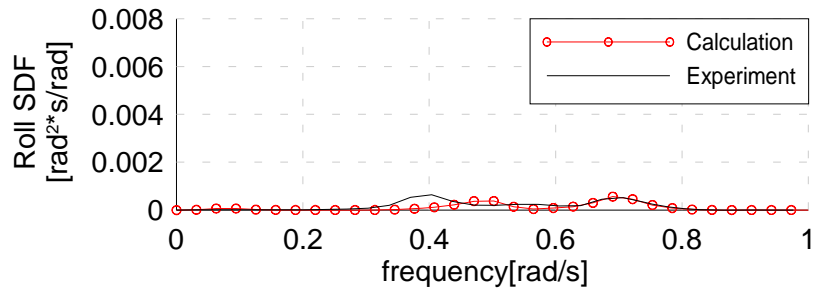
Fig. 5.27 Simulated and experimental results of 37% filling level.
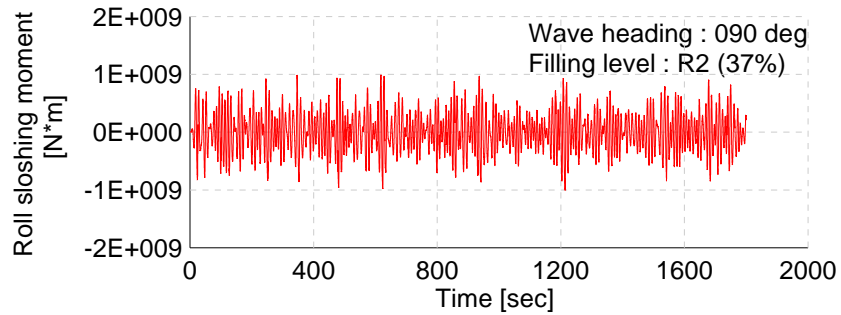
Fig. 5.28 Simulated time series of roll sloshing excitation moment of 37% filling level.
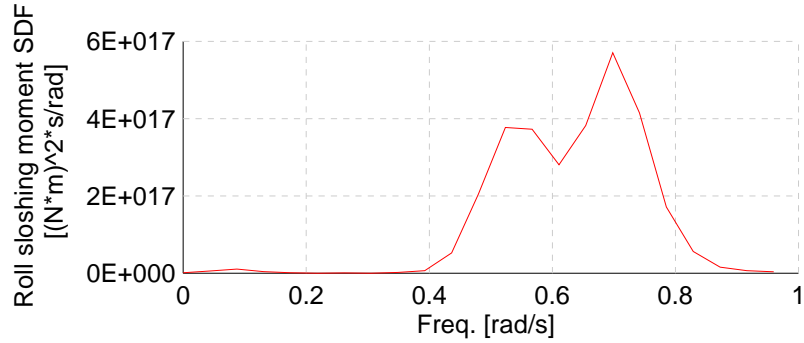
Fig. 5.29 Simulated spectral density of roll sloshing excitation moment of 37% filling level.

The roll amplitudes tend to decrease as the filling level increases. The observed phenomenon is related to the fact that water tanks are effective in reducing the vibration of a tall building caused by an earthquake. Fig. 5.30 shows the time series of both sway and roll for 18% and 37% filling levels. The roll amplitude at 37% filling level is significantly reduced, while the sway is only slightly decreased. The present barge has a soft mooring system, and its sway natural period is much longer than resonant sloshing periods, thus the sway motion is little affected by the inner liquid motions.

(a)
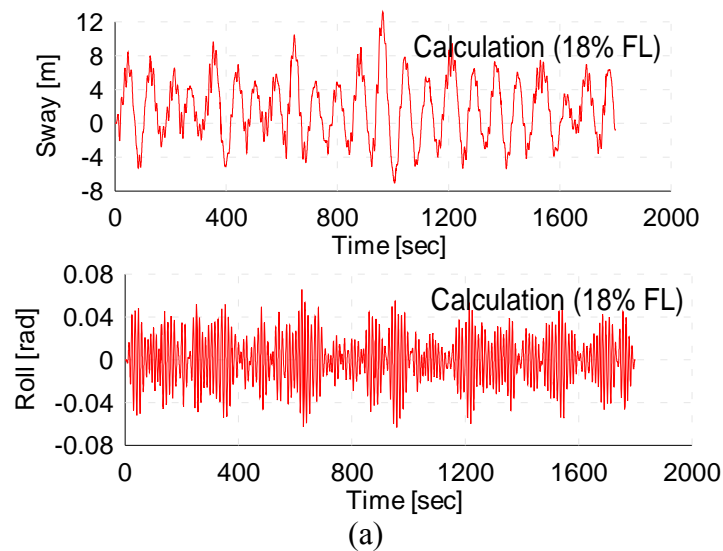
Fig. 5.30 Simulated time series of sway and roll (a) 18% filling level, (b) 37% filling level.
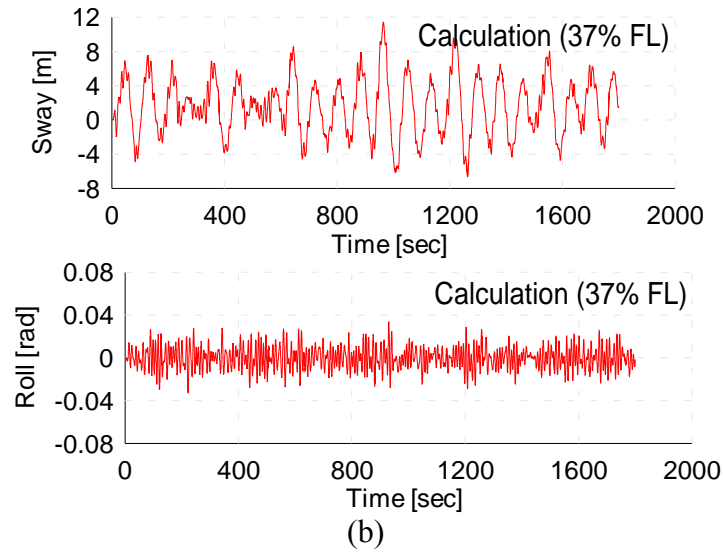
Fig. 5.30 Continued.

Fig. 5.31(a)-(d) represents RAOs of roll motion at different filling levels. Each figure includes experimental results obtained from an irregular wave model test, frequency domain results, and time domain simulation results. As was previously pointed out in Fig. 5.27, we can clearly see in Fig. 5.31 (c) and (d) the split of peaks in the roll RAOs of 37% and 56% fill levels. Since the sloshing resonance frequency of 56% is farther from the hull resonance frequency, we observe greater separation distance between the two peaks. When I consider roll RAOs near the bare-hull's natural frequency 0.5(rad/s), the roll motions continue to decrease with the fill ratio. On the other hand, the roll amplitudes near 0.8(rad/s) continue to increase with the fill ratio. Therefore, the inner liquid motions can increase or decrease the roll motions depending on incident wave frequencies. The peak frequency of the present input spectrum is around 0.5 rad/s, causing the roll motions continue to decrease with increasing filling level. The frequency domain linear potential results in Fig. 5.31 (a)-(d) show a similar trend but the resonance peaks are significantly over-predicted because viscous and nonlinear free-surface effects are not included.

For head sea condition and pitch motions, it can be observed from Fig. 5.32 that the coupling effects of liquid cargo and hull motion are less significant. It is primarily due to the fact that the inertia of longitudinal hull is much larger than the dynamic effect of liquid motion. Fig. 5.32 (a)-(c), for example, show pitch RAOs for different filling levels of liquid cargo. Fig. 5.32 (a) shows pitch RAO without liquid cargo and Fig. 5.32 (b), (c) and (d) show pitch RAOs of 18%, 37%, and 56% filling levels, respectively. In all cases, the effects of liquid cargo sloshing in pitch motions are very minor.

Another reason why pitch motion is not much affected by different filling levels is that the acceleration on each tank's free surface, due to pitch motion, is in same direction. However, roll causes acceleration in opposite direction as shown in Fig. 5.33. It is obvious that the free surface with opposite acceleration direction will be much easier to be excited than the free surface with same acceleration direction throughout its surface.

From the conducted time domain simulations, we can observe the detailed instantaneous coupling effects between the vessel and liquid motions through 3D animation. One such snapshot is given in Fig. 5.34 as an example.
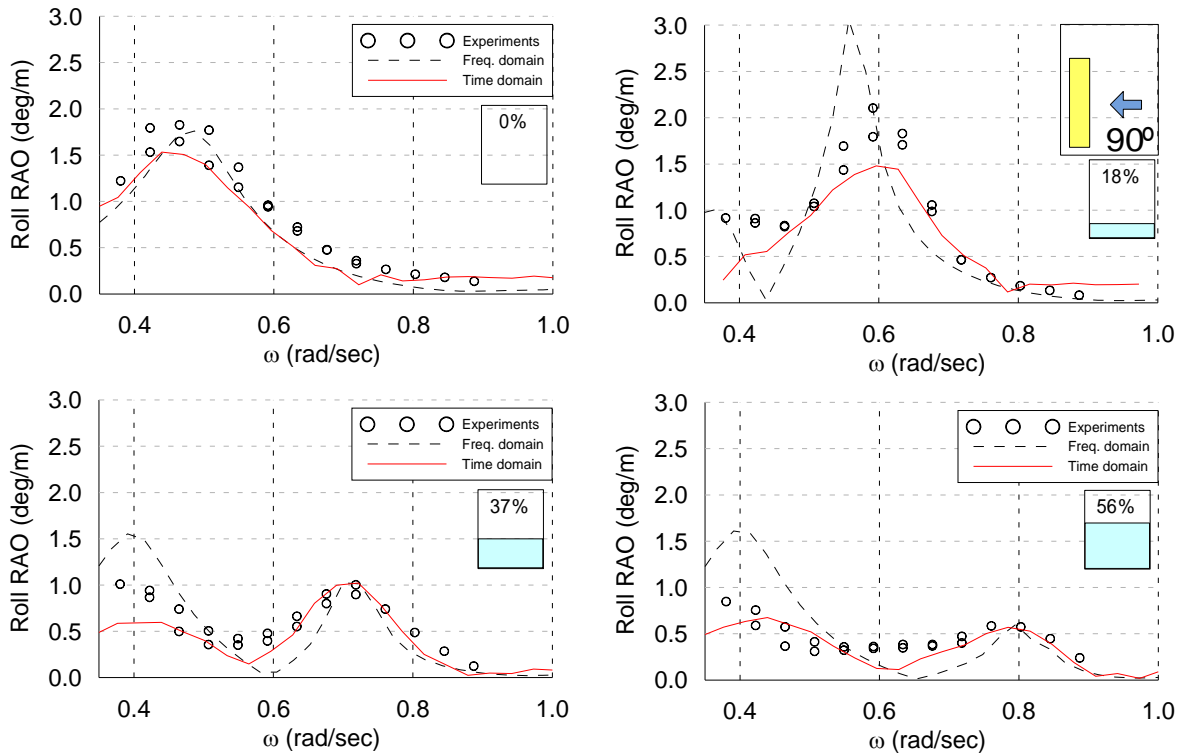
Fig. 5.31 Comparison of coupling effect of roll motion (Wave heading = 90deg)
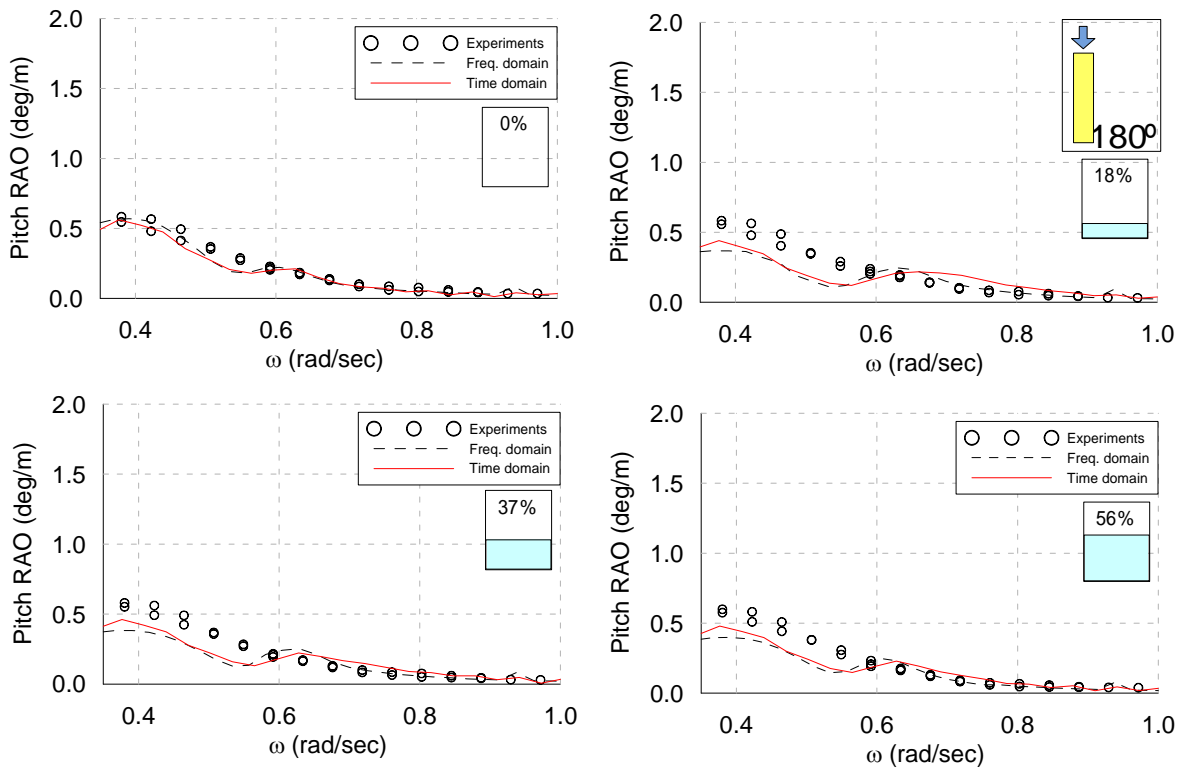
Fig. 5.32 Comparison of coupling effect of pitch motion (Wave heading = 180deg)
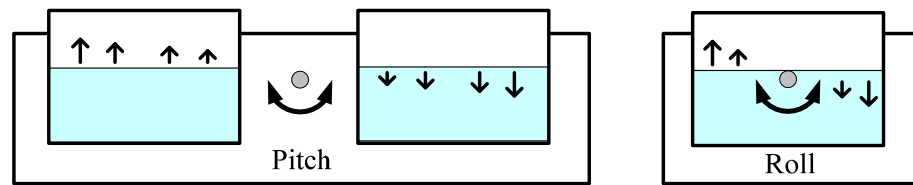
Fig. 5.33 Acceleration on free surface caused by pitch and roll motion.
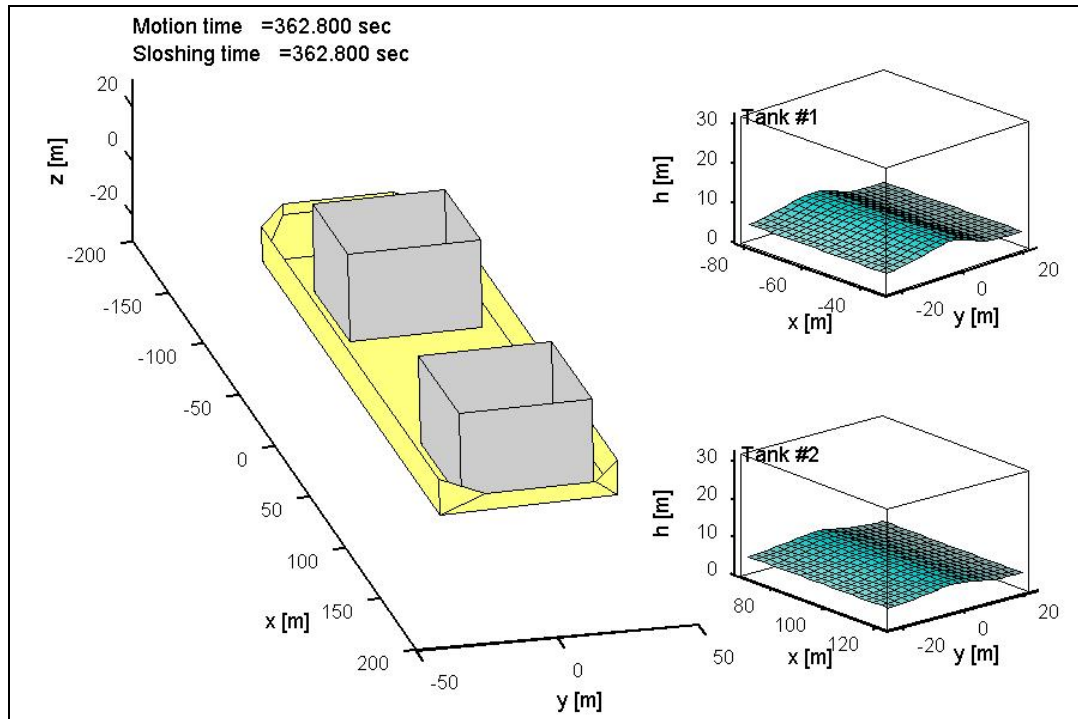
Fig. 5.34 Snapshot of motion-sloshing coupled animation in time domain

(37% FL, Wave heading=90deg)

5.6   Additional Discussion

5.6.1   *Simple Correction Method*

Additionally, let us consider the simplest correction method through mass-stiffness adjustment. The mass correction is the change of liquid mass, mass moment of inertia, and vertical center of gravity due to additional liquid cargo (this effect is minimized in MARIN's experiment by adjusting the ballast). The stiffness correction is the loss of roll-

pitch hydrostatic restoring coefficients due to the presence of inner free surface, which is given by equation (4.35). From equation (4.35), the inner-free-surface restoring correction is affected only by the density of inner fluid and the second moment of inner free surface, not by the filling level of liquid cargo. Therefore, the stiffness correction gives identical results for different filling levels. Fig. 5.35 (d) shows the result of the simple mass-stiffness correction method compared with a case without cargo liquid. The roll natural frequency is shifted lower due to the decrease of roll restoring stiffness. This example illustrates that the simple correction method cannot reproduce the complex dynamic and coupling effects by liquid sloshing.

(a)
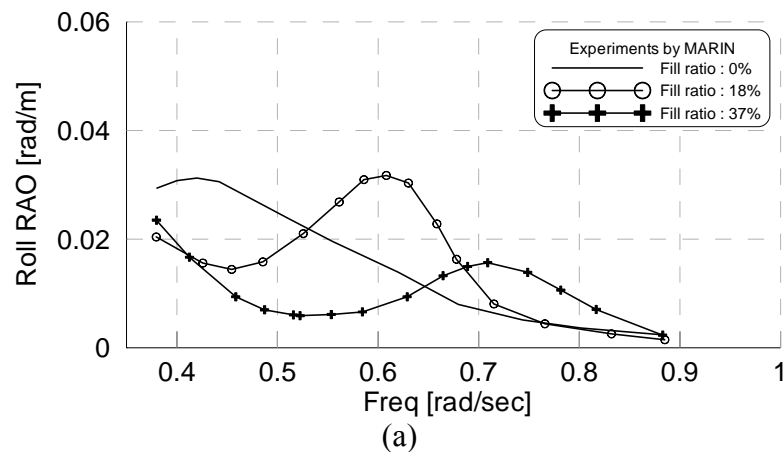
Fig. 5.35 Comparison of roll RAOs. (a) Experiments by MARIN, (b) from time domain simulation, (c) from frequency domain calculation, and (d) by simple approximate method through mass-stiffness correction.
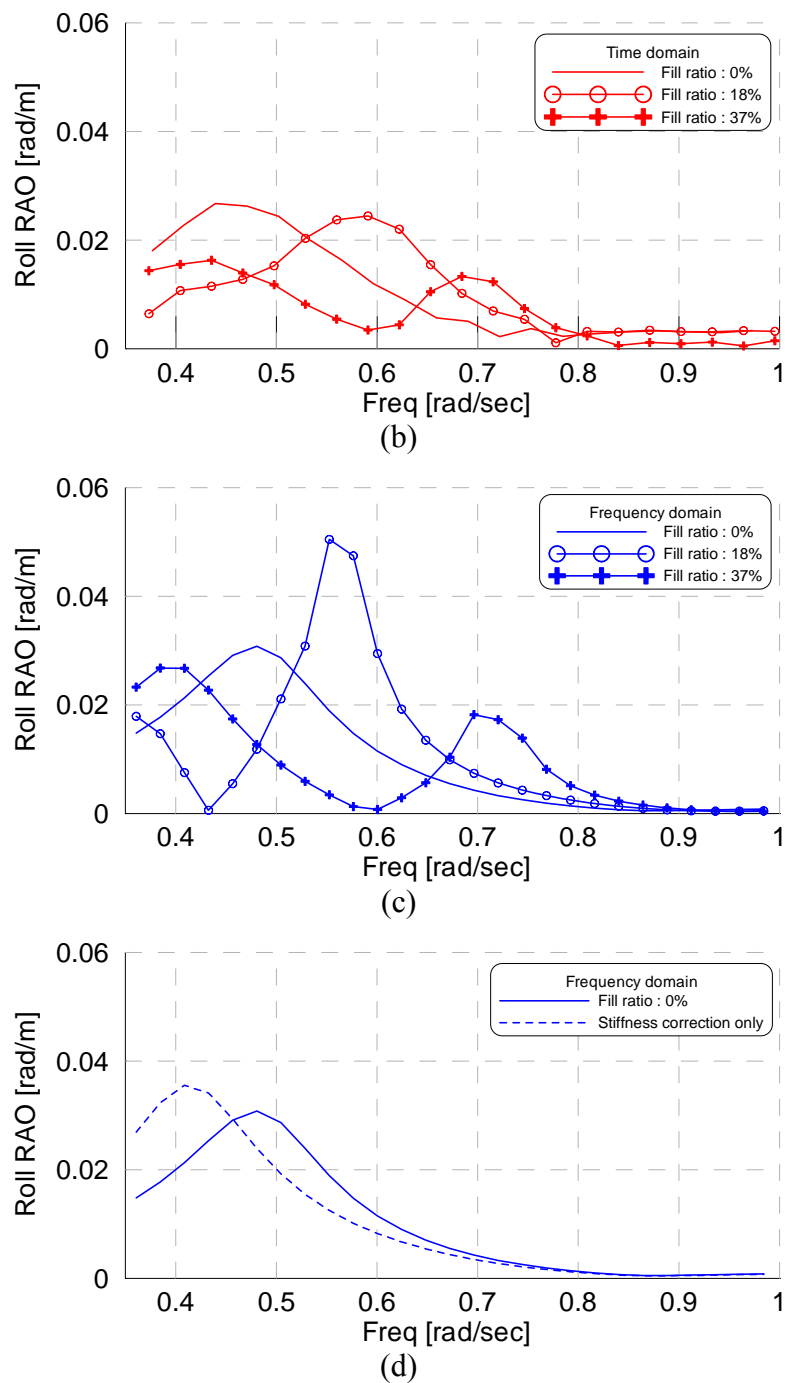
Fig. 5.35 Continued.

5.6.2 Simplified Mass-spring Sloshing Model

Split of roll natural frequency with respect to different filling levels is a major

characteristic of motion and sloshing coupling effect. Separated two natural frequencies can be calculated easily by solving a 2-DOF mass-spring system. In order to predict sloshing effect in roll mode, I can simplify each ship motion and sloshing phenomenon using mass-spring system. Fig. 5.36 shows a simplifying model of ship motion in waves and sloshing fluid inside the tank.
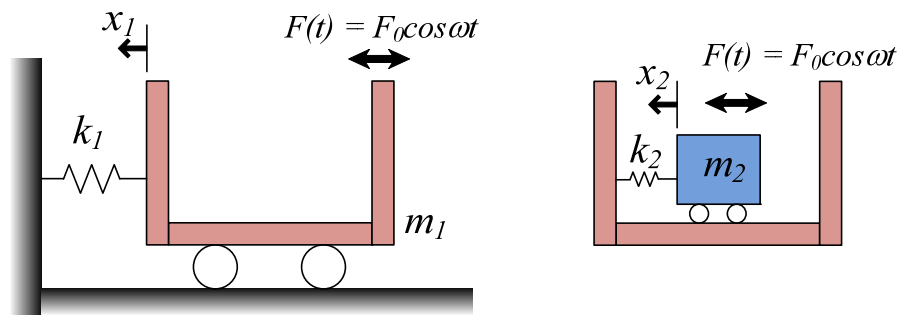
Fig. 5.36 Simplified ship motion and sloshing model (Uncoupled).

Equation of motion of mass m_1 and spring k_1 is:

$$m_1 \cdot \ddot{x}_1(t) + k_1 \cdot x_1(t) = F_0 \cos \omega t \tag{5.1}$$

Assuming x_1 as:

$$x_1(t) = X_1 \cdot \cos \omega t \tag{5.2}$$

Then equation (5.1) can be expressed as:

$$\left(-\omega^2 \cdot m_1 + k_1\right) X_1 = F_0 \tag{5.3}$$

Therefore amplitude of displacement of mass m_1 is:

$$X_1 = \frac{F_0}{-\omega^2 \cdot m_1 + k_1} \tag{5.4}$$

Similarly, amplitude of displacement of mass m_2 is:

$$X_2 = \frac{F_0}{-\omega^2 \cdot m_2 + k_2}$$
(5.5)

When applying this system to roll motion coupling of ship and sloshing, m_1 is virtual mass of ship (roll mass inertia + roll added mass of inertia) and k_1 is determined by natural frequency of ship's roll motion. When there is sloshing fluid, k_1 should be modified considering hydrostatic reduction of restoring due to the existence of inner free surface as showen in equation(4.29). For sloshing components, m_2 the is added mass of sloshing fluid at $\omega \approx 0.0$ to represent mass of sloshing fluid in roll mode. k_1 is calculated using m_2 and the natural frequency of sloshing tank with respect to different filling levels. Therefore, sloshing fluid at different filling levels can be modeled using m_2 and k_2 so that peak behavior of sloshing added mass at natural frequency is included by using this model. These descriptions are summarized in Table 5.7.

I applied this system using real mass and natural frequencies from the MARIN-FPSO case for the comparison with frequency and time domain motion-sloshing coupling program I developed. Table 5.8 shows values of mass and stiffness calculated from MARIN-FPSO case, while Fig. 5.37 shows the natural frequency of simplified body mass and sloshing tank for three different filling levels.

Table 5.7 Description of mass and stiffness of simplified sloshing model.

	Equation	Description
m_1	$m_{44} + m_{44}^a(\omega_n)$	Roll virtual mass of ship.
k_1	$(\omega_n)^2 * \{m_{44} + m_{44}^a(\omega_n)\}$	FL 0%: Ship stiffness from roll natural frequency. FL 18,37,56%: Roll restoring reduction included. ($k_1' = k_1 - I\rho g$)
m_2	$m_{44,fluid}^a(\omega_0)$	Roll added mass of sloshing fluid at $\omega \approx 0.0$.
k_2	$(\omega_n)^2 * m_{44,fluid}^a(\omega_0)$	Stiffness from sloshing natural frequency at each filling level.

Table 5.8 Mass and stiffness values of simplified sloshing model.

	m_1 [kg*m^2]	k_1 [kg*m^2/s^2]	m_2 [kg*m^2]	k_2 [kg*m^2/s^2]
FL 0%	1.482E+11	3.706E+10	N/A	N/A
FL 18%	1.482E+11	2.785E+10	2.595E+10	6.231E+09
FL 37%	1.482E+11	2.785E+10	1.447E+10	6.301E+09
FL 56%	1.482E+11	2.785E+10	1.441E+10	7.889E+09
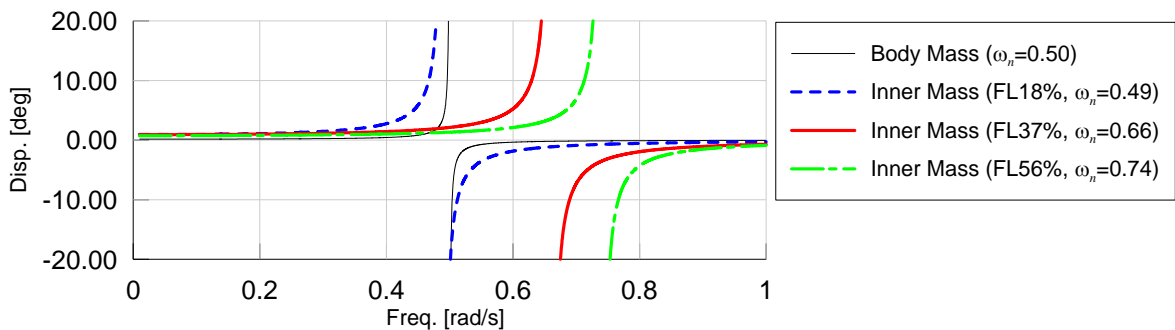
Fig. 5.37 Displacement of simplified sloshing model (Uncoupled).

Motion-sloshing coupled phenomenon can be simplified by combining the above two models as shown in Fig. 5.38.
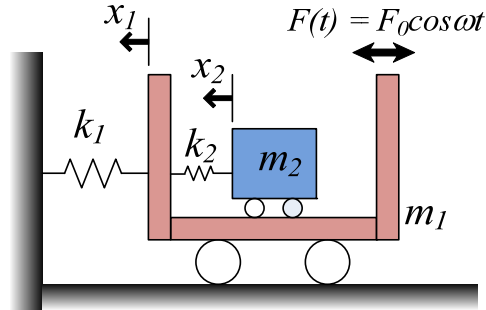
Fig. 5.38 Simplified ship motion and sloshing model (Coupled).

Equations of motion for two degree of freedom spring-mass system are:

$$m_1 \cdot \ddot{x}_1(t) + (k_1 + k_2) \cdot x_1(t) - k_2 \cdot x_2(t) = F_0 \cos \omega t$$
$$m_2 \cdot \ddot{x}_2(t) - k_2 \cdot x_1(t) + k_2 \cdot x_2(t) = 0$$

(5.6)

Assuming,

$$x_1(t) = X_1 \cdot \cos \omega t$$
$$x_2(t) = X_2 \cdot \cos \omega t$$

(5.7)

Euqation of motion is written as matrix form as:

$$\begin{bmatrix} -\omega^2 \cdot m_1 + k_1 + k_2 & -k_2 \\ -k_2 & -\omega^2 \cdot m_2 + k_2 \end{bmatrix} \begin{bmatrix} X_1 \\ X_2 \end{bmatrix} = \begin{bmatrix} F_0 \\ 0 \end{bmatrix}$$

(5.8)

Then the displacements with respect to excitation frequency can be expressed as:

$$X_1 = \frac{\left(-\omega^2 \cdot m_2 + k_2\right) F_0}{\left(-\omega^2 \cdot m_1 + k_1 + k_2\right)\left(-\omega^2 \cdot m_2 + k_2\right) - \left(k_2\right)^2}$$

(5.9)

$$X_2 = \frac{k_2 \cdot F_0}{\left(-\omega^2 \cdot m_1 + k_1 + k_2\right)\left(-\omega^2 \cdot m_2 + k_2\right) - \left(k_2\right)^2}$$

(5.10)

Fig. 5.39 shows results of equations (5.9) and (5.10). This figure clearly represents the coupling effect of sloshing that we have observed in previous sections. Secondary peak due to sloshing effect is moving to a high frequency region as the filling levels get higher. Location of secondary peak frequency can be calculated by characteristic equation of equation (5.8) as followings.

$$\det \begin{bmatrix} -\omega^2 \cdot m_1 + k_1 + k_2 & -k_2 \\ -k_2 & -\omega^2 \cdot m_2 + k_2 \end{bmatrix} = 0 \tag{5.11}$$

or

$$\omega^4 \cdot m_1 \cdot m_2 - \omega^2 \cdot m_1 \cdot k_2 - \omega^2 \cdot m_2 \cdot (k_1 + k_2) + k_1 \cdot k_2 = 0 \tag{5.12}$$

The roots of equation (5.12) will represent analytic value of secondary peak due to sloshing effect.

$$m_1 \cdot m_2 \cdot (\omega^2)^2 - \{m_1 \cdot k_2 + m_2 \cdot (k_1 + k_2)\} \omega^2 + k_1 \cdot k_2 = 0 \tag{5.13}$$

$$\omega^2 = \frac{\{m_1 \cdot k_2 + m_2 \cdot (k_1 + k_2)\} \pm \sqrt{\{m_1 \cdot k_2 + m_2 \cdot (k_1 + k_2)\}^2 - 4 \cdot m_1 \cdot m_2 \cdot k_1 \cdot k_2}}{2 \cdot m_1 \cdot m_2} \tag{5.14}$$

Calculated results of equation (5.14) are summarized in Table 5.9. According to equation (5.14), the analytic secondary motion peak of 18% FL is 0.579, 37% FL is 0.721, and 56% is 0.798. These values match perfectly with the plotted displacement of simplified motion-sloshing coupling model shown in Fig. 5.39, and first peak of roll motion is also predicted exactly as 0.397, 0.403, 0.406rad/s for FL 18%, 37%, 56%, respectively. These results are explaining split of roll natural frequency in frequency and time domain coupling program results in Fig. 5.31. Therefore, we can predict the frequency of first and second peak due to sloshing effect by simply using equation (5.14) in the initial design stage once we know ship virtual mass, sloshing added mass of sloshing at 0.0rad/s, and natural

frequencies of ship motion and sloshing tanks.
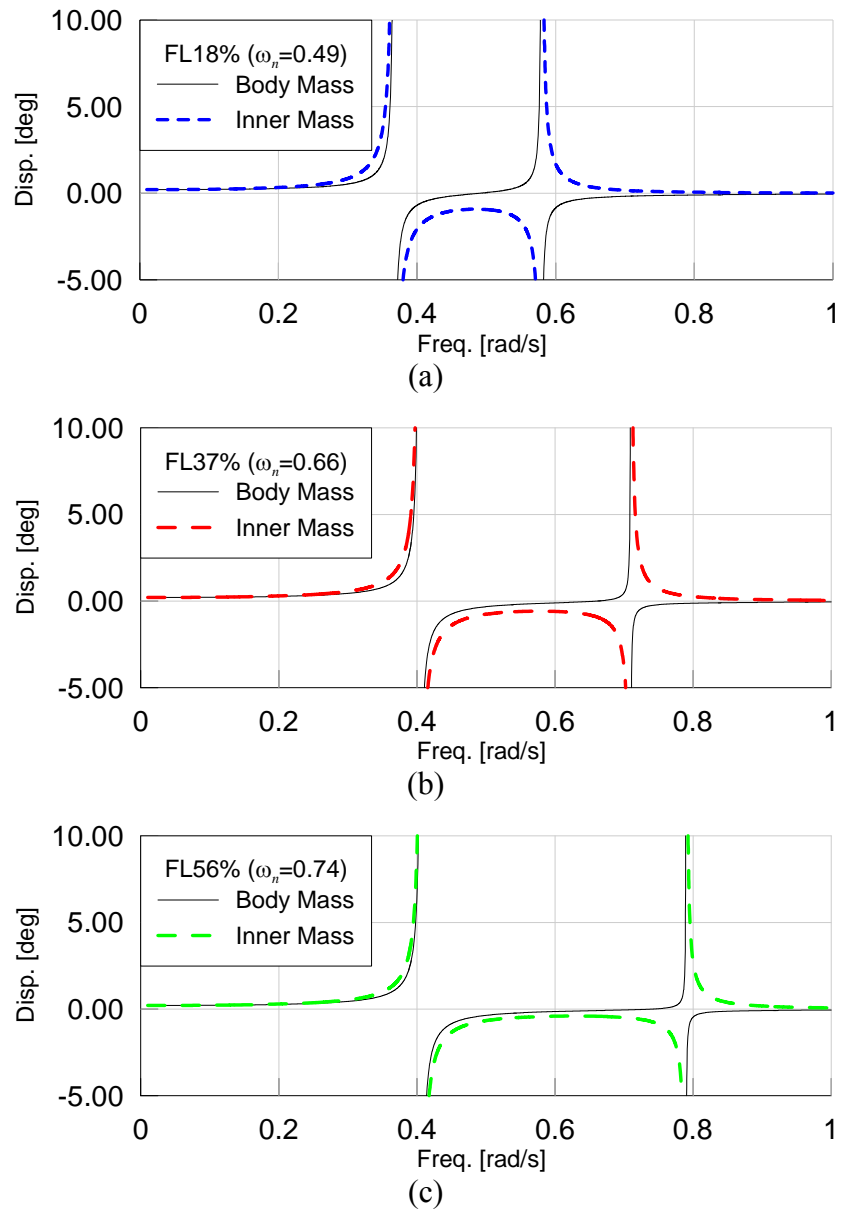
Fig. 5.39 Displacement of simplified sloshing model (Coupled)

(a) 18% FL, (b) 37% FL, and (c) 56% FL.

Table 5.9 Calculated natural frequency by uncoupled/coupled simplified sloshing model.

Uncoupled natural frequency [rad/s]			Coupled natural frequency [rad/s]	
Body mass	Inner mass			
0.50	FL18%	0.49	0.397	0.579
	FL37%	0.66	0.403	0.709
	FL56%	0.74	0.406	0.790

5.6.3 *Effect of Different Incident Wave Slope*

Based on linear theory, body motion RAO should not be changed due to the change of incident wave slope; however, nonlinearity of sloshing phenomenon is playing an important role in motion RAO for different wave slopes (Kim et al., 2007). Fig. 5.40 shows roll RAO in beam sea condition for two different filling levels, 37% and 56%. For 37% filling level, we can observe that roll RAO with wave height 5.0m is higher than that of 2.0m case; for 56% filling level, on the other hand, roll RAO for both wave heights of 2.0m and 5.0m do not look much different. Such a slight difference is due to the behavior of sloshing fluid at a lower filling level, where sloshing fluid is in more nonlinear aspects than that of a higher filling level. This test illustrates nonlinear effect of roll motion RAO due to nonlinearity of sloshing fluid for different incident wave slopes.
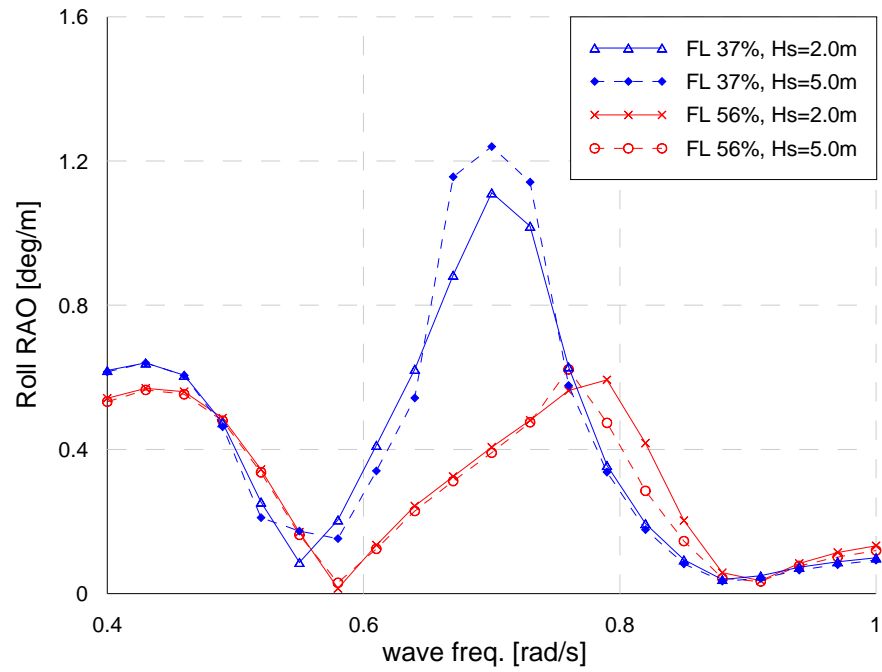
Fig. 5.40 Comparison of roll RAO for 37% and 56% filling levels
with different wave height.

CHAPTER VI

CASE STUDY II: DYNAMIC ANALYSIS OF FLOATING TERMINAL AND LNG-CARRIER

6.1   Introduction

In this study, dynamic coupling analysis of floating terminal and LNG-carrier with sloshing phenomenon in the LNG-carrier side is carried out in a hydrodynamic coupling analysis program. During the offloading operation in offshore site, a LNG-carrier can be moored with a floating terminal either in side-by-side situation or in tandem mooring situation, depending upon feasibility of each body's mooring configuration. If each body structure is symmetric in x-axis and y-axis as spar, selection of side-by-side mooring or tandem mooring does not make any difference to a hydrodynamic point of view. However, floating terminal and LNG-carrier are having relatively remarkable length in x-axis when compared to breadth in y-axis. These structure's characteristic properties can cause completely different hydrodynamic regime in side-by-side or tandem mooring system. Generally, a side-by-side mooring case is more dangerous in terms of ship motion safety due to the gap effect between LNG-carrier and floating terminal. It is for this reason that side-by-side mooring configuration is investigated in this study with various mooring systems such as mooring lines, fenders, and hawsers. Water depth is also an important factor in hydrodynamics of floating body and mooring lines below sea water. In this case, water depth is 100m, an intermediate water depth in offloading configuration. Hydrodynamic effect of water depth in second-order wave drift force is shown to validate

usage of Newman's approximation with intermediate water depth.

Hydrodynamic calculation of multi-body interaction is performed by the WAMIT in frequency domain and implemented into time domain using time-memory function. Two bodies are connected by hawsers and fenders which are strongly nonlinear mooring systems. These systems are modeled using nonlinear springs, including gap distance of two bodies. The hydrodynamic effect of fenders and hawsers are not included in this study due to the assumption that fenders and hawsers are located above free surface. To discover sloshing effect during the offloading operation, this study is investigating the case that two sloshing tanks are only equipped in LNG-carrier side as shown in Fig. 6.1. The Navier-Stokes solver, ABSLO3D, is used for time domain analysis of sloshing, demonstrated by the single-body case in the previous chapter. Sloshing effect in frequency domain is included by the added mass in frequency domain using WAMIT program.
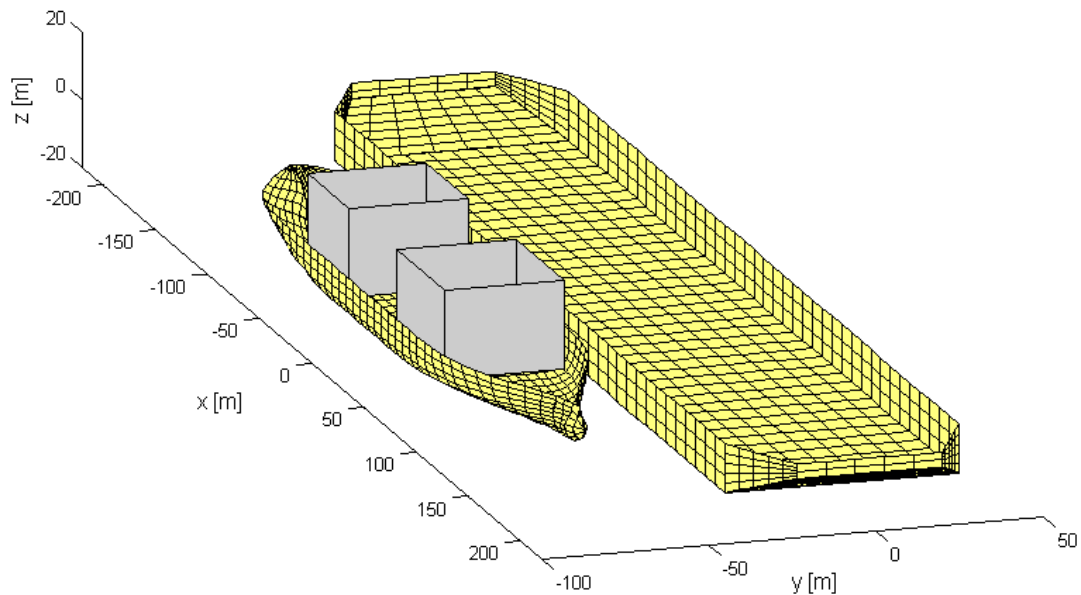
Fig. 6.1 General sketch of Floating terminal, LNG-carrier, and LNG tanks arrangement.

6.2　Principal Particulars

Principal particulars of floating terminal and LNG-carrier are listed in Table 6.1. For the investigation of gap distance effect, gap distance between floating terminal and LNG-carrier is 6m for all cases, except one case of 40m, for investigation of gap distance effect. Table 6.2 shows dimension and location of two sloshing tanks on LNG-carrier. Three different filling levels (0%, 18% and 56% of tank height) are investigated in the simulation, and both tanks are filled with the same filling levels. For the mooring lines, a total of 12 mooring lines are used, 3 lines at each 4 corner of floating structures as shown in Fig. 6.2. Each mooring line is composed of chain-wire-chain components as presented in Table 6.3. Floating terminal and LNG-carrier are connected with hawsers and fenders are located in floating terminal side. A total of 6 hawsers and 2 fenders are used, and their configurations are listed in Table 6.4.

Table 6.1 Principal particulars of floating terminal and LNG-carrier

Description	Unit	Floating Terminal	LNG-carrier
Length	m	428.0	270.0
Breadth	m	70.0	43.4
Draught	m	14.5	11.916
Displacement	ton	418,429.5	102,591.0
LCG	m	214.0	134.878
VCG	m	10.4	4.43
k_{xx}	m	24.5	15.703
k_{yy}	m	107.0	67.5
k_{zz}	m	107.0	69.302

Table 6.2 Characteristics of sloshing tanks on LNG-carrier.

Designation	Magnitude
AFT TANK no.4 (inner dimensions given)	
Tank center from aft perpendicular	80.27 m
Tank bottom from keel line	2.60 m
Tank length	40.04 m
Tank breadth	35.69 m
Tank height	26.30 m
FORWARD TANK no.2 (inner dimensions given)	
Tank center from aft perpendicular	174.29 m
Tank bottom from keel line	2.60 m
Tank length	45.48 m
Tank breadth	35.75 m
Tank height	26.30 m

Table 6.3 Mooring lines characteristics

	AE	EI	Dry mass	Wet mass	CB_{IB}	CB_{DB}
Chain	1.807E+09	0.000E+00	500	65	3.0	2.45
Wire	1.714E+09	0.000E+00	118	79	2.0	1.0
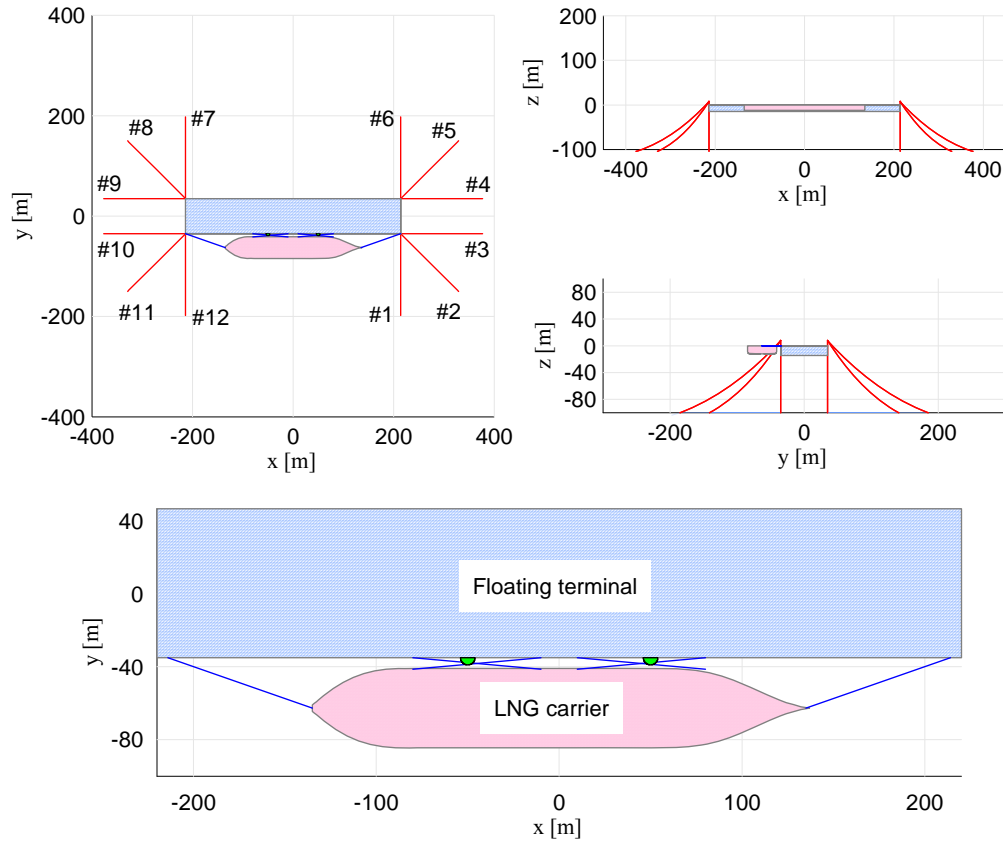
Fig. 6.2 Configuration of mooring lines, fenders, and hawsers.

Table 6.4 Fenders and hawsers characteristics

	Location	Stiffness [N/m]	Slack Length [m]	Orig. Length [m]
Hawsers	Fore	8.00E+06	101.24	100.24
	APT	8.00E+06	101.24	100.24
	Fore Cross1	8.00E+06	81.62	80.62
	Fore Cross2	8.00E+06	81.62	80.62
	APT Cross1	8.00E+06	81.62	80.62
	APT Cross2	8.00E+06	81.62	80.62
Fenders	Fore	1.60E+07	5.00 (Thickness)	6.00
	APT	1.60E+07	5.00 (Thickness)	6.00

6.3 Simulation Conditions

This study performs various simulations including effects of gap distance between two bodies, sloshing effect with respect to different filling levels, mooring lines effect, and various types of environmental conditions. First, gap effect is investigated for two cases (6m and 40m). Sloshing effects are studied by selecting three filling levels (0%, 18%, and 56% of tank height). Mooring effects deal with actual mooring lines, simplified mooring system, and dolphin mooring system. For all cases, two bodies are kept connected with fenders and hawsers. For environmental condition, three types of environments are included; wave, current, and wind. Irregular waves are applied for all cases with three different wave heading conditions such as head sea (180deg), beam sea (90deg), and quartering sea (150deg) conditions. In order to study the most harsh environmental conditions, current and wind are always applied in collinear direction with wave heading angle. A list of all simulation cases are shown in Table 6.5.

6.4 Motion Response in Frequency Domain

Motion RAOs of floating terminal and LNG-carrier in frequency domain are investigated in this section. Fig. 6.3, Fig. 6.4, and Fig. 6.5 show motion RAOs of floating terminal and LNG-carrier that represent modes that, in turn, correspond to three different wave heading angles (90deg, 150deg, and 180deg). Due to the existence of a gap between two bodies, motion characteristics of two bodies are different from that of a single-body. For example, in beam sea condition (90deg) in Fig. 6.3, we can observe heave response that is larger than 1.0 in certain frequency region unlike the single-body case. This is because that trapped wave in the gap is amplifying heave motion, which is called

Table 6.5 Simulation scenarios of floating terminal and LNG-carrier.

		Gap [m]		Sloshing FL [%]			Mooring					Environments		
							Terminal Mooring			connec. w/ LNGC				
		6	40	0	18	56	Real	Simplified	Dolphin	Fender	Hawser	Wave	Current	Wind
Standard Case	1	▼		▼			▼			▼	▼	180°		
Simplified Mooring	2	●		●				●		●	●	180°		
Gap Effect	3		●	●				●		●	●	180°		
Sloshing effect	4-1	●			●			●		●	●	180°		
	4-2	●				●		●		●	●	180°		
	4-3	●			●			●		●	●	90°		
	4-4	●				●		●		●	●	90°		
Mooring Effect	5-1	●		●					●	●	●	180°		
	5-2	●				●			●	●	●	180°		
Environmental effect	6-1	●		●				●		●	●	90°		
	6-2	●		●				●		●	●	150°		
	6-3	●		●				●		●	●	180°	180°	180°
	6-4	●			●			●		●	●	180°	180°	180°
	6-5	●				●		●		●	●	180°	180°	180°
	6-6	●		●				●		●	●	90°	90°	90°
	6-7	●			●			●		●	●	90°	90°	90°
	6-8	●				●		●		●	●	90°	90°	90°
	6-9	●		●				●		●	●	150°	150°	150°

"pumping mode". Among two bodies, generally, the body on weather side shows larger motion than the other body, due to the fact that weather side body, LNG-carrier, is shielding wave force. For the roll mode, we can observe each body's natural frequency: floating terminal is 0.31rad/s and LNG-carrier is 0.47rad/s as presented in Table 6.6. Since sway mode is coupled with roll mode, sway motion peak is also observed at roll motion. In terms of the yaw mode, floating terminal's motion is almost zero while LNG-carrier's motion is a remarkable range from 0.4 rad/s to 1.0 rad/s. This can be clearly explained by the fact that floating terminal is barge type that is a symmetric to y-axis (parallel to wave direction), while LNG-carrier is asymmetric to y-axis. This asymmetric geometry caused yaw motion even though wave condition is beam sea.

The other point of interest regarding the two bodies case is the roll evident in head sea condition. Basically, when body geometry is symmetric to x-axis and wave heading is head sea condition (180deg), there is no roll motion in the single-body case. In Fig. 6.4, however, LNG-carrier's roll motion is observed at roll natural frequency as shown in beam sea case. Although body geometry is symmetric to wave direction, hydrodynamic forces must be asymmetric to wave direction due to the existence of a gap between two bodies. This is a primary reason for roll motion in head sea condition, and also a major characteristic of the two bodies' hydrodynamic interaction.

Table 6.6 Hydrostatic natural frequencies of FT and LNGC (Gap=6m)

unit : [rad/s]	Heave	Roll	Pitch
F.T	0.50	0.31	0.49
LNGC	0.57	0.47	0.6
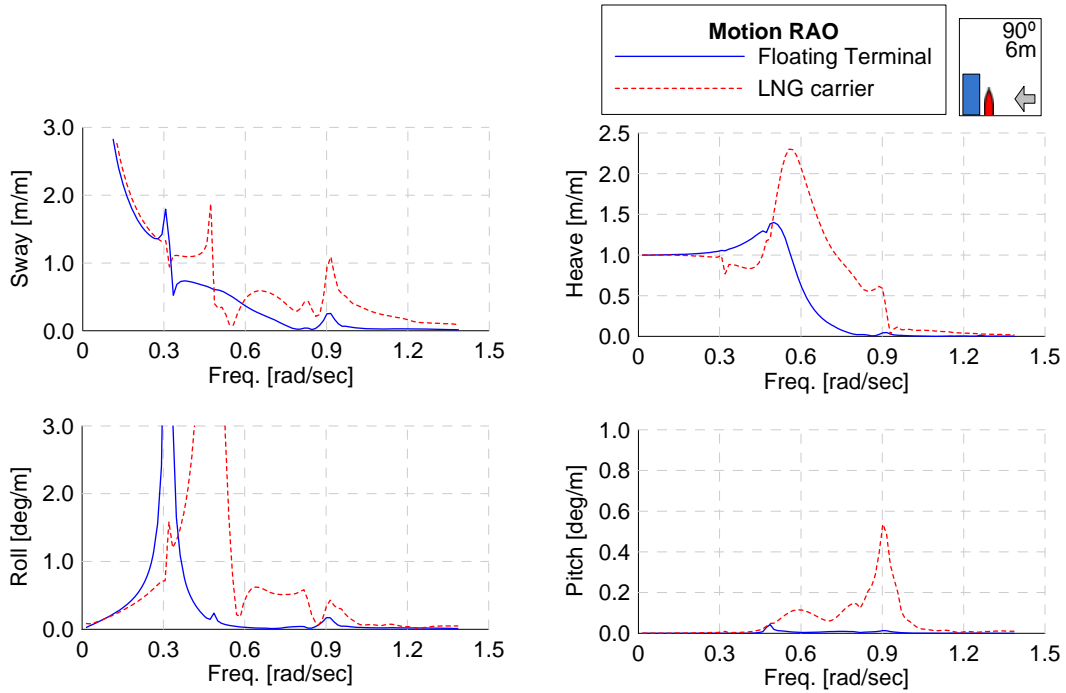
Fig. 6.3 Motion RAOs of FT and LNGC (Wave heading=90deg)
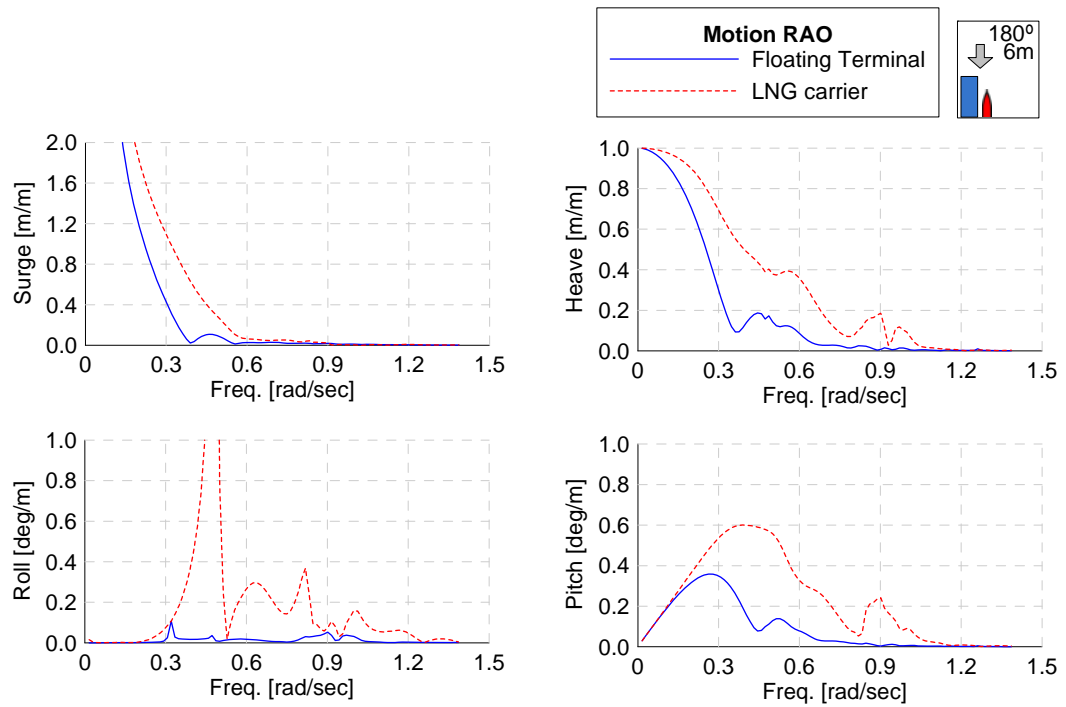
Fig. 6.4 Motion RAOs of FT and LNGC (Wave heading=180deg)
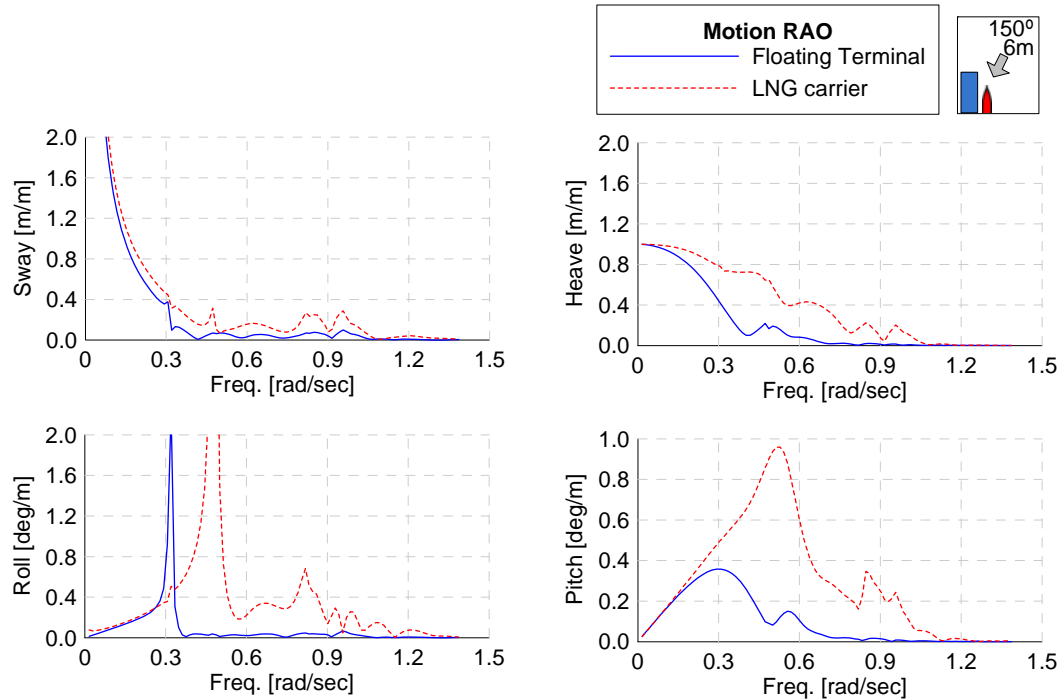
Fig. 6.5 Motion RAOs of FT and LNGC (Wave heading=150deg)

Also of note are the sudden changes of motion RAO at every mode, and every wave heading is observed at 0.9 rad/s. This observation is likely due to the effect of 6m gap distance, and will be tested by comparing the LNGC motion to the different gap distance in order to understand how gap distance is affecting LNGC motion. Fig. 6.6 shows a comparison of LNGC's selected motion RAO for three cases: LNGC only and LNG-carrier with floating terminal at 6m gap and 40m gap. If LNGC is floating without floating terminal in head sea condition, no sway and roll motion are observed; heave and pitch motions show frequency-dependent trend including their natural frequency. If LNGC is moored with a floating terminal with 6m gap, sway and roll motion emerged due to asymmetric hydrodynamic forces along x-axis. Peaks at roll natural frequency (0.47 rad/s) are also shown. For the heave and pitch motion, motions at each natural frequency (heave: 0.66 rad/s, pitch: 0.74 rad/s) are smoothed out by the gap effect. The most remarkable

phenomenon of hydrodynamic gap effect is sudden changes of motion RAOs around 0.9

rad/s at all modes. The pumping mode of a trapped wave between two bodies is causing

this phenomenon. If gap distance is 40m, roll and sway motion at roll natural frequency is

still observed. However, we can clearly see that motion due to gap effect at 0.9 rad/s is

moved to 0.69 rad/s. This phenomenon is also observed at heave and pitch modes. When

the gap distance is wider, the period of trapped wave is getting longer, meaning the gap

effect will be located at a lower frequency than a narrower gap distance.

Fig. 6.7 and Fig. 6.8 shows added mass of FT and LNGC, respectively, as an

example. Each case contains comparison of added mass between 1 body and 2 body case.

Unlike 1 body case, 2 body case shows a peak due to gap effect at 0.9 rad/s at 6 DOF

modes.

Fig. 6.6 Comparison of motion RAOs of LNGC only and LNGC with FT

(Wave heading=180deg).

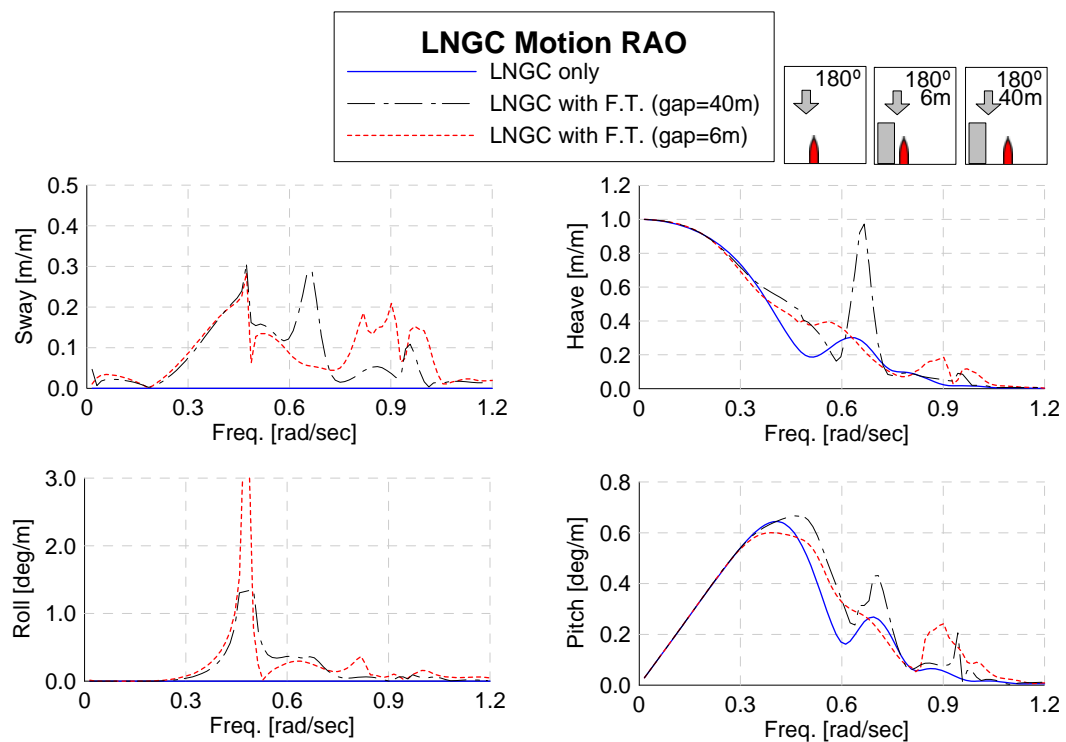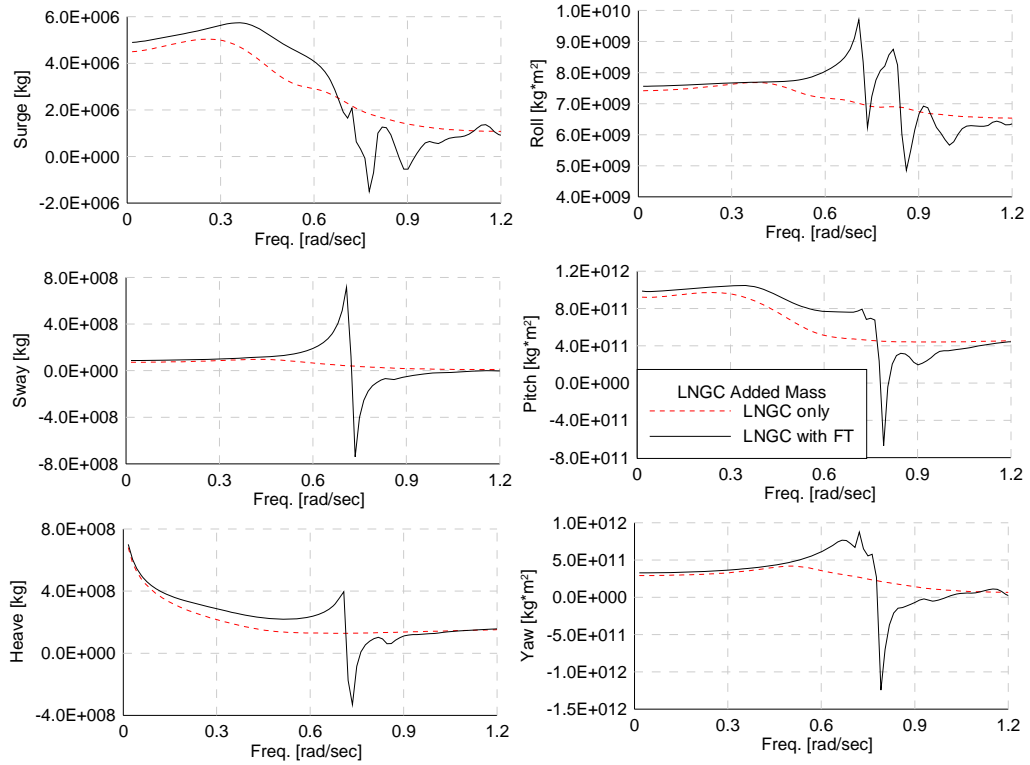Fig. 6.7 Comparison of added mass of LNGC only and LNGC with FT case (Gap=6m).
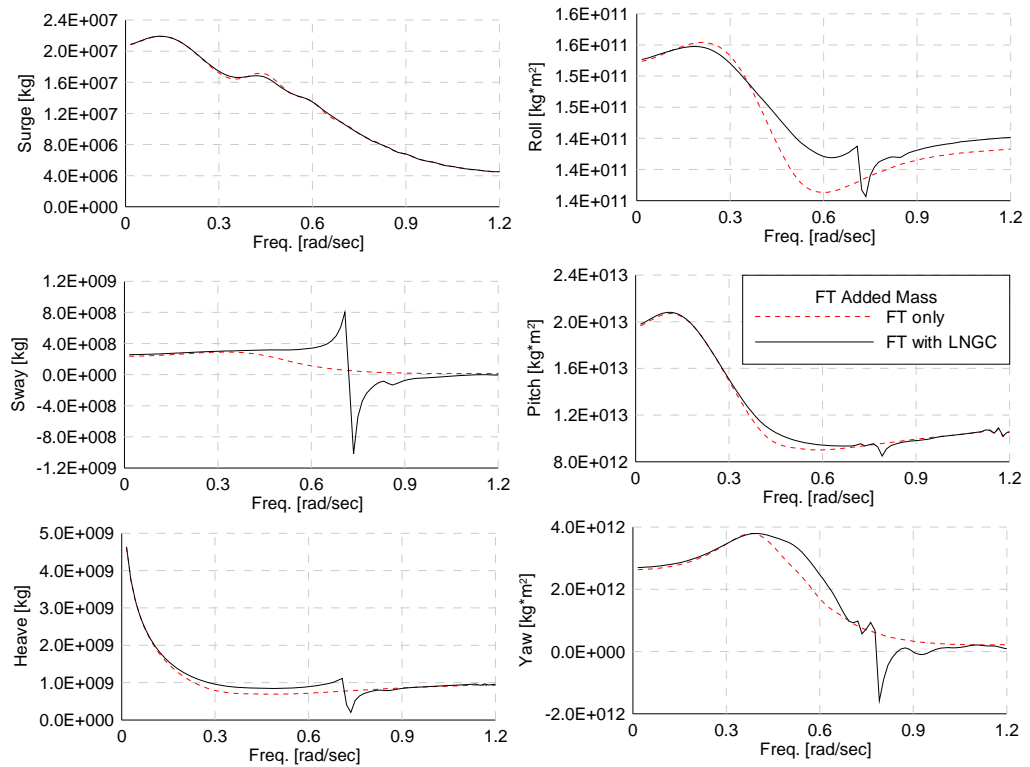
Fig. 6.8 Comparison of added mass of FT only and FT with LNGC case (Gap=6m).

6.5   Verification of Newman's Approximation

In Chapter V, I used Newman's approximation for calculation on second-order drift force taking advantage of not calculating second-order potential and saving computational time with the fact that water depth of MARIN-FPSO's case was a deep water case. However, floating terminal and LNG-carrier case is for a water depth of 100m that is shallow water depth. As I mentioned previously, Newman's approximation is not always valid in shallow water depth since drift force is a function of motion that is also affected by water depth. Therefore, we need to first confirm that Newman's approximation is valid for water depth of 100m. In this chapter, the difference-frequency quadratic transfer function (QTF) is investigated for different water depth cases. In order to calculate full QTF using second-order potential, WAMIT is used with the option of a simpler solution without free surface discretization.

First, a comparison of mean drift force and QTF of LNGC for deep water case is presented. In Fig. 6.9, mean drift force (solid line) and QTF when $\omega_i - \omega_j$ is zero (circle symbol) are a match at every frequencies. Additional plot of QTF when $\omega_i - \omega_j$ is 0.138rad/s (cross symbol) shows small differences at 6DOF. However, drift force is mostly low frequency motion, suggesting that usage of mean drift force (instead of QTF) is valid in deep water cases. When water depth is 30m as in Fig. 6.10, a comparison of mean drift force and QTF when $\omega_i - \omega_j$ equals zero, which also shows good agreement. When $\omega_i - \omega_j$ is 0.138rad/s, we can observe that difference of heave and pitch mode at low frequency is increased. This increase means an approximation of mean drift force, using QTF terms adjacent to diagonal terms, can be causing a larger probability of error to some

degree, providing that Newman's approximation is not always valid in shallow water depths. Next, when water depth is 100m, the water depth used in this study, Fig. 6.11, shows the difference of QTF between $\omega_i - \omega_j$ equals 0.0 rad/s and 0.138 rad/s is decreased compared to the 30m water depth case. With this comparison, our case of water depth is 100m is valid for Newman's approximation without calculation of full QTF from second-order potential. Fig. 6.12 shows heave QTF distribution and mean drift force as an example of full QTF.
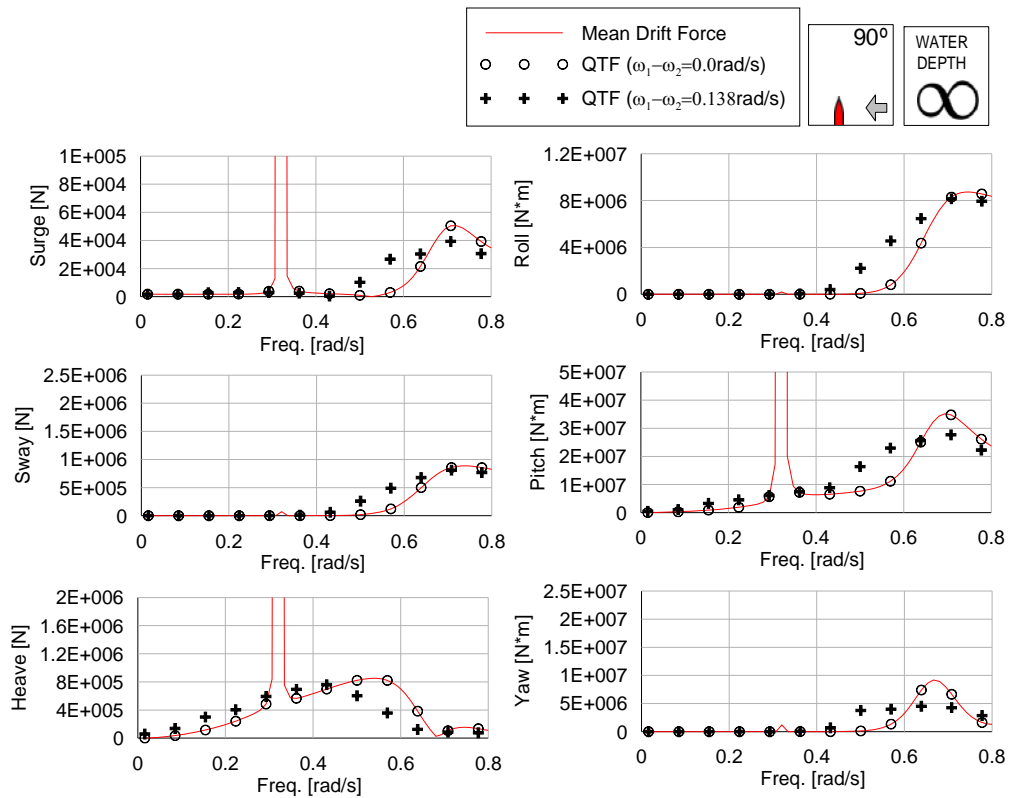
Fig. 6.9 Comparison of Mean Drift Force and QTF diagonal terms (Water depth=infinite).
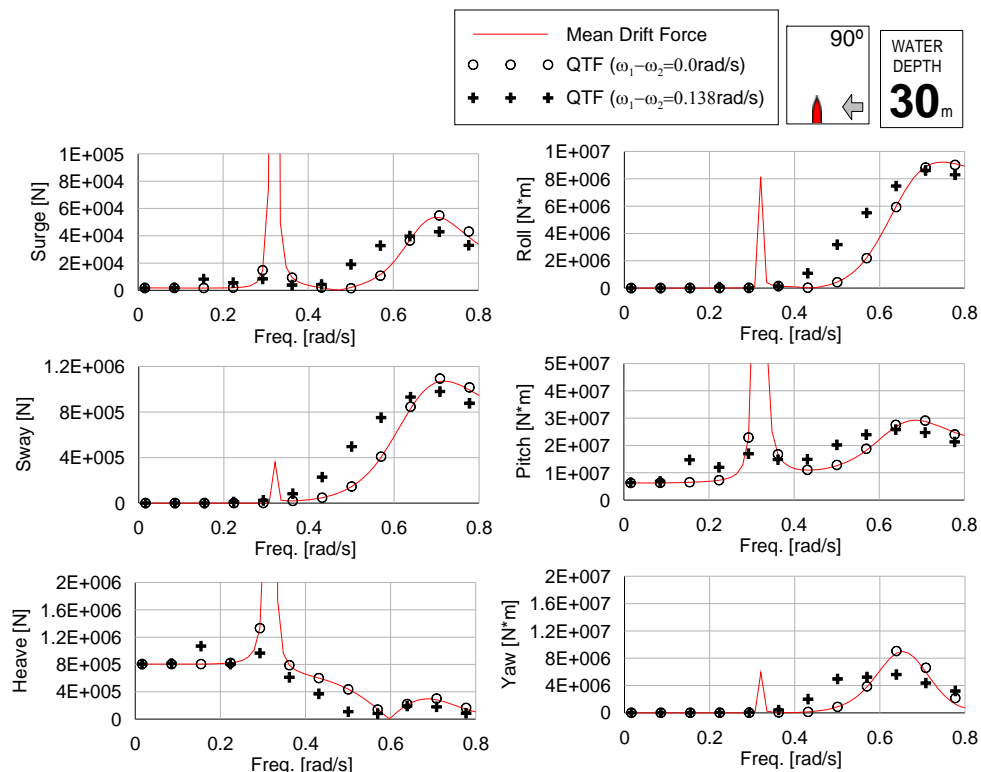
Fig. 6.10 Comparison of Mean Drift Force and QTF diagonal terms (Water depth=30m).
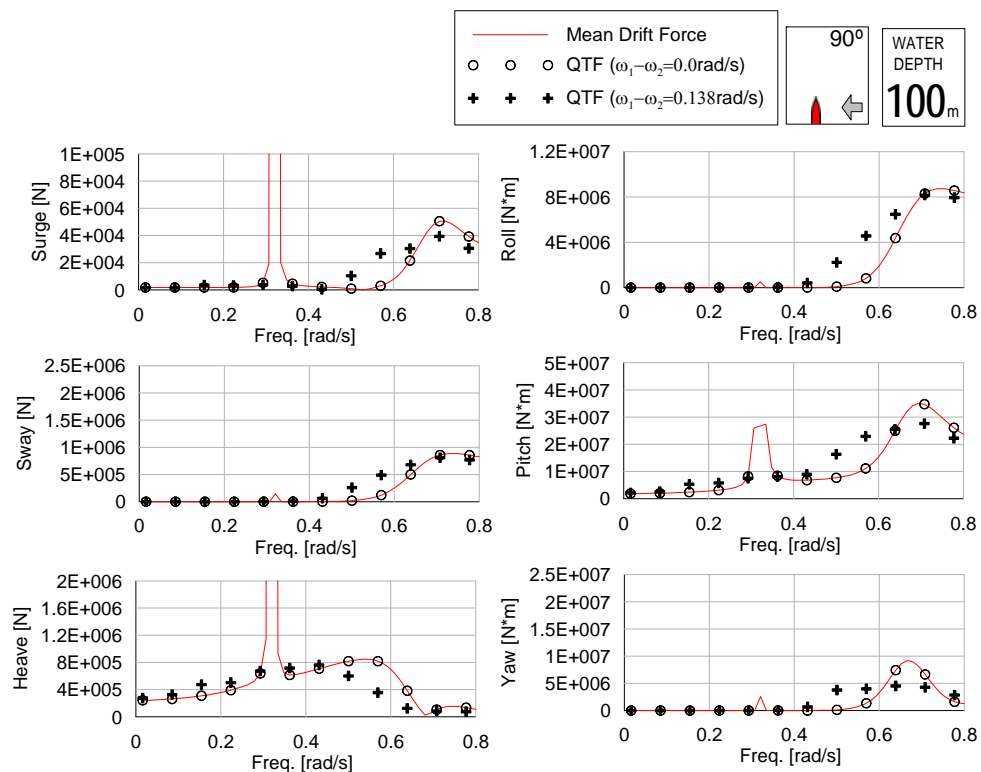
Fig. 6.11 Comparison of Mean Drift Force and QTF diagonal terms (Water depth=100m).
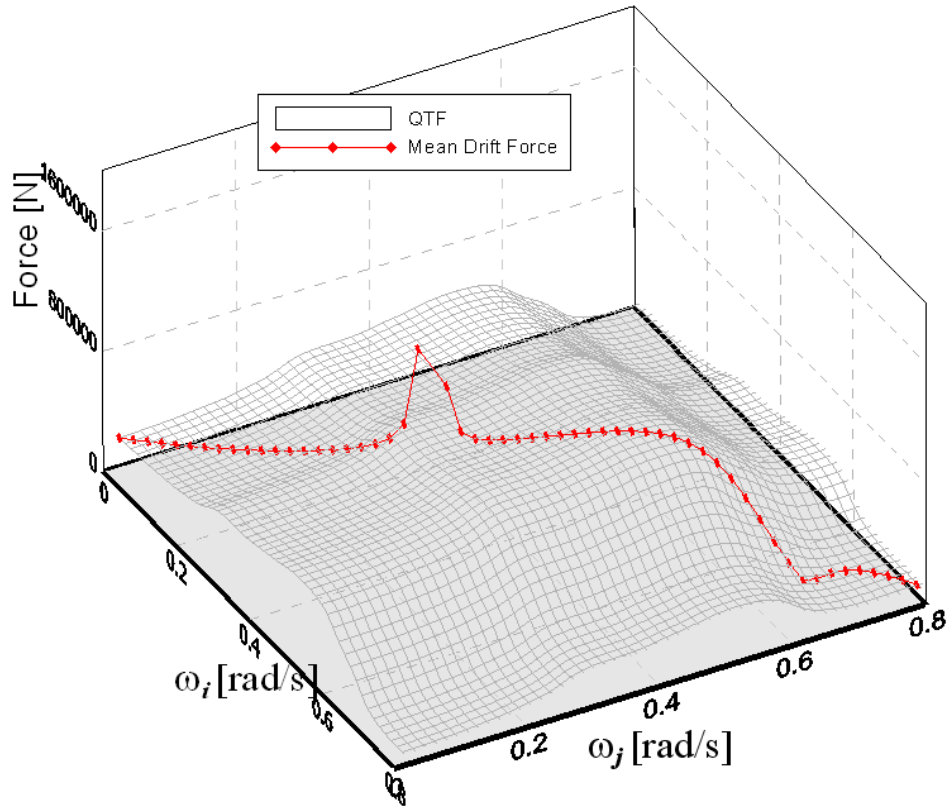
Fig. 6.12 Example of heave QTF plot (Water depth=100m).

6.6   Viscous Damping Modeling

As we discussed in Chapter V, viscous effect of ship motion is modeled using mass-less damping plates for surge and sway modes and critical damping in roll mode. Fig. 6.13 and Fig. 6.14 show the arrangement of damping plates for viscous effect in surge, sway direction for floating terminal and LNG-carrier, respectively. Since no experimental results exist and can be compared with time domain results, common drag coefficient values for a flat plate (1.0~1.5) are used. Table 6.7 shows the area of each damping plate and drag coefficients of floating terminal and LNG-carrier. The current effect is not included in these damping plates, but is included by projected area for wind and current forces as will be shown in Section. 6.9.
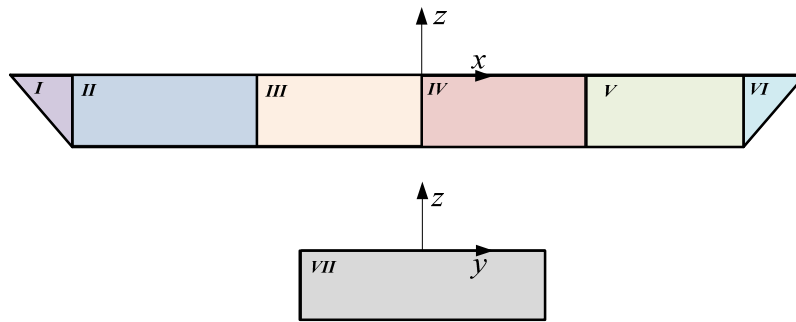
Fig. 6.13 Arrangement of surge and sway plates on Floating Terminal.
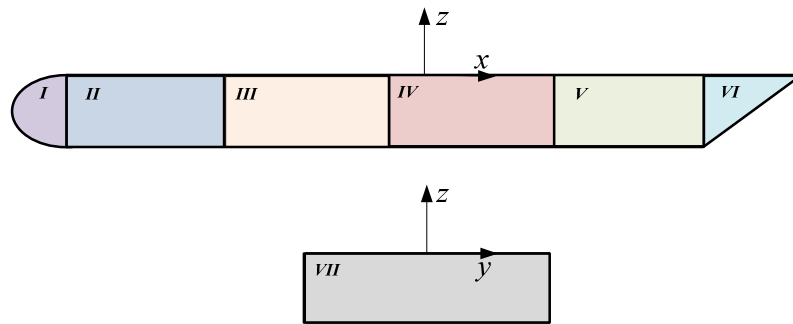
Fig. 6.14 Arrangement of surge and sway plates on LNG-carrier

Regarding roll viscous damping, free decay test results are generally being used for determining damping coefficient in linear and quadratic damping models. However, since floating terminal and LNG-carrier do not have a free decay test, the roll damping model using critical damping is being used as equation (6.1).

$$C_{44}^* = 2\gamma \sqrt{\left\{ M_{44} + M_{44}^a(\omega_n) \right\} K_{44}} \tag{6.1}$$

where γ is the damping ratio, ratio of the system damping divided by critical damping (=0.05), M_{44} is roll mass of inertia, $M_{44}^a(\omega_n)$ is added mass at roll natural frequency, and K_{44} is hydrostatic roll restoring coefficient.

Table 6.7 Surge and sway plates of floating terminal and LNG-carrier.

		No.	C_d	Area (m^2)	$0.5\rho A C_d$
Floating Terminal	Sway plates	I	1.00	99.000	50737.50
		II	1.50	632.500	486234.38
		III	1.50	632.500	486234.38
		IV	1.50	632.500	486234.38
		V	1.50	632.500	486234.38
		VI	1.00	99.000	50737.50
	Surge plate	VII	1.00	468.600	240157.50
LNG carrier	Sway plates	I	1.00	9.817	5031.46
		II	1.50	834.120	641229.75
		III	1.50	714.960	549625.50
		IV	1.50	714.960	549625.50
		V	1.50	714.960	549625.50
		VI	1.00	59.580	30534.75
	Surge plate	VII	1.00	517.154	265041.63

6.7   Approximated Mooring System

In this section, modeling of fender, hawser and simplified mooring system is introduced. For fender and hawser, nonlinear behavior can be modeled using linear spring stiffness, which is only activated when the distance of each fender or hawser is detected to be activated. A simplified mooring system is developed using nonlinear stiffness in 6 modes from a static offset test of floating body with real mooring configuration.

6.7.1   Fender and Hawser Modeling

Generally, fenders are equipped to absorb the impact force by contacting two floating bodies. Since floating terminal allows berthing of various sizes of carriers, several

fenders are attached in floating terminal side. In this study, a half-circle shape fender is used as in Fig. 6.15. When LNG-carrier is closer than the radius of fender, linear spring is activated and relevant coupled force acts on floating terminal and LNG-carrier. On the other hand, when the gap distance of two bodies are getting wider than their initial moored position, hawser is used to avoid separation of two bodies. Hawser is attached to both floating terminal and LNG-carrier at a number of points. This hawser can also be modeled using linear spring model activated only when the distance of two attached points is wider than the length of hawser line. When distance is closer than hawser length, no hawser force is generated to simulate the slack condition of hawser line.
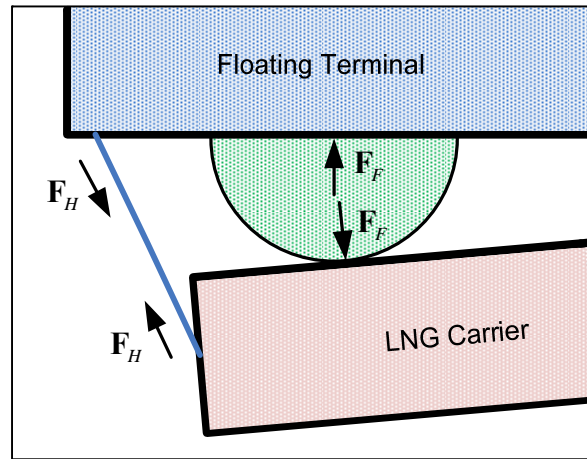
Fig. 6.15 Schematic plot of fender and hawser forces.

Fender and hawser forces and moments are:

$$\mathbf{F}_{FH} = \mathbf{F}_F + \mathbf{F}_H \tag{6.2}$$

$$\mathbf{M}_{FH} = r_{FH} \times \mathbf{F}_{FH} \tag{6.3}$$

where r_{FH} is location vector of fender and hawser connected points on each body with respect to each body's fixed coordinates. Fender force can be modeled using fender

stiffness and effective displacement between two contacted points of each body.

$$\mathbf{F}_F = k_F \cdot d_F^{on} \tag{6.4}$$

$$d_F^{on} = \begin{cases} d_F - d_{F0} & (d_F > d_{F0}) \\ 0 & otherwise \end{cases} \tag{6.5}$$

where k_F is fender stiffness, d_F^{on} is effective displacement for fender force, d_F is distance between location of fender on floating body and touched point on LNG-carrier, and d_{F0} is initial fender thickness. Similarly, fender force can be modeled as equation (6.6).

$$\mathbf{F}_H = k_H \cdot d_H^{on} \tag{6.6}$$

$$d_H^{on} = \begin{cases} d_H - d_{H0} & (d_H > d_{H0}) \\ 0 & otherwise \end{cases} \tag{6.7}$$

where k_H is hawser stiffness, d_F^{on} is effective displacement for hawser force, d_H represents distance between two points where hawser is connected on each body, and d_{F0} is initial hawser length.

When two bodies are contacting on fender, resistance force due to friction is acting on both bodies. This friction force can be modeled by using Coulomb damping force which is regardless of displacement or velocity. This force is only depending on Coulomb damping coefficient μ and normal force $\mathbf{N}$. Since two bodies are moored in a side-by-side situation, only Coulomb damping force in surge and heave direction is considered in this study:

$$\left(\mathbf{F}_{CD} \right)_{1,3} = -\mu \cdot |\mathbf{N}| \cdot sign\left(\left(\mathbf{V}_R \right)_{1,3} \right) \tag{6.8}$$

where μ is coulomb damping coefficient, $\mathbf{N}$ is normal force on contacting point of floating terminal and LNG-carrier, $\left(\mathbf{V}_R\right)_{1,3}$ is relative velocity of surge and heave direction.

6.7.2 Simplified Mooring Lines Modeling

Calculation of mooring lines dynamics requires an additional number of equations. Therefore, a simplified mooring system using nonlinear springs in 6 DOF is proposed in order to reduce the size of global matrix size and save computational time.
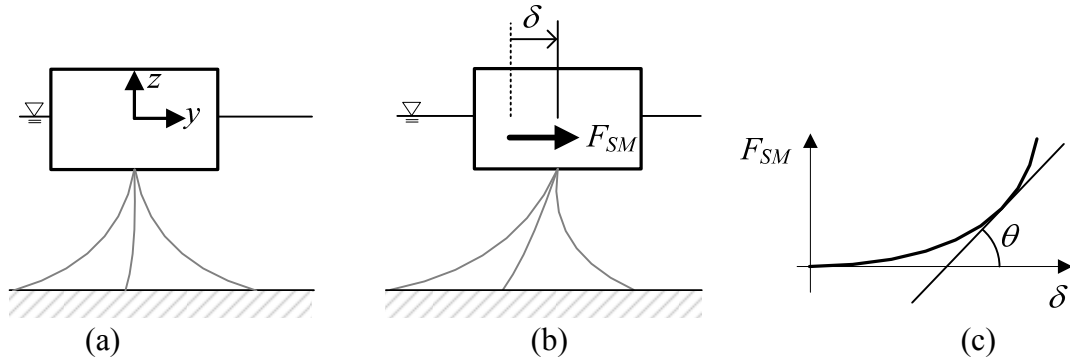
Fig. 6.16 Static offset test for simplified mooring system.

Fig. 6.16 illustrates how equivalent simplified mooring stiffness from static offset test. For example, in surge mode, I can obtain static offset δ by applying static surge force F_{SM} as shown in Fig. 6.16(b). Varying this static force and obtaining static offsets can provide static offset curve as in Fig. 6.16(c). First derivative of this curve at certain offset δ is the simplified mooring stiffness at certain offset δ. For surge, sway and yaw mode:

$$
\begin{aligned}
\left(F_{SM}\right)_i &= \left(k_{SM}\right)_i \cdot \delta_i \\
\left(k_{SM}\right)_i &= \left(F_{SM}\right)_i / \delta_i
\end{aligned}
\qquad \text{i=1,2,6}
\qquad (6.9)
$$

where k_{SM} is equivalent mooring stiffness. For static offset test for heave, roll, and pitch modes, restoring force due to body's hydrostatic restoring coefficients will be already included in applying force in rotational static offset test. Therefore, this original hydrostatic restoring force should be canceled out in order to extract pure equivalent mooring stiffness of a simplified mooring system out of total applying force.

$$
\begin{aligned}
\left(F_{SM}\right)_i &= \left(\Delta F_{restoring}\right)_i + \left(k_{SM}\right)_i \cdot \delta_i \\
&= K_{ii} \cdot \delta + \left(k_{SM}\right)_i \cdot \delta_i \qquad i=3,4,5 \\
\left(k_{SM}\right)_i &= \left(\left(F_{SM}\right)_i - K_{ii} \cdot \delta_i\right)/\delta_i
\end{aligned}
\qquad (6.10)
$$

where K_{ii} is the original restoring coefficient of body. Fig. 6.17 shows the results of pure simplified mooring stiffness from static offset test for surge, sway, heave, roll, pitch, and yaw modes.
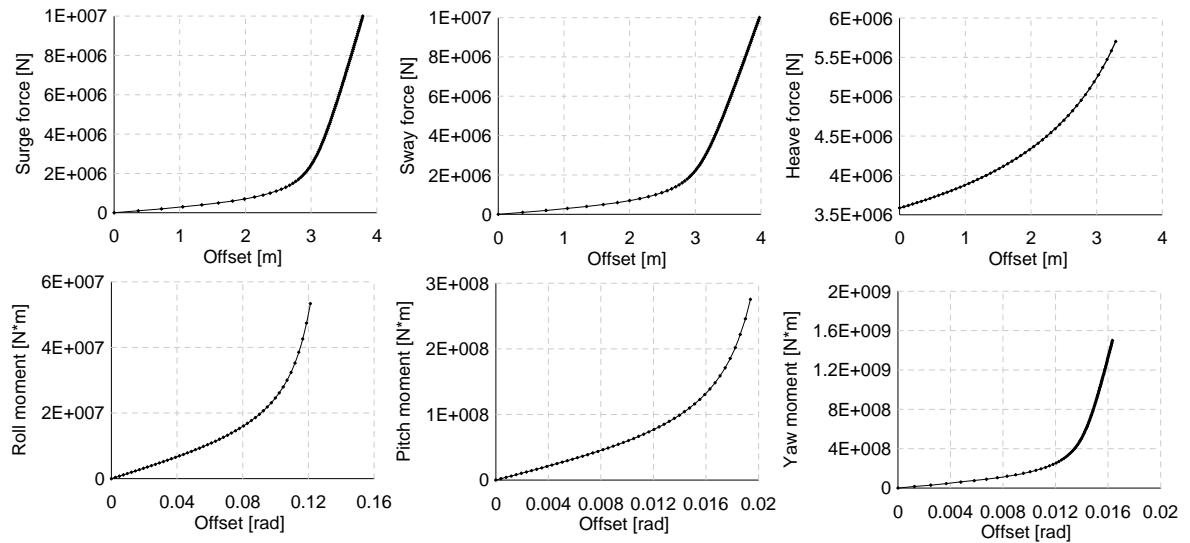
Fig. 6.17 Simplified mooring stiffness from static offset test.
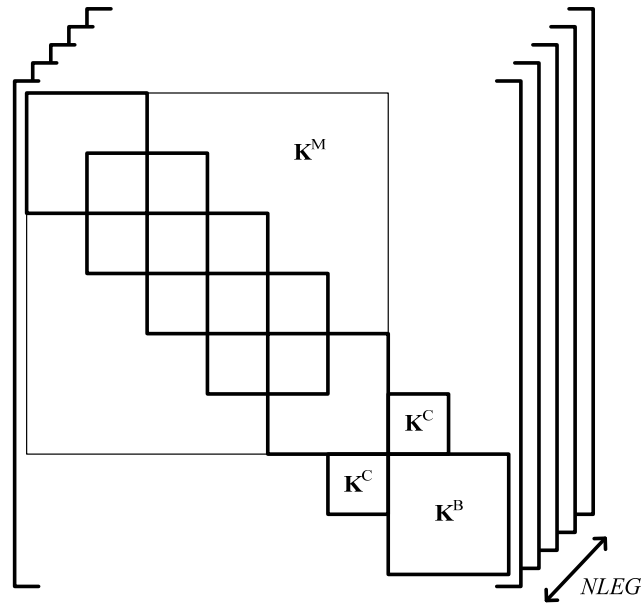
Fig. 6.18 Example of body-mooring coupled matrix

Fig. 6.18 shows global stiffness matrix when real mooring lines are coupled with body stiffness matrix. This figure illustrates how calculations can be greatly reduced by using a simplified mooring system instead of real mooring line dynamics calculation. The matrix $\mathbf{K}^B$ means floating terminal and LNG-carrier matrix with size of $[12\times12]$, $\mathbf{K}^C$ is coupled matrix between body and mooring lines with size of $[6\times6]$, and $\mathbf{K}^M$ is mooring lines stiffness matrix with size of $8\times(N+1)-1$ rows and $8\times(N+1)-1$ columns when each mooring lines has N elements. For an example, when a single mooring line is composed of 5 elements as shown in Fig. 6.18, the size of mooring lines stiffness matrix $\mathbf{K}^M$ is $[47\times47]$. When the number of mooring lines is NLEG, the number of matrices that should be solved is same as $NLEG$. In this study, the number of mooring lines is 12 with 20 elements in each leg, simplified mooring system is taking advantage of 39% reduced computational time by solving size-reduced matrix as shown in

Table 6.8.

Table 6.8 Comparison of computational time between real and simplified mooring system.

Mooring system	size of matrix	Simulation duration	Computational time	comment
Real	[179*179*12]	1800 sec.	18hr. 35min.	
Simplified	[12*12]	1800 sec.	11hr. 20min.	39% faster

6.8 Regular Wave Test

One way to validate that a potential force in frequency domain is exactly implemented in time domain is to conduct a regular wave test without any viscous effect, as is done in this section. Motion amplitudes at each of three different wave heading angles are calculated and compared with frequency domain motion RAOs. At each frequency, a single wave of corresponding wave period is applied and steady motion amplitude of 6 DOF is measured after initial transient motion response is naturally removed. For regular wave test, two bodies are moored with linear spring to avoid drift away during time domain simulation. The floating terminal is moored with external wall by a simple spring and the LNG-carrier is again moored with floating terminal by a simple spring as shown in Fig. 6.19. Stiffness value of each spring is listed in Table 6.9.

Table 6.9 Mooring spring constant for regular wave test.

	Surge	Sway	Yaw
Floating terminal	4.417E+09($K_{1,1}$)	7.139E+09($K_{2,2}$)	3.351E+11($K_{6,6}$)
LNG-carrier	1.050E+07($K_{7,7}$)	2.094E+07($K_{8,8}$)	3.595E+10($K_{12,12}$)
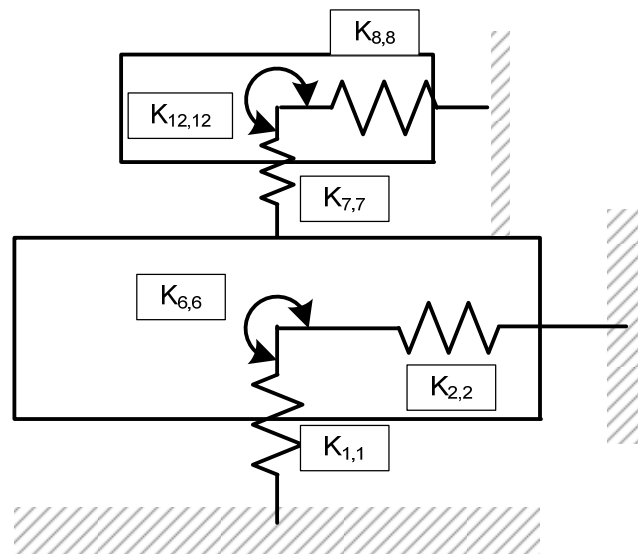
Fig. 6.19 Spring mooring for motion comparison and regular wave test.

Fig. 6.20, Fig. 6.21, and Fig. 6.22 show a comparison of motion RAO for wave headings of 150deg, 180deg, and 90deg, respectively. From those figures, I can learn that time domain program perfectly calculates potential hydrodynamic forces for all wave heading conditions.
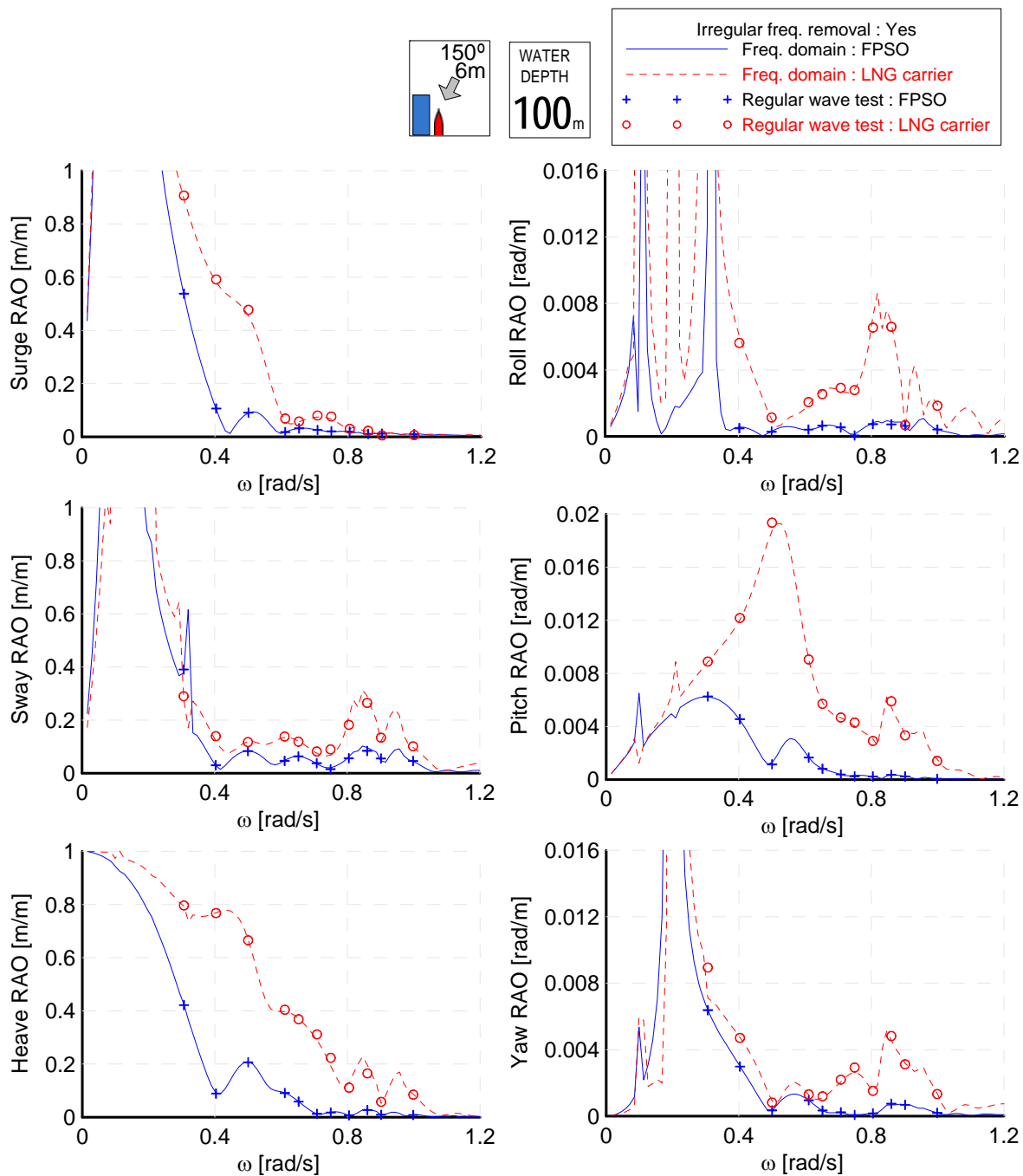
Fig. 6.20 Regular wave test of FT and LNGC

(Full load condition, wave heading=150deg, water depth=100m)
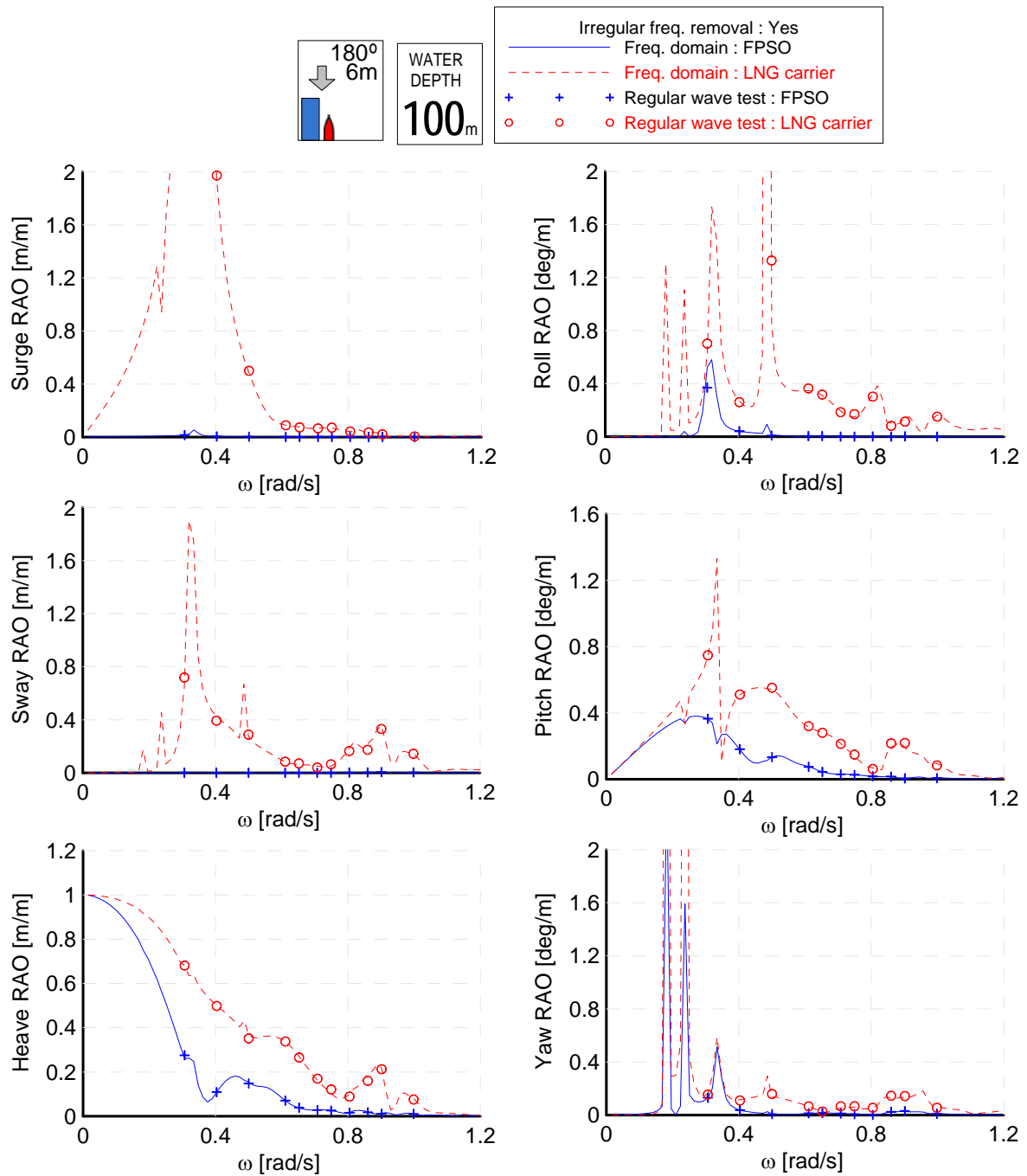
Fig. 6.21 Regular wave test of FT and LNGC

(LNGC in ballast condition, wave heading=180deg, water depth=100m)
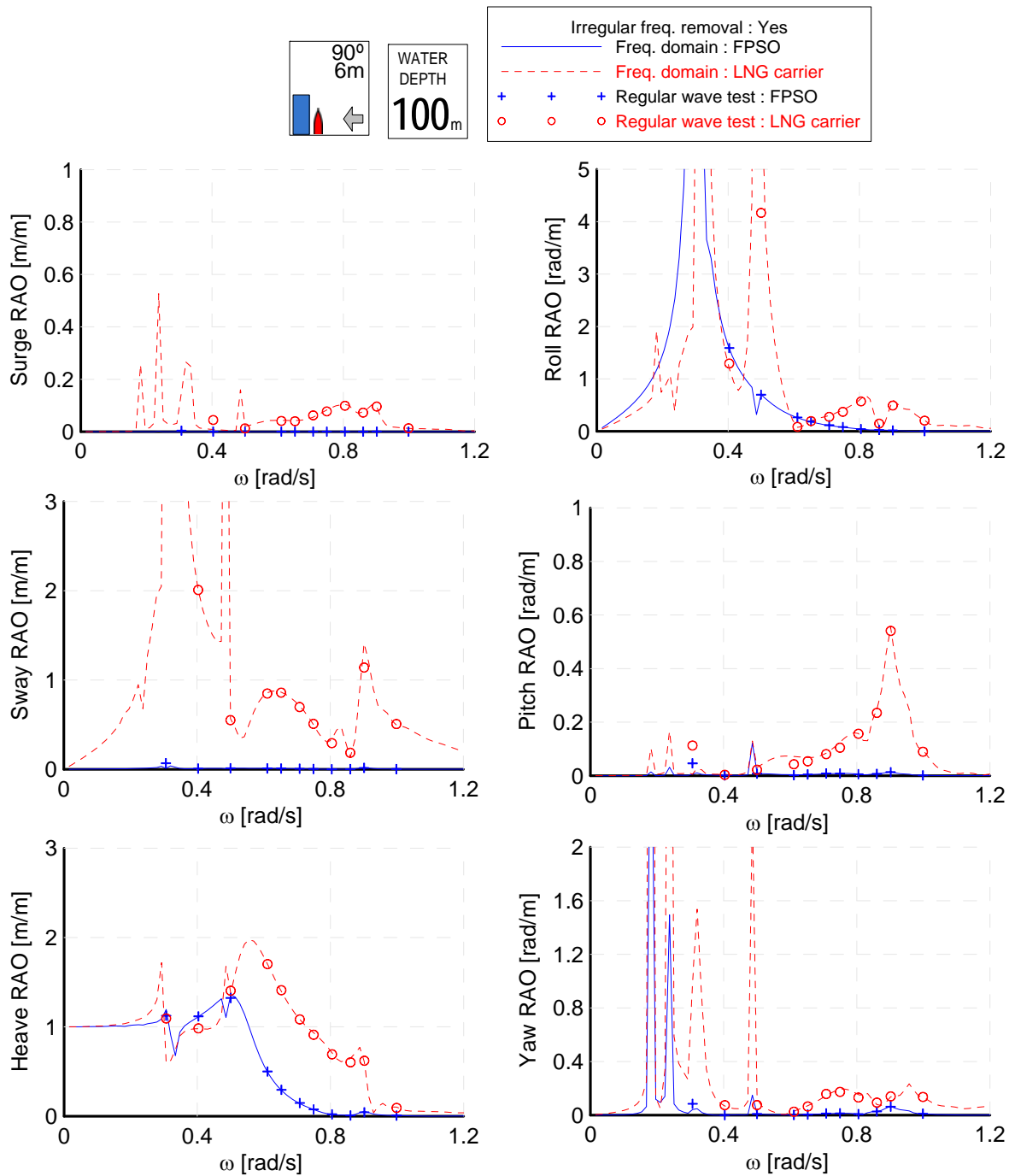
Fig. 6.22 Regular wave test of FT and LNGC

(LNGC in ballast condition, wave heading=90deg, water depth=100m)

6.9 Environmental Loads

For the environmental loading condition for LNG-carrier moored with floating terminal in a side-by-side mooring case, sea state 4 in Table 6.10 is used since sea state 3-4 is normal wave environmental condition for side-by-side mooring configuration. JONSWAP spectrum is used to generate an irregular wave with significant wave height of 2.0m. Wave period for JONSWAP spectrum is 12sec, and γ is 3.0. Details of the JONSWAP wave spectrum are introduced in Chapter IV, and are not repeated in this chapter.

Table 6.10 Pierson - Moskowitz Sea Spectrum vs Beaufort Force (Sea State Table)

Force	Sea State	Wind speed (m/s)	Significant Wave (m)	Average Period (sec)	Average Waves Length (m)
1	0	1.80	<0.015	1	0.61
2	1	3.43	0.152	1.5	2.90
3	2	5.53	0.610	3	7.92
4	3	7.97	1.067	4	15.24
5	4	9.77	1.829	5	24.38
6	5	11.70	2.438	6-7	39.62
7	6	15.43	5.486	8-9	67.06
8	7	21.35	9.754	10-12	121.92
9	8	27.27	15.850	13-15	198.12
10					
11	9	33.44	18.29-30.48	16-19	243.0-365.0
12					

For wind loads, the measured wind velocity may be expressed as various types of a spectrum. The simple shape wind spectrum used in this study is the API (American

Petroleum Institute) wind spectrum:

$$S(\omega) = \frac{\sigma^2(z)}{2\pi f_p \left[1 + \frac{1.5\omega}{2\pi f_p}\right]^{\frac{5}{3}}}$$ (6.11)

where f_p is the average factor derived from measured spectrum as:

$$f_p = \frac{0.025V_w(z)}{z}$$ (6.12)

The symbol $\sigma(z)$ is the standard deviation of wind speed and related to turbulence intensity. The values of $\sigma(z)$ can be expressed as:

$$\sigma(z) = \begin{cases} 0.15\left(\frac{z}{20}\right)^{-0.125} V_w(z) & \text{when } z \leq z_R \\ 0.15\left(\frac{z}{20}\right)^{-0.275} V_w(z) & \text{when } z > z_R \end{cases}$$ (6.13)

where $z_R = 20m$ is the thickness of the "surface layer" and $V_w(z)$ is the one hour mean wind speed (m/s) z meters above water level. $V_w(z)$ can be written as follows:

$$V_w(z) = V_{10}\left(\frac{z}{z_R}\right)^{0.125}$$ (6.14)

where V_{10} is one hour mean wind speed (m/s) 10 meter above water level (API, 1994). From target API wind spectrum in Fig. 6.23, we can generate a wind velocity time series as shown in Fig. 6.24. Re-generated wind spectrum from this time series and target API spectrum are compared in Fig. 6.23.
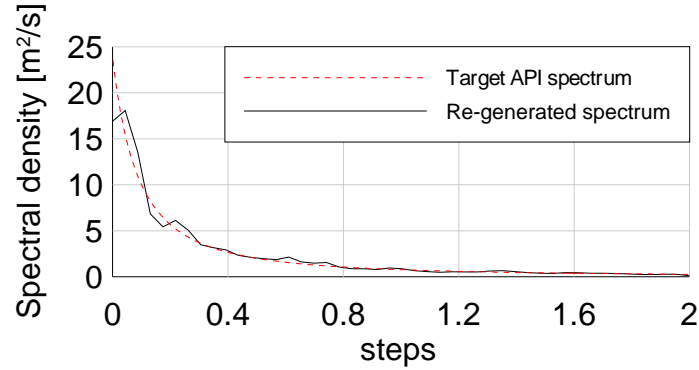
Fig. 6.23 Target API wind spectrum and re-generated spectrum

(at 10m above MWL, V_{10}=14.0m/s).
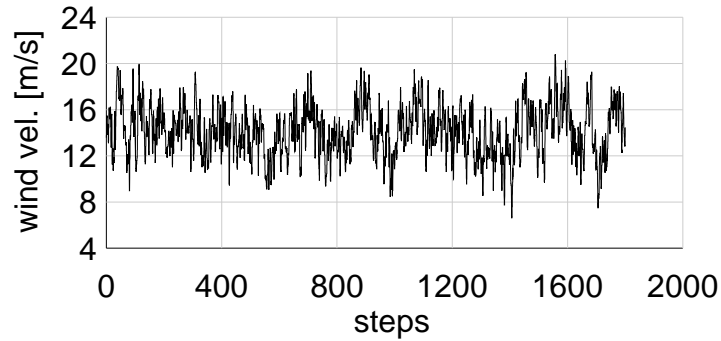
Fig. 6.24 Generated wind velocity time series.

Wind force from generated wind velocity can be used in obtaining longitudinal, transverse, and rotational wind force and moments as follows:

$$F_{xw} = C_{xw}\rho_A \left(V_w\right)^2 A_T \tag{6.15}$$

$$F_{yw} = C_{yw}\rho_A \left(V_w\right)^2 A_L \tag{6.16}$$

$$M_{xyw} = C_{xyw}\rho_A \left(V_w\right)^2 A_T L_{BP} \tag{6.17}$$

where F_{xw}, F_{yw}, and M_{xyw} are longitudinal wind force, lateral wind force and wind yaw moment, respectively. V_w is wind velocity generated from API wind spectrum as shown in Fig. 6.24. A_T is transverse wind area and A_L is longitudinal wind area. L_{BP} is the

length between perpendiculars. Table 6.11 shows projected areas for wind and current forces. C_{xw}, C_{yw}, and C_{xyw} are coefficients for wind force and moment presented by Oil Companies International Marine Forum (OCIMF) in 1977.
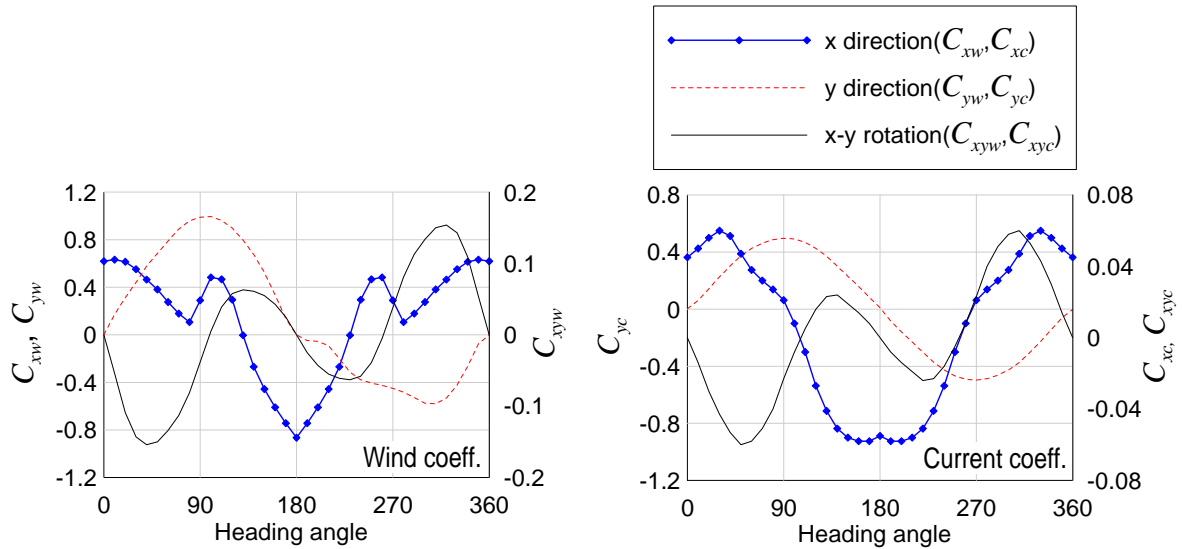
Fig. 6.25 OCIMF wind and current force coefficients

Similarly, current force can be expressed using OCIMF coefficients as equations below demonstrate.

$$F_{xc} = C_{xc}\rho_C \left(V_C\right)^2 TL_{BP} \tag{6.18}$$

$$F_{yc} = C_{yc}\rho_C \left(V_C\right)^2 TL_{BP} \tag{6.19}$$

$$M_{xyc} = C_{xyc}\rho_C \left(V_C\right)^2 T \left(L_{BP}\right)^2 \tag{6.20}$$

where F_{xc}, F_{yc}, and M_{xyc} are longitudinal current force, lateral current force and current yaw moment, respectively. V_C is current velocity on the free surface. T is the average draft and L_{BP} is length between perpendicular.

Summarized wave, wind and current conditions are presented in Table 6.12. For the simulation cases described in Table 6.3, wind and currents are always assumed as the same direction as the wave in order to simulate the most severe condition.

Table 6.11 Projected areas for wind and current force

	Length[m]	Breadth[m]	Draft[m]	Freeboard[m]	$A_{tran}[m^2]$	$A_{long}[m^2]$
FT	428.0	70.0	14.5	20.0	1400.00	8560.00
LNGC	270.0	43.4	9.59	30.0	1302.00	8100.00

Table 6.12 Environmental conditions

Wind	V_{10}	14.0 m/s
	Peak in API spectrum	0.025
Current	1.0 m/s on free surface	
Wave	Significant height	2.0 m
	Peak period	12 sec
	γ of JONSWAP spectrum	3.0

6.10 Irregular Wave Test

6.10.1 Simplified Mooring System

Comparison of a real mooring system and the previously introduced simplified mooring system on floating terminal is conducted. Fig. 6.26 shows floating terminal's time series and spectral density function (SDF) of two mooring systems under head sea wave condition. Surge, sway, and yaw motion are compared since mooring lines control low

frequency planar motion. Pitch motion is also presented as an example of not low frequency motion. Simplified mooring system for surge, sway and yaw mode accurately predicts the natural frequency of each mode. However, amplitude of time series is different after the initial duration. This is because simplified mooring system does not calculate hydrodynamics of mooring lines under free surface, but provides stiffness of real mooring lines in each mode. In pitch results, an example of non planar motion, simplified mooring system is a perfectly match with the result of real mooring system because pitch is inertia dominant mode, and not affected by slowly varying force.
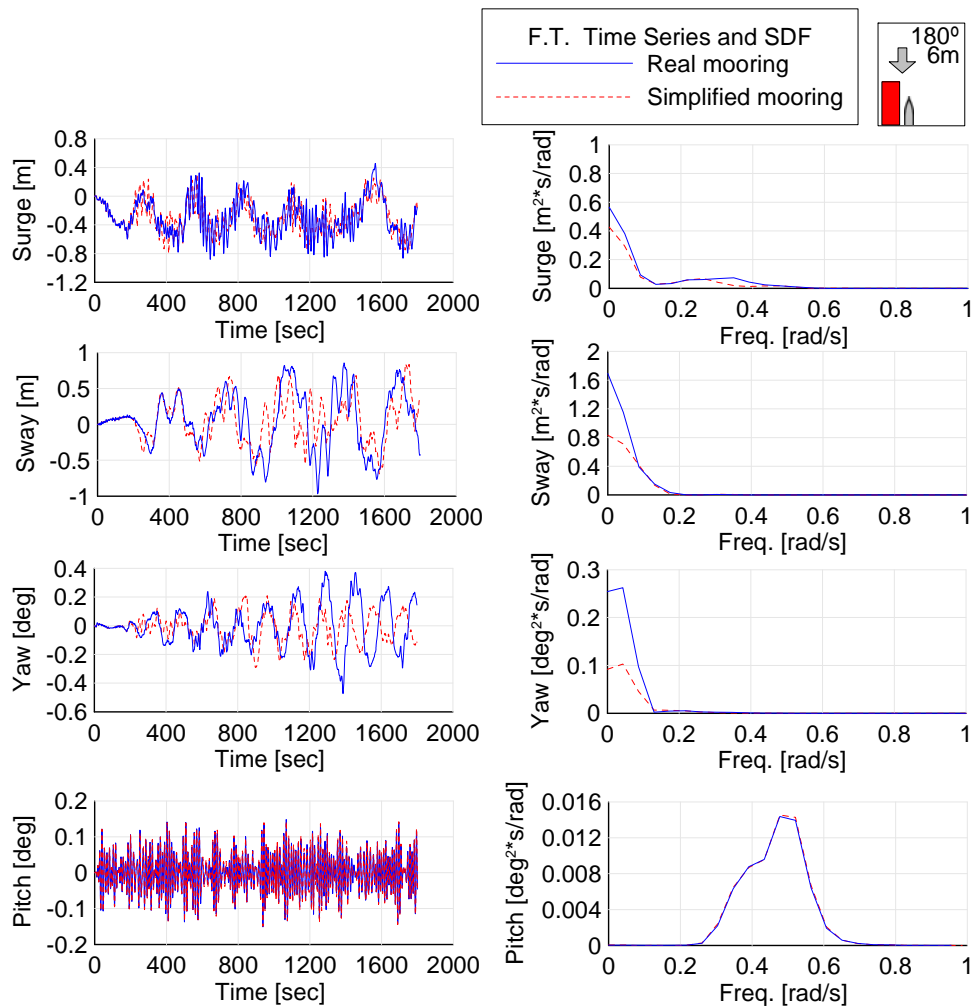
Fig. 6.26 Comparison of real and simplified mooring system.

6.10.2 *Sloshing Coupling Comparison between Frequency Domain and Time Domain*

In order to verify coupling of LNGC motion and sloshing, a comparison of motion-sloshing coupling in frequency domain and time domain is presented for both only LNGC and floating terminal. Since two sloshing tanks are equipped on the LNGC side only, coupling scheme in frequency and time domain introduced in Chapter V is not repeated in this section. In order to see the effect of motion-sloshing coupling clearly, LNGG is moored with a simple spring in the regular wave test configuration. Fig. 6.27 shows a snapshot of time domain motion-coupling program result.
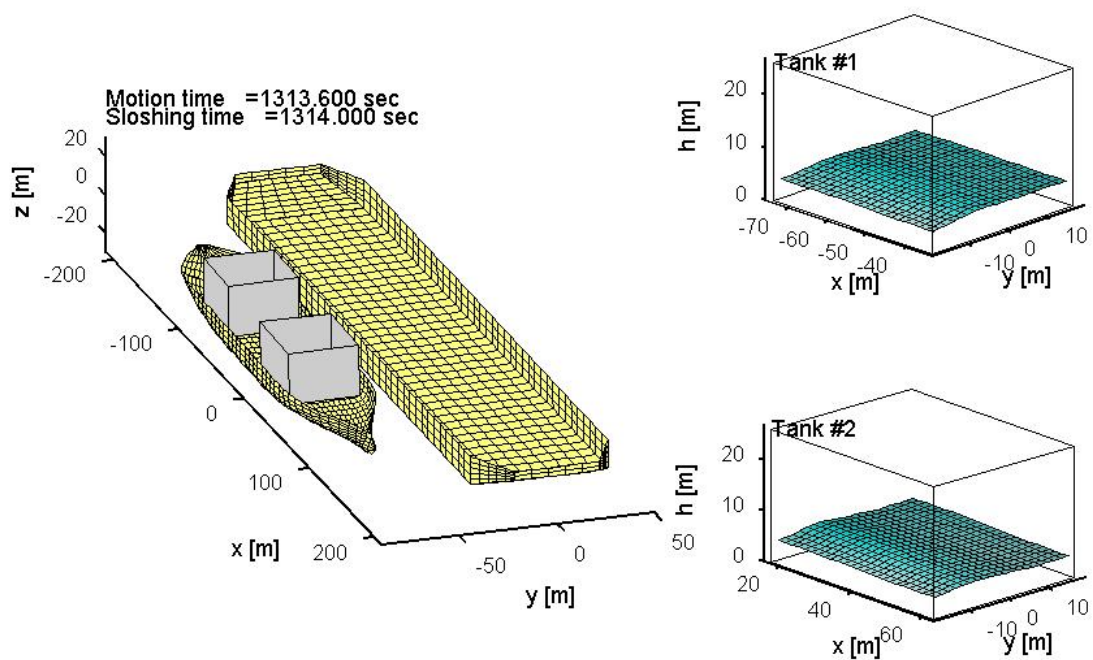
Fig. 6.27 Snapshot of motion-sloshing time domain simulation program.

Natural frequency of LNGC and sloshing tank with respect to different filling levels is summarized in Table 6.13. Due to the fact that the breadth of two tanks is slightly different as shown in Table 6.2, the transverse natural frequencies of each sloshing tank is

not the same unlike MARIN-FPSO sloshing tanks that have same tank breadth. Fig. 6.28 shows examples of sloshing fluid's added mass calculated by WAMIT. In roll added mass as a representative transverse mode, filling 18% has resonance peak at 0.582-0.583rad/s, and filling 56% has resonance peak at 0.861-0.862rad/s. These are the same results that we can expect from Table 6.13. For surge added mass as a representing longitudinal mode, each filling level has two separated resonances. Since the length of two tanks are different (40.04m and 45.48m), two different resonance peaks were predicted at each filling level: 0.523 & 0.463rad/s for 18% filling level and 0.794 & 0.722rad/s for 56% filling level. Calculated sloshing surge added mass exactly matches with two peaks at each filling level. In MARIN-FPSO case, roll natural frequency and transverse sloshing frequency at filling level 18% was almost the same. Sloshing tank's geometry of LNGC, however, causes a higher frequency (0.582-0.583rad/s) than roll natural frequency (0.47rad/s).

Table 6.13 Natural frequencies of LNG-carrier and sloshing tanks.

		Natural frequencies (rad/sec)							
		Transverse mode				Longitudinal mode			
Bare hull		Roll : 0.47				Pitch : 0.40			
Sloshing Tanks		#4 tank		#2 tank		#4 tank		#2 tank	
		1st	2nd	1st	2nd	1st	2nd	1st	2nd
	FL:18%	0.583	1.535	0.582	1.533	0.523	1.394	0.463	1.248
	FL:56%	0.862	1.848	0.861	1.846	0.794	1.738	0.722	1.619
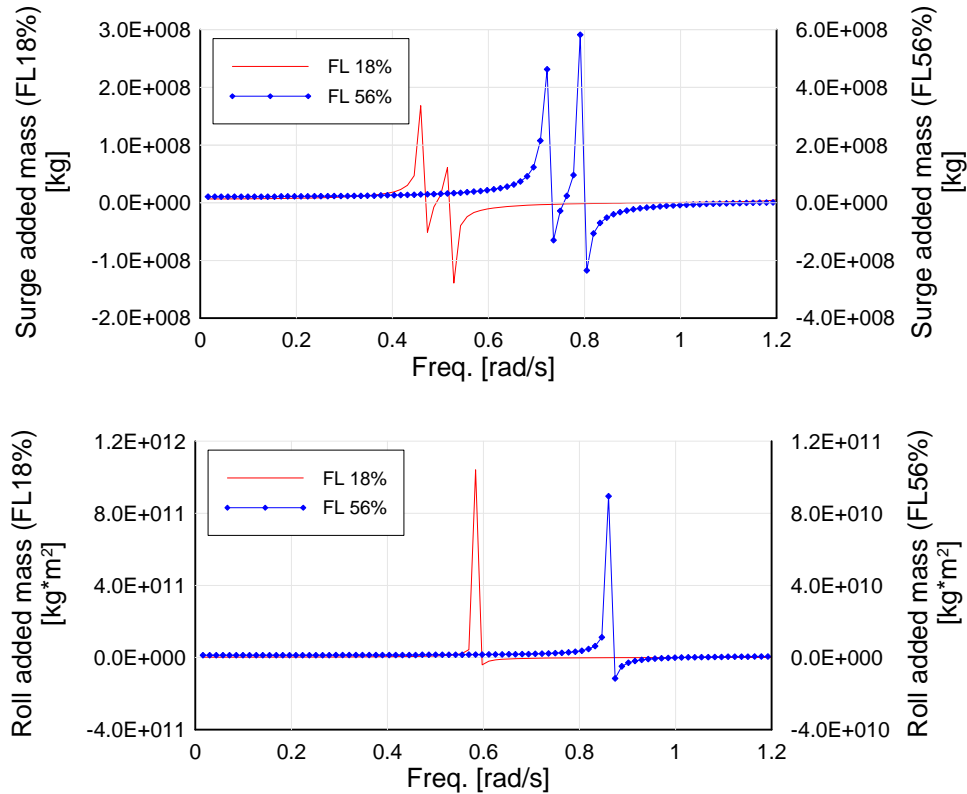
Fig. 6.28 Surge and roll added mass of LNGC's sloshing fluid

First, LNGC under beam sea condition is presented in Fig. 6.29. Coupling in frequency domain is done by adding sloshing added mass to ship added mass, and sloshing calculation in time domain calculation is done by coupling CHARM3D and ABSLO3D as introduced in Chapter V. When there is no sloshing fluid in the sloshing tank, both frequency domain and time domain results show roll natural frequency, 0.47 rad/s, as shown in Table 6.13. If filling level is 18%, roll natural frequency of LNGC is moved to 0.72rad/s. Roll amplitude in frequency is over-predicted compared to time domain results, because of the neglecting of sloshing's viscous effect at a lower filling level where viscous effect is more dominant than a higher filling level. This phenomenon is also observed in MARIN-FPSO case in Chapter V. When filling level goes to 56%, peak of roll motion is separated and second peak at 0.9rad/s is observed, while the amplitude of both peaks is

reduced compared with 18% filling level.
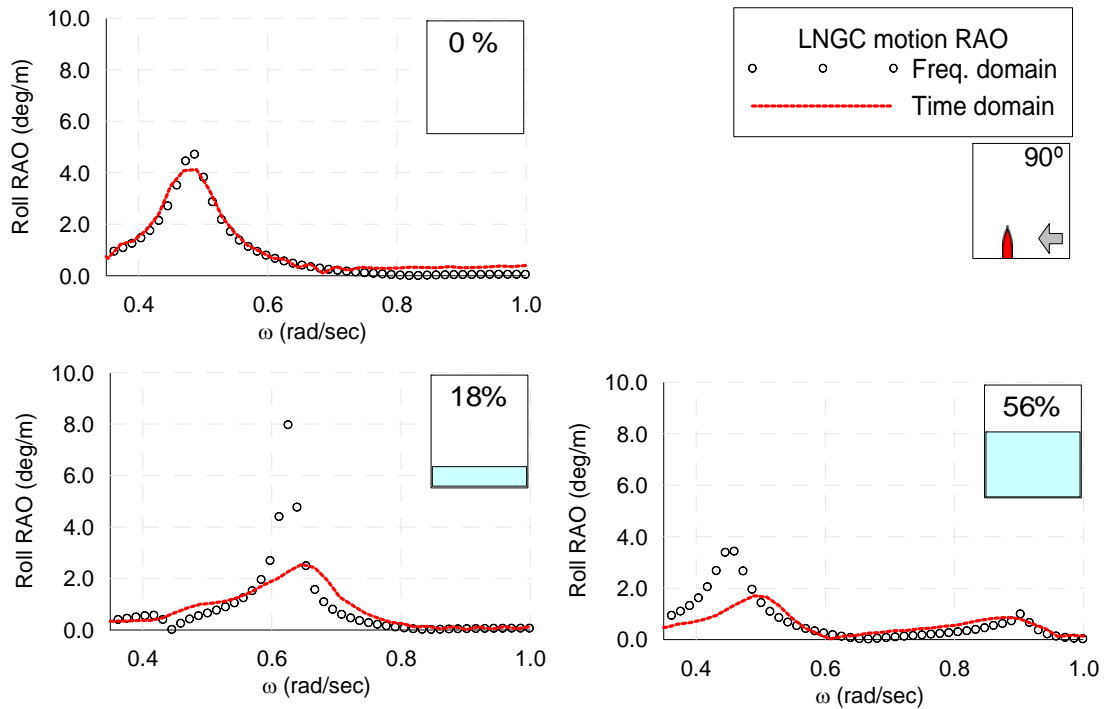
Fig. 6.29 Motion-sloshing coupling effect of roll RAO.

(LNGC only, Linear spring mooring system, Wave heading=90deg)

Next, LNGC moored with floating terminal in head sea condition is investigated. Fig. 6.30 shows roll motion RAO of LNGC moored with floating terminal for beam sea condition. When there is no sloshing fluid in the sloshing tank, roll natural frequency is 0.47rad/s as LNGC only case. Increased roll motion RAO in the both regions lower than 0.4 rad/s and higher than 1.0rad/s is because the motion RAO in time domain is calculated by motion SDF divided by very small wave amplitude SDF. In filling level 18% case, roll motion peak is split into two frequencies; 0.43 and 0.61rad/s. In the LNGC only case, this split phenomenon was not quite observed in filling level 18%. It is clearly seen, however, that the second motion peak is caused by a natural mode of sloshing fluid at filling level

18% (0.585-0.583rad/s). We can see another motion peak at 0.9rad/s due to the gap effect of the two bodies. In the previous section, it is explained that hydrodynamic effect of 6m gap distance occurs at 0.9 rad/s. For the filling level 56% case, this second motion peak is also observed at 0.82rad/s in both frequency and time domains. A more reduced second peak due to sloshing effect is also shown as I have learned from the MARIN-FPSO case. However, time domain program predicts first motion peak at 0.52rad/s, higher than the frequency domain coupling result (0.49rad/s). At 0.9rad/s, the gap effect on LNGC motion is observed as well.

Fig. 6.30 Motion-sloshing coupling effect of roll RAO.
(LNGC with FT, Linear spring mooring system, Wave heading=90deg)

Roll motion coupled with sloshing, when wave is head sea condition, is shown in Fig. 6.31. As it is introduced, roll motion in head sea condition is due to asymmetric

hydrodynamics caused by a gap between two bodies. When filling level is 0%, roll peak is observed at 0.82 rad/s, and the peak is more clearly observed here rather than beam sea condition. Both frequency and time domain results show this phenomenon. For filling level is 18% case, we can also see three motion peaks as beam sea case: 0.45, 0.62, and 0.82rad/s . Now it is evident that motion peaks at 0.45 and 0.62 rad/s are split phenomenon due to the coupling of motion and sloshing. Peak at 0.82rad/s is due to gap effect. For filling level of 56%, two peaks are observed at 0.52rad/s and 0.82rad/s. Time domain program predict first motion peak at higher than frequency domain result (0.49rad/s). Generally, due to sloshing effect, the second peak was getting smaller as the filling level went higher, a trend we have seen in MARIN-FPSO and LNGC with floating terminal in beam sea condition. However, in this case, second peak of roll RAO at 0.82 rad/s is greater (0.95 deg/m) than 18% filling level result (0.5deg/m). It is because the location of peak of roll motion RAO at head sea condition (0.82rad/s) coincides with sloshing natural frequency of 56% filling level (0.82rad/s).
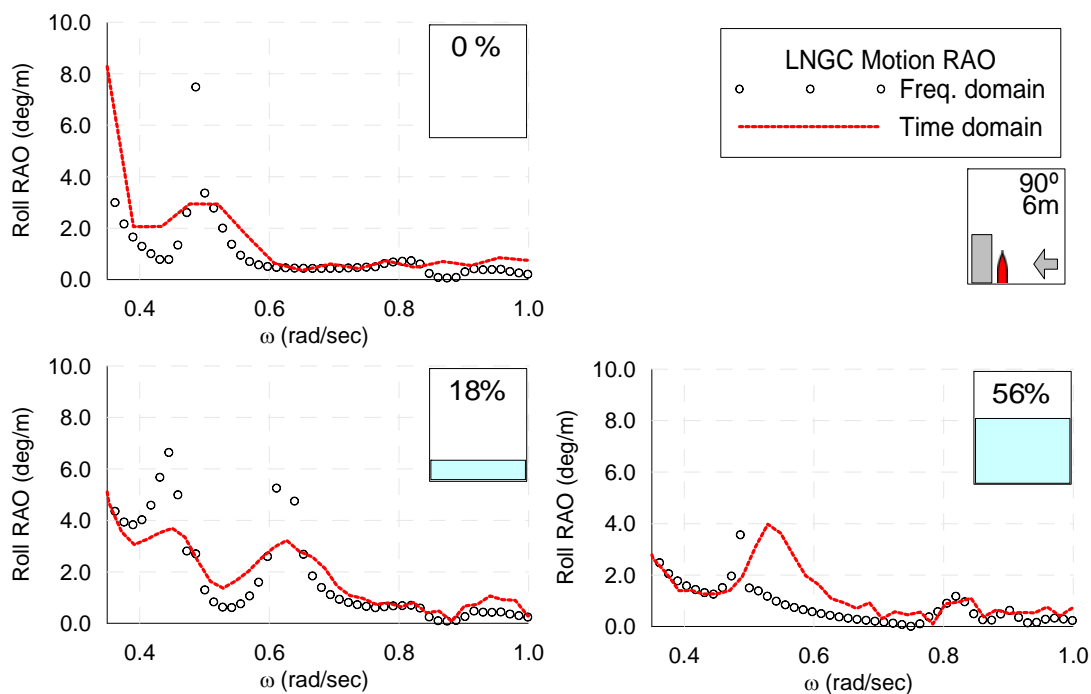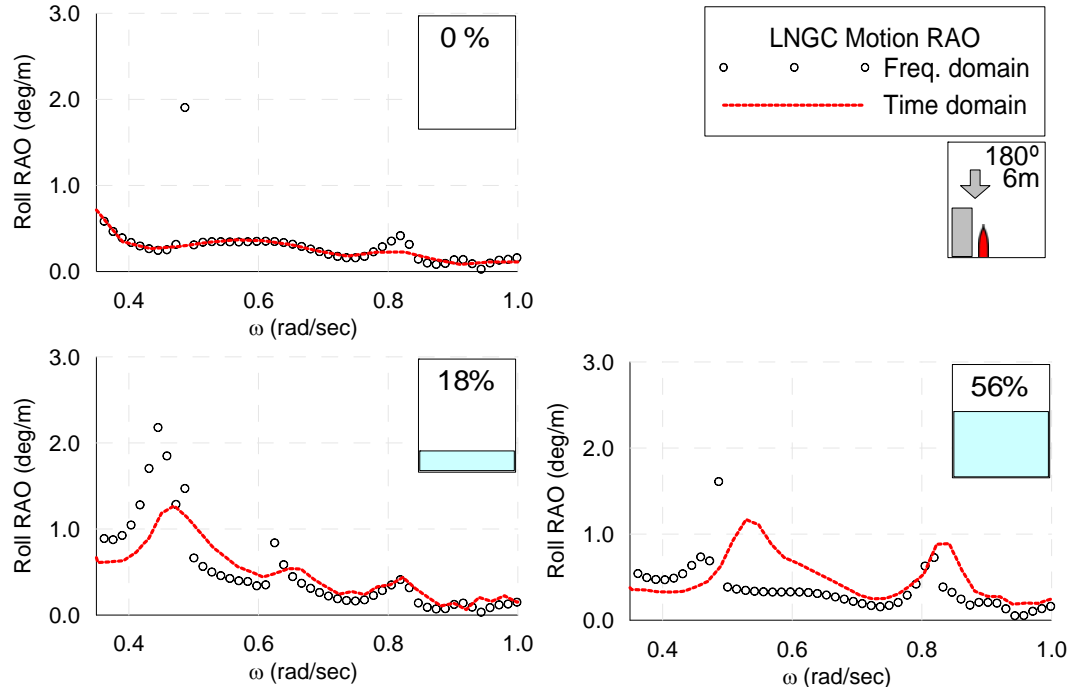
Fig. 6.31 Motion-sloshing coupling effect of roll RAO.

(LNGC with FT, Linear spring mooring system, Wave heading=180deg)

Now time domain simulation results, including realistic nonlinear mooring system using simplified mooring system, fender, and hawser, are presented. Fig. 6.32 shows a comparison of roll and pitch RAOs for head sea and beam sea conditions. For the roll in beam sea condition, general aspects of the second peak of motion RAO from motion-sloshing coupling is observed. Magnitude of the second peak decreases as the filling level increases. Also, location of the second motion peak was the same as the spring mooring case we observed previously. For the roll in head sea condition, second motion peak at filling level 56% is larger than that of 18% filling level. In terms of sloshing effect on longitudinal motion, pitch motion RAO is also presented, and it is not affected by sloshing since longitudinal inertia is much larger than that of sloshing fluid.
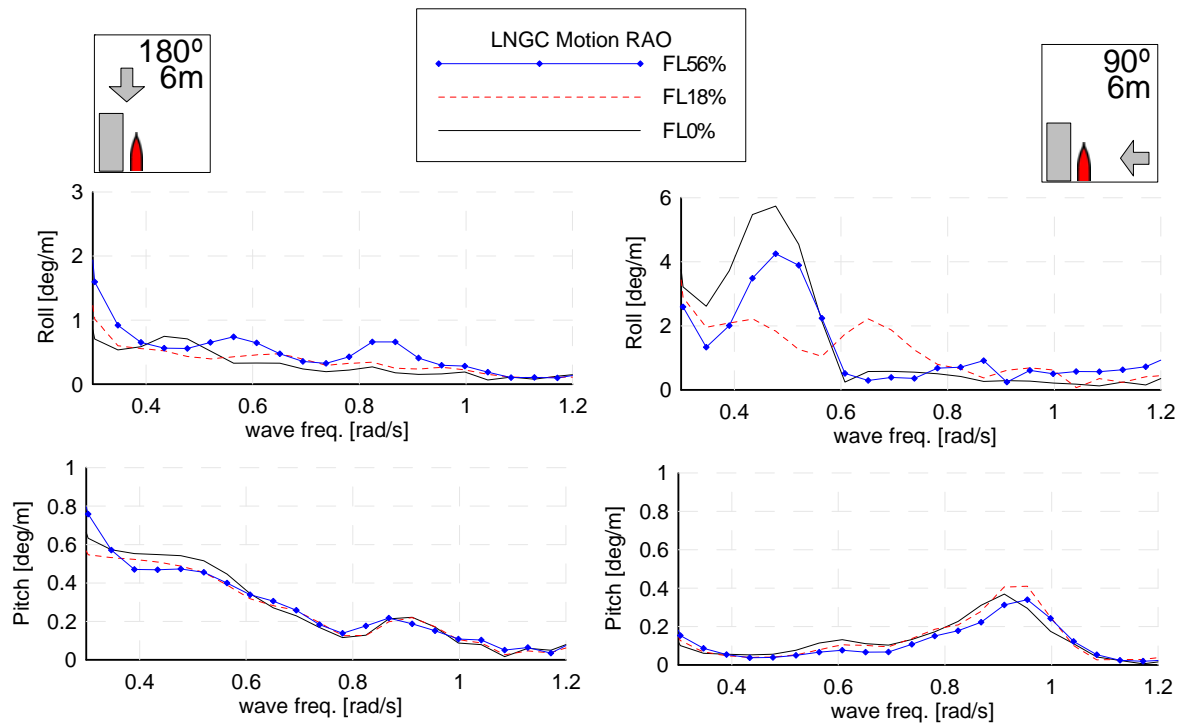
Fig. 6.32 Sloshing effect of LNGC roll and pitch RAO

for head sea and beam sea conditions (Nonlinear mooring system).

Fig. 6.33 shows roll motion time series of LNGC in head sea and beam sea condition and Table 6.14 shows the statistics of roll time series.

Fig. 6.34 shows examples of #2 and #3 hawser tensions in head sea condition. Since hawser tension is calculated based on additionally extended length compared to initial length, we can see that it is activated only when hawser length is larger than initial length. Larger tension occurs with larger motion at 56% filling level than 18% filling level case.
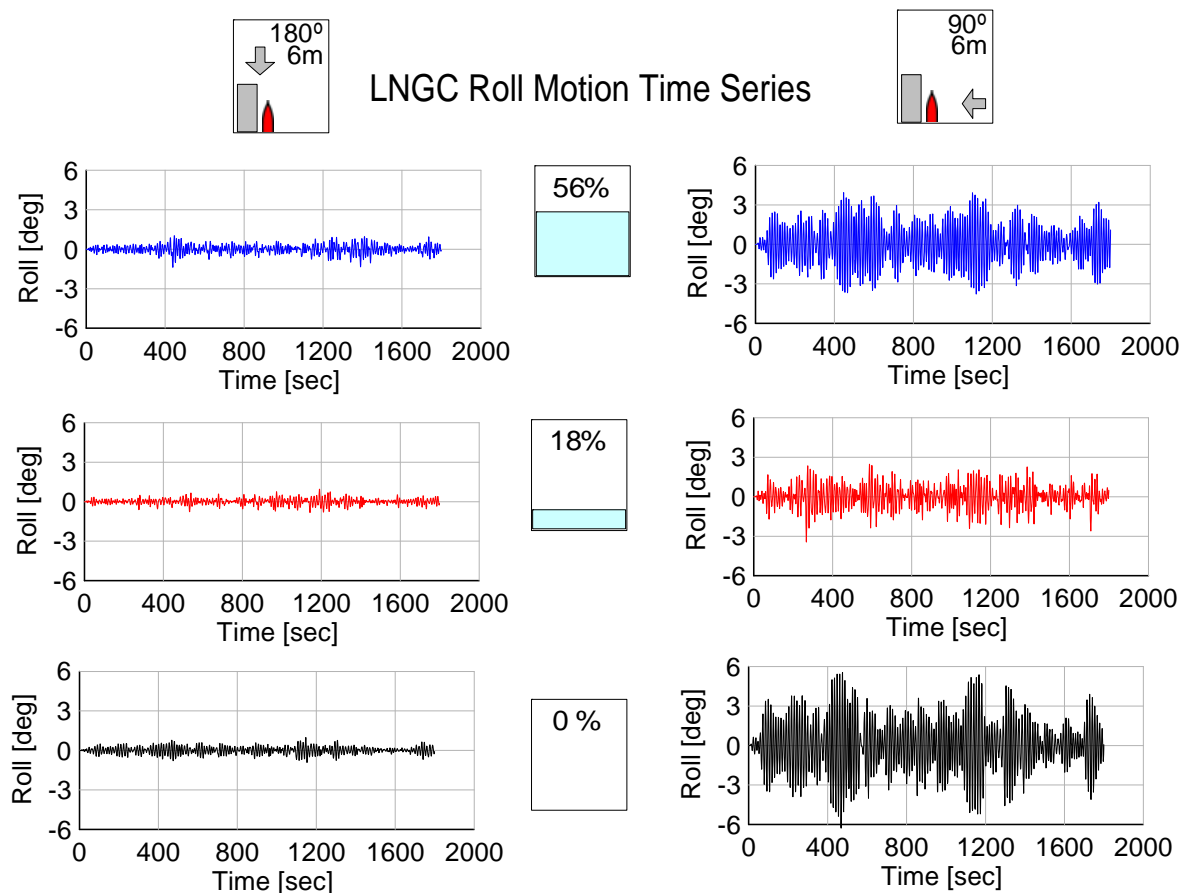
Fig. 6.33 LNGC roll motion time series with respect to filling levels.

(Wave heading=90deg, 180deg)

Table 6.14 Statistics of roll time series in head sea and beam sea conditions

unit : [deg]		Mean	STD	Max.	Min
Head Sea	FL 0%	0.385E-02	0.269	0.988	-0.928
	FL 18%	0.556E-02	0.227	0.946	-0.833
	FL 56%	0.279E-02	0.315	1.032	-1.365
Beam Sea	FL 0%	-0.913E-02	2.000	5.556	-6.278
	FL 18%	0.132E-02	0.839	2.471	-3.441
	FL 56%	0.930E-02	1.484	3.941	-3.781
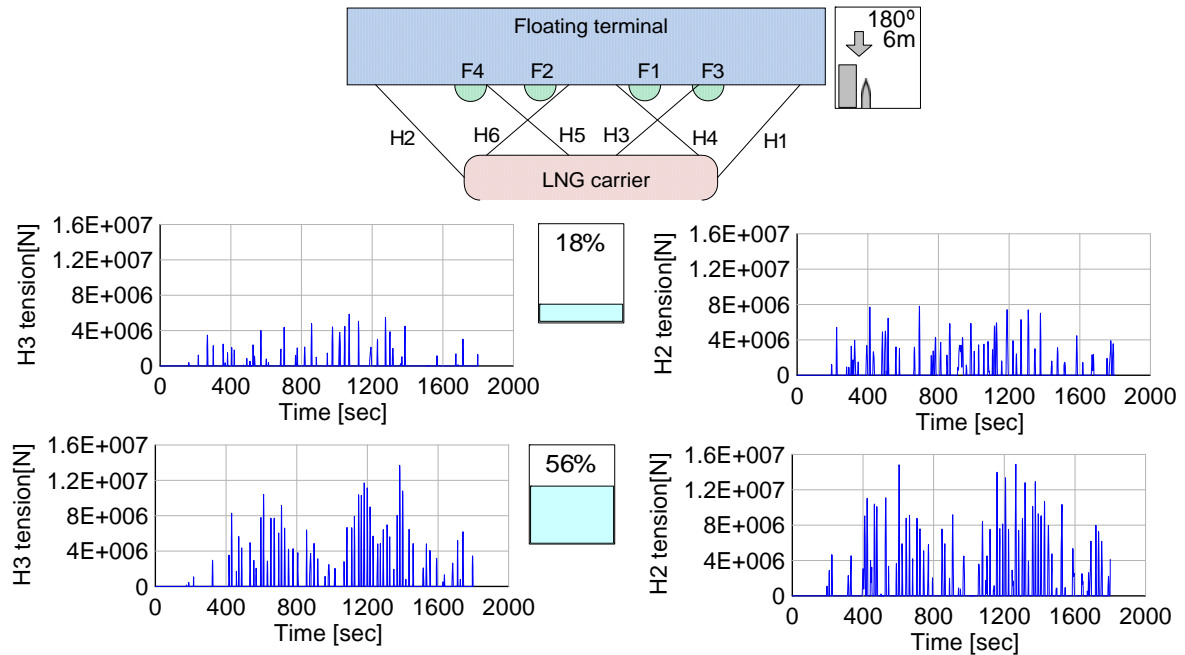
Fig. 6.34 Examples of hawser tension in head sea condition

6.10.3 Effect of Gap Distance

Gap distance between two bodies varies depending on floating terminal's berthing facilities. In order to calculate the effect of this gap effect on motion of LNGC, I selected 6m and 40m gap as representative cases of narrow and wide gap distance. Fig. 6.35 shows comparison of roll and pitch motion RAOs with respect to different gap distances in head sea condition. For the 6m gap case, we have previously investigated hydrodynamic effect on ship motion itself and motion-coupling effect as well. For the 40m gap case as a wide gap, roll natural frequency at 0% filling level at 0.47rad/s is observed. And gap effect is also observed at 0.69rad/s which is lower than 6m gap effect frequency. For 18% filling level, second motion peak was observed at 0.69rad/s. Magnitude of the second peak is larger than first peak, unlike the previous cases of MARIN-FPSO or LNGC with floating terminal with 6m gap. Resonance frequency of sloshing at 18% filling level (0.58rad/s) is closer to the gap effect frequency (0.69rad/s) than in previous cases. For 56% filling level,

second motion peak is located at 0.9rad/s. This is similar to LNGC only case that gap effect frequency (0.69rad/s) stands aside from both roll motion natural frequency (0.47rad/s) and sloshing resonance frequency (0.86rad/s)
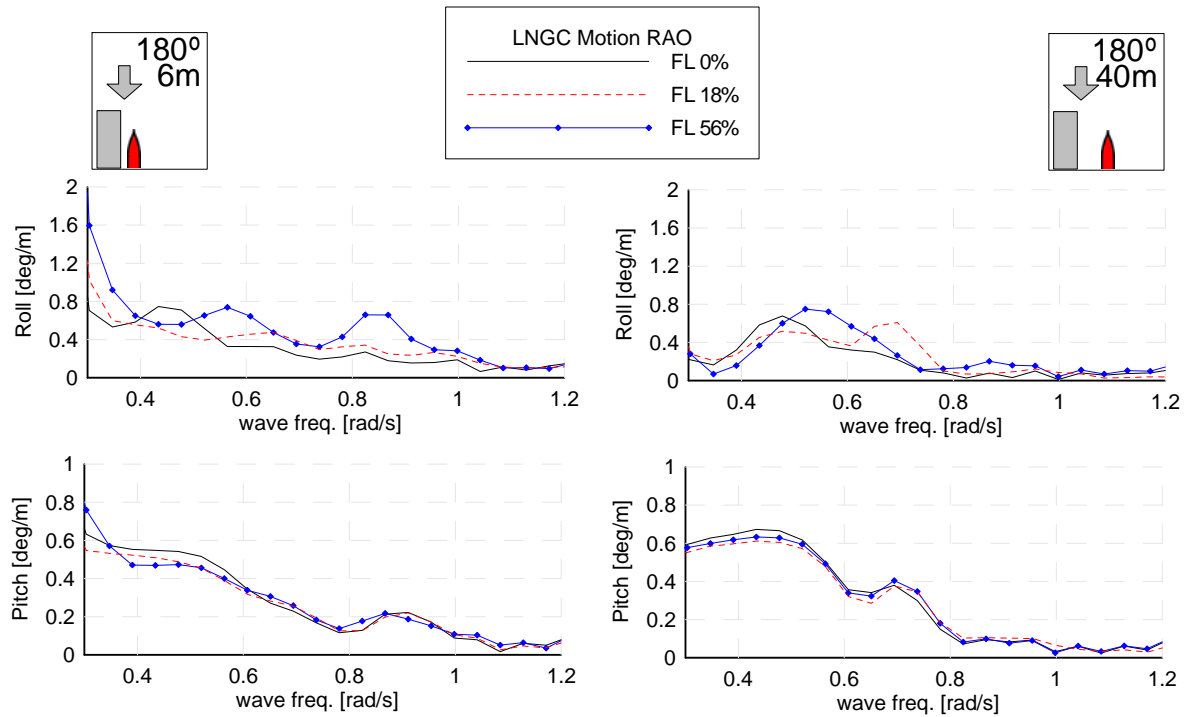
Fig. 6.35 Effect of gap distance of LNGC roll and heave RAO.
(Wave heading=180deg)

6.10.4 Effect of Mooring

Mooring configuration of floating terminal can be varied by water depth or geological environment. A dolphin mooring system, which restricts planar motion, and surge-sway-yaw, is selected to be compared with a simplified mooring system. Fig. 6.36 illustrates the configuration of a dolphin mooring system on floating terminal. A linear spring in surge, sway and yaw direction is attached to floating terminal with high stiffness so that its planar motion is restricted. LNGC is moored with floating terminal with 6

hawsers and 2 fenders located between the two bodies. Table 6.15 shows stiffness of dolphin mooring in each direction.
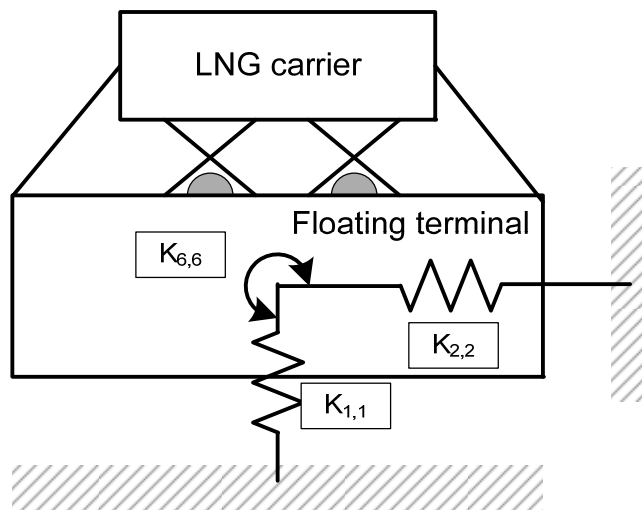
Fig. 6.36 Configuration of dolphin mooring system.

Table 6.15 Dolphin mooring stiffness

	$K_{1,1}$	$K_{2,2}$	$K_{6,6}$
Floating terminal	1.000E+09	2.000E+09	1.000E+12

Fig. 6.37 shows a comparison of surge-sway-yaw's time series and SDF of floating terminal for both simplified mooring and dolphin mooring system when filling level is 0%. By using the high stiffness of the dolphin mooring system, floating terminal's planar motion is confined that dolphin mooring system's spectral density function at low frequency is negligible when compared to simplified mooring system.
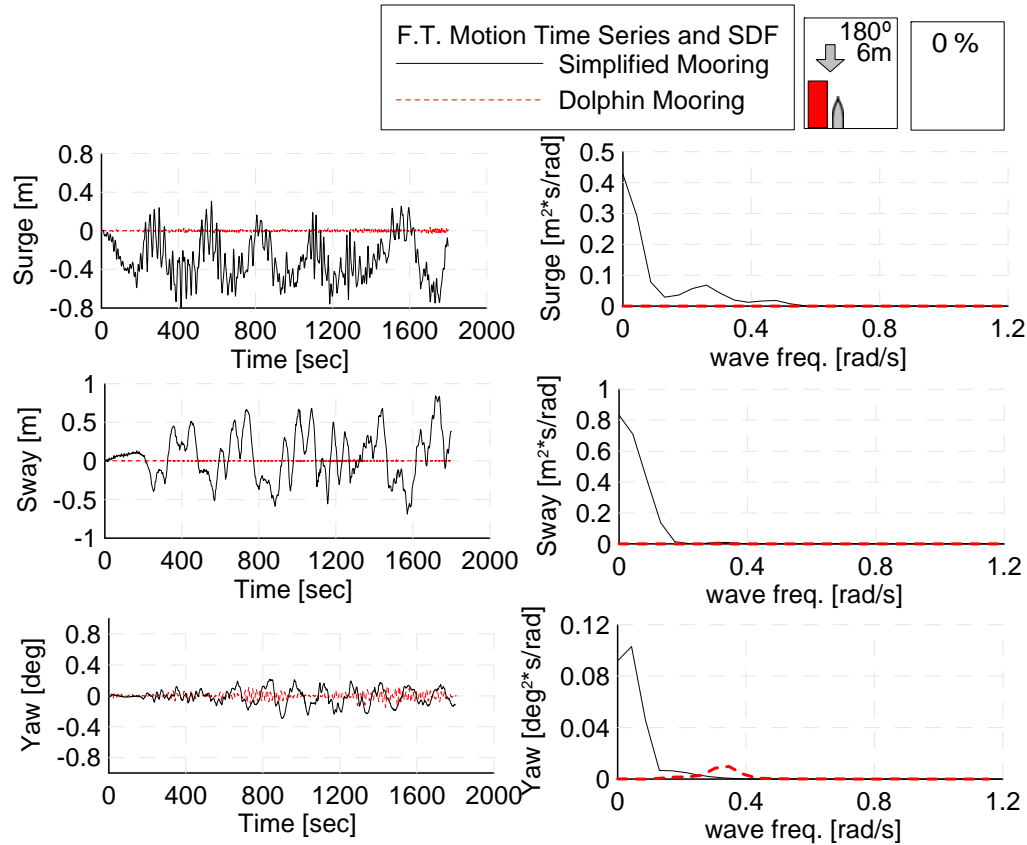
Fig. 6.37 Dolphin mooring effect in surge, sway, and yaw time series and SDF of FT.
(Wave heading=180deg, FL=0%)

Fig. 6.38 shows surge, sway and yaw motion SDF of LNGC when filling level is 0%. We can observe that dolphin mooring system shows large SDF in the low frequency region. This can be explained by relative motion between floating terminal and LNGC. When floating terminal is moored with dolphin mooring system in head sea condition, fixed floating terminal's motion can cause stronger tension than a simplified mooring system in longitudinal direction. Fig. 6.39 shows #3 and #6 hawsers' tension time history and SDF. In low frequency regions in SDF, dolphin mooring case exhibits a larger tension SDF than in the simplified mooring case. Large surge and yaw motion in low frequency region is therefore caused by strong tension due to relative motion of the floating terminal and LNGC.
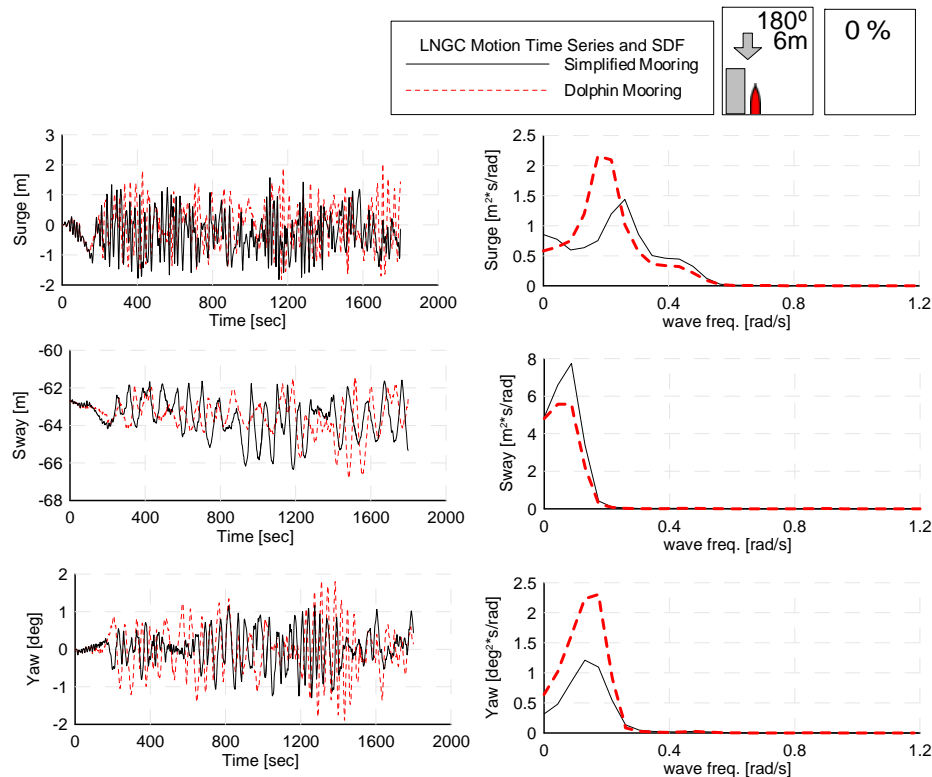
Fig. 6.38 LNGC motion time history and SDF of surge, sway, and yaw.

(Wave heading=180deg, filling level=0%)
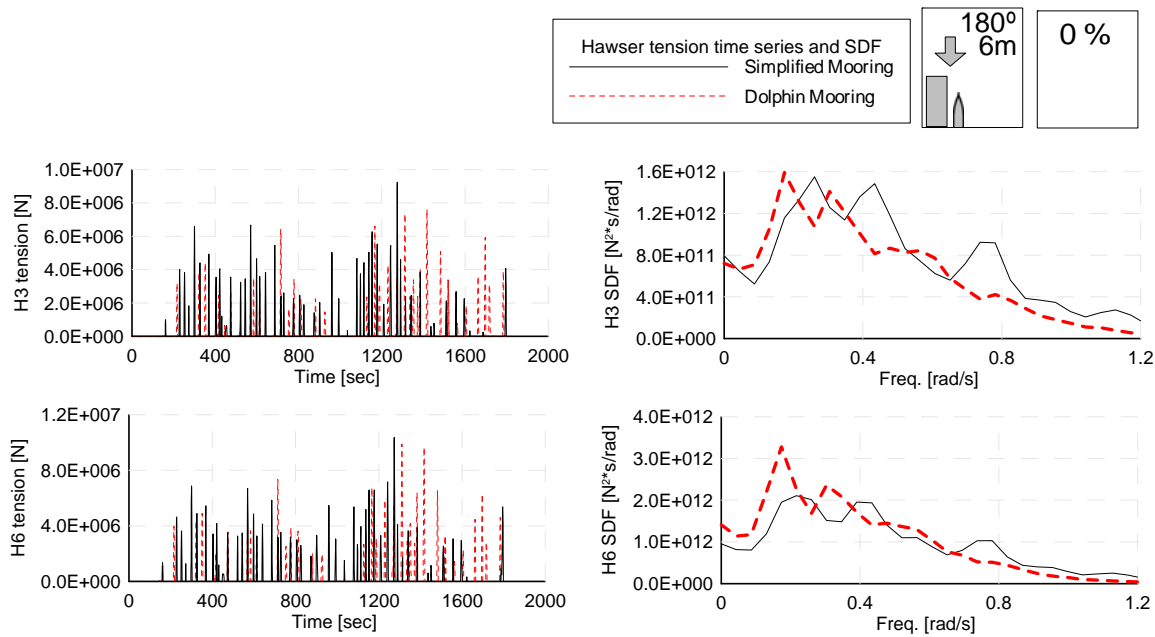
Fig. 6.39 Hawser tension time series and SDF

(#3 and #6 hawsers, wave heading=180deg, filling level=0%)

Fig. 6.40 shows time history and SDF of LNGC in head sea condition when filling level is 0%. Non-planar motions, heave, roll, and pitch, are not much affected by mooring system.
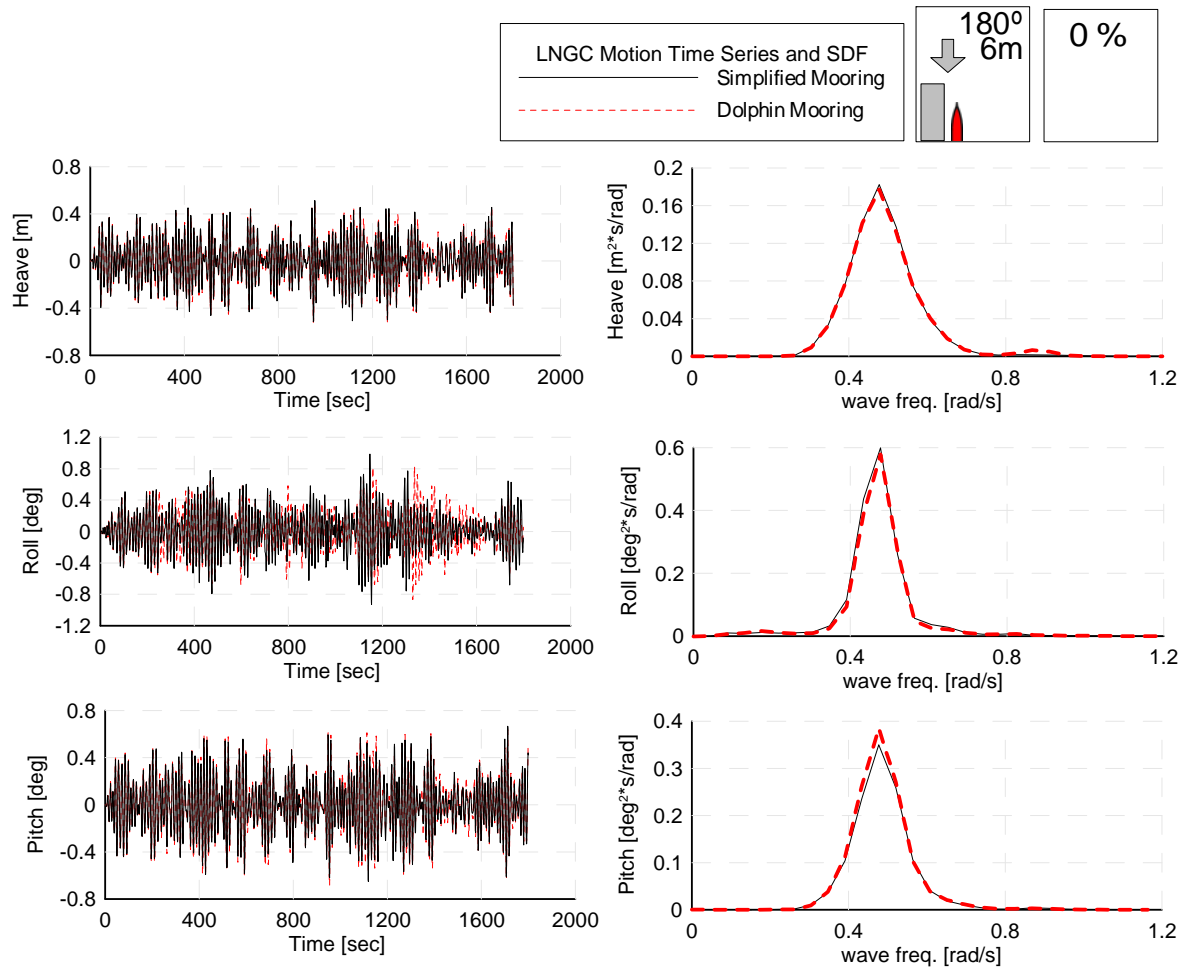
Fig. 6.40 LNGC motion time history and SDF of heave, roll, pitch.
(Wave heading=180deg, filling level=0%)

For the roll motion when filling level is 56%, in Fig. 6.41, dolphin mooring case is smaller than simplified mooing system. Absolute maximum roll displacement of simplified mooring is 1.365deg and dolphin mooring is 1.112deg when the maximum value was reduced to 84%. These statistics are presented in Table 6.16. However, second roll motion

peak of dolphin mooring system is slightly increased from 0.67deg to 0.8deg, as shown in

Fig. 6.42.
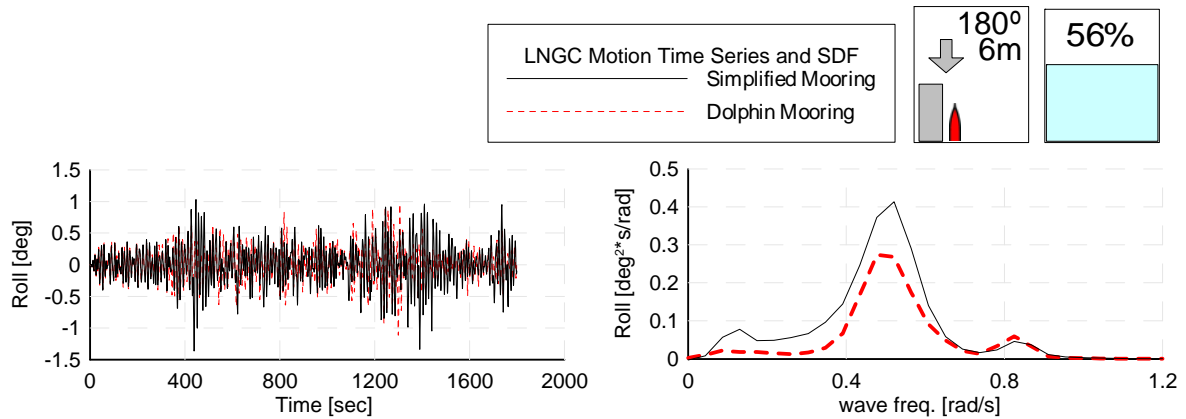
Fig. 6.41 Comparison of LNGC roll RAO between simplified mooring and dolphin

mooring systems. (Wave heading=180deg, filling level=56%)

Table 6.16 Statistics of roll time series in head sea and beam sea conditions

unit : [deg]		Mean	STD.	Max.	Min.
FL 56%	Simplified Mooring	0.279E-02	0.315	1.032	-1.365
	Dolphin Mooring	0.581E-02	0.246	0.965	-1.112
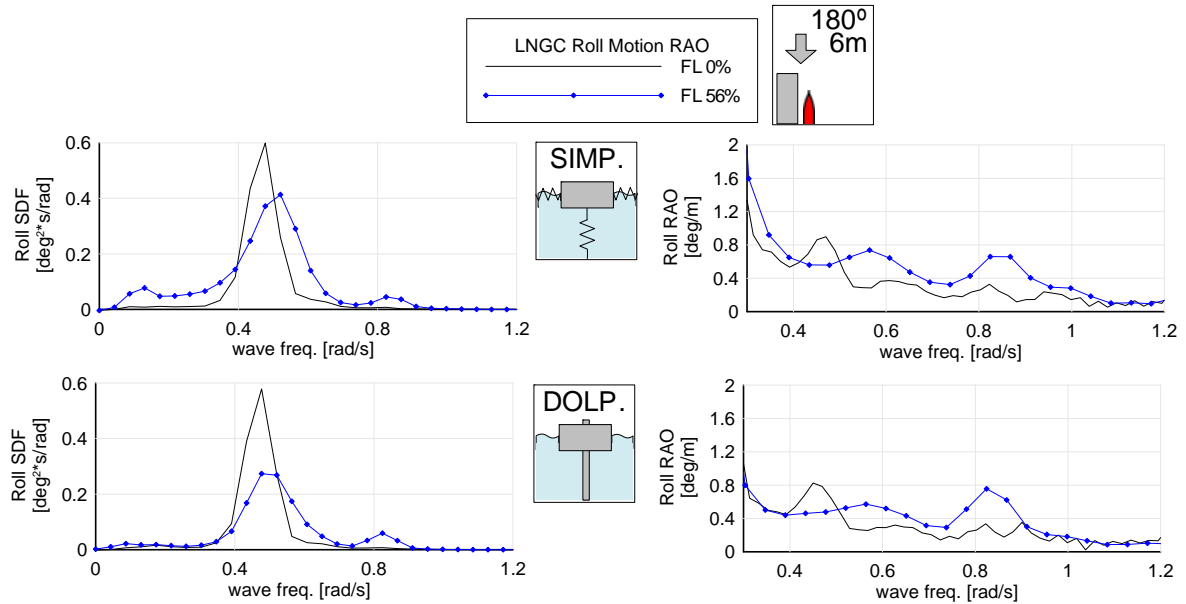
Fig. 6.42 LNGC roll motion RAO comparison between simplified mooring and dolphin mooring systems. (Wave heading=180deg)

6.10.5 Effect of Environment

To investigate the effect of various environmental conditions, wind and current are additionally applied to floating terminal and LNGC. Direction of wind and current is assumed as collinear with wave direction for simulating severe environments. First, the environmental effect on 6 DOF motion of 0% filling level for three environmental direction will be shown; next, roll motion effect due to change of different filling level will be described. Fig. 6.43 and Table 6.17 show a comparison of LNGC motion time history

and statistics when the environmental angle is 90deg. Wind and current coming from -y direction shifted their mean of sway to +y direction, from -0.425m to 1.85m. Yaw motion was increased so that standard deviation was increased from 0.469deg to 0.611deg. The mean of surge motion was also shifted to +x direction from 0.209m to 0.634m. Statistical changes of pitch motion do not appear remarkable as standard deviation change is 0.000deg. However, pitch SDF shows wave induced pitch motion at 0.55rad/s is decreased, while pitch motion due to gap effect at 0.9rad/s is increased. When environmental angle is 150deg shown in Fig. 6.44 and Table 6.18, we can observe more surge shifting than in the 90deg case. Mean of surge was affected by wind and current in –x direction from -0.364m to -0.895m. Surge SDF is increased in low frequency region. For the sway mode, mean is also shifted to +y direction from -0.299m to -2.07m. For 180deg environmental angle, as can be seen in Fig. 6.45 and Table 6.19, effect of the environments on mean of surge is most dominant as it is changed from -0.296m to -1.12m. Surge SDF also shows low frequency motion is mostly affected by wind and current. Change of standard deviation in sway and yaw is small at -0.028m and -0.023 deg, respectively.
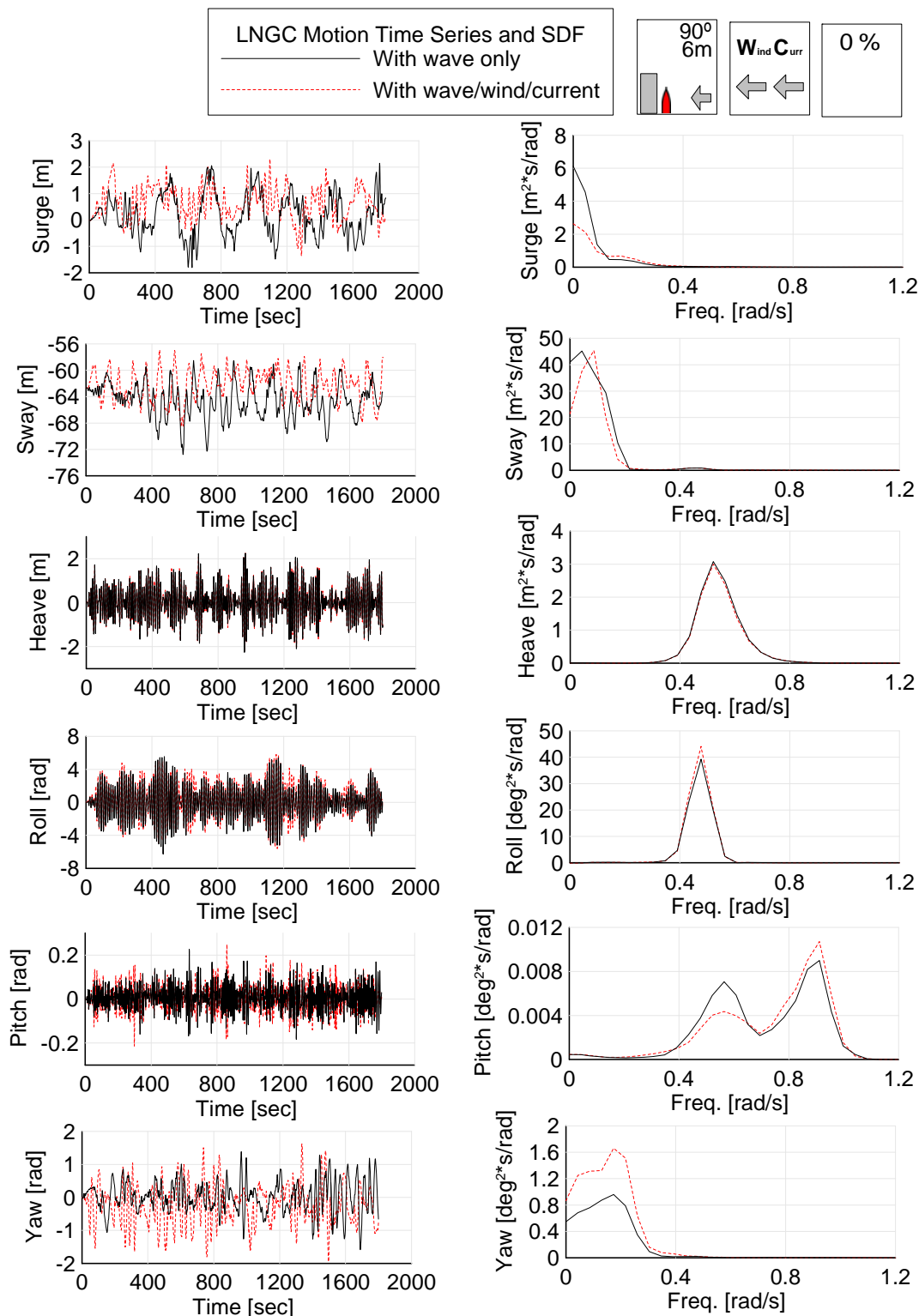
Fig. 6.43 Environmental effect of 6DOF time series and SDF of LNGC.

(Wave, wind and current direction=90deg, FL=0%)
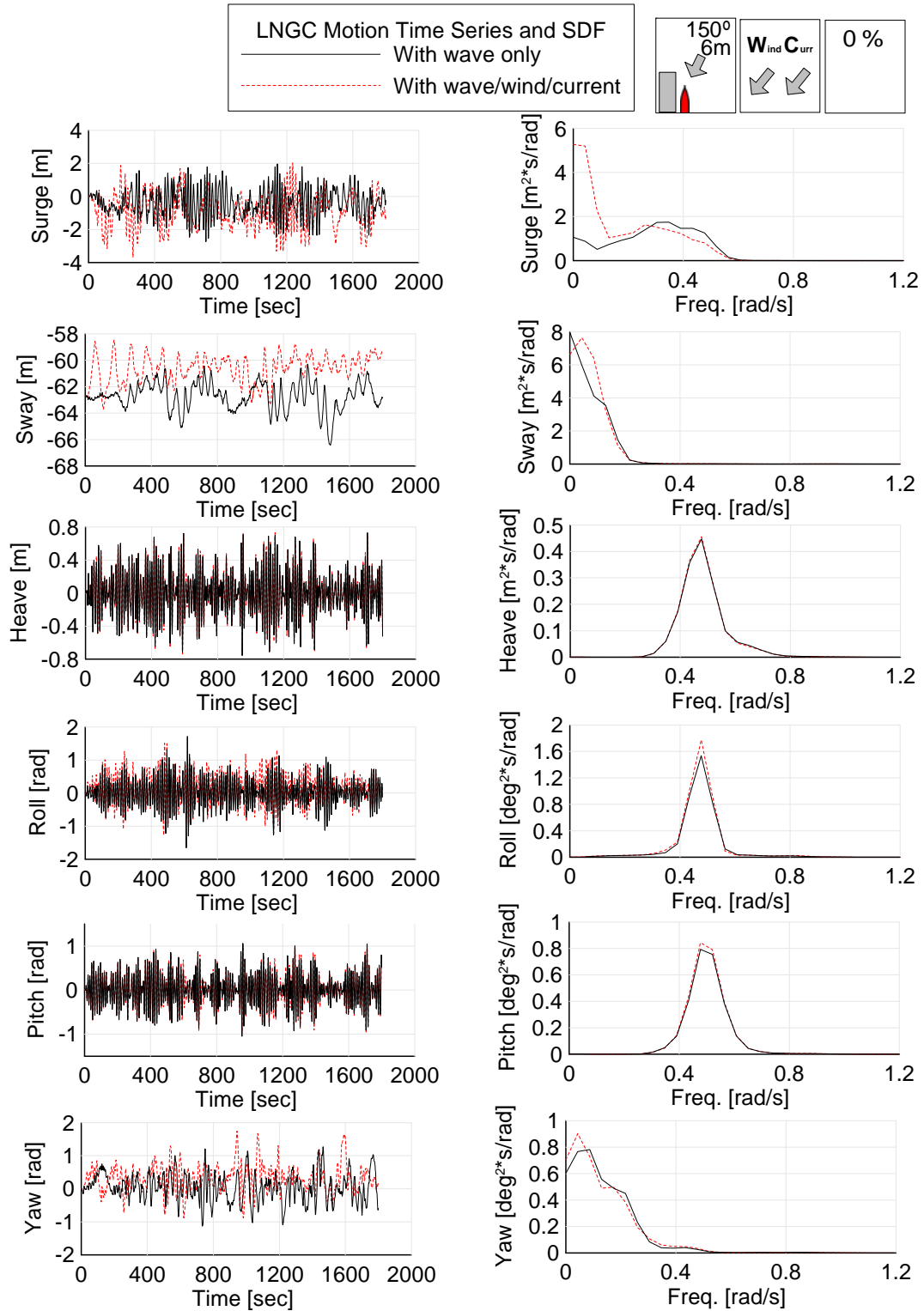
Fig. 6.44 Environmental effect of 6DOF time series and SDF of LNGC.

(Wave, wind and current direction=150deg, FL=0%)
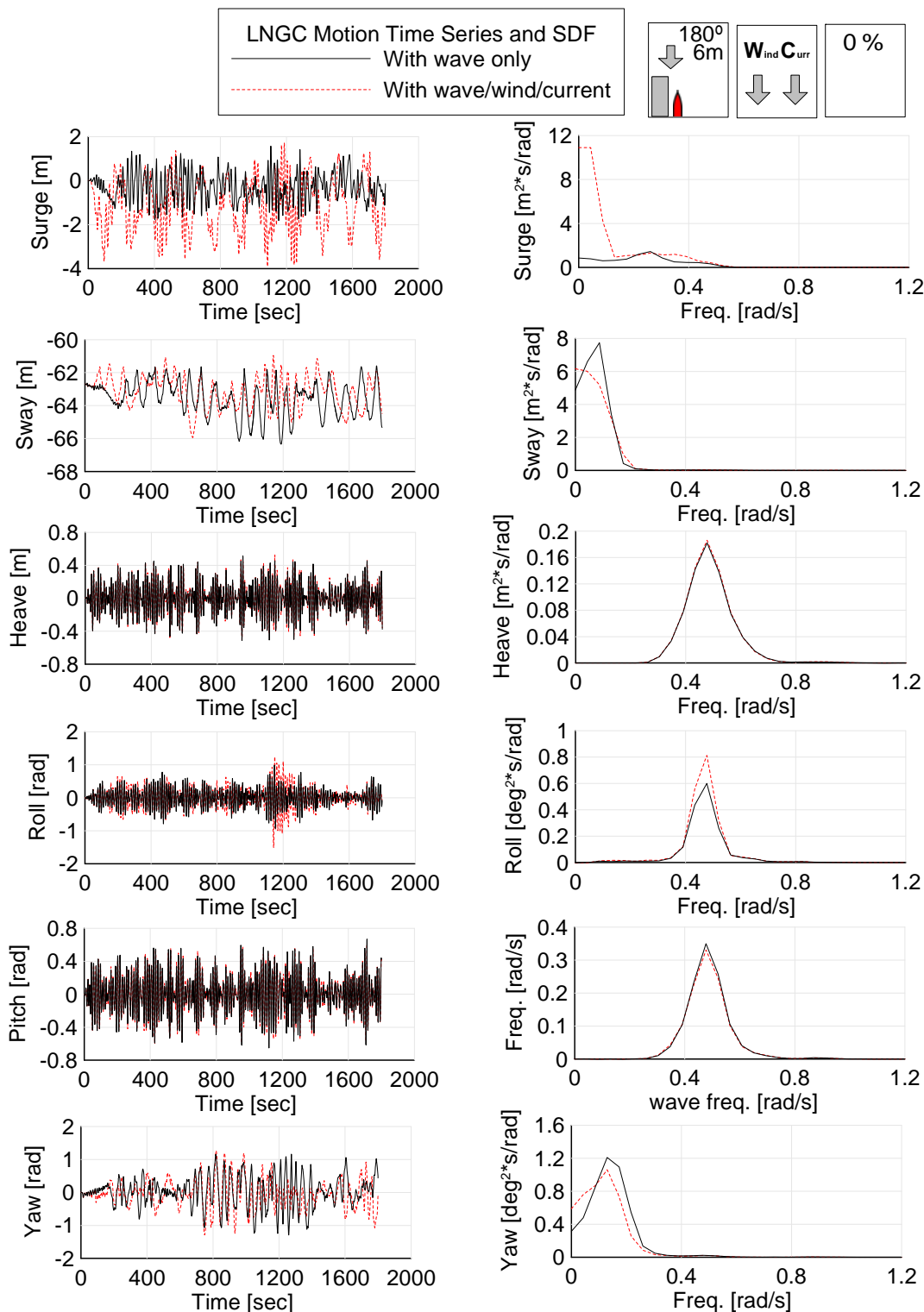
Fig. 6.45 Environmental effect of 6DOF time series and SDF of LNGC.

(Wave, wind and current direction=180deg, FL=0%)

Table 6.17 Statistics of motion of LNGC (Wind, wave and current direction=90deg)

		Mean	STD	Max.	Min.
Surge [m]	Wave only	0.209E+00	0.780	2.149	-1.804
	Wave + W&C	0.634E+00	0.598	2.305	-1.360
Sway [m]	Wave only	0.185E+01	2.597	4.175	-10.078
	Wave + W&C	-0.425E+00	2.329	5.777	-5.882
Heave [m]	Wave only	0.239E-01	0.712	2.248	-2.253
	Wave + W&C	0.231E-01	0.699	2.279	-2.213
Roll [deg]	Wave only	-0.913E-02	2.000	5.556	-6.278
	Wave + W&C	0.197E+00	2.085	5.804	-5.597
Pitch [deg]	Wave only	0.621E-02	0.055	0.226	-0.184
	Wave + W&C	0.621E-02	0.055	0.249	-0.213
Yaw [deg]	Wave only	0.222E-01	0.469	1.385	-1.587
	Wave + W&C	-0.253E+00	0.611	1.614	-1.952

Table 6.18 Statistics of motion of LNGC (Wind, wave and current direction=150deg)

		Mean	STD	Max.	Min.
Surge [m]	Wave only	-0.364E+00	0.806	1.969	-2.740
	Wave + W&C	-0.895E+00	0.993	2.033	-3.684
Sway [m]	Wave only	0.299E-01	1.034	2.412	-3.722
	Wave + W&C	-0.207E+01	1.027	4.225	-1.014
Heave [m]	Wave only	0.159E-02	0.262	0.730	-0.755
	Wave + W&C	0.151E-02	0.262	0.729	-0.738
Roll [deg]	Wave only	0.847E-02	0.416	1.721	-1.656
	Wave + W&C	0.116E+00	0.440	1.509	-1.279
Pitch [deg]	Wave only	0.485E-02	0.347	1.061	-1.049
	Wave + W&C	0.512E-02	0.355	1.018	-0.975
Yaw [deg]	Wave only	0.509E-01	0.418	1.273	-1.131
	Wave + W&C	0.321E+00	0.415	1.745	-0.880

Table 6.19 Statistics of motion of LNGC (Wind, wave and current direction=180deg)

		Mean	STD	Max.	Min.
Surge [m]	Wave only	-0.296E+00	0.625	1.571	-1.814
	Wave + W&C	-0.112E+01	1.173	1.724	-3.903
Sway [m]	Wave only	0.857E+00	1.001	1.114	-3.641
	Wave + W&C	0.480E+00	0.973	1.743	-3.234
Heave [m]	Wave only	0.371E-03	0.178	0.513	-0.514
	Wave + W&C	0.361E-03	0.180	0.523	-0.507
Roll [deg]	Wave only	0.385E-02	0.269	0.988	-0.928
	Wave + W&C	0.304E-02	0.302	1.245	-1.513
Pitch [deg]	Wave only	0.167E-02	0.227	0.667	-0.651
	Wave + W&C	0.204E-02	0.224	0.609	-0.602
Yaw [deg]	Wave only	0.326E-01	0.453	1.165	-1.294
	Wave + W&C	-0.516E-01	0.430	1.268	-1.288

Effect of environments on LNGC motion due to different filling levels is investigated by comparing roll RAO of LNGC. Fig. 6.46 and Table 6.20 represent roll motion RAO and statistics with respect to filling levels when the environmental angle is 180deg. When filling level is 0%, effect of wave and current increased absolute maximum value from 0.928deg to 1.513deg. SDF at roll natural frequency is also increased from 0.6deg^2*s/rad to 0.8 deg^2*s/rad. For the 18% filling level, absolute maximum value is increased from 0.833deg to 1.362deg, but the change of SDF is small. When filling level is 56%, overall SDF is decreased while the change of maximum value is from 1.032deg to 1.213deg. Fig. 6.47 and Table 6.21 illustrate the case of 90deg environmental angle. In this case, mean of roll displacement at every filling level is shifted to positive values, 0.197deg, 0.283deg, and 0.287deg at a filling level of 0%, 18%, and 56%, respectively.
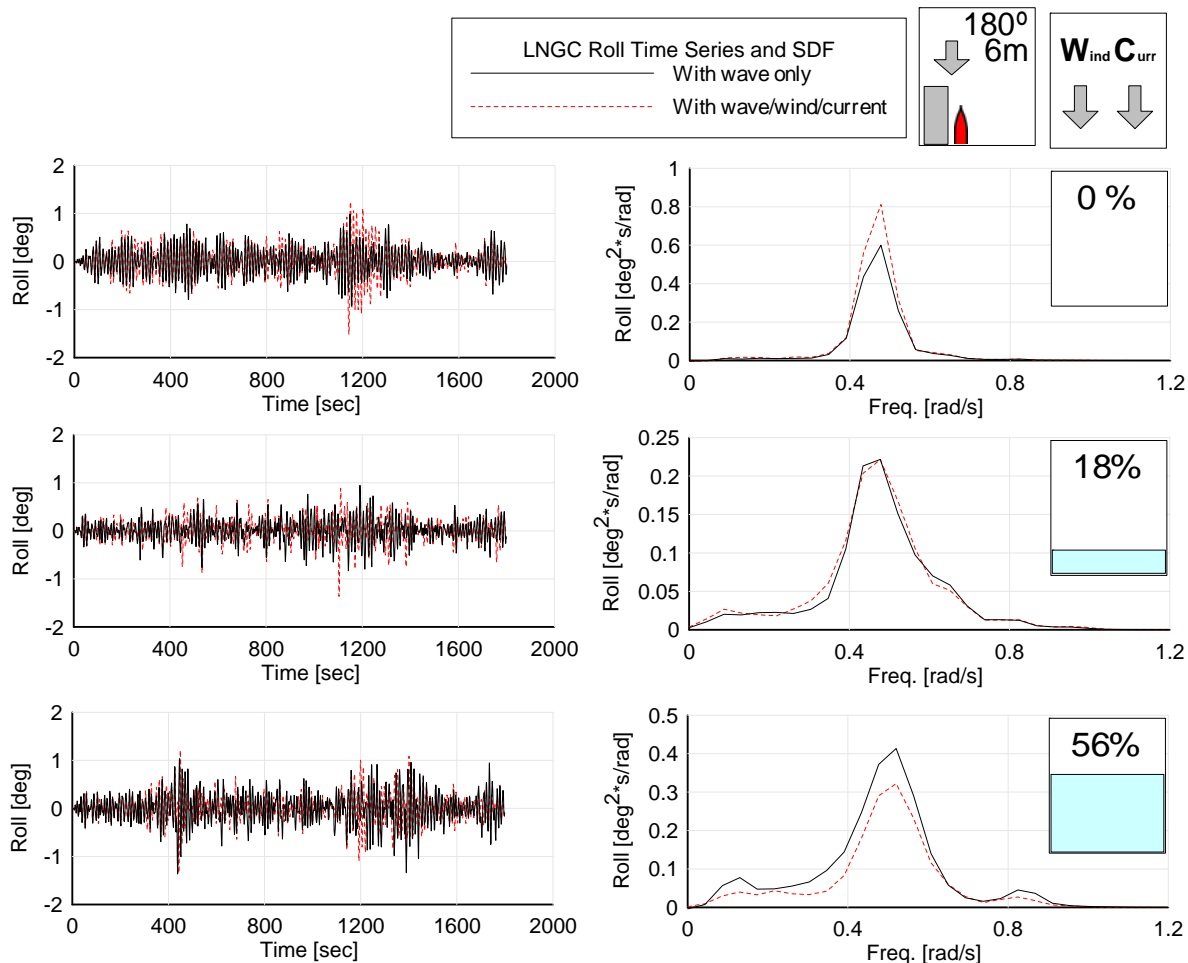
Fig. 6.46 Environmental effect in roll RAO of LNGC with respect to filling levels.

(Wave, wind and current direction=180deg)

Table 6.20 Statistics of roll motion (Wind, wave and current direction=180deg)

unit : [deg]		Mean	STD	Max.	Min.
FL 0%	Wave only	0.385E-02	0.269	0.988	-0.928
	Wave + W&C	0.304E-02	0.302	1.245	-1.513
FL 18%	Wave only	0.556E-02	0.227	0.946	-0.833
	Wave + W&C	0.460E-02	0.232	0.880	-1.362
FL 56%	Wave only	0.279E-02	0.315	1.032	-1.365
	Wave + W&C	0.490E-02	0.269	1.213	-1.349
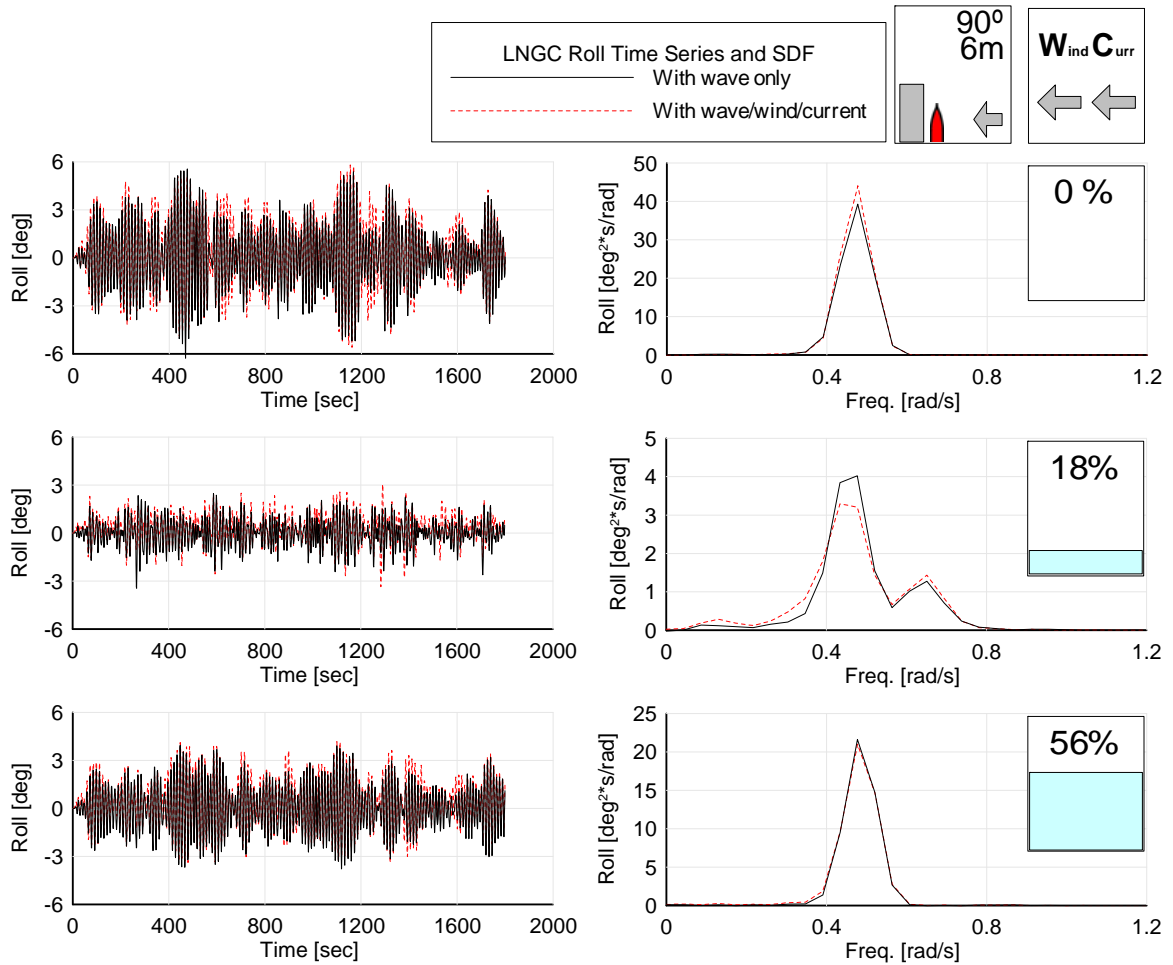
Fig. 6.47 Environmental effect in roll RAO of LNGC with respect to filling levels.

(Wave, wind and current direction=90deg)

Table 6.21 Statistics of roll motion (Wind, wave and current direction=90deg)

unit : [deg]		Mean	STD	Max.	Min.
FL 0%	Wave only	-0.913E-02	2.000	5.556	-6.278
	Wave + W&C	0.197E+00	2.085	5.804	-5.597
FL 18%	Wave only	0.132E-02	0.839	2.471	-3.441
	Wave + W&C	0.283E+00	0.848	3.059	-3.351
FL 56%	Wave only	0.930E-02	1.484	3.941	-3.781
	Wave + W&C	0.287E+00	1.502	4.170	-3.392
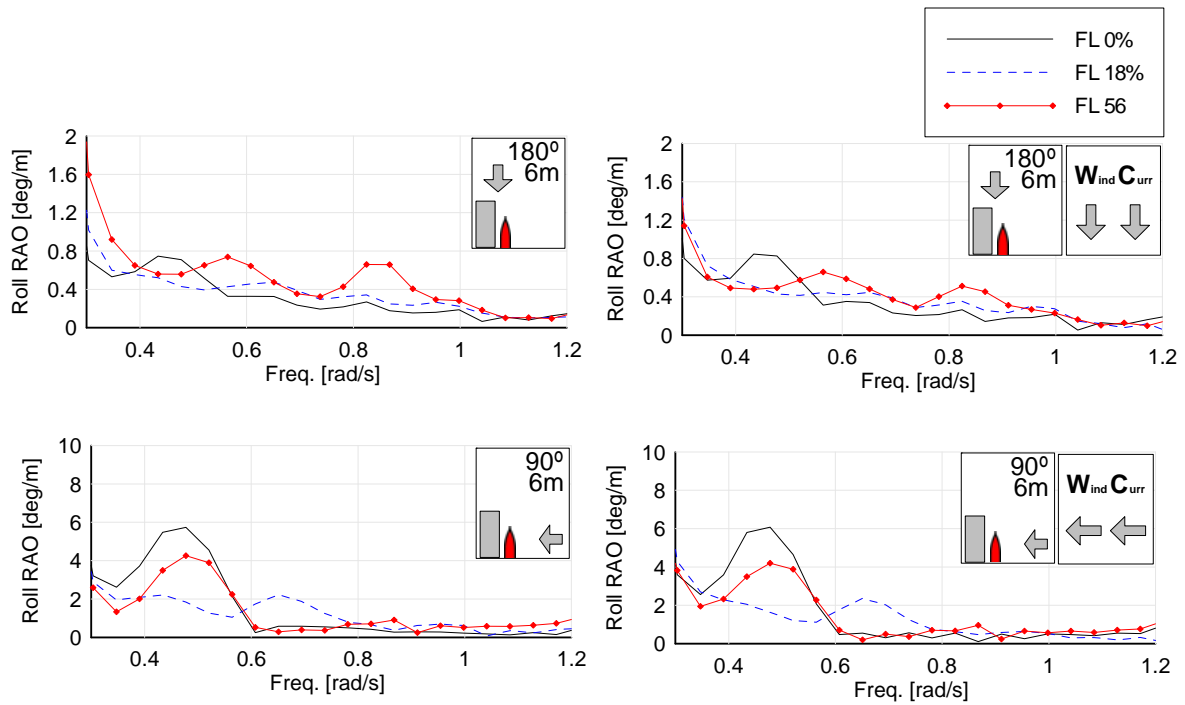
Fig. 6.48 Environmental effect on roll motion RAO of LNGC

Fig. 6.48 shows how the summarized roll motion RAO is affected by environments with different environmental angles. For head sea condition, motion RAO at 0% filling level is slightly increased at roll natural frequency (0.47rad/s). RAO is not much changed at 18% filling level motion. When filling level is 56%, however, second motion peak around 0.85rad/s is decreased from 0.65deg/m to 0.47deg/m. When environmental angle is 90deg, wind and current effect on motion RAO at every filling level are not remarkable.

CHAPTER VII

CONCLUSION AND FUTURE WORK

The interaction effects between ship motion and inner-tank liquid sloshing are investigated by a newly developed potential-viscous hybrid time domain computer program. The results are also compared with those based on linear potential theory in the frequency domain. For time domain simulations, both potential-flow ship-motion program and viscous-flow inner-tank-sloshing program are independently developed. In the ship-motion program, the hydrodynamic coefficients including wave forces and drift forces are obtained from a 3D panel-based diffraction/radiation program. The time domain sloshing program is based on the Navier-Stokes equation solver, including the SURF method for free surface. During the time marching, the tank sloshing program is coupled with the vessel-motion program so that the influence of tank sloshing on vessel motions can be assessed. On the other hand, the frequency domain analysis is done by adding the 3D panel method for interior problems. The inner-tank-sloshing effect is characterized by the increase in added mass, the decrease in restoring forces of sloshing fluid, and the hydrostatic correction of inner free surface. Although the frequency domain analysis is based on linear potential theory, the results generally reproduce the qualitative trend of the coupling effect between inner-liquid and ship motions. By using the potential-viscous hybrid method in time domain, I have a better quantitative agreement when compared with the experimental data. This agreement is due to the inclusion of viscous and nonlinear free-surface effects of the liquid motion in the hybrid method. Apart from resonance sloshing frequencies, the liquid cargo generally functions as a vibration absorber. The peak

frequency of roll motions can be shifted due to the tank sloshing effect. The secondary peak appears near the sloshing natural frequency, and its effects increase as the filling ratio increases, an increase which can be observed in both numerical and experimental results. The pitch-motion amplitudes are much less affected by inner-tank liquid sloshing compared to roll motions even in head-sea condition.

I have also studied hydrodynamic characteristics of two body interactions by investigating more cases on LNGC moored with FT. Hydrodynamic interaction, analyzed in frequency domain, was successfully implemented into time domain program and validated through regular wave test in time domain. The effects of two different gap distances are observed, both in hydrodynamic coefficients and motion RAOs, at each frequency corresponds to pumping mode of gap distance. Since water depth of FT and LNGC was selected as relatively shallow water, calculation of second-order drift force using Newman's approximation was done by an investigation of the validity of approximation with respect to water depth. Coupling of multi-body motion and sloshing was successfully coupled. The influence of sloshing on the LNGC with FT case was also able to be characterized by second motion peak around natural frequency of the sloshing tank. In particular, this second motion peak was amplified when natural frequency of sloshing is near gap effect frequency. This means that, when LNGC and FT are moored in side-by-side configuration, additional attention is required in determining gap distance considering natural frequency of sloshing tank. Instead of a real mooring line model, a developed simplified mooring line system provides reduction of computational time and simplicity of mooring system modeling once the static offset test result is known. Nonlinear fender and hawser models were modeled successfully in simulating real

mooring configuration with a side-by-side case. To simulate various types of configuration between LNGC and FT, various simulation cases containing gap effect between bodies, mooring effect on selecting mooring type of FT, and environmental effect on various environmental conditions are studied.

In the future, a more realistic offloading configuration can be investigated with this program. Both floating terminal and LNGC can actually be equipped with sloshing tanks. In this case, subsequently, each sloshing tank on each body needs to be coupled in motion-sloshing point of view. Even the change of sloshing fluids' mass in both sloshing tanks during the transfer of LNG from one tank to the other can be investigated by this quasi-static approach. Regarding time domain sloshing analysis program, I have used the program developed for analysis of sloshing fluid in mild-slope condition, a condition that does not allow either splash or overturning, but focuses on global behavior of sloshing fluid for the purpose of coupling with the ship motion program. However, by using a different type of sloshing analysis program that can simulate a more violent flow and can calculate more accurate local pressure, the effect of sloshing impact on the pump tower is another important issue of sloshing from a structural point of view that can be studied and extended to fatigue analysis.

REFERENCES

Abramson, H. N., Bass, R. L., Faltinsen, O., and Olsen, H. A., 1974, Liquid slosh in LNG carriers. 10th Symposium on Naval Hydrodynamics, 371–388.

ANSI/API RP-2A WSD, 2000, Recommended Practice for Planning, Designing and Constructing Fixed Offshore Platforms - Working Stress Design. Washington, DC., American Petroleum Institute.

Bass, R. L., Bowles, E. B., Jr., Trudell, R. W., Navickas, J., Peck, J. C., Yoshimura, N., Endo, S., and Pots, B. F. M., 1985, Modeling criteria for scaled LNG sloshing experiments. Journal of Fluids Engineering. Transactions of the ASME 107, 272-280.

Blackman, R. B., and Tukey, J. W., 1958, The measurement of power spectra from the point of view of communications engineering. I-II: Bell System Technical Journal 37, 185-282.

Cho, S., Hong, S. Y., Kim, J., and Park, I., 2007, Studies on the coupled dynamics of ship motion and sloshing including multi-body interactions. Proc. 17th 2007 International Offshore and Polar Engineering Conference, ISOPE, 1900-1904.

Cummins, W. E., 1962, The impulse response function and ship motions. Symposium on Ship Theory, Hamburg, Germany, Schiffstechnik 9, 101–109.

Faltinsen, O. M., 1978, Numerical nonlinear method of sloshing in tanks with two-dimensional flow. Journal of Ship Research 22, 193-202.

Faltinsen, O. M., 1990, Wave loads on offshore structures. Annual Review of Fluid Mechanics 22, 35-56.

Faltinsen, O. M., 2002, Asymptotic modal approximation of nonlinear resonant sloshing in

a rectangular tank with small fluid depth. Journal of Fluid Mechanics 470, 319-57.

Faltinsen, O., Rognebakke, O. F., Lukovsky, I. A., and Timokha, A. N., 2000, Multidimensional modal analysis of nonlinear sloshing in a rectangular tank with finite water depth. Journal of Fluid Mechanics 407, 201-234.

Faltinsen, O. M., Rognebakke, O. F., and Timokha, A. N., 2003, Resonant three-dimensional nonlinear sloshing in a square-base basin. Journal of Fluid Mechanics 487, 1-42.

Faltinsen, O. M., and Timokha, A. N., 2001, An adaptive multimodal approach to nonlinear sloshing in a rectangular tank. Journal of Fluid Mechanics 432, 167-200.

Frank, W., 1967, Oscillation of cylinders in or below the free surface of deep fluids. Technical Report of Naval Ship Research & Development Center (NSRDC), Annapolis, MD.

Gaillarde, G., Ledoux, A., and Lynch, M., 2004, Coupling between liquefied gas and vessel's motion for partially filled tanks: Effect on seakeeping. Design & Operation of Gas Carriers, London, UK.

Garrett, D. L., 1982, Dynamic analysis of slender rods. Journal of Energy Resources Technology, Transaction of ASME 104, 302-307.

Goda, Y., 1970, Numerical experiments on wave statistics with spectral simulation. Report of the Port and Harbour Research Institute 9, 3-57.

Haskind, M. D., 1953, Two papers on the hydrodynamic theory on heaving and pitching of a ship. Technical and Research Bulletin of Society of Naval Architects and Marine Engineers, 1-12, New York.

Haskind, M. D., 1962, The Eexciting Forces and Wetting of Ships in Waves. David Taylor

Model Basin Report No.AD0288661, Washington D.C.

Huijsmans, R. H. M., Pinkster, J. A., and De Wilde, J. J., 2001, Diffraction and radiation of waves around side-by-side moored vessels. Proc. of the 11th International Offshore and Polar Engineering Conference 406-412.

Kim, J. W., Kim, K., Kim, P. S., and Shin, Y. S., 2005, Sloshing-ship motion coupling effect for the sloshing impact load on the LNG containment system. Proc. of the 15th International Offshore and Polar Engineering Conference, 282-291.

Kim, M. H., Ran, Z., Zheng, W., Bhat, S., and Beynet, P., 1999, Hull/mooring coupled dynamic analysis of a truss spar in time-domain. Proceedings of the International Offshore and Polar Engineering Conference 1, 301-308.

Kim, M. H., and Yue, D. K. P., 1991, Sum- and difference-frequency wave loads on a body in unidirectional Gaussian seas. Journal of Ship Research 35, 127-140.

Kim, M. H., Koo, B. J., Mercier, R. M. and Ward E. G., 2005, Vessel/mooring/riser coupled dynamic analysis of a turret-moored FPSO compared with OTRC experiment. Journal of Ocean Engineering 32, 1780-1802.

Kim, Y., 2001, Numerical simulation of sloshing flows with impact load. Applied Ocean Research 23, 53-62.

Kim, Y., Lin, W. M., Shin, Y. S., and Yue, D. K. P., 2003, Study on sloshing problem coupled with ship motion in waves. The 8th International Conference on Numerical Ship Hydrodynamics, September 22-25, 2003, Busan, Korea.

Kim, Y., Nam, B. W., Kim, D. W., and Kim, Y. S., 2007, Study on coupling effects of ship motion and sloshing. Ocean Engineering 34, 2176-2187.

Kodan, N., 1984, The motions of adjacent floating structures in oblique waves. Proc. 3rd.

Offshore Mechanics and Arctic Engineering, OMAE 1, 206-213.

Kotchin, N. E., 1967, The theory of waves generated by oscillations of a body under the free surface of a heavy incompressible fluid. Technical and Research Bulletin of Society of Naval Architects and Marine Engineers, 1-10, New York.

Lee, C. H., 1995, WAMIT Theory Manual. MIT Report 95-2, Dept. of Ocean Engineering, Massachusetts Institute of Technology, Cambridge, MA.

Lee, D. H., Kim, M. H., Kwon, S. H., Kim, J. W., and Lee, Y. B., 2005, A parametric and numerical study on LNG-tank sloshing loads. Proc. of the 15th International Offshore and Polar Engineering Conference, 228-232.

Lee, S. J., Kim, M. H., Lee, D. H., Kim, J. W., and Kim, Y. H., 2007, The effects of LNG-tank sloshing on the global motions of LNG carriers. Ocean Engineering 34, 10-20.

Malenica, S., Zalar, M., and Chen, X. B., 2003, Dynamic coupling of seakeeping and sloshing. Proc. 13th International Offshore and Polar Engineering Conference, 486-492.

Maruo, H., 1960, Drift of body floating on waves. Journal of Ship Research 4, 1-10.

McIver, P., 2005, Complex resonances in the water-wave problem for a floating structure. Journal of Fluid Mechanics 536, 423-443.

Mikelis, N. E., and Journee, J. M. J., 1984, Experimental and numerical simulations of sloshing behaviour in liquid cargo tanks and its effect on ship motions. National Conference on Numerical Methods for Transient and Coupled Problems, 1-12.

Molin, B., Remy, F., Rigaud, S., and de Jouette, C., 2002, LNG-FPSO's : frequency domain, coupled analysis of support and liquid cargo motions. Proceedings of IMAM conference.

Newman, J. N., 1967, Drift force and moment on ships in waves. Journal of Ship Research

11, 51-60.

Newman, J. N., 2005, Wave effects on vessels with internal tank. The 20th Workshop on Water Waves and Floating Bodies.

Nordgren, R. P., 1974, On computation of the motion of elastic rods. Journal of Applied Mechanics, Transactions ASME 41 Ser E, 777-780.

Ogilvie, T. F., 1983, Second-order hydrodynamic effects on ocean platforms. International Work Shop on Ship and Platform Motions, 205-243.

Oil companies International Marine Forum (OCIMF), 1977, Prediction of wind and current loads on VLCCs.

Papanikolaou, A., and Spanos, D., 2002, On the Modelling of Floodwater Dynamics And It's Effects On Ship Motion. Proc. 6th International Ship Stability Workshop, 1-9.

Papanikolaou, A., and Spanos, D., 2004, 24th ITTC Benchmark Study on Numerical Prediction of Damage Ship Stability in Waves Preliminary Analysis of Results. 7th International Workshop on Stability and Operational Safety of Ships.

Park, J. J., Kim, M. S., and Ha, M. K., 2005, Three-dimensional sloshing analysis of LNG carriers in irregular waves. 209-213.

Ran, Z., 2000, Coupled Dynamic Analysis of floating Structures in Waves and Currents. Ph.D. Dissertation.

Rognebakke, O. F., and Faltinsen, O. M., 2003, Coupling of sloshing and ship motions. Journal of Ship Research 47, 208-221.

Tahar, A., and Kim, M. H., 2003, Hull/mooring/riser coupled dynamic analysis and sensitivity study of a tanker-based FPSO. Applied Ocean Research 25, 367-382.

Tucker, M. J., Carter, D. J. T., and Challenor, P. G., 1984, Numerical simulation of random

sea: A common error and its effect upon wave group statistics. Applied Ocean Research 6, 118-122.

Wehausen, J. V., 1971, The motion of floating bodies. Annu. Rev. Fluid. Mech, 237-268.

Wichers, J. E. W., 1998, A simulation model for a single point moored tanker. Ph.D Dissertation, Delft University of Technology, The Netherlands.

Yang, C. Y., 1986, Random Vibration of Structures. Wiley-Interscience Publication, John Wiley & Sons, New York.

VITA

Seung Jae Lee was born in Busan, Korea. He graduated from Pusan National University with a Bachelor of Science in naval architecture and ocean engineering in February, 1996. He entered the graduate school at Pusan National University and received a Master of Science in ocean engineering in February, 1998. After graduation, he entered the graduate program at Texas A&M University in September, 2002 and received a Ph.D. in ocean engineering in May, 2008.

His permanent address is:

SsangYong Apt. 104-2201

Bugok-dong, Geumjeong-gu

Busan, Korea 607-062

E-mail address: sjzest@gmail.com